FLORIAN KRANZL

QUANTUM SIMULATIONS OF THE HEISENBERG MODEL WITH TRAPPED IONS

QUANTUM SIMULATIONS OF THE HEISENBERG MODEL WITH TRAPPED IONS

FLORIAN KRANZL

Thesis submitted to the
Faculty of Mathematics, Computer Science and Physics
of the
LEOPOLD-FRANZENS UNIVERSITY OF INNSBRUCK
in partial fulfillment
of the requirements for the degree of

DOCTOR OF PHILOSOPHY
(Physics)

Carried out under the supervision of

o. Univ.-Prof. Dr. Rainer Blatt
and
Assoz. Prof. Dr. Christian F. Roos

at the
Institute for Quantum Optics and Quantum Information (IQOQI)
of the Austrian Academy of Sciences
Technikerstraße 21a, 6020 Innsbruck, Austria

Innsbruck, October 2025

ABSTRACT

This PhD thesis presents quantum simulation experiments of the Heisenberg model. The experiments were carried out on a trapped-ion quantum simulator that is capable of operating with up to 50 individually addressable calcium ions. Quantum simulators of this size can be used to study complex quantum systems that begin to become intractable with classical computers.

First, long ion crystals are characterized and their collision rates and axial heating rates are measured. Correlation spectroscopy is applied to measure ion positions with a precision down to a few nanometers and the potential of the ion trap is extracted.

Motional spin-locking spectroscopy is introduced as a technique that allows one to directly measure the noise spectrum of the motional modes of a trapped ion. The noise spectrum is probed in a range from 200 Hz to 5 kHz, revealing both incoherent and coherent fluctuations in the trapping frequency.

The Heisenberg model is implemented using a Trotter approximation. Details are given on the Trotterization sequences and error mitigation strategies are discussed. Two quantum simulation experiments of the Heisenberg model are reported:

One experiment observes thermalization of a closed quantum system under the Heisenberg model. The existence of conserved quantities in the Heisenberg model that belong to mutually noncommuting operators impede previous theoretical predictions on the resulting thermal equilibrium. We observe the thermalization towards a non-Abelian thermal state for the first time in an experiment.

A second experiment observes the formation of bound states between quasiparticles in the long-range, anisotropic Heisenberg model. A quench of the pseudo-spins formed by the ion crystal reveals that the bound states spread in a light-cone-like fashion. The propagation velocity and the entanglement growth of the bound states are measured for different interaction strengths.

A brief outlook discusses upgrades the experiment will undergo when a new ion trap and a new vacuum chamber are going to be installed in the near future.

ZUSAMMENFASSUNG

In der vorliegenden Dissertation werden Quantensimulationen des Heisenberg-Modells präsentiert. Die Experimente wurden auf einem ionenbasierten Quantensimulator durchgeführt, der bis zu etwa 50 einzeln adressierbare Ionen kontrollieren kann. Quantensimulatoren dieser Größe eignen sich zur Untersuchung komplexer Quantensysteme, für welche klassische Rechnungen bereits sehr schwer werden.

Zunächst werden lange Ionenkristalle charakterisiert und deren Kollisionsraten und axiale Heizraten werden gemessen. Mittels Korrelationsspektroskopie bestimmen wir die Positionen der Ionen mit einer Präzision von wenigen Nanometern und ermitteln daraus Anharmonizitäten im Fallenpotential.

Spin-Locking-Bewegungsspektroskopie (Motional Spin-Locking Spectroscopy) wird als Technik eingeführt, die es erlaubt direkt das Rauschspektrum der Bewegungsmoden eines gefangenen Ions zu messen. Das Rauschspektrum wird in einem Bereich von 200 Hz bis 5 kHz aufgenommen, wobei sich sowohl inkohärente als auch kohärente Fluktuationen in der Fallenfrequenz nachweisen ließen.

Das Heisenberg-Modell wird mittels einer Trotter-Approximation implementiert. Dabei ist die Trotter-Sequenz in einer Form gestaltet, die die Reduktion von Rotations- und Dephasierungsfehlern ermöglicht. Es wird von zwei Quantensimulationsexperimenten des Heisenberg-Modells berichtet:

Ein Experiment beobachtet eine Thermalisierung innerhalb eines geschlossenen Quantensystems unter dem Heisenberg-Modell. Das Heisenberg-Modell besitzt Erhaltungsgrößen, welche zu untereinander nicht kommutierenden Observablen gehören. Dies führt dazu, dass sich bisher existierende theoretische Vorhersagen zum resultierenden thermischen Gleichgewichtszustand nicht auf das Heisenberg-Modell anwenden lassen. Wir beobachten die Thermalisierung hin zu einem nicht-Abelschen thermischen Zustand.

In einem zweiten Experiment wird die Bildung von gebundenen Zuständen zwischen Quasiteilchen im langreichweitigen, anisotropen Heisenberg-Modell beobachtet. Die zeitliche Dynamik von Pseudospins, welche durch die Ionenkette gebildet werden, zeigt, dass sich die gebundenen Zustände Lichtkegel-artig ausbreiten. Die Ausbreitungsgeschwindigkeit und das Verschränkungswachstum der gebundenen Zustände werden für verschiedene Wechselwirkungsstärken gemessen.

Die Arbeit schließt mit einem kurzen Ausblick auf ein anstehendes Upgrade des Experiments, in Zuge dessen eine neue Ionenfalle und eine neue Vakuumkammer installiert werden.

ACKNOWLEDGMENTS

All the work of an experimental physicist builds on generations of predecessors, the join efforts of the research group, and collaborators all over the world. It is only through this symbiosis that my PhD research has been possible. It is therefore my pleasure to express my gratitude to a number of people:

First of all, I would like to thank Rainer Blatt and Christian Roos for giving me the opportunity to work at a highly advanced experiment and to gain experiences that have been unique in my lifetime. Rainer steered the experiment to its successful state and created a group that provided all the support needed for this work. Christian guided our work in the laboratory and shared his detailed understanding of the experiment. He always found time to answer my questions and taught me how to develop a sense of finding the essence of a physics problem.

I want to thank my working colleagues of the quantum simulation experiment for kindly welcoming me in the team and all the work we carried out together. Namely, I want to thank: Our postdoc Manoj Joshi for introducing me to all bits and pieces of our experiment, for sharing his expertise and his experience, and for our countless discussions; My direct predecessors Christine Maier and Tiff Brydges, and my successor Johannes Franke for the exchange of knowledge and our time spent together in the lab.

I also want to thank the many members of the Blatt group who provided me with advice, discussions, and with a friendly environment. Out of many people, I want to name Dominik Kiesenhofer and Helene Hainzer who were lab neighbors at IQOQI at the beginning of my work.

This work was much facilitated by the professional and friendly environment created by the IQOQI. The administrative staff always helped us kindly and swiftly with bureaucracy, orders, and questions, for which I want to thank Elisabeth, Klaus, and Katrin. Of great help was our IT department, Valentin and David, who took care of our IT infrastructure, so I could focus on physics. And of course I want to thank our mechanical workshop and our electronics workshop: Having such technical expertise and capabilities in the same building was of great value for our experiment. I want to thank Andreas, Bernhard, David, and Tanja for many immaculate parts they have produced for us, and Gerhard for his help whenever I had an electronics problem.

Zu guter Letzt möchte ich meinen Eltern meinen tiefen Dank dafür aussprechen, mich in meinem Drang nach Wissen stets bestärkt und unterstützt zu haben — sie haben den Grundstein dafür gelegt, dass ich mir mit dieser Arbeit einen Traum verwirklichen konnte.

CONTENTS

1

INTRODUCTION

Nature is governed by the laws of quantum physics at its foundations. The behavior of atoms, molecules, light, solid matter, and many other constituents can only be understood by quantum physics. This makes it necessary to find solutions to the underlying equations. As only for a small minority of problems an analytical solution can be found, most practical problems need to be solved numerically. While this is certainly possible for small systems, large quantum systems are hard to compute numerically. The problem lies in the exponential growth of the dimension of the mathematical space that describes a quantum system. Consider a number of atoms where each atom can be in two states. Such a two-state quantum system is referred to as qubit. Adding another qubit *doubles* the dimension of the underlying mathematical space. Consequently, a system of 50 qubits has already a dimension of $2^{50} \approx 10^{15}$, surpassing the capabilities of classical computers.

Motivated by this situation, it was proposed in the 1980s to use a well-controlled quantum system to simulate another quantum system of interest [1]. Such a well-controlled quantum system is referred to as *quantum simulator*. One physical system that is used to build quantum simulators are ions trapped by electromagnetic fields. Trapped ions constitute a well-controllable system, with the ability to manipulate and detect the quantum state of individual ions with high fidelity.

A quantum simulator is only of practical interest, if it can surpass the capabilities of classical computers. In particular, this requires a quantum simulator to be comprised of a large number of qubits. In recent years, there is considerable experimental effort to scale quantum simulators to more qubits. For trapped-ion systems, sizes of more than 100 site-resolved qubits have been realized [2–4]. The experimental setup that was used for the work presented in this thesis holds one-dimensional ion crystals of up to approximately 50 trapped calcium-40 ions.

Scaling to a large number of trapped ions aggravates a number of problems: Increasing the number of ions increases the rate of collisions between ions and molecules of the background gas in the vacuum chamber. Collisions heat up the ion crystal, or, in the worst case, lead to a chemical reaction causing the atomic ion of interest to get lost. The spatial extent of large ion crystals makes addressing of individual ions difficult. Furthermore, the entangling interactions between the ions depend on the mass of the ion crystal and become weaker with increasing crystal mass.

However, scaling up the number of qubits is only one requirement for useful quantum simulators. Additionally, a quantum simulator needs to be able to

simulate interactions between qubits in order to be of interest. In our system, the interactions are engineered with laser fields, that use the motional modes of the ion crystal to couple the internal states of different ions. This creates spin-spin interactions that are of the type of the transverse Ising model. Naturally, the question arises whether other models can also be implemented on our quantum simulator? A widely studied model is the Heisenberg model, an extension of the Ising model that incorporates additional couplings. While the Heisenberg model is not natively available in our experiment, it can be approximated by a *Trotter approximation*.

A Trotter approximation splits the time evolution of a Hamiltonian into small building blocks to get an approximation of the exact evolution [5]. In the case of our experimental setup, we have access to the building blocks required to approximate the long-range Heisenberg model. A first proof-of-principle demonstration was done for a small ion crystal of up to six ions [6]. When working with larger ion crystals, complications arise, such as the inhomogeneous coupling of the laser light over the ion crystal which results in rotation errors. Care needs to be taken when designing Trotter sequences to mitigate these rotation errors. The present thesis describes Trotter sequences that exhibit certain robustness against rotation errors and dephasing noise. The Heisenberg model is implemented for systems of up to 21 ions and interactions between quasiparticles under the Heisenberg model are observed.

The second part of this thesis presents two experiments that study physics of the Heisenberg model. The first experiment observes thermalization under the Heisenberg model to test the consequences of noncommutation of operators of the Hamiltonian. The second experiment studies properties of bound states between quasiparticles in the anisotropic Heisenberg model.

The main part of this thesis is structured as follows:

Chapter 2 gives an overview over the theoretical concepts used in this thesis. The relevant energy levels of a calcium ion are presented and the Hamiltonians governing the light-atom interaction are given.

Chapter 3 presents the experimental setup and characterizes the behavior of long ion crystals. The implementation of a new beam shaping optics is described. The technique of correlation spectroscopy is applied to long ion crystals to precisely measure the ion positions in the crystal.

Chapter 4 gives an overview over the concept of Trotter approximation of Hamiltonians. Technical details on the Trotter approximation of the Heisenberg model are given and the leading sources of error are investigated. Finally, an example of a 21-ion quench dynamics under the Trotter-approximated Heisenberg model is presented.

Chapter 5 introduces a method for noise spectroscopy on the motional state of a trapped ion. The method is based on spin-locking spectroscopy and allows one to directly measure the power spectral density.

Chapter 6 reports on the first experimental observation of the thermalization under noncommuting charges. A subsystem of a closed quantum system of

up to 21 ions is found to thermalize towards the theoretically predicted form of the thermal state.

Chapter 7 studies the properties of bound states between quasi-particles in the long-range, anisotropic Heisenberg model. The formation of bound states is observed in dependence on the interaction strength between the magnons. The dispersion relation of a single magnon and of a two-magnon bound state is measured.

Chapter 8 provides a summary of the thesis and an outlook to future directions of the quantum simulation experiment.

2

THEORETICAL FRAMEWORK

This chapter gives an overview over the theoretical concepts that are used in this thesis. First, the concept of quantum simulation is introduced. Then, the notation for describing qubits is defined. The relevant level structure of $^{40}Ca^{+}$ is presented and discussed from the perspective of quantum optics experiments with trapped ions. Some basic properties of the physics of ion trapping are recapitulated. Then, the Hamiltonians that describe the interaction between a light field and trapped ions are presented. Finally, the entangling interactions and their Hamiltonians are given.

2.1 QUANTUM SIMULATIONS

Computation of large quantum systems is a difficult problem. The number of parameters that are required to describe a quantum system scales exponentially with its size. Only for a tiny fraction of problems analytical solutions could be found. Most problems can practically only be solved by making approximations or by numerical computation. The exponential scaling of the number of parameters makes it practically impossible to predict the behavior of large quantum systems. While classical computers can in principle solve every quantum physical problem, the computation times become prohibitively large.

This was the motivation to propose a new kind of computer: quantum computers, respectively quantum simulators [1]. A quantum simulator is a well-controllable quantum system that is used to make predictions about a quantum system of interest. The principle is sketched in Figure 2.1. A quantum system of interest is initially in a state $|\phi(0)\rangle$. The system evolves under a Hamiltonian H to a final state $|\phi(t)\rangle$. This final state might be hard to compute on a classical computer. Thus, a quantum simulator is used to mimic the behavior of the system. The initial state of the system is represented by a state $|\psi(0)\rangle$. Then, the quantum simulator undergoes a well-controlled evolution under a Hamiltonian H' that implements the behavior of the system. Finally, the time-evolved state $|\psi(t)\rangle$ of the simulator is measured. Properties of $|\psi(t)\rangle$ allow one to make predictions about the system.

Applications range from simulation of condensed-matter physics [7–10], chemistry [11–13], and high-energy physics [14]. This small selection only includes applications that have been demonstrated in proof-of-principle experiments. A far more exhaustive list of demonstrated and proposed applications can be found in Reference [15].

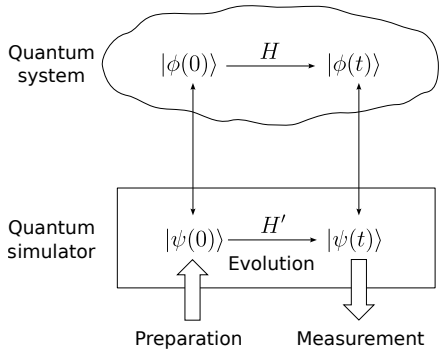

Figure 2.1: Quantum simulation. A quantum simulator mimics the behavior of a quantum system. The initial state $|\phi(0)\rangle$ of the system is represented by an initial state $|\psi(0)\rangle$ of the simulator. The behavior of the system is governed by a Hamiltonian H. In the simulator, the system Hamiltonian is realized by the Hamiltonian H'. The well-controlled evolution of the simulator gives a final state $|\psi(t)\rangle$ that can be measured and allows one to study properties of the system state $|\phi(t)\rangle$. Figure based on [15].

2.1.1 *Requirements for quantum simulators*

An experimental apparatus needs to satisfy a number of criteria to qualify as a quantum simulator. The following criteria for quantum simulators were suggested in Ref. [16]. A similar list of criteria tailored for quantum computers was given by Di Vincenzo [17]. The criteria below are commented from the perspective of trapped-ion quantum simulators.

1. **Large quantum system.** A quantum simulator is based on a well-controllable physical system. The system should be composed of a large number of constituents, i.e. a large number of degrees of freedom, to offer an advantage over classical computers. — Systems of trapped ions have reached sizes of more than 100 site-resolved ions [2–4].
2. **Initialization.** The quantum simulator needs to be initialized in a well-defined initial state. — The state of an ion can be initialized with high fidelity by optical pumping, see e.g. Ref. [18]. Creation of product states is possible with individual-ion operations using a tightly focused laser beam.
3. **Hamiltonian engineering.** The physical system has to be controlled according to a target Hamiltonian of interest. — Hamiltonians that act on the quantum state of ions can be realized with laser fields; Entangling operations may be mediated by the common motional modes of ion crystals.
4. **Detection.** After the system has evolved under the Hamiltonian under consideration, the resulting quantum state has to be detected. In most cases, detection of the states of individual particles is required. — The electronic state of an ion is detected with the electron-shelving technique with efficiencies close to unity [19, 20].
5. **Verification.** An important point is the verification of the result of a quantum simulation. At the time of writing this thesis, the primary outcomes of quantum simulations could still be calculated with classical computers, al-

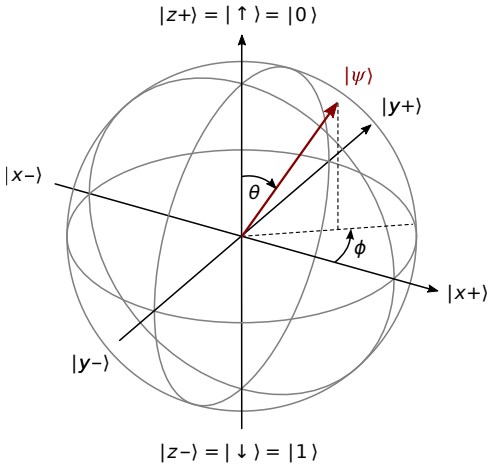

Figure 2.2: Visualization of a state $|\psi\rangle$ of a qubit on the Bloch sphere. A basis is formed by the states $|\uparrow\rangle$ and $|\downarrow\rangle$. States on opposite points on the sphere are orthogonal, contrary to geometric intuition. The state $|\psi\rangle$ is parameterized by two angles θ and ϕ.

beit under the use of approximation methods. This, however, contradicts the purpose of quantum simulators, i.e. having a tool that allows one to simulate systems that are not accessible with classical computers. As the capabilities of quantum simulators start to surpass those of classical computers, methods of verification become necessary. A number of ideas for verification protocols have been proposed and tested, including self-verification of a ground state via fluctuations [21], verification via Hamiltonian learning, cross-platform verification [22], and time-reversal of Hamiltonians [23].

2.2 QUANTUM STATES

In this section, a few basic concepts of the description of quantum states and their properties are recapitulated. In particular, the notation for qubits that is used in this thesis is defined.

2.2.1 *Qubits*

The basic building block in quantum information is the quantum bit, the qubit. The two base states of a qubit are $|0\rangle$ and $|1\rangle$ and are described by points in a two-dimensional complex-valued vector space and are denoted by

$$|0\rangle \doteq \begin{pmatrix} 1 \\ 0 \end{pmatrix} \quad \text{and} \quad |1\rangle \doteq \begin{pmatrix} 0 \\ 1 \end{pmatrix}. \tag{2.1}$$

Further commonly used notations are[1]

$$|0\rangle \equiv |\uparrow\rangle \equiv |z+\rangle \quad \text{and} \quad |1\rangle \equiv |\downarrow\rangle \equiv |z-\rangle\,. \tag{2.2}$$

1 The notation $|\uparrow\rangle$ ($|\downarrow\rangle$) refers to the two-level system (qubit) which is the same as a spin 1/2 system [24], whereas $|0\rangle$ ($|1\rangle$) refers to the ion being dark (bright) during fluorescence detection.

A qubit is equivalent to a spin-1/2 system [24] which allows one to describe the state of a qubit by the states $|uparrow\rangle$, $|downarrow\rangle$ of a (pseudo-)spin.

The state of a qubit can be visualized on a Bloch sphere, as shown in Figure 2.2. The basis states $|\uparrow\rangle$ and $|\downarrow\rangle$ are usually depicted as the north and the south pole, respectively. Two orthogonal states are on opposite points of the sphere, contrary to geometric intuition. Further noteworthy states are

$$|x\pm\rangle = \frac{1}{\sqrt{2}}\left(|\uparrow\rangle \pm |\downarrow\rangle\right) \quad \text{and} \quad |y\pm\rangle = \frac{1}{\sqrt{2}}\left(|\uparrow\rangle \pm \mathrm{i}\,|\downarrow\rangle\right), \tag{2.3}$$

which lie on the equatorial plane. In general, a pure state on the Bloch sphere is of the form

$$|\psi\rangle = \cos\left(\frac{\theta}{2}\right)|\uparrow\rangle + \mathrm{e}^{\mathrm{i}\phi}\sin\left(\frac{\theta}{2}\right)|\downarrow\rangle\,, \tag{2.4}$$

where θ is the angle between the state vector and the z axis, and ϕ is the angle between the projection of the state vector onto the equatorial plane and the x axis.

A mixed state is a probabilistic mixture of pure states. A mixed state is written as a density matrix, which is a convex combination of pure states,

$$\rho = \sum_i p_i\,|\psi_i\rangle\,\langle\psi_i|\,, \tag{2.5}$$

where $p_i \geq 0$ are the probabilities of preparing $|\psi_i\rangle$ in an experiment and $\sum_i p_i = 1$. Pure states are located on the surface of the Bloch sphere, while mixed states are located inside the sphere. In the extreme case, the fully mixed state is at the center of the sphere.

2.2.2 *Composite systems*

The state of a composite system is constructed by a linear combination of tensor products of states of the subsystems. If the states of subsystems are elements of Hilbert spaces $\mathcal{H}_1, \mathcal{H}_2, \ldots, \mathcal{H}_n$, then the state of the total system is an element of

$$\mathcal{H} = \mathcal{H}_1 \otimes \mathcal{H}_2 \otimes \cdots \otimes \mathcal{H}_n. \tag{2.6}$$

This property of composite systems leads to the exponential scaling of the dimension of the Hilbert space of the composite system. For example, a composite system of qubits doubles in dimension for every added qubit.

2.2.3 *Entanglement*

An important property of quantum systems of multiple particles is that they can exhibit the phenomenon of entanglement. In an entangled system, separate measurements on parts of the system are not sufficient to learn the state of the total system. Consider a system AB that is composed of two subsystems A and B. A pure bipartite state $|\psi_{AB}\rangle$ is entangled if and only if it cannot be written as a product state [25],

$$|\psi_{AB}\rangle \neq |\psi_A\rangle\,|\psi_B\rangle\,, \tag{2.7}$$

where $|\psi_A\rangle$ and $|\psi_B\rangle$ are the wavefunctions describing only the subsystems A and B, respectively. States that are not entangled are called separable. Examples of entangled states are the Bell states

$$|\phi^{\pm}\rangle = \frac{1}{\sqrt{2}}\left(|0_A 0_B\rangle \pm |1_A 1_B\rangle\right) \quad \text{and} \quad |\psi^{\pm}\rangle = \frac{1}{\sqrt{2}}\left(|0_A 1_B\rangle \pm |1_A 0_B\rangle\right). \tag{2.8}$$

In general, a mixed state of n systems is called entangled if it cannot be written as a convex combination of product states [26],

$$\rho \neq \sum_i p_i \rho_1^i \otimes \cdots \otimes \rho_n^i. \tag{2.9}$$

The creation of entanglement is a crucial aspect of quantum simulation experiments. In the case of our trapped-ion quantum simulator, entanglement between the internal quantum states of ions is created via mediation of the common motional modes of an ion crystal. An important question is how the presence of entanglement can be measured. For this purpose, a number of entanglement measures were constructed, see for instance Ref. [27].

2.3 TRAPPED CALCIUM IONS

Trapped ions offer an attractive platform for quantum information experiments. Ions can be trapped individually in electromagnetic traps and their motion can be cooled close to the motional ground state. Ions with a single outer electron — such as calcium ions — allow one to encode a qubit on two states of the outer electron. The quantum state of the ion can be manipulated and detected with high fidelity.

The following section gives a brief overview over the level scheme of calcium ions, trapping of charged particles, and the motional mode structure of long ion crystals.

2.3.1 *Level scheme of a calcium ion*

A single-ionized calcium atom has one electron in its outer shell, leading to a simple hydrogen-like energy level scheme. Figure 2.3(a) shows the level scheme of $^{40}Ca^{+}$. The relevant transitions for quantum information experiments lie in the optical range. The dipole-allowed $S_{1/2} \leftrightarrow P_{1/2}$ transition has a wavelength of 397 nm and is used for Doppler cooling [28–30] of the ion and for detection [31, 32] of the quantum state. The $P_{1/2} \leftrightarrow D_{3/2}$ transition at 866 nm needs to be driven for repumping during Doppler cooling and detection. The optical qubit is encoded in the subspace spanned by the levels $S_{1/2} \leftrightarrow D_{5/2}$ which are coupled by an optical quadrupole transition at 729 nm. This transition has a linewidth of only 1 Hz [33] as it is a dipole-forbidden transition. A fourth transition $P_{3/2} \leftrightarrow D_{5/2}$ at 854 nm is used for repumping during state preparation and sideband cooling.

More specifically, the qubit is encoded in the Zeeman sub-levels of the $S_{1/2}$ level and the $D_{5/2}$ level, as shown in Figure 2.3(b). In a magnetic field, the first-order Zeeman effect leads to a frequency shift between the Zeeman sub-levels [18],

$$\Delta\nu = \frac{\mu_B}{h}\left[g_j(D_{5/2})m' - g_j(S_{1/2})m\right] B, \tag{2.10}$$

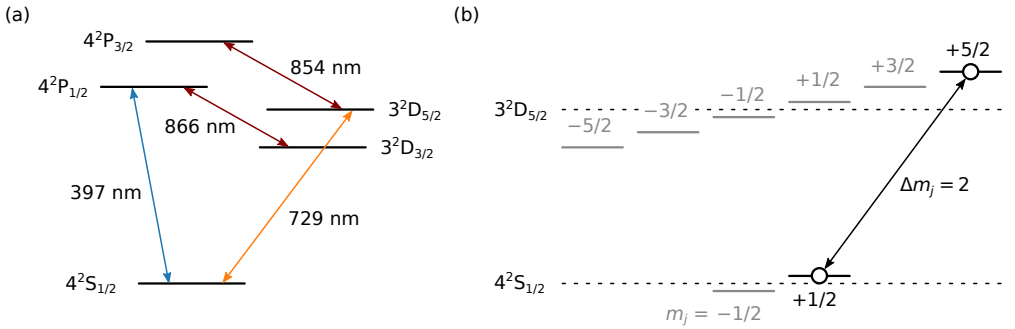

Figure 2.3: Level scheme of $^{40}Ca^+$. (a) A dipole transition at 397 nm is used for Doppler cooling of the ion and detection of the quantum state. Repumping during Doppler cooling is done at 866 nm. The qubit is manipulated with a laser on the quadrupole transition at 729 nm which has a linewidth of approx. 1 Hz. The dipole transition at 854 nm is used for state preparation and for quenching [34] during sideband cooling. (b) Zeeman levels. The qubit is encoded in the Zeeman levels $|S_{1/2}, m_j = 1/2\rangle \leftrightarrow |D_{5/2}, m_j = 5/2\rangle$ for most of the experiments presented in this thesis.

where μ_B is Bohr's magneton, h Planck's constant, g_j are the Landé g-factors of the respective levels, m' (m) is the magnetic quantum number of the $D_{5/2}$ ($S_{1/2}$) state, and B is the magnetic field strength. Numerical values for a $^{40}Ca^+$ ion are $\mu_B/h \approx 1.399\,\mathrm{MHz/G}$, $g_j(D_{5/2}) \approx 2$, and $g_j(S_{1/2}) \approx 1.2$. This encoding makes the qubit sensitive to magnetic field fluctuations, which are one of the main contributions to decoherence. For most measurements presented in this thesis, the qubit was encoded with the states $|1\rangle = |\downarrow\rangle = |S_{1/2}, m_j = 1/2\rangle$ and $|0\rangle = |\uparrow\rangle = |D_{5/2}, m_j = 5/2\rangle$. While this qubit has the highest magnetic field sensitivity, it is nevertheless attractive as it allows sideband cooling on a nearly closed transition and high coupling strengths between the qubit states can be achieved with the same laser beam [35, p. 40].

2.3.2 *Trapping of charged particles*

While a charged particle cannot be trapped with a constant electric field alone (Earnshaw's theorem), it is possible to trap it with an oscillating electric field [36–38]. The potential of an ion trap is shown in Figure 2.4(a). Two pairs of electrodes are supplied with oscillating voltages of opposite sign, creating a quadrupole field between the electrodes. The movement of a charged particle in this potential is described by the Mathieu equation. When operating the radio-frequency (r.f.) trap in the correct regime, a stable trajectory of the ion can be achieved. A single barium ion was first trapped in an r.f. trap consisting of a ring and two endcap electrodes [38]. A linear r.f. trap was later introduced [39], the so-called linear Paul trap, as sketched in Figure 2.4(b). Four r.f. blades create oscillating electric fields that confine the ions radially. Two tip electrodes create a constant electric field, for axial confinement. The linear Paul trap is particularly useful for confining long,

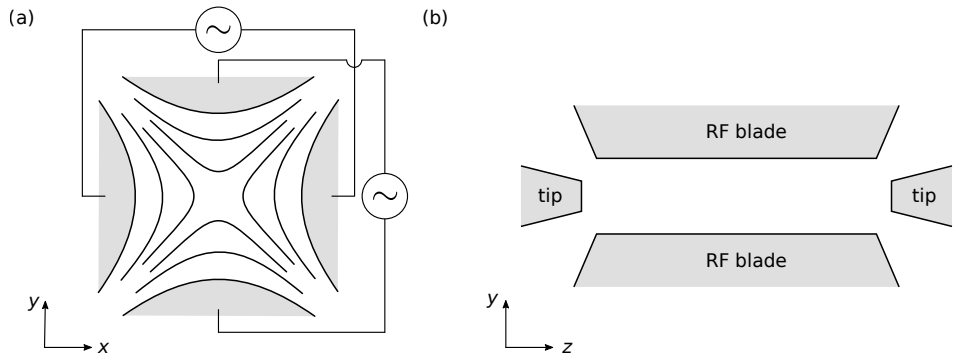

Figure 2.4: Ion trap. (a) Potential of a quadrupole field. The two pairs of electrodes are supplied with an oscillating voltage. (b) Linear Paul trap. Four radio-frequency (RF) blades create the quadrupole field for radial confinement, two tip electrodes supply a constant electric field for axial confinement.

linear crystals of ions. Details on the linear Paul trap used for the work presented in this thesis and its characterization can be found in the thesis of C. Hempel [18].

In the context of this thesis, describing a trapped ion as a quantum harmonic oscillator is sufficient. A quantum harmonic oscillator is described by the Hamiltonian

$$H^{(\mathrm{m})} = \frac{p^2}{2m} + \frac{1}{2}m\omega^2 x^2, \tag{2.11}$$

where m is the particle mass, ω the trapping frequency, p the momentum operator, and x the position operator. Using annihilation and creation operators a and $a^\dagger$, the Hamiltonian of a quantum harmonic oscillator can be expressed as

$$H^{(\mathrm{m})} = \hbar\omega\left(a^\dagger a + \frac{1}{2}\right). \tag{2.12}$$

The eigenstates of the quantum harmonic oscillator are the Fock states $|n\rangle$. For most experiments presented in this thesis, the ions are brought to the motional ground state $|0\rangle$. If multiple ions are trapped and cooled into a crystalline arrangement, their motion can be described by a set of collective motional modes (for more information, see Ref. [40]).

Combining the internal degrees of freedom of an ion, the electronic states or (pseudo-)spin states, with the external degrees of freedom, the motional states, gives joint spin-motional states. Figure 2.5) shows this process: The Hilbert space formed by the spin states and the Hilbert space formed by the motional states are combined by a tensor product into the Hilbert space of spin-motional states. The level scheme of spin-motional states is useful for the description of a trapped ion interacting with a light field, as this describes processes where light adds (removes) quanta of motional energy to (from) the system. An example of such a process is resolved sideband cooling, which is later discussed in Sec. 3.1.2.

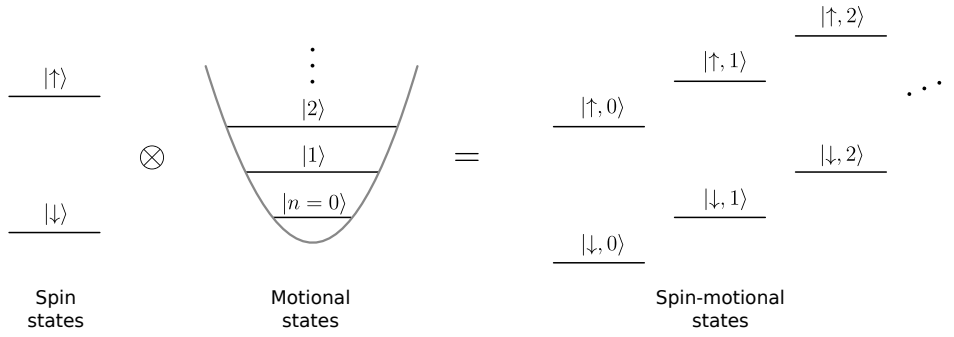

Figure 2.5: Combined level picture. Pseudo-spin states are formed by a two-level system of the electronic states of an ion (internal degrees of freedom). Motional states are formed by a quantum harmonic oscillator (external degrees of freedom). Combining both by a tensor product gives spin-motional states.

2.3.3 *Motional mode structure of long ion crystals*

The motional modes of an ion crystal are the result of the trapping potential and the Coulomb interaction between the ions. The equilibrium positions, the axial and radial mode structure and frequencies can be obtained from the Lagrangian of the system [41]. One aspect that is important for quantum simulation experiments with long ion crystals is the spatial arrangement of the ions. Ions arrange in a linear crystal only if the axial confinement is sufficiently weak compared to the radial confinement. For strong axial confinement, the crystal undergoes a phase transition to a zigzag configuration. Such transitions have been studied numerically [42, 43], analytically [44], and experimentally [45, 46]. For the quantum simulation experiments presented in this thesis, it is necessary that the crystal remains linear to realize a simple mode spectrum. In this section, numerical values for the maximally allowed axial confinement are given.

The potential energy of a crystal of N ions can be described by [47]

$$U = \frac{m}{2}\sum_{i=1}^{N}\left(\omega_x^2 x_i^2 + \omega_y^2 y_i^2 + \omega_z^2 z_i^2\right) + \frac{q^2}{4\pi\epsilon_0}\sum_{i=1,j>i}^{N}\frac{1}{r_{ij}} \tag{2.13}$$

where m is the ion mass, ω_x, ω_y, and ω_z are the radial trapping frequencies, x_i, y_i, and z_i are the coordinates of the ions, q is the ion charge, ϵ_0 is the electric field constant, and r_{ij} is the distance between two ions. The ratio between axial and radial trapping frequencies ($\omega_{\mathrm{rad}} = \omega_x = \omega_y$) is described by the parameter $\alpha = (\omega_z/\omega_{\mathrm{rad}})^2$. The resulting motional mode spectrum [40] for a 50-ion crystal with the (single-particle) trapping frequency $\omega_{\mathrm{rad}} = 2\pi \times 2.9\,\mathrm{MHz}$ is shown in Figure 2.6(a). For each axial trapping frequency, the eigenmode frequencies $\omega_{\mathrm{rad,eig}}$ are plotted, with the center-of-mass mode having the highest frequency. The lowest-frequency mode occurs at a frequency that depends on the axial confinement. The ion crystal remains linear as long as the lowest frequency mode has a frequency greater than zero. With increasing axial confinement, the radial mode spectrum spreads to lower and lower values, until the lowest radial

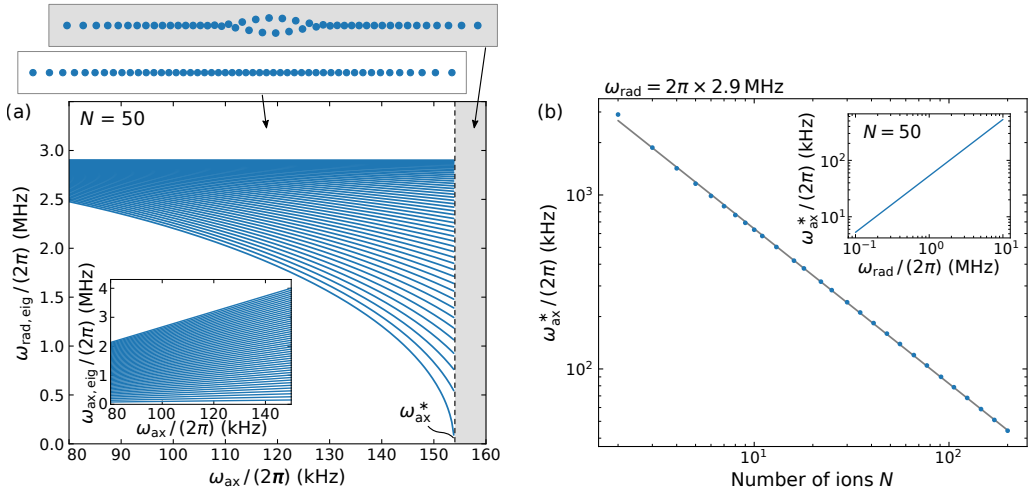

Figure 2.6: Motional mode structure of long ion crystals (numerical simulations). A 50-ion crystal is harmonically trapped with a radial (single-particle) trapping frequency $\omega_{\mathrm{rad}} = 2\pi \times 2.9\,\mathrm{MHz}$. (a) The radial motional eigenmode frequencies $\omega_{\mathrm{rad,eig}}$ are shown as a function of the axial trapping frequency ω_{ax}. With increasing axial frequency, the radial mode frequency spectrum spreads to lower values. At the transition frequency $\omega^*_{\mathrm{ax}} \approx 2\pi \times 154\,\mathrm{kHz}$, the crystal changes from a linear to a zigzag configuration (gray region). The inset shows the axial eigenmode frequencies. (b) Transition frequency vs. number of ions N (points). The solid line is a power-law fit of $\omega^*_{\mathrm{ax}} = (cN^{\beta})^{1/2}\omega_{\mathrm{rad}}$, where $\beta = -1.78$ and $c = 2.93$. Furthermore, ω^*_{ax} scales linearly with the radial trapping frequency (inset).

mode frequency becomes zero. At this transition frequency $\omega_{\mathrm{ax}}^{*} \approx 2\pi \times 154\,\mathrm{kHz}$, the crystal changes from a linear to a zigzag configuration.

The transition frequency ω_{ax}^{*} is evaluated as a function of the number of ions N, as shown in Figure 2.6(b). The dependency is well described by a power-law scaling, as first pointed out in Ref. [42] and experimentally observed with crystals of up to ten $^{40}Ca^{+}$ ions [46]. A least-squares fit of the ansatz $\omega_{\mathrm{ax}}^{*} = (cN^{\beta})^{1/2}\omega_{\mathrm{rad}}$ to the numerical simulation yields the parameters $\beta = -1.78$ and $c = 2.93$, in agreement with Ref. [46] and rough agreement with Ref. [42].

The requirement of low axial confinement to achieve linear ion crystals makes working with long ion crystals increasingly difficult. For example, a 100-ion crystal at 2.9 MHz radial trapping frequency requires an axial trapping frequency of less than 82 kHz. However, with such low trapping frequencies, technical difficulties such as axial heating rates become more problematic. Axial heating rates $\mathrm{d}\bar{n}/\mathrm{d}t$ typically depend on the axial trapping frequency by a polynomial function of the form $\mathrm{d}\bar{n}/\mathrm{d}t \propto \omega_{\mathrm{ax}}^{\alpha}$ with most experiments having an exponent lying between $\alpha \approx 0.5 \ldots 2$ [48]. Therefore, if the axial trapping frequency is set to low values, the axial heating rate can quickly become unacceptably high.

2.4 LIGHT-ATOM INTERACTION

In this section, some basic properties of light-atom interactions are given. First, interactions of light with the free atom are described; then interactions of light with the trapped atom. The structure of this section follows Ref. [19].

2.4.1 *Free atom interacting with light*

The Hamiltonian of a free ion that is interacting with a classical light field is composed of a part $H^{(\mathrm{e})}$ describing the electronic structure of the atom and a part $H^{(\mathrm{i})}$ describing the interaction between light and atom,

$$H = H^{(\mathrm{e})} + H^{(\mathrm{i})}. \tag{2.14}$$

For many cases, the relevant electronic structure is that of a two-level system,

$$H^{(\mathrm{e})} = \hbar\frac{\omega_0}{2}\sigma_z, \tag{2.15}$$

where σ_z is the Pauli z operator, ω_0 is the transition frequency between the two levels, and $\hbar$ is the reduced Planck's constant. Here, the energy offset $\frac{\hbar}{2}(\omega_{\mathrm{e}} + \omega_g)(|g\rangle\langle g| + |e\rangle\langle e|)$ has been subtracted, where $|g\rangle$ is the atom's ground level and $|e\rangle$ is the atom's excited level. The interaction Hamiltonian for a quadrupole transition depends on the gradient of the electric field and is of the form [49]

$$H_{\mathrm{Q}}^{(\mathrm{i})} = -\boldsymbol{Q}\cdot\boldsymbol{\nabla}\boldsymbol{E}(\boldsymbol{r}), \tag{2.16}$$

where $\boldsymbol{Q}$ is the atomic quadrupole moment operator and $\boldsymbol{E}(\boldsymbol{r})$ the electric field at position $\boldsymbol{r}$. For an atom interacting with a traveling-wave laser field along the

x-direction, this Hamiltonian can be brought into a simple form [19, 50] which couples the ground state $|g\rangle$ and the excited state $|e\rangle$,

$$H^{(\mathrm{i})} = \frac{\hbar}{2}\Omega(\sigma^+ + \sigma^-)\left(\mathrm{e}^{\mathrm{i}(kx-\omega t+\phi)} + \mathrm{e}^{-\mathrm{i}(kx-\omega t+\phi)}\right) \tag{2.17}$$

$$= \hbar\Omega\sigma_x \cos\left(kx - \omega t + \phi\right), \tag{2.18}$$

where Ω is the Rabi frequency, $\sigma^+ = |e\rangle\langle g|$ ($\sigma^- = |g\rangle\langle e|$) is the raising (lowering) operator, k the wavenumber, x the position operator, ω the frequency of the light field, t is time, and ϕ is a global light phase. The Rabi frequency contains the information on the quadrupole transition, the light polarization and propagation direction. A general expression for the Rabi frequency can be found in Ref. [40] and its evaluation for the quadrupole transition in $^{40}Ca^+$ in Ref. [51, 52]. A geometric form factor takes the light's polarization and propagation direction into account [51].

Hamiltonian (2.17) can be transformed into the interaction picture with respect to $H_0 = \hbar\omega_0/2\sigma_z$ which yields, after a rotating-wave approximation, the Hamiltonian describing the interaction between a free atom and a light field [18],

$$H_{\mathrm{int}} = \hbar\frac{\Omega}{2}\left[\cos(\Delta t + \phi)\sigma_x + \sin(\Delta t + \phi)\sigma_y\right] \tag{2.19}$$

$$= \hbar\frac{\Omega}{2}\left(\mathrm{e}^{-\mathrm{i}(\Delta t+\phi)}\sigma^+ + \mathrm{e}^{\mathrm{i}(\Delta t+\phi)}\sigma^-\right). \tag{2.20}$$

Here, the detuning between the light field and the atomic transition has been introduced, $\Delta = \omega - \omega_0$.

2.4.2 *Single-qubit operations*

On resonance ($\Delta = 0$), Hamiltonian (2.19) leads to the time-evolution operator

$$U(\theta,\phi) = \begin{pmatrix} \cos\left(\frac{\theta}{2}\right) & -\mathrm{i}\mathrm{e}^{-\mathrm{i}\phi}\sin\left(\frac{\theta}{2}\right) \\ -\mathrm{i}\mathrm{e}^{\mathrm{i}\phi}\sin\left(\frac{\theta}{2}\right) & \cos\left(\frac{\theta}{2}\right) \end{pmatrix}. \tag{2.21}$$

This operator describes a rotation around an axis that lies in the equator, separated by an angle ϕ from the x axis [Fig. 2.7(a)]. The rotation angle is given by $\theta = \Omega t$. Such rotations of the state vector are referred to as Rabi flops. Consider a qubit that is initially prepared in the state $|\downarrow\rangle$. Then the probability of finding the qubit in the state $|\uparrow\rangle$ at time t is $p_\uparrow = |\langle\uparrow|U(t)|\downarrow\rangle|^2$ and evaluates to

$$p_\uparrow = \sin^2\left(\frac{\Omega t}{2}\right) = \frac{1}{2} - \frac{1}{2}\cos(\Omega t). \tag{2.22}$$

In the limiting case of large detuning ($\Delta \gg \Omega$), the light field gives rise to an ac-Stark shift on the qubit transition,

$$\delta_{\mathrm{ac}} = -\frac{\Omega^2}{2\Delta}. \tag{2.23}$$

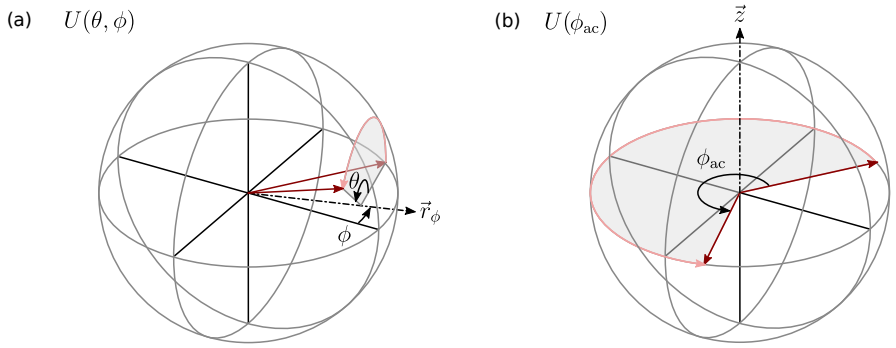

Figure 2.7: Operations on a qubit. (a) Resonant operation. A resonant light field implements a rotation $U(\theta,\phi)$ around an axis $\boldsymbol{r}_\phi$ in the equatorial plane. (b) Far off-resonant operation. A far-off-resonant light field leads to a rotation $U(\phi_{AC})$ around the z axis. The rotation angle $\phi_{ac} = \delta_{ac}t$ is given by the detuning δ_{ac} and the interaction time t.

Then the atom-light interaction can be described by the approximate time-evolution operator

$$U_{ac} = \begin{pmatrix} e^{-i\frac{\delta_{ac}}{2}t} & 0 \\ 0 & e^{i\frac{\delta_{ac}}{2}t} \end{pmatrix}. \tag{2.24}$$

This operator gives rise to rotations around the z axis [Fig. 2.7(b)].

An important application is the single-ion addressing with a tightly focused laser beam. Consider a qubit in a pure state that lies in the equatorial plane, described by $|\psi_0\rangle = (|\uparrow\rangle + e^{i\phi}|\downarrow\rangle)/\sqrt{2}$. The far off-resonant light field rotates the state to $|\psi_1\rangle = U_{ac}|\psi_0\rangle = (e^{-i\delta_{ac}t/2}|\uparrow\rangle + e^{i(\phi+\delta_{ac}t/2)}|\downarrow\rangle)/\sqrt{2}$. A global phase of a quantum state has no physical relevance and can be suppressed. Thus, the final state after an ac-Stark shift operation is

$$|\psi\rangle = (|\uparrow\rangle + e^{i(\phi+\delta_{ac}t)}|\downarrow\rangle)/\sqrt{2}, \tag{2.25}$$

describing a rotation around the z-axis by an angle $\phi_{ac} = \delta_{ac}t$.

2.4.3 *Trapped atom interacting with light*

A trapped ion has motional states that can take part in the interactions between the ion and the light field. Eventually, motional states are used to mediate entangling interactions between different ions. The total Hamiltonian of a trapped ion, interacting with a light field is

$$H = H^{(m)} + H^{(e)} + H^{(i)}, \tag{2.26}$$

where in addition to (2.14) the motional Hamiltonian $H^{(m)}$ appears. It is of the simple form of a harmonic oscillator, $H^{(m)} = \hbar\omega(a^\dagger a + \frac{1}{2})$. By a number of approximations [19], this Hamiltonian can be brought into a simple form. First, the Hamiltonian is transformed into the interaction picture with respect to $H_0 = H^{(m)} + H^{(e)}$. Next, by applying a rotating-wave approximation, rapidly

oscillating terms are neglected. Finally, the Hamiltonian can be conveniently described by introducing the Lamb-Dicke parameter $\eta = kx_0$ and replacing the position operator by a and $a^\dagger$, leading to

$$H_{\text{int}}(t) = \frac{\hbar}{2}\Omega_0\sigma^+ e^{i\eta(ae^{-i\nu t}+a^\dagger e^{i\nu t})}e^{i(\phi-\Delta t)} + \text{h.c.} \tag{2.27}$$

The Lamb-Dicke parameter quantifies the extension of the motional ground-state[2] $x_0 = \sqrt{\hbar/(2m\omega_t)}$. This Hamiltonian can drive transitions between different motional states. When resonantly coupling to one of the sidebands, $\Delta = m\nu$, the coupling strength is [19, 30]

$$\Omega_{n,n+m} = \Omega_{n+m,n} = \Omega_0 e^{-\frac{1}{2}\eta^2}\eta^{|m|}\sqrt{\frac{n_<!}{n_>!}}L_{n_<}^{(|m|)}(\eta^2), \tag{2.28}$$

where $n_<$ ($n_>$) is the lesser (greater) of $n+m$ and n, $L_n^{(\alpha)}$ is the generalized Laguerre polynomial. The Hamiltonian simplifies further if the ion is in the Lamb-Dicke regime, i.e. the wave packet extension is much smaller than the wavelength of light $\eta\sqrt{\langle(a+a^\dagger)^2\rangle} \ll 1$. Then, the interaction Hamiltonian is approximated by

$$H_{\text{int}}(t) = \frac{\hbar}{2}\Omega_0\sigma^+\left[1 + i\eta(ae^{-i\nu t} + a^\dagger e^{i\nu t})e^{i(\phi-\Delta t)}\right] + \text{h.c.} \tag{2.29}$$

This Hamiltonian gives rise to carrier and sideband transitions with a phonon-dependent coupling strength:

- First red sideband transition ($m = -1$), $|g\rangle|n\rangle \leftrightarrow |e\rangle|n-1\rangle$:
  $\Omega_{n,n} = \Omega_0\eta\sqrt{n}$
- Carrier transition ($m = 0$), $|g\rangle|n\rangle \leftrightarrow |e\rangle|n\rangle$:
  $\Omega_{n,n} = \Omega_0$
- First blue sideband transition ($m = +1$), $|g\rangle|n\rangle \leftrightarrow |e\rangle|n+1\rangle$:
  $\Omega_{n,n} = \Omega_0\eta\sqrt{n+1}$

2.4.4 *Entangling interactions*

The electronic states (spins) of multiple ions can be entangled using the common motional modes as a mediator. A light field creates a coupling between different ions that depends on their spin states[53]. As the coupling is mediated by the motional modes, the properties of the entangling interactions depend on the motional modes' structure. By changing the detuning of the light field from the motional modes, the entangling interactions can be tuned from longer to shorter range [54].

The scheme that creates spin-spin interactions is shown in Figure 2.8(a). A N-ion crystal is radially confined with a trapping frequency ω_{rad}. The two radial axes x and y give rise to $2N$ radial motional modes. The interactions are mediated via these radial motional modes: A light field couples the internal electronic states of the ions to the motional modes of the ion crystal. As the motional

2 A single $^{40}Ca^+$ ion trapped at $\omega_t = 2\pi \times 2.9\,\text{MHz}$ has a ground-state extension of $x_0 = 6.6\,\text{nm}$.

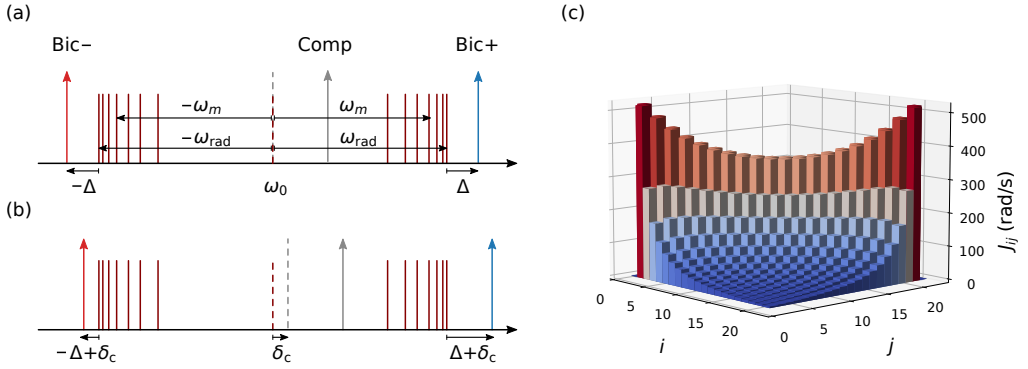

Figure 2.8: Long-range spin-spin interaction. (a) Entangling interactions between ions are mediated via the radial motional sidebands. A light field consists of two frequency components, forming a bichromatic beam. Two components, Bic+ and Bic−, are detuned by a frequency Δ from the center-of-mass mode. The radial trapping frequency is ω_{rad} and the radial mode frequencies are ω_m. A third component, Comp, is used for compensation of the ac-Stark shift. (b) An additional centerline detuning δ_c allows for tuning between the XX model ($\delta_c = 0$), the transverse field Ising model ($|\delta_c| > 0$), and the XY model ($|\delta_c| \gg 0$). (c) The bichromatic light field gives rise to approximate power-law interactions with coupling strength J_{ij} between ion i and j [Eq. (2.37)]. Example of J_{ij} for 21 ions with $\Omega = 2\pi \times 109\,\mathrm{kHz}$, $\Delta = 2\pi \times 27\,\mathrm{kHz}$, $\omega_x = 2\pi \times 2.93\,\mathrm{MHz}$, $\omega_y = 2\pi \times 2.90\,\mathrm{MHz}$, $\omega_{\mathrm{ax}} = 2\pi \times 0.22\,\mathrm{MHz}$, and $\theta = 45°$.

modes are *common* motional modes, the internal states of different ions affect each other, resulting in interactions between the spin states of the ions. The ion crystal is illuminated with a light field that contains two frequency components (Bic+ and Bic−) that are each detuned by a frequency Δ from the center-of-mass (c.o.m.) mode frequency. This bichromatic light field couples to each of the motional modes of frequency ω_m. A third frequency component (Comp) is used for compensation of ac-Stark shifts.[3] By shifting both frequencies of the bichromatic light field by an amount δ_c from the carrier frequency ω_0 the interactions can be modified [Figure 2.8(b)]. This detuning δ_c is called centerline detuning. Three cases are particularly relevant:

$\underline{\delta_c = 0}$: The detuning of both frequency components Bic+ and Bic− of the bichromatic light field is symmetric around the motional mode structure. This setup gives rise to long-range spin-spin interactions that realize the XX model,

$$H_{\mathrm{XX}} = \sum_{i<j} J_{ij} \sigma_x^{(i)} \sigma_x^{(j)}, \tag{2.30}$$

where J_{ij} is the spin-spin coupling matrix, and $\sigma_x^{(i)} = \mathbb{1} \otimes \cdots \otimes \mathbb{1} \otimes \sigma_x \otimes \mathbb{1} \otimes \cdots \otimes \mathbb{1}$, with σ_x occurring at the i^{th} place of the tensor product, is the Pauli matrix that acts on ion i.

3 Typical values in our experiment are $\omega_{\mathrm{rad}} \approx 2\pi \times 2.9\,\mathrm{MHz}$, $\Delta \approx 2\pi \times 20 \ldots 40\,\mathrm{kHz}$, $\omega_{\mathrm{Comp}} \approx 2\pi \times 1.4\,\mathrm{MHz}$.

$|\delta_c| > 0$ and $|\delta_c| \ll \Delta$: An additional transverse field term leads to the transverse Ising model,

$$H_{\text{Ising}} = \sum_{i<j} J_{ij}\sigma_x^{(i)}\sigma_x^{(j)} + \sum_i B_i\sigma_z^{(i)}, \tag{2.31}$$

where the magnetic field term B_i consists of the centerline detuning δ_c and single-ion level shifts[4] $B_i = -\frac{1}{2}(\delta_c + \delta_i)$.

$|\delta_c| \gg J_0$ and $|\delta_c| \ll \Delta$: Setting the centerline detuning much larger than the coupling strength realizes the XY model in the rotating-frame approximation,

$$H_{\text{XY}} = \frac{1}{2}\sum_{i<j} J_{ij}\left(\sigma_x^{(i)}\sigma_x^{(j)} + \sigma_y^{(i)}\sigma_y^{(j)}\right). \tag{2.32}$$

The coupling strength between two spins is described by the coupling matrix [53, 57]

$$J_{ij}^{(q)} = \Omega_i\Omega_j \sum_{m=1}^{N} \eta_{i,m}^{(q)}\eta_{j,m}^{(q)} \frac{\omega_m^{(q)}}{\left(\omega_{\text{rad}}^{(q)} + \Delta^{(q)}\right)^2 - \left(\omega_m^{(q)}\right)^2} \tag{2.33}$$

for the two transverse trapping axes $q = x, y$. The coupling strength Ω_i is the Rabi frequency of ion i when one component of the bichromat beam is driving the carrier transition resonantly. The total coupling matrix is the sum over both axes, $J_{ij} = J_{ij}^{(x)} + J_{ij}^{(y)}$. The Lamb-Dicke parameter for each ion i is

$$\eta_{i,m}^{(q)} = k\cos\left(\theta^{(q)}\right) b_{i,m}^{(q)} \sqrt{\frac{\hbar}{2M\omega_m^{(q)}}}, \tag{2.34}$$

where k is the wavenumber of the light, $\theta^{(q)}$ is the angle between the k vector of the light and the $q = x$ axis (respectively the y axis), $(b_{i,m})$ the normalized eigenvector of mode m with eigenfrequency ω_m, and M the mass of a single ion. An example of the coupling matrix for a 21-ion crystal is shown in Figure 2.8(c).

The presence of the third tone for ac-Stark compensation alters the coupling matrix J_{ij} [58]. This effect becomes noticeable when the third tone is placed in proximity to the lowest motional mode. For instance, for a 51-ion chain confined at $\omega_x = 2\pi \times 2.93\,\text{MHz}$ and $\omega_{\text{ax}} = 2\pi \times 128\,\text{kHz}$, the lowest radial mode is at 1.6 MHz. Placing the third tone at 1.4 MHz already creates a noticeable effect on the spin-spin interactions, which needs to be taken into account by an additional term in Eq. (2.33). The coupling matrix then becomes [58]

$$J_{ij}^{(q)} = \Omega_i\Omega_j \sum_{m=1}^{N} \eta_{i,m}^{(q)}\eta_{j,m}^{(q)} \frac{\omega_m^{(q)}}{\left(\omega_{\text{rad}}^{(q)} + \Delta^{(q)}\right)^2 - \left(\omega_m^{(q)}\right)^2} + \tag{2.35}$$

$$\frac{1}{2}\Omega_i^{(c)}\Omega_j^{(c)} \sum_{m=1}^{N} \eta_{i,m}^{(q)}\eta_{j,m}^{(q)} \frac{\omega_m^{(q)}}{\left(\omega^{(c)}\right)^2 - \left(\omega_m^{(q)}\right)^2}, \tag{2.36}$$

where $\Omega_i^{(c)}$ is the Rabi frequency of the compensation beam of ion i when driving the carrier transition resonantly and $\omega^{(c)}$ is the detuning of the compensation beam from the two-level atomic transition.

4 For example quadrupole shifts [55, 56]

For practical purposes, it is often enough to work with a power-law approximation of the spin-spin coupling matrix. The interaction strength between the spins can be approximated by a (empirical) power-law decay [10],

$$J_{ij} \approx \frac{J_0}{|i-j|^\alpha}, \tag{2.37}$$

where $J_0 = \max_{i,j}(J_{ij})$ is the maximum coupling strength. The exponent α theoretically ranges from $\alpha = 0$ (detuning $\Delta \to 0$) to $\alpha = 3$ ($\Delta \to \infty$) [54]. In practice, the range used in experiments is $\alpha \approx 0.7 \ldots 1.4$. Smaller values of α are problematic as the bichromatic beam gets too close to the c.o.m. mode and starts to directly drive transitions on the sidebands.[5] Larger values of α are problematic as the coupling strength decreases and the accessible maximal evolution time drops.

5 See Fig. 4.8 for measurement data of the error rate.

3

CHARACTERIZATION OF LONG ION STRINGS

Parts of the work presented here is published in
Physical Review A **105**, 052426 (2022)
Physical Review X **14**, 011033 (2024)

Long crystals of trapped ions offer an attractive platform for quantum simulations: Ions are identical quantum objects and can be manipulated and their state can be detected with high fidelity. Entanglement between ions can be created. System sizes of tens of ions can be realized – well beyond the limit that can be simulated with classical computers. Experimental challenges arise when scaling the system size from a few to tens of ions. The progress that enabled the extension to 50 ions is described in the theses that the present work is built upon [18, 35, 59, 60].

In the present chapter, I give an experimental characterization of long ion strings of up to 52 ions. First, an overview of the experimental setup is provided. Then, collisions of background gas molecules with the ion crystal and axial heating rates are measured. The error source of tilted wavefronts in light-ion interactions is demonstrated and an optical setup that solves this problem is presented. Correlation spectroscopy is used to measure ion positions with a precision of a few nanometers and to investigate anharmonicity in the trapping potential. Finally, the technical implementation of the Trotter approximation of the Heisenberg model is discussed.

3.1 EXPERIMENTAL SETUP

The experimental setup that was used in this thesis has been set up and extended by a number of PhD students and postdocs in the past ten years. Details on the setup can be found in References [18, 35, 59, 60]. In this section, I will give a short overview of the experimental setup. The Quantum Simulation experiment is shown in Fig. 3.1. The setup spans over two optical tables. The main optical table contains the vacuum chamber that is located inside a mu-metal shield.

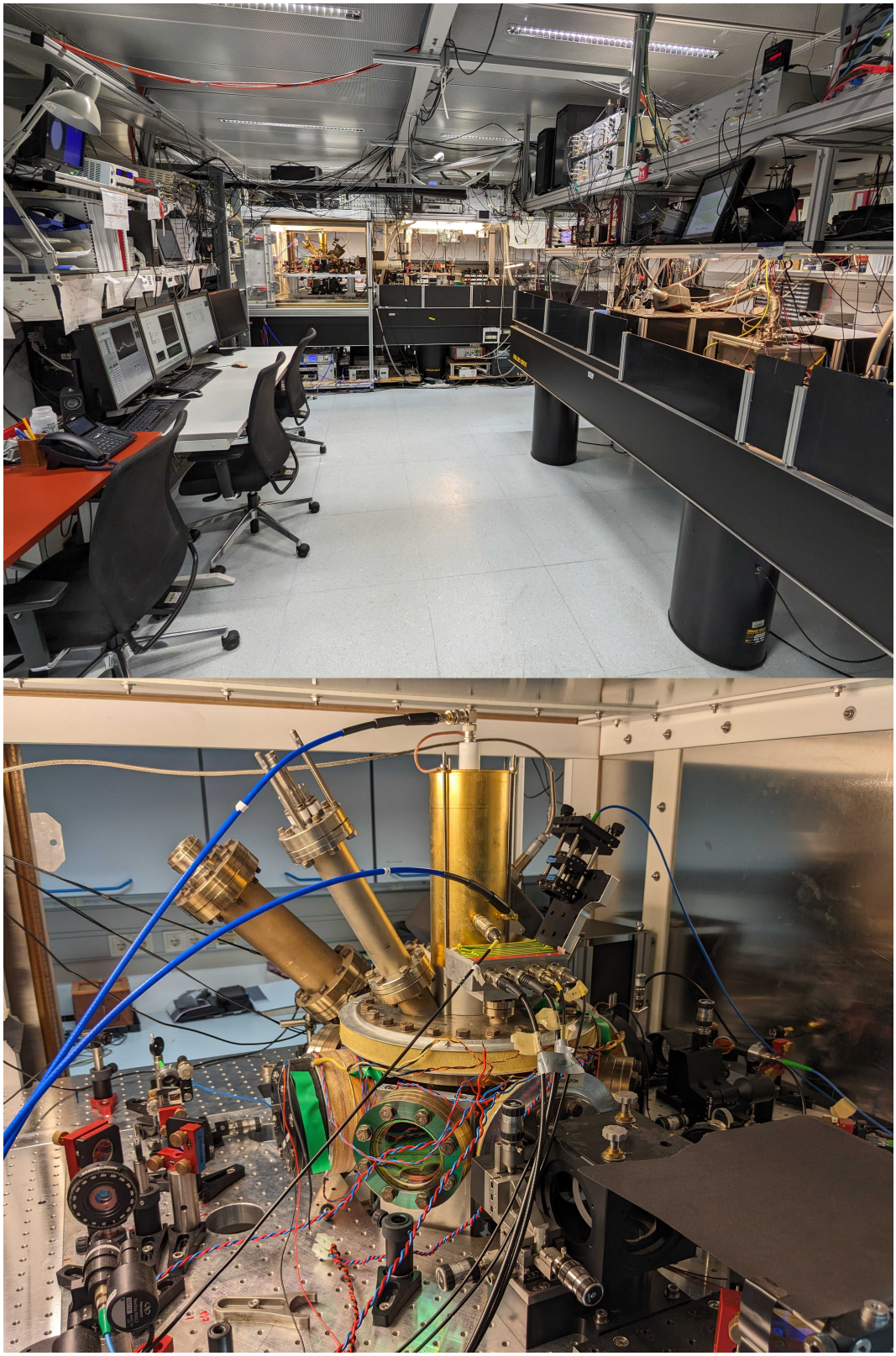

Figure 3.1: The Quantum Simulation experiment at IQOQI, Innsbruck (October 2024). Top: Control station, main optical table containing the vacuum chamber, and optical table containing cooling, repumping, and photoionization lasers (from left to right). Bottom: Vacuum chamber containing the ion trap.

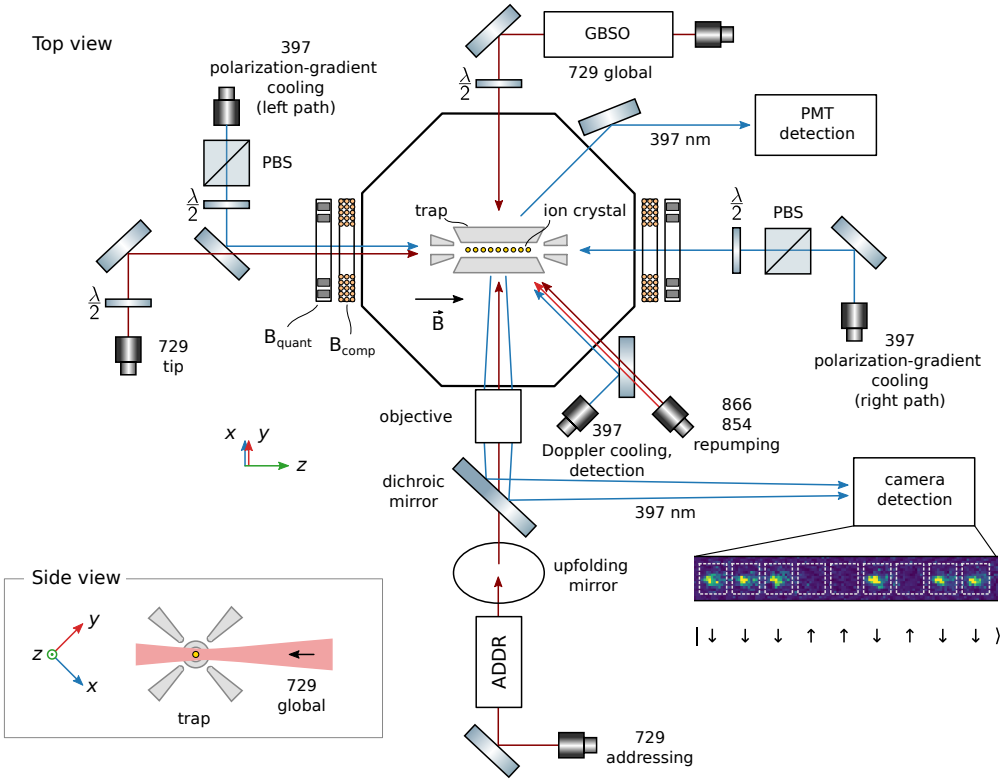

Figure 3.2: Experimental setup. The ion trap is inside a vacuum chamber with optical access. Cooling and state manipulation of the ion crystal is done by a number of laser beams with wavelengths of 397 nm, 866 nm, 729 nm, and 854 nm, respectively. The magnetic field B_{quant} that defines the quantization axis is created by permanent magnets, a compensation field B_{comp} by a pair of coils. Global operations on the ions are performed by a global 729 nm beam. This beam is shaped into an elliptical beam while maintaining plane wavefronts by a global beam shaping optics (GBSO). Single-ion operations are done by a tightly focused 729 nm beam that is controlled by an addressing optics (ADDR). The quantum state after an experiment is detected by a photomultiplier tube (PMT) and by a camera which images the ion crystal through an objective.

3.1.1 *Ion trap and magnetic field*

The heart of the experimental setup is the ion trap situated in a vacuum chamber, as shown in Figure 3.2. An ion crystal of up to 60 ions is trapped in a linear Paul trap. The radial confinement is achieved with oscillating r.f. fields. The electric radio-frequency (r.f.) signal has a frequency of 28.8 MHz with a power of approximately 7 W fed into a helical resonator, leading to a radial trapping frequency of $\omega_{\mathrm{rad}} \approx 2\pi \times 2.9\,\mathrm{MHz}$. The axial confinement is achieved by a constant electrical field that is applied to the tip electrodes. The voltages at the tip electrodes are in the range $U_{\mathrm{tip}} = 6\,\mathrm{V} \ldots 500\,\mathrm{V}$, leading to axial trapping frequencies between 90 kHz and 0.9 MHz. Details on the Paul trap used in our setup and its characterization can be found in Ref. [18].

The ion trap is placed inside a vacuum chamber. The vacuum is maintained by continuous pumping by an ion pump and a non-evaporable getter. The pressure of the background gas is approximately 2×10^{-11} mbar at the location of the ion.[1] The quantization axis is set by a magnetic field which is provided by a pair of arrays of permanent magnets [60]. Using permanent magnets has the advantage that they can provide a more stable magnetic field than the previously used coil, as permanent magnets do not require a stabilized electrical current. The permanent magnets are samarium-cobalt magnets and provide a magnetic field strength of 4.18 G at the position of the ion crystal. The direction of the magnetic field defines the z axis of the coordinate system used in this thesis.

One pair of coils is still used to apply a magnetic field for compensation of ambient time-varying magnetic fields [61, 62]. The ions are used as a sensor to probe the magnetic field. Then, a compensation field of same strength but opposite phase is applied to cancel magnetic field variations. This approach is possible as the ambient time-varying magnetic fields are mainly caused by currents of electric appliances in the laboratory oscillating at integer multiples of 50 Hz that were found to remain constant over weeks.

3.1.2 *Cooling of the ion crystal*

The ions are cooled by three different laser cooling techniques: Doppler cooling, polarization-gradient cooling, and sideband cooling.

1. **Doppler cooling.** First, the ions are cooled by Doppler cooling for typically 3 ms. For a two-level atom, the temperature limit of Doppler cooling is $T_{\mathrm{Doppler}} = \hbar\gamma/(2k_{\mathrm{B}})$ for the maximum cooling rate that is achieved by setting the laser detuning to half of the natural linewidth γ [30]. Here, k_{B} is the Boltzmann constant. For $^{40}\mathrm{Ca}^{+}$, we use the dipole transition $4^2\mathrm{S}_{1/2} \leftrightarrow 4^2\mathrm{P}_{1/2}$ at 397 nm which has a natural linewidth of $\Gamma = 2\pi \times 22.4\,\mathrm{MHz}$ [63]. This results in a temperature limit[2] of $T_{\mathrm{Doppler}} \approx 0.5\,\mathrm{mK}$. In our experiments, we observe slightly higher temperatures that we attribute to the multi-level

1 This pressure is estimated from the rate of collisions between background gas and a trapped ion.

2 The mean phonon number $\langle\bar{n}\rangle$ at this temperature limit is $\langle\bar{n}\rangle = k_{\mathrm{B}}T_{\mathrm{Doppler}}/(\hbar\omega)$, with a trapping frequency $\omega = 2\pi \times 3\,\mathrm{MHz}$ yielding $\langle\bar{n}\rangle \approx 3.5$.

system coupled by the Doppler cooling beams. The cooling beam illuminates the ion crystal at a 45° angle (Fig. 3.2). This direction overlaps with all trap axes, and in combination with lifting of the degeneracy of the radial trapping frequencies, ensures cooling along all three spatial directions.

2. **Polarization-gradient cooling.** As a second cooling step, polarization-gradient cooling is applied to cool the ion crystal along the axial direction [64]. The motion is cooled to a few phonons. A typical mean phonon number after polarization-gradient cooling of a 51-ion crystal at an axial trapping frequency of 127 kHz is $\langle \bar{n} \rangle \approx 5$ [64]. This cooling step typically has a length of 1 ms.

3. **Sideband cooling.** The radial motional modes of the ion crystal are cooled close to the motional ground state by sideband cooling [65]. For small ion crystals of around $N = 10$ to 20 ions, it is still practical to cool all $2N$ radial motional modes. Each mode is cooled for 0.5 to 1 ms, leading to prohibitively long total cooling times for larger ion crystals. However, for large ion crystals multiple motional modes can be cooled at the same time, as the density of radial modes increases with increasing number of ions. For a 51-ion crystal, the radial motional modes can be cooled by evenly distributing up to 20 cooling frequencies. This cooling step is the longest, taking up to about 15 ms. For long ion crystals, a short period (approx. 100 µs) of polarization-gradient cooling is repeated after sideband cooling, as sideband cooling heats up the axial motional modes.

3.1.3 *Encoding of the qubit*

For most experiments, the qubit is encoded in the states $|4^2S_{1/2}, m_j = 1/2\rangle$ and $|3^2D_{5/2}, m_j = 5/2\rangle$, which are connected by an optical quadrupole transition. This qubit is susceptible to magnetic field fluctuations and laser phase noise. The life time of the qubit is limited by spontaneous emission to approximately 1 s.

3.1.4 *State preparation*

Throughout this thesis, the ions were initially prepared in the $|4^2S_{1/2}, m_j = 1/2\rangle$ state. The state preparation is achieved by transferring unwanted population from the $|4^2S_{1/2}, m_j = -1/2\rangle$ state to the $|3^2D_{5/2}, m_j = 3/2\rangle$ state with the narrow-linewidth 729 nm light. Population from this excited state is pumped out by 854 nm light to the $|4^2P_{3/2}\rangle$ state from where the population decays to the ground state. After a few tens of microseconds, most of the population has been transferred to the desired state $|4^2S_{1/2}, m_j = 1/2\rangle$. This state-preparation scheme is known as frequency-resolved optical pumping. A detailed description of the process used in our setup can be found in Ref. [18].

3.1.5 *Coherent operations*

Coherent operations on the quantum state of the ions can be carried out with several different laser beams, as sketched in Figure 3.2. The qubit transition $|S_{1/2}, m_j = 1/2\rangle \leftrightarrow |D_{5/2}, m_j = 5/2\rangle$ is an optical quadrupole transition that is driven with a sub-10 Hz-linewidth laser at 729 nm.

1. **Global single-qubit rotations.** An elliptically shaped laser beam illuminates the entire ion crystal from a transverse direction, i.e. perpendicular to the z axis ("729 global"). This global beam is used for single-qubit rotations that are applied to all ions simultaneously.
2. **Entanglement operations**. The global beam can create entanglement between ions. The entanglement is created via the common radial motional modes of the ion crystal by a bichromatic light field.
3. **Individual single-qubit rotations.** A tightly focused laser beam can be steered onto single ions ("729 addressing"). This addressing beam is used for single-qubit rotations on individual ions.

Details on coherent operations on long ion crystals are given in Refs. [59, 62]. Worth mentioning are effects that limit the fidelity of coherent operations (nonexhaustive enumeration): (1) Phase noise on the 729 laser, (2) magnetic field noise, (3) qubit rotation errors due to inhomogeneous coupling, (4) motional heating (in particular axially), and (5) collisions with background gas. The single-ion addressing of long ion crystals suffers from nonlinear effects in the acousto-optic deflector that create an additional laser spot at a position corresponding to twice the set addressing frequency.

A laser system that drives the Raman transition between the ground state qubit $|S_{1/2}, m_j = -1/2\rangle \leftrightarrow |S_{1/2}, m_j = 1/2\rangle$ has been set up at our experiment [60]. However, this system has not been put into regular use, as improvements on the fidelity of operations are still required.

3.1.6 *Detection*

The quantum state of the ions is detected by state-dependent fluorescence: By driving the dipole-allowed transition $4^2S_{1/2} \leftrightarrow 4^2P_{3/2}$, the quantum state collapses either to the bright state $|1\rangle = 4^2S_{1/2}$ that fluoresces or to the dark state $|0\rangle = 3^2D_{5/2}$ that does not fluoresce. This technique is known as electron shelving [31]. Our experiment provides two ways of detection: A photomultiplier tube (PMT) measures the mean state population of all ions in the crystal. Additionally, an EMCCD[3] camera images the ion crystal and allows us to detect the quantum state of each ion individually. An example of a single camera detection result is shown in Figure 3.2. The camera detection was used for most measurements presented in this thesis.

3 electron-multiplying charge-coupled device

3.1.7 *Stabilization of the environment*

A stable environment of the qubit is a prerequisite for coherent operations. In particular, the magnetic field needs to be stable, as the qubit is encoded in Zeeman sublevels of $^{40}Ca^{+}$ that are sensitive to changes in the magnetic field. The magnetic field is stabilized both with passive and with active means. The passive shielding is achieved with a mu-metal shield [18, p. 61]. The active stabilization is realized by a feed-forward mechanism, which first measures the time-varying magnetic field with the ions as a sensor and then applies a canceling field [61, 62].

Another source of error acting on the ions is caused by leakage light. If light from unused beams is not shut off completely, this leakage light gives rise to unwanted couplings that introduce errors. We observed this effect in our setup for the coherent 729 nm beam from the axial crystal direction ("tip beam") and for the 854 nm laser. In the case of the "tip beam", the leakage light is caused by residual first-order light from an AOM. If not in use, this light is blocked by a mechanical beam blocker. In the case of the 854 nm laser, a better alignment of the aperture that blocks the zeroth-order light in a double-pass AOM setup was sufficient.

Apart from error sources that act directly on the qubit, there is a number of environmental factors influencing the experimental setup. A few examples are: (1) Temperature changes in the laboratory lead to drifts in the laser cavities and the optical setups. The laboratory temperature is kept constant to within a few tenths of a Kelvin. (2) Mechanical vibrations in the setup mainly affect the frequency lock of the sub-10 Hz-linewidth laser at 729 nm.[4,5] (3) Drifts of the ion crystal. For an axial confinement frequency of 217 kHz the ion crystal drifts by about 40 nm in 10 minutes. This drift is compensated by a feedback to the axial tip electrode voltage [59].

3.2 COLLISIONS WITH BACKGROUND GAS

Collisions with background gas heat up the ion crystal. Depending on the energy transferred by the collision, this can deteriorate the fidelity of quantum operations on the systems, or even melt the entire crystal. For our experiment, we have evaluated the rate of such melting events. The analysis is based on time stamps of the melting events that are logged by the experiment control system QFP. This data was analyzed for an ion crystal of 51 ions and 25 ions, respectively. The

4 As an example, the *Quantum Frequency Conversion* experiment at the University observed a significant impact of vibrations from the air conditioning (AC) of the laboratory on the laser lock of the narrow-linewidth 729 nm laser system. The linewidth was measured to be $\Delta\nu = 165(2)$ Hz with the AC on, and $\Delta\nu = 4.6(1)$ Hz with the AC off [66, p. 86].

5 At our Quantum Simulation experiment, we observed the strong impact of acoustic and mechanical noise on the coherence time. Insulating the cooling water hoses and electrical cables that touch the main optical table (housing the high-finesse cavity and the 729 laser) with foam plastic increased the 1/e-coherence time of a Ramsey experiment on the $|S_{1/2}, m_j = 1/2\rangle \leftrightarrow |D_{5/2}, m_j = 3/2\rangle$ transition from 92(15) ms to 172(12) ms. The coherence time on the $|S_{1/2}, m_j = 1/2\rangle \leftrightarrow |D_{5/2}, m_j = 5/2\rangle$ transition was increased from approx. 40 ms to 113(8) ms.

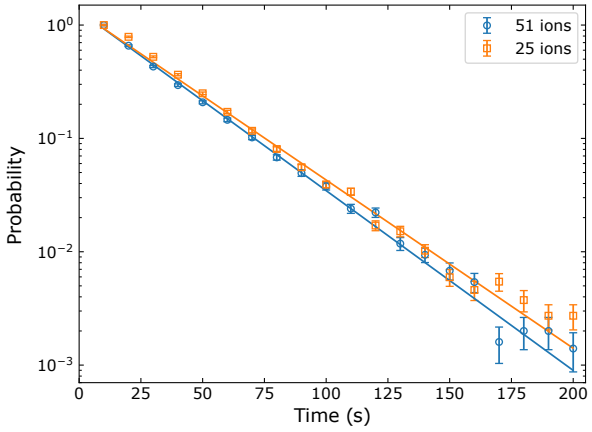

Figure 3.3: Melting of the ion crystal. Shown is the probability that an ion crystal has not melted after a certain time. The data points are measurements for a 25-ion crystal and a 51-ion crystal, respectively. The lines are exponential fits of Eq. (3.1), yielding survival times of 29.3(8) s for 25 ions and 27.4(7) s for 51 ions.

probability that an ion crystal has survived (i.e. has not melted) after a time t is described by

$$p = \mathrm{e}^{-(t-t_0)/\tau}, \tag{3.1}$$

where τ is the $1/\mathrm{e}$ survival time. A time offset t_0 accounts for the delay until the previous refreeze procedure has finished.

The measured survival time of the crystal is shown in Figure 3.3. A fit of Eq. (3.1) leads to a survival time of 29.3(8) s for the 25-ion crystal and of 27.4(7) s for the 51-ion crystal (axial trapping frequency 126 kHz; time offset $t_0 = 8(3)$ s in both cases). Interestingly, the survival time is similar in both cases, despite the larger 51-ion crystal being expected to undergo twice as many collisions with background gas molecules than the 25-ion crystal. This may be explained by a distribution of the transferred collision energy over the entire crystal. While a large ion crystal experiences more collisions than a small one, it also requires a more energetic collision to reach the melting temperature. Importantly, the measured survival time of long ion crystals does not pose a limitation for the measurements presented in this thesis. The probability that an experimental data point needs to be retaken due to a molten ion crystal is small enough that data acquisition is still efficient.

3.3 AXIAL HEATING RATES

Cooling of the motional modes of an ion crystal close to the motional ground state is important as the atom-light coupling strength depends on the phonon number. This dependency creates unwanted effects for a number of operations on the ions. For example, thermal motional states lead to damped Rabi flops or damped ac-Stark flops. Even when the ion crystal is cooled close to the ground state at the beginning of an experimental cycle, the crystal is heated continuously by sources

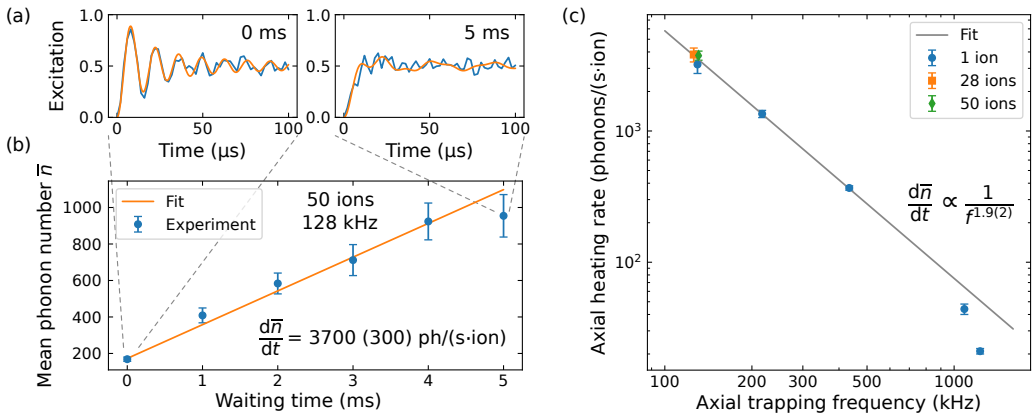

Figure 3.4: Axial heating rates. (a) Decay of Rabi oscillations directly after Doppler cooling and polarization-gradient cooling (left) and after a 5 ms waiting time (right). The solid lines are fits of Eq. (3.4). (b) When adding a waiting time before the Rabi flops, the mean phonon number increases with the heating rate $d\bar{n}/dt$. (c) Axial heating rate as a function of the axial trapping frequency, measured for various ion numbers. The solid line is a fit according to a power law.

of electric noise. Experiments that take tens of milliseconds can be impaired by such heating. Thus, it is important to characterize the heating rate of a trap. For our trap, the radial heating rates of a 9-ion crystal have been measured for various common modes [35]. The heating rates of the axial center-of-mass (c.o.m.) mode have been measured as a function of the *radial* trapping frequency [18, p. 85].

In this thesis, a measurement of the axial heating rates as a function of the *axial* trapping frequency is presented. The measurement is based on the damping rate of a Rabi oscillation. The coupling strength to a motional mode depends on the phonon number. The Rabi frequency $\Omega_{n,n}$ of a carrier transition on a Fock state with phonon number n is [19, Eq. 70]

$$\Omega_{n,n} = \Omega_0 e^{-\eta^2/2} L_n(\eta^2), \tag{3.2}$$

where η is the Lamb-Dicke parameter and L_n is the Laguerre polynomial. If the ion crystal is in a thermal state, the probability p_n of finding the phonon number n is described by a thermal distribution [19],

$$p_n = \frac{1}{\bar{n}+1}\left(\frac{\bar{n}}{\bar{n}+1}\right)^n, \tag{3.3}$$

where $\bar{n}$ is the mean phonon number. In an experiment, an ion crystal is cooled and prepared in the state $|\downarrow\rangle$. Applying a light pulse of duration t on the carrier transition brings the ion into the state $|\uparrow\rangle$ with probability

$$p_\uparrow = \sum_n p_n \sin^2(\Omega_{n,n} t). \tag{3.4}$$

Figure 3.4 shows the measured axial heating rate. First the ion crystal is cooled by Doppler cooling and polarization-gradient cooling. Then, the ion crystal is left idle for a waiting time, during which the ion crystal heats up. After the

waiting time, Rabi oscillations are driven. Immediately after cooling, the Rabi oscillations show little damping [Fig. 3.4(a)]. After a waiting time of 5 ms, the Rabi oscillations show stronger damping. Measuring the mean phonon number $\bar{n}$ as a function of the waiting time [Fig. 3.4(b)] yields the heating rate $\mathrm{d}\bar{n}/\mathrm{d}t = 3700(300)\,\text{phonons}\,\mathrm{s}^{-1}\,\mathrm{ion}^{-1}$ for a 50-ion crystal and an axial trapping frequency of 128 kHz. Additionally, the axial heating rate was measured as a function of the axial trapping frequency [Fig.3.4(c)]. We found that the axial heating rate can described by a polynomial function of the axial trapping frequency f, $\mathrm{d}\bar{n}/\mathrm{d}t \propto f^{-1.9(2)}$, in the accessible range of $f \approx 100\,\mathrm{Hz} \ldots 1\,\mathrm{kHz}$. The heating rate frequency exponent α found in other experiments varies over a large range, with most experiments yielding $\alpha \approx 0.5 \ldots 2$ [48].

The high axial heating rate poses a problem for experiments that require single-ion addressing after a long (tens of milliseconds) experimental sequence[6]. This is typically the case when performing state tomography after entangling interactions on long ion crystals. This problem will be hopefully solved by replacing the current trap with a new trap that is manufactured by the company *Alpine Quantum Technologies* and that is specified to a lower heating rate than we currently have.

3.4 WAVEFRONT MEASUREMENT OF THE GLOBAL BEAM

The quantum state of the ions in an ion crystal is manipulated collectively with a laser beam that illuminates the whole ion crystal. The laser is focused to maximize the overall light intensity on the ion crystal. However, global operations performed with such a laser beam can suffer from one particular source of phase error: Uncontrolled phase modulation by tilted wavefronts. In this section, the underlying mechanism is explained and a measurement technique is introduced with which a tilt of the wavefronts can be detected. Finally, an optical setup is presented that delivers parallel wavefronts and removes this source of error.

3.4.1 *Errors caused by tilted wavefronts*

Tilted wavefronts can cause errors in the atom-light interaction when the laser beam has a focus whose focal plane does not coincide with the plane of the ions. This situation was created by the previously used beam shaping optics [35] and is shown in Figure 3.5(a). A Gaussian beam is focused by two cylindrical lenses (lenses not shown), which creates a tight focus along the vertical axis at the position of the ion crystal. However, the focus along the horizontal axis is not centered on the ion crystal. As the wavefronts outside the focus of a Gaussian beam are curved, the angle between wavefront and the longitudinal ion crystal axis z varies.

A tilt between the wavefront and the longitudinal ion crystal axis leads to a spatial phase modulation along the direction of the ion crystal. Figure 3.5(b) shows a single ion illuminated by light with tilted wavefronts. The wave vector $\boldsymbol{k}$ is tilted by an angle α with respect to the axis z. The phase modulation can be

6 An example is presented in C. Maier's thesis [59, Fig. 4.10]

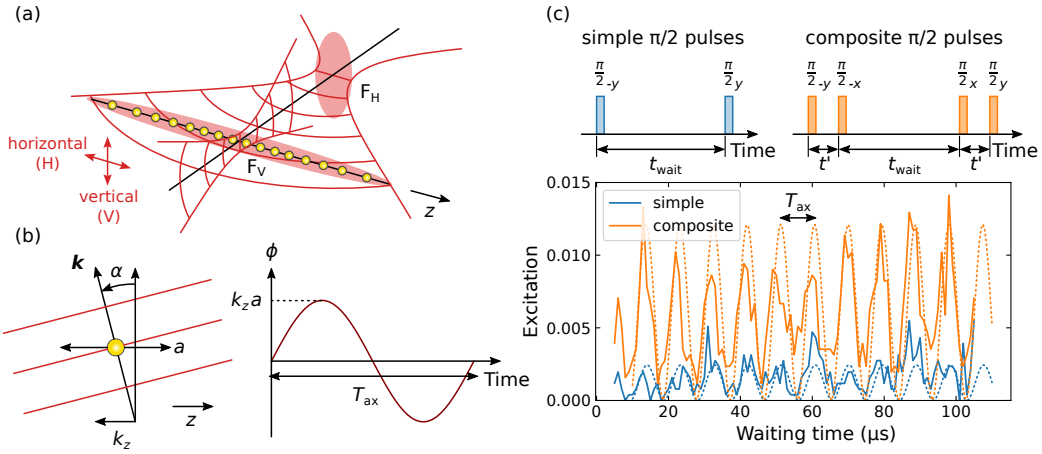

Figure 3.5: Effect of tilted wavefronts. (a) In the previously used beam shaping optics [35], the vertical focus F_V and the horizontal focus F_H of the laser beam do not overlap. The ion chain is placed at the vertical focus, where the horizontal wavefronts are already curved. (b) An ion is illuminated by a light field with wave vector $\boldsymbol{k}$ and wavefronts that are tilted by an angle α. If the ion oscillates with an amplitude a, it experiences a modulation of the phase ϕ. The period of this modulation is given by the trapping period T_{ax}. (c) This phase modulation was probed with a Ramsey experiment, using simple or composite pulses. The trapping frequency is $\omega_z = 2\pi \times 108\,\mathrm{kHz}$. The dotted lines are fits to Eq. (3.6) and (3.7).

understood easily in a semi-classical picture: The ion has a nonzero temperature which makes it oscillate with amplitude a along the weakly confining z axis. During the oscillation, the phase ϕ between ion and light field changes. In the semi-classical picture, the ion follows the trajectory $z(t) = a\sin(\omega_{ax}t)$, where ω_{ax} is the axial trapping frequency and t is the time. The phase between light field and ion is then

$$\phi(t) = k_z z(t) = k_z a \sin(\omega_{ax} t), \tag{3.5}$$

where k_z is the overlap between wave vector and z axis, $k_z = |\boldsymbol{k}|\sin(\alpha)$. The period of this modulation is the axial trapping period T_{ax}. The maximum phase change is $\phi_{max} = k_z a$.

The effect of the phase modulation by tilted wavefronts can be detected by a Ramsey experiment, as shown in Figure 3.5(c). First, the ion is prepared in an equal superposition of $|\uparrow\rangle$ and $|\downarrow\rangle$ by applying a $\pi/2$ pulse. In the absence of any phase modulation, this rotation would be carried out around the $-y$ axis with phase $\pi/2$. However, in the presence of phase modulation, the rotation axis is shifted by a phase ϕ_i. Then, the ion is left for a waiting time t_{wait}. After the waiting time, the phase between light field and ion has changed to a value ϕ_f. Finally, the phase difference $\phi_f - \phi_i$ is analyzed by applying a second $\pi/2$ pulse and measuring the ion's excitation.

The signal of the Ramsey experiment is maximized when the initial $\pi/2$ pulse is applied at one of the turning points of the ion motion and the final $\pi/2$ pulse is applied at the other turning point. This occurs when the two $\pi/2$ pulses are

separated by half a trapping period, $\frac{1}{2}T_{ax}$. Additionally, this criterion is also met when an integer multiple of the trapping frequency is added. Therefore, the peaks in excitation occur when the waiting time of the Ramsey experiment is $(\frac{1}{2}+n)T_{ax}$, with $n = 0, 1, 2, \ldots$. The separation between two consecutive peaks is a trapping period T_{ax}.

In an experiment, the initial phase of an ion is determined by its thermal motion and thus cannot be controlled. The average measurement outcome is the result of averaging over all possible initial phases. For a Ramsey experiment that uses simple $\pi/2$ pulses, the average excitation is described by (see A.1)

$$e = \frac{1}{2}(k_z a)^2 \sin^2\left(\frac{1}{2}\omega_{ax} t_{wait}\right), \tag{3.6}$$

where t_{wait} is the time between the start of the first and the second $\pi/2$ pulse.

Figure 3.5(c) shows the measured average excitation for a 51-ion crystal, axially confined with a trapping frequency of $\omega_{ax} = 108\,\text{kHz}$. The crystal is Doppler-cooled and sideband-cooled along the radial axes. In a first experiment, a Ramsey sequence with simple $\pi/2$ pulses was used. The excitation is oscillating at the trapping frequency, with a maximum excitation of $e_{max} \approx 3 \times 10^{-3}$. When using a Ramsey sequence where the initial and the final rotation are realized by composite $\pi/2$ pulses, the average excitation is described by (see A.1)

$$e = \frac{1}{2}(k_z a)^2 \left[\sin^2\left(\frac{1}{2}\omega_{ax} t_{wait}\right) + 4\cos^2\left(\frac{1}{2}\omega_{ax}(t_{wait}+t')\right)\sin^2\left(\frac{1}{2}\omega_{ax} t'\right)\right], \tag{3.7}$$

where t' is the time between the beginning of the first and the second pulse of the composite $\pi/2$ pulse. Depending on the timing t' of the composite $\pi/2$ pulses the oscillation of the excitation becomes even more pronounced.

3.4.2 *Design and implementation of a new beam shaping optics*

Errors caused by tilted wavefronts can be avoided by focusing the laser beam in such a way that the wavefronts are planar and parallel to the ion crystal. For this purpose, I designed and implemented a new, suitable beam shaping optics. The optics consists of two crossed, cylindrical-lens objectives. One cylindrical-lens objective focuses the beam along the vertical axis, while the other cylindrical-lens objective focuses the beam along the horizontal axis. The crucial point is that both the vertical focus and the horizontal focus lie on the ion crystal, therefore delivering plane wavefronts. While the basic design of the optical setup is simple, a considerable complication was caused by a whole list of requirements:

1. The optics delivers an elliptically shaped focus with plane wavefronts.
2. The mechanical dimensions of the new optical setup have to fit into the constrained space of the existing setup. The focal position is fixed by the position of the ion crystal.
3. The vertical focus is as small as possible.
4. The size of the horizontal focus can be adjusted while maintaining plane wavefronts.

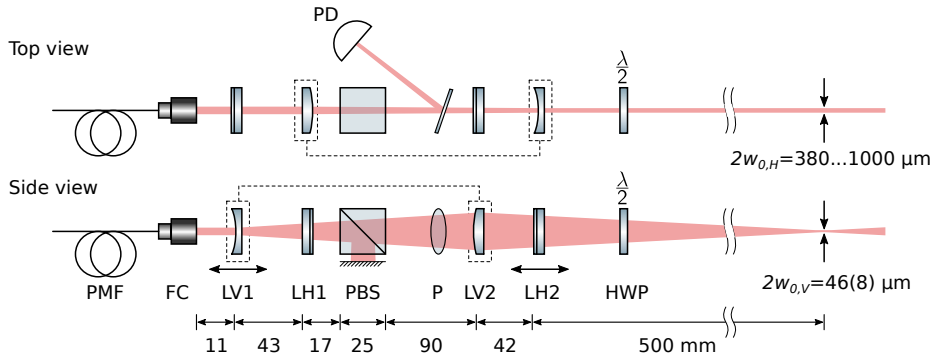

Figure 3.6: Global beam shaping optics. Two crossed cylindrical-lens objectives create a elliptically shaped Gaussian beam that has plane wavefronts at the focus. PMF: polarization-maintaining fiber, FC: fiber collimator, LV: vertical cylindrical lens, LH: horizontal cylindrical lens, PBS: polarizing beam splitter, P: pellicle, HWP: half-wave plate, PD: photo diode.

5. Possibility of fine adjustment of the vertical focus. Correction of the unavoidable beam rotation to maximally overlap the elliptical beam with the ion crystal over its entire length.

The beam shaping optics that meets all these requirements is shown in Figure 3.6. The 729 nm light is supplied by a polarization-maintaining fiber PMF. A fiber collimator FC[7] delivers a collimated beam. A first vertical cylindrical lens LV1[8] enlarges the beam in the vertical direction. This lens is positioned on a micrometer stage for fine adjustment of the vertical focal position. The distance from the end of the beam shaping optics to the ion crystal is approximately 500 mm. A first horizontal cylindrical lens LH1[9] focuses the beam in the horizontal direction. The polarization of the light is defined by a polarizing beam splitter cube PBS[10]. A pellicle P samples light for stabilization of the light intensity via a sample-and-hold circuit. A second vertical cylindrical lens LV2[11] focuses the light onto the ion crystal along the vertical axis. The resulting vertical beam diameter was measured to be $46(8)$ µm. This lens can be tilted by a piezo stage around the beam propagation axis which allows us to correct the beam rotation and to maximize the overlap between the elliptical beam and the ion crystal. Finally, a second horizontal cylindrical lens LH2[12] collimates the beam along the horizontal axis. This lens is mounted on a linear piezo stage and can be moved along the beam propagation axis. This allows us to adjust the horizontal beam diameter between 380 µm and 1000 µm. During the design process, care was taken to ensure that the Rayleigh range is large enough, such that the ion crystal always remains inside the focus during the adjustment.

7 Schäfter+Kirchhoff 60FC-4-M20-10
8 Thorlabs LK1336L1-B $f = -50$ mm
9 Thorlabs LJ1277L1-B $f = 250$ mm
10 Thorlabs PBS252 1″ Polarizing Beamsplitter Cube
11 Thorlabs LJ1836L1-B $f = 700$ mm and LJ1653L1-B $f = 200$ mm
12 Thorlabs LK1743L1-B $f = -100$ mm

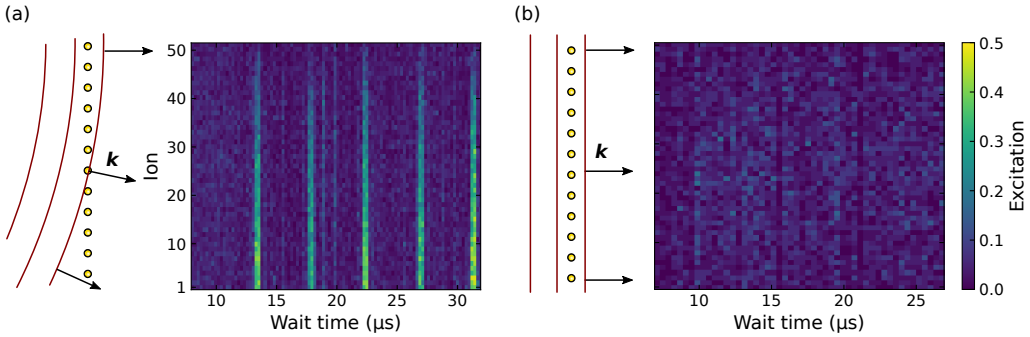

Figure 3.7: Effect of parallel wavefronts. (a) The wavefronts of the old beam shaping optics were curved which resulted in a variation of the wave vector $\boldsymbol{k}$ over the ion crystal. The tilted wavefronts give rise to peaks in the excitation [Eq. (3.8)] when probed with a CPMG sequence ($N_\mathrm{p} = 20$ pulses, axial trapping frequency $\omega_z = 2\pi \times 112\,\mathrm{kHz}$, ion crystal temperature $T = 4.6\,\mathrm{mK}$, ion mass $m = m_{\mathrm{Ca40}}$). The main peaks are separated by one axial trapping period $T_\mathrm{ax} = 2\pi/\omega_z$. The intermediate peaks are the result of the finite pulse length. (b) After installation of the new beam shaping optics that delivers plane and parallel wavefronts, the signal of the CPMG sequence vanishes. The noise floor gives an upper bound for the wavefront tilt of $\alpha \leq 0.8\,\mathrm{mrad}$.

3.4.3 *Measurement of wavefronts using ions*

The effectiveness of the new beam shaping optics was assessed by measuring the wavefront tilt with the ions acting as the sensor. The underlying idea of probing phase variations caused by tilted wavefronts with an ion in a Ramsey experiment was discussed in Sec. 3.4.1 above. The sensitivity of such a measurement can be increased drastically by inserting π pulses into the waiting period. If the π pulses are spaced equally in time, the resulting sequence is called a Carr-Purcell-Meiboom-Gill (CPMG) sequence [67]. By matching the waiting time between two subsequent π pulses with the trapping period, the phase modulation from tilted wavefronts gets amplified. This results in a signal with clear peaks in the ions' excitation. The height of the peaks is a measure for the wavefront tilt. The peak excitation of an ion under a tilted wavefront, probed with a CPMG sequence is [62]

$$e_\mathrm{max} = \frac{1}{2}\left[1 - \exp\left(-\frac{2k_\mathrm{B}Tk_z^2(N_\mathrm{p}+1)^2}{m\omega_z^2}\right)\right], \tag{3.8}$$

where N_p is the number of π pulses in the CPMG sequence, k_z the wave vector component along the z axis, ω_z the axial trapping frequency, T the temperature of the ion, m the mass of the ion, and k_B is Boltzmann's constant.

A measurement of the wavefront tilt using a CPMG sequence is presented in Figure 3.7. In a first measurement, the wavefronts of the old beam shaping optics were measured [Fig. 3.7(a)]. The measurement was carried out with a long 51-ion crystal, allowing to probe spatial changes in the wavefront ($N_\mathrm{p} = 20$, $\omega_z = 2\pi \times 112\,\mathrm{kHz}$, $T = 4.6\,\mathrm{mK}$, $m = m_{\mathrm{Ca40}}$). The excitation exhibits clear peaks which vary in height, indicating a curvature of the wavefronts at the ion crystal.

The inferred wavefront tilt changes from $\alpha_1 = 4.8\,\text{mrad}$ at one end of the ion crystal to $\alpha_{51} = 1.4\,\text{mrad}$ at the other end. This change of $\Delta\alpha = 3.4\,\text{mrad}$ over the crystal length of $\Delta z = 269\,\mu\text{m}$ corresponds to a wavefront curvature of $R = \Delta z/\Delta\alpha = 79(2)\,\text{mm}$. The parameters of the old beam shaping optics suggest a smaller value of $36(2)\,\text{mm}$. Possible explanations for this mismatch could be deviations in the wavefronts of the old optics, or an inaccurate estimate of the temperature after Doppler cooling. The main peaks in excitation are separated by one axial trapping period, T_{ax}. The weaker intermediate peaks are the result of the finite pulse length. The emergence of the intermediate peaks is studied by numerical simulations in Section 3.4.4.

After implementation of the new beam shaping optics, the wavefront measurement was repeated [Fig. 3.7]. With the new optics, the excitation remains close to zero, indicating plane and parallel wavefronts. The noise floor of the excitation gives an upper bound for the wavefront tilt of $\alpha \leq 0.8\,\text{mrad}$ over the whole ion crystal.

3.4.4 *Finite pulse length effects – numerical simulations*

Describing the effect of tilted wavefronts with a semi-classical model has the advantage of giving a simple description at hand for practical use. However, it does not capture fine details such as finite-pulse-length effects. These can be studied by numerically solving the evolution of a trapped ion interacting with a traveling light wave. A numerical study of this phenomenon is the content of this section.

The evolution of a trapped ion that interacts with a traveling light wave is described by the Hamiltonian

$$H_{\text{I}} = \hbar\omega\left(a^\dagger a + \frac{1}{2}\right) + \frac{1}{2}\hbar\Omega\left(\mathrm{e}^{\mathrm{i}\eta(a+a^\dagger)}\sigma^+\mathrm{e}^{-\mathrm{i}\Delta t} + \text{h.c.}\right). \tag{3.9}$$

The first term describes the free evolution of the quantum harmonic oscillator, where ω is the trapping frequency and a ($a^\dagger$) denotes the annihilation (creation) operator. The second term describes the interaction between a traveling light wave and the states of the harmonic oscillator, where Ω is the Rabi frequency, σ^+ is the raising operator, η the Lamb-Dicke parameter, Δ the detuning between light and atomic transition, and t is time.

The problem is modeled by a 1-dimensional oscillator, consisting of a single ion. The tilt of the wavefront is taken into account by incorporating it into the Lamb-Dicke parameter,

$$\eta = \cos(\pi/2 - \alpha)\sqrt{\hbar/(2m\omega)}, \tag{3.10}$$

with the tilt angle α and the ion mass m. For wavefronts that are parallel to the oscillation axis of the oscillator, the tilt is zero, $\alpha = 0$. The numerical simulation is carried out as follows:

1. The initial state is assigned to the trapped ion.
2. The evolution of the trapped ion under a CPMG sequence is solved numerically by evaluating Eq. (3.9) in QuTiP [68].

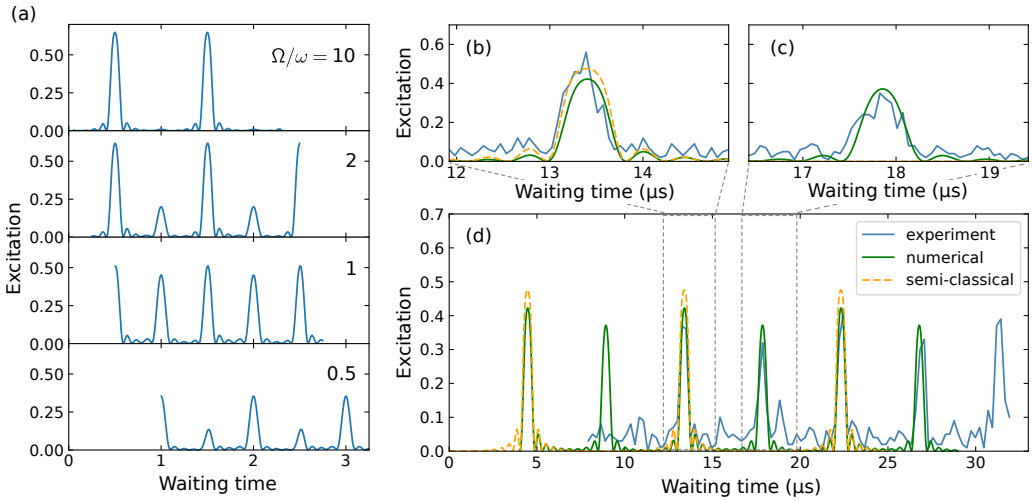

Figure 3.8: Effects of finite pulse lengths for interactions under tilted wavefronts. (a) Numerical simulation of a trapped ion interacting with tilted traveling wave. The excitation after a CPMG-10 sequence is evaluated for different ratios of the Rabi frequency Ω to the trapping frequency $\omega = 2\pi$ (detuning $\Delta = 0$, $\eta = 0.01$). If $\Omega \gg \omega$, only the mains peaks at times $n + \frac{1}{2}$ are present. When $\Omega \approx \omega$, intermediate peaks emerge. (b-d) Comparison between experiment and numerical simulation. The experiment was carried out for $N_\mathrm{p} = 20$ pulses, axial trapping frequency $\omega_z = 2\pi \times 112\,\mathrm{kHz}$ and an ion crystal temperature of $T = 4.6\,\mathrm{mK}$. (b) The main peaks at times $(n + \frac{1}{2})T_\mathrm{ax}$ ($n = 0, 1, 2, \dots$) are well described by the semi-classical model and are in agreement with the numerical simulation. (c) At intermediate times, only the numerical simulation predicts the peaks that are observed in the experiment. (d) Scan over a larger range of waiting times revealing the periodic structure of the CPMG signal.

3. The final state is used to calculate the excitation.

In a first step, the excitation is simulated for a set of initial Fock states, $|\downarrow, n\rangle$. Then, in a second step, the excitation is averaged over the Fock state distribution of a thermal state.

The results of this numerical simulation are shown in Figure 3.8. In a first set of simulations, the influence of finite pulse length of the π ($\pi/2$) pulses in the CPMG sequence is studied. The trapping frequency is fixed, $\omega = 2\pi$, while the Rabi frequency Ω is varied from calculation to calculation. Consequently, the length of the π ($\pi/2$) pulses changes. Figure 3.8(a) shows simulations ranging from short pulses ($\Omega/\omega = 10$) to long pulses ($\Omega/\omega = 0.5$). For short pulses, the excitation after the CPMG sequence shows only the main peaks that occur at times $n + \frac{1}{2}$ ($n = 0, 1, 2, \dots$). When the length of the pulses becomes comparable to the trapping period, the semi-classical approximation becomes inaccurate and intermediate peaks emerge. For $\Omega = \omega$, the intermediate peaks are almost as strong as the main peaks. When the length of the pulses is larger than the trapping period, $\Omega < \omega$, the main peaks even start to vanish and the intermediate peaks become dominant.

A comparison between experiment and numerical simulation is presented in Figure 3.8(b-d). In the experiment, an ion crystal was probed with a CPMG sequence consisting of $N_\mathrm{p} = 20$ pulses. The ratio of Rabi frequency to trapping frequency was $\Omega/\omega = 1.1$. At times $(n + \frac{1}{2})T_\mathrm{ax}$, the experimentally observed excitation is well described by both the semi-classical model and the numerical simulation [Fig. 3.8(b)]. However, at intermediate times, the semi-classical description fails to predict the observed peaks, while the numerical solution predicts them correctly [Fig. 3.8(c)]. A scan over a large range of waiting times reveals the periodic structure of the CPMG signal [Fig. 3.8(d)].

3.5 CORRELATION SPECTROSCOPY

Correlations between qubits can serve as a useful resource for measuring magnetic fields, spatial level shifts, or ion positions. The method of correlation spectroscopy makes use of such correlations. It is possible to extract phase information from two opposite sides: On the one hand, phase differences between ions can be measured in the presence of collective phase noise – This allows us to determine levels shifts or ion positions with high accuracy, even under the presence of laser phase noise. On the other hand, global phase changes can be measured when individual-qubit level shifts are taken into account – This allows one to measure, for instance, magnetic field changes with single repetitions of an experiment, making phase changes on time scales of a few milliseconds accessible with a trapped-ion experiment.

The working principle of correlation spectroscopy was first demonstrated for two ions [69]. Recently, it has been extended to up to 91 ions in two experiments in our group [70]. The following chapter presents two applications of correlation spectroscopy for characterization of a long ion crystal: First, the anharmonicity of the trapping potential is determined from a precise measurement of ion positions. Second, the transition between a linear to a zigzag configuration of the ion crystal is observed.

3.5.1 *Anharmonicity of the trapping potential*

At equilibrium, the trapping force balances the electrostatic repulsion between the ions. The trapping potential can be determined from a precise measurement of the ion positions. The working principle of sensing ion positions by correlation spectroscopy is depicted in Figure 3.9(a). A crystal is formed by N ions located at positions $\boldsymbol{r_i}$. In a Ramsey experiment, two laser beams are used that illuminate the N-ion crystal from different directions. The initial $\pi/2$ pulse is done with the first laser beam with wave vector $\boldsymbol{k_1}$. The phase between the first light wave and ion i is $\phi_i^{(1)} = \boldsymbol{k_1} \cdot \boldsymbol{r_i}$. This first pulse initializes the phase of the superposition $(|\downarrow\rangle + \mathrm{e}^{\mathrm{i}\phi_i^{(1)}}|\uparrow\rangle)/\sqrt{2}$. Then, the analysis $\pi/2$ pulse is done with the second laser

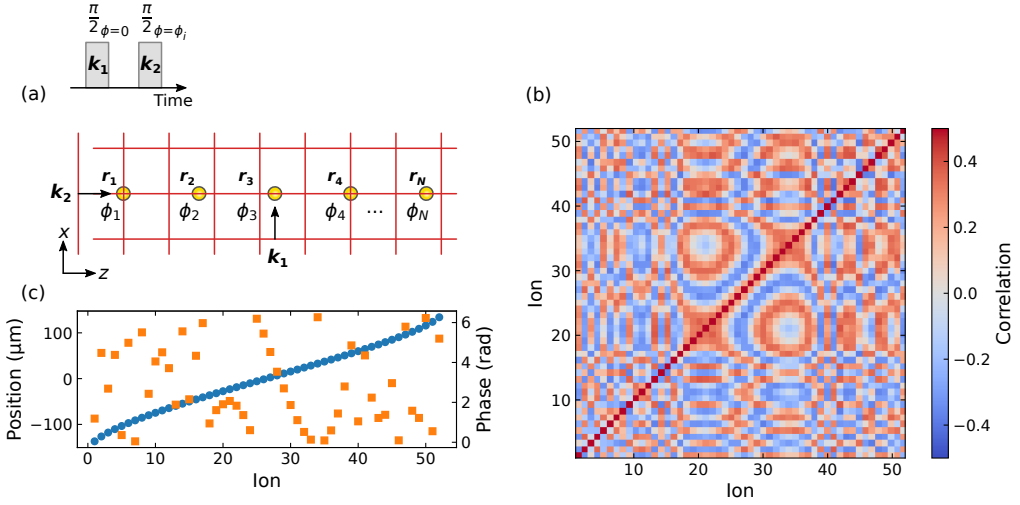

Figure 3.9: Correlations from radial-axial interrogation and measurement of ion positions. (a) A Ramsey experiment uses two beams with different wave vectors $\boldsymbol{k_1}$ and $\boldsymbol{k_2}$ for the initial and for the final rotation, respectively. Each ion at position $\boldsymbol{r_i}$ experiences a different phase relation ϕ_i between the light phase of the initial and the final pulse. (b) Measured ion-ion correlations for a 52-ion crystal trapped at 108 kHz when probed with a Ramsey experiment using the axial and the radial beam. (c) From the correlations, the phase ϕ_i (orange squares) can be extracted by fitting Eq. (3.12). Using an initial estimate of the ion positions allows for a calculation of the exact ion positions (blue disks) from the phases.

beam with wave vector $\boldsymbol{k_2}$. The phase between the second light wave[13] and ion i is $\phi_i^{(2)} = \boldsymbol{k_2} \cdot \boldsymbol{r_i}$. The outcome of the Ramsey sequence depends on the phase difference between the two light pulses[14], $\phi_i = \phi_i^{(2)} - \phi_i^{(1)}$. If the wave vectors of both light fields are known, the phases

$$\phi_i = \phi_i^{(2)} - \phi_i^{(1)} = (\boldsymbol{k_2} - \boldsymbol{k_1}) \cdot \boldsymbol{r_i} \tag{3.11}$$

can be used to extract the ion positions $\boldsymbol{r_i}$. To be more precise, one can determine the component of the position difference vector between two ions that is not perpendicular to $\boldsymbol{k_2} - \boldsymbol{k_1}$. The perpendicular component is negligible in our case, as the radial confinement is much stronger than the axial confinement, restricting the ion crystal along the axial axis.

In the simple case depicted in Fig. 3.9(a), the first light field is perpendicular to the ion crystal and the second light field is oriented along the crystal. Thus, the phases that are probed by the Ramsey experiment are $\phi_i = [(0,0,k_2) - (k_1,0,0)]^{\mathrm{T}} \cdot (0,0,z_i)^{\mathrm{T}} = k_2 z_i$. For this special case it is crucial to have a laser beam

13 If the axial beam has a depth of focus that is not much larger than the extent of the ion crystal, the Gouy phase has to be taken into account. While the value of the depth of focus is unknown for the tip beam, a measurement of the axial trapping frequency [Fig. 3.10(b)] suggests that the Gouy phase is negligible.

14 A Ramsey experiment can be carried out with different light fields from different directions. While the coupling strength may vary between the ion and the two light fields, the resulting quantum state does not "remember" from which direction the light field came.

with wavefronts that are plane and parallel to the ion crystal. The optical system that delivers this beam and its characterization is described in Sec. 3.4.

The phase ϕ_i for each ion $i = 1, 2, \ldots, N$ can be extracted by measuring the correlations in the measurement outcomes of $\sigma_z^{(i)}$ and $\sigma_z^{(j)}$ in a Ramsey experiment. The correlation C_{ij} is [69]

$$C_{ij} \equiv \langle \sigma_z^{(i)} \sigma_z^{(j)} \rangle = \frac{1}{2} \cos(\phi_i - \phi_j). \tag{3.12}$$

From the measurement, the correlations $C_{ij} \equiv \langle \sigma_z^{(i)} \sigma_z^{(j)} \rangle$ can be evaluated. The phases can be determined by a fit, up to a constant offset and a global phase. An example of such a correlation measurement is shown in Figure 3.9(b). A 52-ion crystal is trapped at 108 kHz trapping frequency. The ion crystal is polarization-gradient cooled to increase the fidelity of the axial operation (in addition to Doppler and sideband cooling). The two $\pi/2$ pulses ($|S_{1/2}, m_j = 1/2\rangle \leftrightarrow |D_{5/2}, m_j = 5/2\rangle$) of the Ramsey sequence are applied immediately after one another such that spatially varying level shifts become negligible.

For the example of the 52-ion crystal, the phases that were obtained from the fit are shown in Figure 3.9(c). In a next step, the ion phases can be used to calculate the ion position. This is, however, only possible up to an offset of an integer multiple of the wavelength. It is therefore necessary to have a prior estimate of the ion positions. Such an estimate can be the ion positions of a harmonically trapped crystal.

The ion positions which are measured from correlations can be used to analyze the anharmonicity of the trapping potential, respectively the trapping force. This analysis is shown in Figure 3.10. For an ion crystal in an equilibrium state, the trapping force $F_{\text{trap},i}$ that acts on ion i balances the electrostatic force from all other ions, $F_{\text{el},i}$, that is

$$F_{\text{trap},i} + F_{\text{el},i} = 0 \quad \text{for all } i = 1, \ldots, N. \tag{3.13}$$

The electrostatic force is

$$F_{\text{el},i} = \frac{e^2}{4\pi\epsilon_0} \sum_{j=1, j\neq i} \frac{z_i - z_j}{(z_i - z_j)^2}, \tag{3.14}$$

where e is the elementary charge, ϵ_0 the electric constant, and z_i is the ion position of ion i along the z axis. From these two equations and the measured ion positions, the trapping force $F_{\text{trap},i}$ can be calculated for each ion. The result for our linear Paul trap used in the Quantum Simulation experiment is shown in Figure 3.10(a). Towards one end of the ion crystal, the trapping force deviates from a harmonic, linear behavior, indicating a third-order term in the trapping force.

The trapping potential can be retrieved by fitting an anharmonic potential to the measured ion positions. For the potential, the ansatz

$$U(z) = \frac{1}{2} m \omega_0^2 z^2 \left[1 + \frac{z}{l_3} + \left(\frac{z}{l_4} \right)^2 \right] \tag{3.15}$$

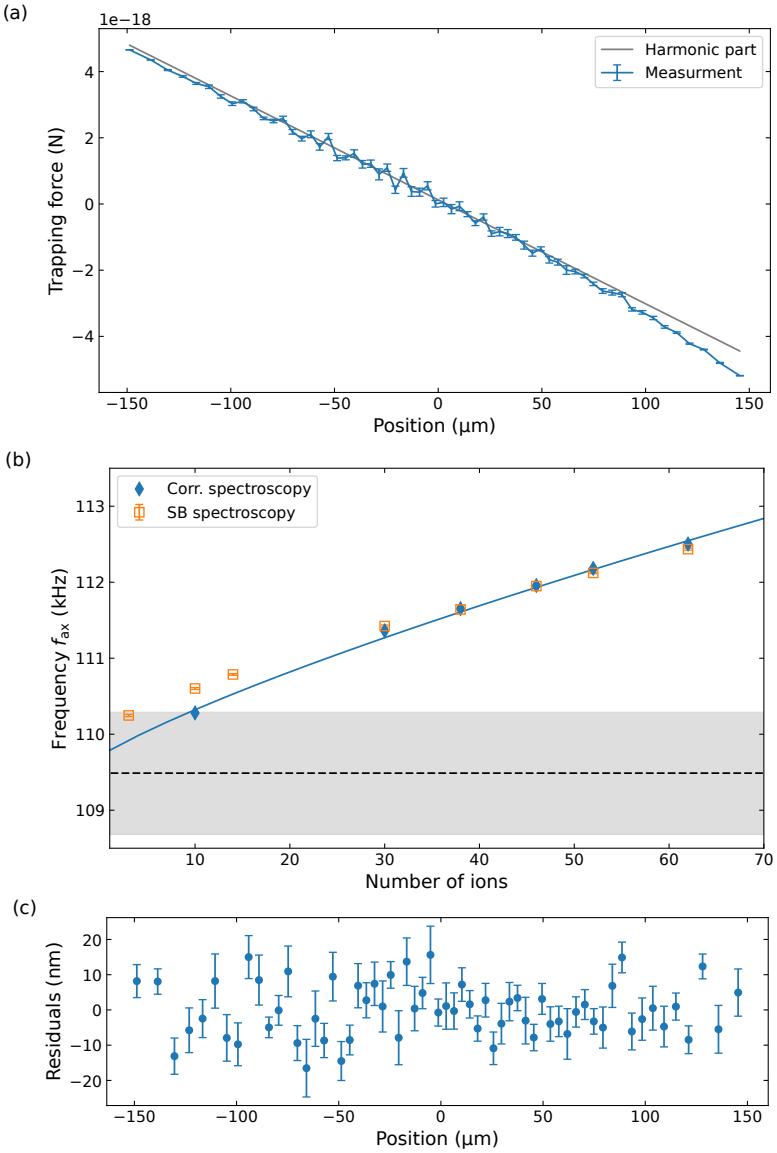

Figure 3.10: Trap anharmonicity from correlation measurements. (a) Reconstructed trapping force. The trapping force is calculated for a 62-ion crystal from the ion positions with Eq. (3.13). The straight line is the harmonic part. Towards the right end of the crystal, the trapping force exhibits anharmonic behavior. (b) Measured and calculated c.o.m.-mode frequency. Sideband spectroscopy of the axial c.o.m.-mode frequency $\omega_{ax} = 2\pi f_{ax}$ is carried out for ion crystals with varying number of ions. As a comparison, the c.o.m.-mode frequency of the ion crystal is calculated from the ion positions that are obtained from correlation spectroscopy (blue diamonds: for each ion number separately, solid line: using the 62-ion crystal potential for all calculations). The gray dashed line shows the harmonic part of the potential, which gives the single-ion trapping frequency ω_0, Eq. (3.15). The shaded area shows the uncertainty of ω_0 (one standard deviation). (c) Reconstructed ion positions from the trapping potential. The anharmonic trapping potential Eq. (3.15) is varied in a least-squares fit to give the best description of the measured ion positions. The ion positions that are measured scatter by a standard deviation of only 8 nm around the theory description, i.e. roughly by the size of the ground state wave function of 7 nm at 3 MHz radial trapping frequency.

gives a convenient description in the length scale of the trap. For the 62-ion crystal, the trap is characterized by[15] the trapping frequency of a single ion $\omega_0 = 2\pi \times 109.74(2)$ kHz, the length scale of the cubic potential term $l_3 = 2.121(4)$ mm, and the length scale of the quartic potential term $0.801(3)$ mm.

This analysis of the anharmonicity of the trapping potential was verified by an independent measurement method: The axial trapping frequency was measured with sideband spectroscopy and then compared with a calculation based on the anharmonic trapping potential. For an anharmonic trapping potential, the trapping frequency of long ion crystals depends on the number of ions. The longer the crystal, the more of the anharmonic part of the potential is experienced by the crystal, thus changing the trapping frequency. This comparison is shown in Figure 3.10(b). The number of ions was varied by successively kicking[16] ions out of the trap, starting from a 62-ion crystal. For each ion crystal, the axial c.o.m.-mode frequency was measured by probing the transition $|S_{1/2}, m_j = 1/2\rangle \leftrightarrow |D_{5/2}, m_j = 3/2\rangle$ with the axial beam. As a comparison, the c.o.m.-mode frequency is extracted from the fitted potential [Eq. (3.15)]. In one analysis, this was done for each ion crystal size individually (blue diamonds). In a second analysis, the potential was evaluated once for the 62-ion crystal; then, the c.o.m.-mode frequency was calculated for all ion numbers from 62 to 1 ion (solid line). The measured c.o.m.-mode frequency shows a clear dependency on the number of ions, as expected for an anharmonic trapping potential. Correlation spectroscopy is in good agreement with sideband spectroscopy. Deviations between the two methods might stem from the residual tilt in the wavefront of the global beam (tilt $\lesssim 0.8$ mrad). Inaccuracies in the knowledge of the wavefronts directly transfer into errors of the extracted phases.

Lastly, the precision of the position measurement with correlation spectroscopy was analyzed. The fitted trapping potential (3.15) is used to calculate the equilibrium positions of the ions. The residuals between the measured and the calculated ion positions is shown in Figure 3.10(c). The residuals have a standard deviation of only 8 nm, demonstrating the precision of the correlation spectroscopy method. As a comparison to other methods, the displacement of an ion was measured with fits to the EMCCD image with an accuracy of 4 nm [71], or with depletion microscopy with 10 nm [72]. It should be noted, however, that these other methods only measure *displacements* of an ion, whereas correlation spectroscopy is capable of measuring distances between several ions.

3.5.2 *Transition between crystal configurations*

Another application of the correlation spectroscopy technique lies in the observation of the transition between different crystal configurations. Namely, the transition from an ion crystal in a linear configuration to a 'zigzag' configuration.

15 The trapping potential can also be obtained from directly fitting the potential (3.15) to the correlation data. This approach was used in Ref. [70], leading to different fit uncertainties. However, both approaches give the same result within error bars.

16 Ions are kicked out of the trap by temporarily making the trapping potential highly anisotropic (trap imbalancing approx. 28 to 30 V) and executing the refreeze procedure. This probabilistically throws a few ions out of the trap.

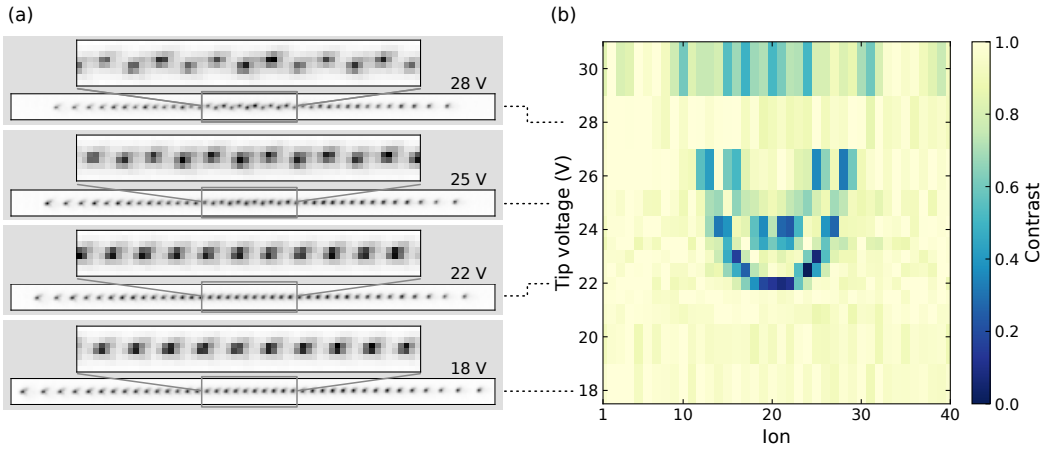

Figure 3.11: Transition from a linear to a zigzag configuration. The axial trapping frequency of a 40-ion crystal was varied by setting the (axial) tip electrode voltage. For each voltage, the phase differences between the ions were measured with correlation spectroscopy. (a) Camera images show a linear configuration at a low tip voltage. At the highest voltage, the zigzag configuration becomes obvious. (b) Correlation spectroscopy data clearly shows a sharp transition at 22 V, where the ion crystal goes from a linear to a zigzag configuration. The contrast is obtained from a fit of Eq. (3.16) to the correlation data. However, the camera image does not reveal this transition point. With increasing axial confinement, the two points at which the lowest radial mode frequency becomes zero move away from the center, leading to a parabola-like curve. The radial trapping potential is anisotropic, which results in two curves for the two radial trapping axes.

By increasing the axial confinement of an ion crystal, the radial motional modes have less and less energy until the linear configuration becomes unstable and the crystal rearranges in a zigzag configuration. At the transition point, the radial confinement of the central ion becomes zero, leading to a large uncertainty in its radial position. The measurement relies on the fact that correlation spectroscopy not only enables a determination of ion positions but its outcome is also linked to the stability of the ion positions.

The observed transition from a linear to a zigzag configuration is shown in Figure 3.11. A large ion crystal of 40 ions is first trapped at a low axial confinement ($f_{\mathrm{ax}} = 150\,\mathrm{kHz}$) which ensures a linear configuration of the crystal. Then, the axial trapping frequency is increased step-by-step until the ions arrange in a zigzag configuration (up to $f_{\mathrm{ax}} = 214\,\mathrm{kHz}$). For sufficiently large axial tip electrode voltages, the zigzag configuration can be seen on the camera image [Fig. 3.11(a)]. For each axial trapping frequency, the phase differences between the ions are measured with correlation spectroscopy on the $|S_{1/2}, m_j = 1/2\rangle \leftrightarrow |D_{5/2}, m_j = 5/2\rangle$ transition. In addition to Eq. (3.12), a contrast of the correlations is introduced in the ansatz, leading to

$$C_{ij} \equiv \langle \sigma_z^{(i)} \sigma_z^{(j)} \rangle = \frac{1}{2} c_i c_j \cos(\phi_i - \phi_j), \tag{3.16}$$

where the contrast c_i of ion i ranges from 0 to 1. By fitting this ansatz to the correlation data, both the phases ϕ_i and the contrast c_i are obtained.

Plotting the contrast c_i over the ion string and against the axial tip electrode voltage clearly shows the transition point as a loss of contrast at 22 V [Fig. 3.11(b)]. At the transition from the linear to the zigzag configuration, the radial confinement of the central ions becomes unstable; hence, the contrast drops for these ions. For increasing axial confinement, this instability occurs at two points that move away from the center. Due to the anisotropic radial trapping potential, a second transition occurs for the second radial trapping axis. This description can be substantiated by the experimental parameters: The ion crystal was confined at radial trapping frequencies of $\omega_x = 2\pi \times 2.93\,\mathrm{MHz}$ and $\omega_y = 2\pi \times 2.88\,\mathrm{MHz}$. The lowest radial mode frequency becomes zero for an axial trapping frequency of $\omega_{\mathrm{ax}} \approx 186\,\mathrm{MHz}$ and $\omega_{\mathrm{ax}} \approx 189\,\mathrm{MHz}$, respectively. These frequencies correspond to tip voltages of approximately 22.0 V and 22.8 V, agreeing with the observed behavior.

4

TROTTER APPROXIMATION OF HAMILTONIANS

Quantum simulators try to replicate the Hamiltonian of a system of interest [1]. However, the number of Hamiltonians that are available in a specific physical implementation of a quantum simulator is limited. One way to make more Hamiltonians available is the use of an approximation method [73]. If a Hamiltonian of interest $H = \sum_k H_k$ consists of a sum of multiple Hamiltonians H_k that are already available in the system, then the Hamiltonian H can be approximated by splitting up the time evolution into small steps evolving under H_k. This method is the so-called Trotter approximation.

The present chapter gives a brief theoretical overview over the Trotter approximations used in this thesis. Then, experimental details on the implementation of the Trotter approximations are given. In particular, possible sources of errors are discussed, such as unwanted coupling to spectrally broadened light. Finally, an example of a quench dynamics is presented, in which a 21-ion system is evolved under the Trotter-approximated Heisenberg model.

4.1 THEORETICAL BASICS OF TROTTER APPROXIMATIONS

Hamiltonians that can be implemented in our experiment with a single interaction beam are the XX (YY) model, the transverse Ising model, and the XY model. Further Hamiltonians can be realized by approximating the time evolution of the desired Hamiltonian with a number of short, simple evolutions of available

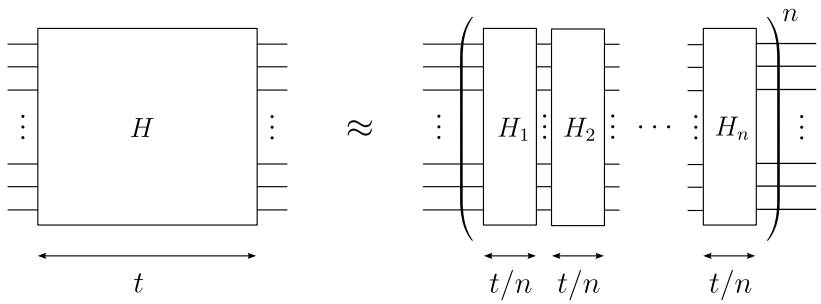

Figure 4.1: Trotter approximation of a Hamiltonian. The time evolution under a Hamiltonian $H = H_1 + H_2 + \cdots + H_n$ is approximated by splitting the total evolution time t into n smaller steps that evolve under Hamiltonian H_1, H_2,..., H_n.

Hamiltonians. This is called a Trotter approximation. In a Trotter approximation, one uses the fact that the time evolution operator $U = \exp(-\mathrm{i}Ht)$ of a Hamiltonian $H = H_1 + H_2 + \cdots + H_n$ can be decomposed into n steps by [5, 73]

$$\mathrm{e}^{-\mathrm{i}Ht} = \left(\mathrm{e}^{-\mathrm{i}H_1 t/n} \cdots \mathrm{e}^{-\mathrm{i}H_n t/n}\right)^n + \mathcal{O}(t^2), \tag{4.1}$$

where $\mathcal{O}(t^2)$ are terms of second order or higher in time t. Such a Trotter approximation is depicted in Figure 4.1. A well-readable, more mathematical treatment of Trotter approximations can be found in Ref. [74–76]. In particular, this approach allows one to approximate the time-evolution operator of Hamiltonians of the form

$$H_{\mathrm{XYZ}} = aH_{\mathrm{XX}} + bH_{\mathrm{YY}} + cH_{\mathrm{ZZ}} \tag{4.2}$$

by

$$\mathrm{e}^{-\mathrm{i}H_{\mathrm{XYZ}}t} = \left(\mathrm{e}^{-\mathrm{i}aH_{\mathrm{XX}}t/3}\mathrm{e}^{-\mathrm{i}bH_{\mathrm{YY}}t/3}\mathrm{e}^{-\mathrm{i}cH_{\mathrm{ZZ}}t/3}\right)^3 + \mathcal{O}(t^2). \tag{4.3}$$

As the error term scales with t^2, it is favorable to split up the evolution into smaller blocks. Replacing $t \to t/n$ and exponentiating both sides with n yields

$$\mathrm{e}^{-\mathrm{i}H_{\mathrm{XYZ}}t} \approx \left(\mathrm{e}^{-\mathrm{i}aH_{\mathrm{XX}}\frac{t}{3n}}\mathrm{e}^{-\mathrm{i}bH_{\mathrm{YY}}\frac{t}{3n}}\mathrm{e}^{-\mathrm{i}cH_{\mathrm{ZZ}}\frac{t}{3n}}\right)^{3n}. \tag{4.4}$$

Besides a decomposition of this simple form, there exist higher-order Trotter approximations. For a list of higher-order decompositions see for instance Ref. [77].

Trotter approximations are used for two main experimental results presented in this thesis which are detailed in Sections 6 and 7. By setting $a = b = c = \frac{1}{3}$, the (isotropic) Heisenberg Hamiltonian is approximated,

$$H_{\mathrm{Heis}} = \frac{1}{3}\sum_{i<j} J_{ij}\left(\sigma_x^{(i)}\sigma_x^{(j)} + \sigma_y^{(i)}\sigma_y^{(j)} + \sigma_z^{(i)}\sigma_z^{(j)}\right). \tag{4.5}$$

Setting $a = b = \frac{1}{3}$ and $c = \frac{\tilde{\Delta}}{3}$ realizes an approximation of the anisotropic Heisenberg model or the XXZ model,

$$H_{\mathrm{XXZ}} = \frac{1}{3}\sum_{i<j} J_{ij}\left(\sigma_x^{(i)}\sigma_x^{(j)} + \sigma_y^{(i)}\sigma_y^{(j)} + \tilde{\Delta}\sigma_z^{(i)}\sigma_z^{(j)}\right). \tag{4.6}$$

Experiments demonstrated the applicability of Trotter approximations for quantum simulations in nuclear magnetic resonance systems [78], trapped ions [6], and superconducting qubits [79]; further, experiments on ultracold quantum gases [80] and Rydberg atoms [81]. In recent years, the engineering of error-robust Hamiltonians has received increased attention [82–84]. In Section 6.2, a detailed description of the design of a Trotter sequence is given that has some robustness against detuning errors and pulse length errors.

4.1.1 *Example: Trotter approximation of the XY model*

The evolution under the XY model (2.32) can be approximated by the first-order Trotter decomposition

$$U_{\mathrm{XY}}(t) \approx \left[U_{\mathrm{T}}^{(1)}(\Delta t)\right]^n = \left[U_{\mathrm{YY}}(\Delta t)U_{\mathrm{XX}}(\Delta t)\right]^n, \tag{4.7}$$

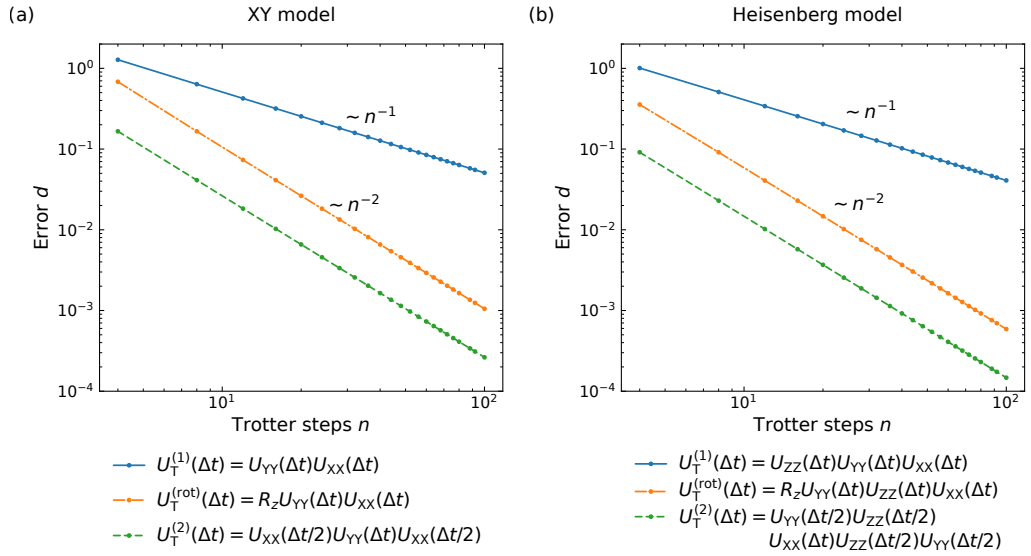

Figure 4.2: Convergence of Trotter sequences. The error d [Eq. (4.8)] is measured by the distance between the Trotter-approximated $[U_T(\Delta t)]^n$ and the ideal time-evolution operator $U(t)$ and is plotted against the number of Trotter steps n. First-order Trotter approximation $U_T^{(1)}$ (blue solid line), Trotter approximation with rotation $U_T^{(\mathrm{rot})}$ (orange dash-dotted line) where R_z is a $\pi/2$ rotation around the z axis, and second-order Trotter approximation $U_T^{(2)}$ (green dashed line). The Trotter-approximation error decreases with increasing number of steps. (a) XY model, Eq. (2.32), $\Delta t = 1/(2n)$. (b) Heisenberg model, Eq. (4.5), $\Delta t = 1/(3n)$. For all cases the numerical simulation is carried out for a system size of 6 qubits, $t = 1$, $J_0 = 1$, and $\alpha = 1$.

with n Trotter steps $U_T^{(1)}$ and $\Delta t = t/(2n)$. A Trotter step consists of the time-evolution operators $U_{XX}(\Delta t) = \exp(-\mathrm{i}H_{XX}\Delta t)$ and $U_{YY}(\Delta t) = \exp(-\mathrm{i}H_{YY}\Delta t)$. In order to match a decomposition that is analogous to Eq. (4.4), the number of Trotter steps has to be even, $n \in 2\mathbb{N}$.

The convergence of the Trotter approximation can be measured by the distance d between the evolution of the Trotter approximation $(U_T)^n$ and the ideal evolution $U = U_{XY}$,

$$d = \| [U_T(\Delta t)]^n - U(t) \|_2, \tag{4.8}$$

where $\|A\|_2 \equiv \sqrt{\mathrm{tr}(A^\dagger A)}$ is the Frobenius norm. A numerical example is shown in Figure 4.2(a). A system of 6 qubits evolves under the XY model for a time $t = 1$ with coupling parameters $J_0 = 1$ and $\alpha = 1$. The evolution is approximated by a Trotter sequence of n steps. The Figure shows the Trotter approximation error d for different Trotter approximation schemes. With increasing number of Trotter steps n, the Trotter-approximation error decreases for all cases. The error d of the first-order approximation $U_T^{(1)}$ scales as n^{-1}, showing that the more Trotter steps are used for a fixed evolution time, the better the ideal Hamiltonian is approximated.

Faster convergence with an error of order n^{-2} can be achieved by a symmetrized second-order Trotter decomposition [74]

$$U_{\mathrm{T}}^{(2)}(\Delta t) = U_{\mathrm{XX}}(\Delta t/2)U_{\mathrm{YY}}(\Delta t)U_{\mathrm{XX}}(\Delta t/2). \tag{4.9}$$

Approximations of higher orders can be constructed [75] by decompositions of the form

$$\mathrm{e}^{x(A+B)} = \mathrm{e}^{t_1 A}\mathrm{e}^{t_2 B}\mathrm{e}^{t_3 A}\mathrm{e}^{t_4 B}\cdots\mathrm{e}^{t_M A} + \mathcal{O}(x^{m+1}), \tag{4.10}$$

with finite M. If complex time steps $t_i \in \mathbb{C}$ are permitted, there exists a third-order decomposition with five terms[1]. The simplest real decomposition ($t_i \in \mathbb{R}$) of third order is a product of seven factors[2]. However, for order $m \geq 3$, real decompositions of this form always require negative time steps $t_i < 0$ [76]. This is not easily achieved in the experiment.

Interestingly, the numerical simulations in Fig. 4.2(a) suggest that introducing a base rotation around the z axis after each Trotter step also creates a convergence speed of n^{-2}. This approach is possible as the XY Hamiltonian conserves the total z magnetization $\sigma_z^{(\mathrm{tot})}$, which implies $[H_{\mathrm{XY}}, \sigma_z^{(\mathrm{tot})}] = 0$. Consequently, a rotation $R_z = \exp\left(-\mathrm{i}\pi/4 \sum_i \sigma_z^{(i)}\right)$ commutes with the time-evolution operator, $[U_{\mathrm{XY}}(t), R_z] = 0$. This allows one to distribute rotations into the time evolution and to approximate each time step by a Trotter decomposition of the form

$$\begin{aligned} U_{\mathrm{XY}}(t) &= (R_z^\dagger)^n [R_z U_{\mathrm{XY}}(t/n)]^n && (4.11)\\ &\approx (R_z^\dagger)^n [R_z U_{\mathrm{YY}}(\Delta t) U_{\mathrm{XX}}(\Delta t)]^n, && (4.12) \end{aligned}$$

where a Trotter step is given by

$$U_{\mathrm{T}}^{(\mathrm{rot})}(\Delta t) = R_z U_{\mathrm{YY}}(\Delta t) U_{\mathrm{XX}}(\Delta t). \tag{4.13}$$

As can be seen in the numerical computation in Fig. 4.2(a), this sequence has the same convergence speed of n^{-2} as the second-order decomposition (4.9). This behavior can be understood using the algebraic relations given in Appendix C.1 to pull all rotations to the left. As an example, $n = 2$ steps are considered,

$$\begin{aligned} U_{\mathrm{XY}}(t) &\approx (R_z^\dagger)^2 [R_z U_{\mathrm{YY}}(\Delta t) U_{\mathrm{XX}}(\Delta t)][R_z U_{\mathrm{YY}}(\Delta t) U_{\mathrm{XX}}(\Delta t)] && (4.14)\\ &= U_{XX}(\Delta t) U_{\mathrm{YY}}(\Delta t) U_{\mathrm{YY}}(\Delta t) U_{\mathrm{XX}}(\Delta t) && (4.15)\\ &= U_{\mathrm{T}}^{(2)}(2\Delta t). && (4.16) \end{aligned}$$

This pattern repeats for $n > 2$. Hence, the rotations create a second-order Trotter decomposition of step size $2\Delta t$.

1 Complex third-order decomposition: $\mathrm{e}^{x(A+B)} = \mathrm{e}^{\frac{1}{2}axA}\mathrm{e}^{axB}\mathrm{e}^{\frac{1}{2}xA}\mathrm{e}^{a^* xB}\mathrm{e}^{\frac{1}{2}a^* xA} + \mathcal{O}(x^3)$, where $a = \frac{1}{6}(3 \pm \sqrt{3}\mathrm{i})$ and a^* is the complex conjugate, see Ref. [75] and citation therein.

2 Real third-order decomposition: $\mathrm{e}^{x(A+B)} = \mathrm{e}^{\frac{1}{2}sxA}\mathrm{e}^{sxB}\mathrm{e}^{\frac{1}{2}(1-s)xA}\mathrm{e}^{(1-2s)xB}\mathrm{e}^{\frac{1}{2}(1-s)xA}\mathrm{e}^{sxB}\mathrm{e}^{\frac{1}{2}sxA} + \mathcal{O}(x^3)$, where $s = \frac{1}{2-\sqrt[3]{2}}$, see Ref. [75]. This decomposition is even correct up to fourth order.

4.1.2 *Example: Trotter approximation of the Heisenberg model*

The time-evolution under the Heisenberg model (4.5) is approximated in first order by

$$U_{\text{Heis}}(t) \approx \left[U_{\text{T}}^{(1)}\right]^n = \left[U_{ZZ}(\Delta t)U_{YY}(\Delta t)U_{XX}(\Delta t)\right]^n, \tag{4.17}$$

with $\Delta t = t/(3n)$. While U_{XX} and U_{YY} are native interactions in the experiment, U_{ZZ} has to be realized by a base transformation[3], $U_{ZZ} = R_x^\dagger U_{YY} R_x$. Here, R_x denotes a global $\pi/2$ rotation around the x axis, $R_x = \exp\left(-\mathrm{i}\frac{\pi}{4}\sum_i \sigma_x^{(i)}\right)$. Rotations R_y and R_z are defined analogously. Thus, in the experiment, a single Trotter step can be implemented as

$$\begin{aligned} U_{\text{T}} &= U_{ZZ}U_{YY}U_{XX} && (4.18)\\ &= R_x^\dagger U_{YY} R_x U_{YY} U_{XX}. && (4.19)\end{aligned}$$

A numerical example of the convergence of this approximation is shown in Fig. 4.2(b). A system of 6 qubits evolves under the Heisenberg model for a time $t = 1$ with coupling parameters $J_0 = 1$ and $\alpha = 1$. As in the previous example, the Figure presents the Trotter approximation error for different Trotter approximation schemes. The first order approximation (4.17) again has an approximation error d that scales with the number of Trotter steps n as n^{-1}. As in the case of the XY model, the convergence speed can be increased to second order n^{-2} by introducing base rotations. The Heisenberg model conserves each component of total magnetization, hence $[U_{\text{Heis}}(t), R_z] = 0$. Distributing the rotations into the evolution steps yields

$$\begin{aligned} U_{\text{Heis}}(t) &= (R_z^\dagger)^n [R_z U_{\text{Heis}}(t/n)]^n && (4.20)\\ &\approx (R_z^\dagger)^n [R_z U_{YY}(\Delta t)U_{ZZ}(\Delta t)U_{XX}(\Delta t)]^n && (4.21)\end{aligned}$$

with a Trotter step (substitute $\Delta t \to \Delta t/2$)

$$U_{\text{T}}^{(\text{rot})}(\Delta t) = R_z U_{YY}(\Delta t)U_{ZZ}(\Delta t)U_{XX}(\Delta t). \tag{4.22}$$

It is important to note that the sub-step U_{ZZ} has to be in the center of the three sub-steps in order to achieve the convergence speedup. This behavior was tested with numerical simulations, but the reason for it remains unclear. Again, this sequence can be brought into the form of a symmetric second-order decomposition, as can be seen for $n = 2$,

$$\begin{aligned} U_{\text{Heis}} &\approx (R_z^\dagger)^2 [R_z U_{YY}(\Delta t)U_{ZZ}(\Delta t)U_{XX}(\Delta t)][R_z U_{YY}(\Delta t)U_{ZZ}(\Delta t)U_{XX}(\Delta t)] && (4.23)\\ &= U_{YY}(\Delta t)U_{ZZ}(\Delta t)U_{XX}(2\Delta t)U_{ZZ}(\Delta t)U_{YY}(\Delta t) && (4.24)\\ &= U_{\text{T}}^{(2)}(2\Delta t), && (4.25)\end{aligned}$$

with a second-order Trotter step

$$U_{\text{T}}^{(2)}(\Delta t) = U_{YY}(\Delta t/2)U_{ZZ}(\Delta t/2)U_{XX}(\Delta t)U_{ZZ}(\Delta t/2)U_{YY}(\Delta t/2). \tag{4.26}$$

3 A list of base transformations is given in Appendix C.1.

The second-order Trotter approximation has an error d that scales with the number of Trotter steps n as n^{-2}, as is shown in Fig. 4.2(b).

While a simple second-order Trotter approximation (4.26) has the same convergence speed as the Trotter sequence using base rotations (4.22), the use of additional base rotations in a Trotter sequence helps to mitigate experimental imperfections as detailed in Sec. 6.2.1:

1. Base rotations can be used to incorporate dynamical decoupling into the Trotter sequence.
2. The number of base rotations can be reduced by algebraic manipulations. Having fewer base rotations helps to circumvent limitations of the experimental pulse control hardware.

Examples of such Trotter sequences are given in Sections 6 and 7.

4.2 TECHNICAL DETAILS ON THE TROTTER APPROXIMATION

While in theory the implementation of a Trotter sequence is straightforward, in practice, a number of technical issues have to be considered:

1. The phase of the XX interaction has to be calibrated and the ac-Stark shift during the XX interaction has to be compensated at the Hertz level,
2. ac-Stark shifts during the qubit rotations can become relevant,
3. switching on and off the laser light leads to spectral broadening that gives rise to unwanted resonant coupling, and
4. decoherence is caused by magnetic-field fluctuations and laser noise.

In this section, I give a description of how to set up the experiment for the application of Trotter sequences and how to identify and avoid the listed problems. Finally, I give an example of an experimentally observed quench dynamics in a 21-ion crystal under the Trotter-approximated Heisenberg Hamiltonian.

4.2.1 *Setting up the XX interactions*

The basic building block for the Trotter sequences used throughout this thesis is an interaction of the XX type. This entangling interaction has to be set up with the correct light phase and the ac-Stark shift has to be compensated correctly. A procedure for setting up the ac-Stark compensation is given in Ref. [35, Sec. 5.3.1]: An initial state, $\psi_0 = |\downarrow\downarrow \ldots \downarrow\rangle$, is evolved under the entangling interactions. If the ac-Stark shift is not compensated, the frequency shift leads to a transverse component $B_i \neq 0$ in the interaction Hamiltonian $H_{\text{Ising}} = \sum_{i<j} J_{ij}\sigma_x^{(i)}\sigma_x^{(j)} + \sum_i B_i\sigma_z^{(i)}$. For $|B_i| \gg J_{ij}$, the total magnetization $\langle z_{\text{tot}}\rangle = \sum_i \langle\sigma_z^{(i)}\rangle$ is conserved and the initial state $\psi_0 = |\downarrow\downarrow \ldots \downarrow\rangle$ remains unchanged. If the ac-Stark shift is compensated, i.e. $B_i = 0$, the interaction Hamiltonian $H_{XX} = \sum_{i<j} J_{ij}\sigma_x^{(i)}\sigma_x^{(j)}$ does not conserve $\langle z_{\text{tot}}\rangle$, which can be observed as a rising excitation in the experiment. This rising excitation can be used as a measure in the experiment to set up the ac-Stark compensation and consequently to set up a Hamiltonian of the XX type.

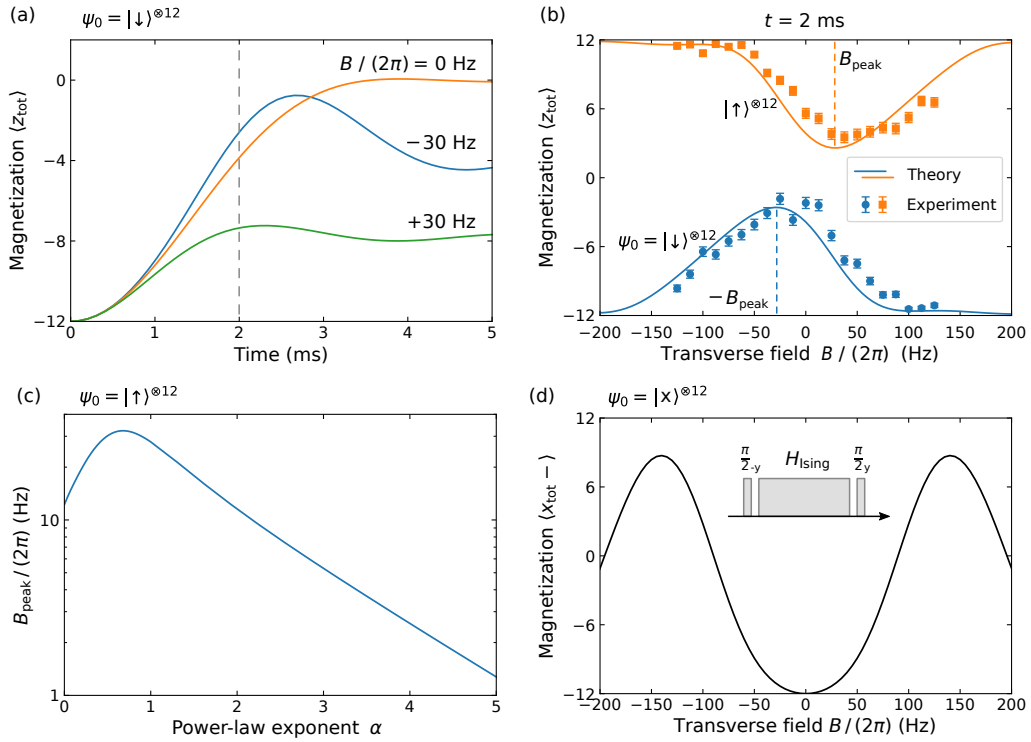

Figure 4.3: Setting up an XX-type Hamiltonian. An XX-type Hamiltonian can be obtained from a transverse-field Ising Hamiltonian $H_{\text{Ising}} = \sum_{i<j} J_{ij}\sigma_x^{(i)}\sigma_x^{(j)} + \sum_i B_i\sigma_z^{(i)}$ by setting the transverse field $B = 0$. (a) Time evolution for different transverse fields B. Maximizing the magnetization of the time-evolved state $\psi_0 = |\downarrow\rangle^{\otimes 12}$ as discussed in Ref. [35] does not always lead to an XX-type Hamiltonian, as the magnetization rises faster for a negative value of $B = -2\pi \times -30\,\text{Hz}$ than for $B = 0$. The parameters used in the simulation are $J_0 = 220\,\text{rad/s}$ and $\alpha = 0.96$ with $J_{ij} = J_0/|i-j|^\alpha$. (b) Magnetization after a fixed evolution time vs. transverse field. For the initial state $\psi_0 = |\downarrow\rangle^{\otimes 12}$, the peak magnetization after 2 ms occurs at $B_{\text{peak}} = -2\pi \times 29\,\text{Hz}$. For $\psi_0 = |\uparrow\rangle^{\otimes 12}$, the sign of B_{peak} changes. Simulations (solid lines) and experimental data (points) are in agreement. (c) Dependence on the power-law exponent α. The shift B_{peak} of the peak magnetization depends on the extent of the long-range interactions, i.e. on the exponent α. The shift becomes maximal for long-range interactions at $\alpha = 0.68$ but becomes negligible as the interactions become more and more short-range, i.e. $\alpha \to \infty$. (d) The shift of B_{peak} can be avoided by probing the magnetization $\langle x_{\text{tot}}-\rangle = -\sum_i \langle\sigma_x^{(i)}\rangle$ with a Ramsey-type experiment that evolves $|\psi_0\rangle = |x\rangle^{\otimes 12} = (|\downarrow\rangle + |\uparrow\rangle)^{\otimes 12}$, as the two components of the superposition have shifts of same magnitude but opposite sign. In this Ramsey-type experiment, the minimum magnetization occurs at $B = 0$.

However, numerical simulations and experimental data show that simply maximizing the observed magnetization can lead to an erroneous ac-Stark compensation for which the resulting Hamiltonian is not the XX Hamiltonian. The results of these simulations and experiments are presented in Fig. 4.3. First, the time-evolution of the initial state $\psi_0 = |\downarrow\downarrow \ldots \downarrow\rangle$ under the Ising Hamiltonian is simulated. Fig. 4.3(a) shows a numerical simulation of the total magnetization $\langle z_{\text{tot}}\rangle$ as a function of time for three different transverse field strengths B. This simulation is carried out for a 12-qubit system with long-range interactions $J_{ij} = J_0/|i-j|^\alpha$ (where $\alpha = 0.96$, $J_0 = 220\,\text{rad/s}$). An important observation is that the magnetization for a negative transverse field $B = -2\pi \times 30\,\text{Hz}$ initially increases faster than for $B = 0$. Therefore, if one maximizes the magnetization at a time of e.g. 2 ms, the ac-Stark shift would not be compensated and the resulting Hamiltonian would not be of the XX type, but instead of the type of a transverse Ising Hamiltonian with $B \neq 0$.

A solution to this problem can be found by noticing that this shift of maximum magnetization takes an opposite sign when starting from the initial state $\psi_0 = |\uparrow\uparrow \ldots \uparrow\rangle$, as shown in Fig. 4.3(b). The magnetization after a fixed evolution time of $t = 2\,\text{ms}$ is evaluated as a function of the transverse field B. For the initial state $|\downarrow\downarrow \ldots \downarrow\rangle$ the maximum magnetization $\langle z_{\text{tot}}\rangle$ occurs at a transverse field of $B = -2\pi \times 29\,\text{Hz}$, whereas for the initial state $|\uparrow\uparrow \ldots \uparrow\rangle$ the maximum occurs at $+2\pi \times 29\,\text{Hz}$. Numerical simulations (solid lines) agree with experimental data (points). In this experiment, the transverse field B was varied by changing the centerline detuning $\delta_c = 2B$ of the laser.

The magnitude of the shift B_{peak} of the maximum magnetization depends on the extent of the long-range interactions, i.e. on the exponent α in the spin-spin coupling strength $J_{ij} = J_0/|i-j|^\alpha$. Numerical simulations of this dependency are shown in Fig. 4.3(c). The shift gets maximum at a power-law exponent of $\alpha = 0.68$ for the studied example of a 12-ion chain. For interactions that become more and more short range, i.e. $\alpha \to \infty$, the shift vanishes.

The solution of setting up XX-type interactions without suffering from erroneous shifts in the peak magnetization consists of using a superposition of $|x\rangle = (|\downarrow\rangle + |\uparrow\rangle)^{\otimes 12}$ as an initial state and probing the magnetization in a Ramsey-type experiment. Numerical simulations showing this case are presented in Fig. 4.3(d). The system is initially prepared in the state $|x\rangle$ and then evolved under the Ising Hamiltonian for a time t (instead of a free-evolution period). Finally, the magnetization $\langle x_{\text{tot}} - \rangle = -\sum_i \langle \sigma_x^{(i)} \rangle$ is measured. Using this superposition as initial state leads to a signal that takes its minimum at $B = 0$, as the two components of the superposition have shifts of same magnitude but opposite sign, allowing to accurately set up the ac-Stark compensation and interactions of the XX type.

The reason why the superposition $|x\rangle$ is a good choice for setting up XX-type interactions can be understood from conservation properties of the XX Hamiltonian $H_{XX} = \sum_{i<j} J_{ij} \sigma_x^{(i)} \sigma_x^{(j)}$. The state $|x\rangle^{\otimes N}$ (with N being the system size) is an eigenstate of H_{XX}. Therefore, a system that is initially prepared in $|x\rangle^{\otimes N}$ does not evolve under H_{XX} (up to a global phase) and the magnetization $\langle x_{\text{tot}} - \rangle$ remains constant. A Ramsey-type experiment as shown in Fig. 4.3(d) tests

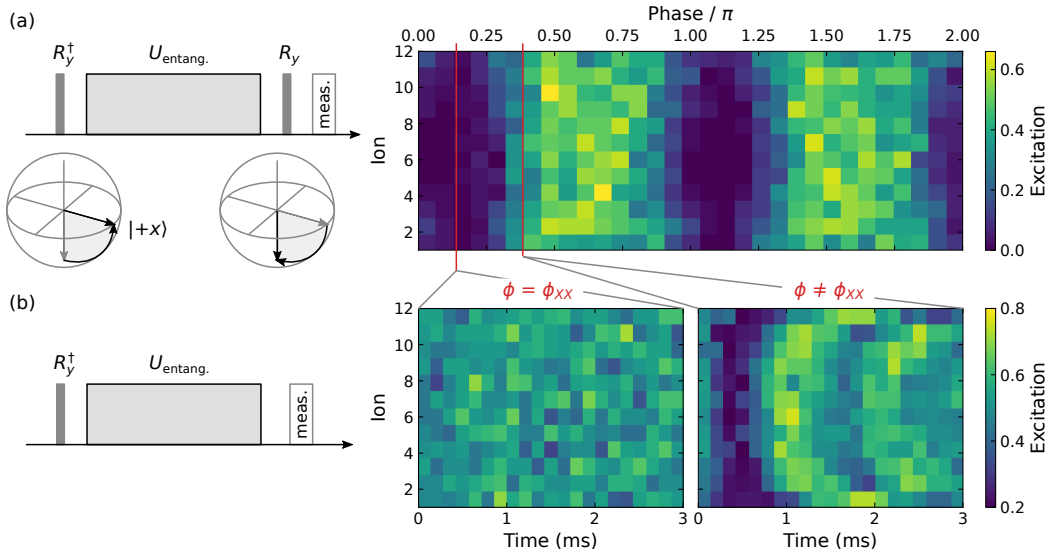

Figure 4.4: Setting up the XX interaction. (a) Phase scan, in which the light phase between the state preparation pulse $R_y^\dagger$ and the entangling pulse $U_{\text{entang.}}$ is varied in a Ramsey-type experiment. When the value of the light phase realizes the H_{XX} Hamiltonian, the initial state $|x\rangle$ is an eigenstate and does not evolve. At this phase $\phi = \phi_{\text{XX}}$, the measured excitation becomes minimal. (b) Time evolution of the initial state $|x\rangle$ under the entangling operation $U_{\text{entang.}}$. A time evolution at $\phi = \phi_{\text{XX}}$ realizes H_{XX}, which keeps the initial state $|x\rangle$ constant. When the phase is set differently, $\phi \neq \phi_{\text{XX}}$, the initial state is no longer an eigenstate of the realized Hamiltonian $H \neq H_{\text{XX}}$ and the state changes.

for such a conservation of magnetization. If the Hamiltonian is of the XX type, the magnetization $\langle x_{\text{tot}} - \rangle$ is conserved throughout the time evolution.

4.2.2 *Phase calibration of H_{XX}*

By setting the light phase (with respect to the first light pulse in an experiment), the interactions can be tuned between H_{XX} and H_{YY}. The light phase can be calibrated to implement H_{XX} with a Ramsey-type experiment as shown in Figure 4.4(a). The experiment uses the fact that the $|x\rangle$ state is an eigenstate of the XX Hamiltonian and thus remains constant during time evolution, up to a global phase. An initial $\pi/2$ pulse prepares the 12-ion crystal in $|x\rangle$. An entangling period of typically 1 ms ($J_0 \approx 220\,\text{rad/s}$) evolves the initial state under the Hamiltonian [35, Eq. (3.72)]

$$H = J \sum_{i<j} \left(\sigma_i^+ \sigma_j^+ \mathrm{e}^{-2\mathrm{i}\phi} + \sigma_i^+ \sigma_j^- + \sigma_i^- \sigma_j^+ + \sigma_i^- \sigma_j^- \mathrm{e}^{2\mathrm{i}\phi} \right), \tag{4.27}$$

where ϕ is the light phase. Two important cases are

$$H(\phi = 0) = H_{\text{XX}} \quad \text{and} \quad H(\phi = \pi/2) = H_{\text{YY}}. \tag{4.28}$$

A final analysis $\pi/2$ pulse measures $\langle x^{(i)} - \rangle$. The phase is set correctly, when the excitation is minimized. At the minimum, the excitation that is reached in our

experiment is around 10^{-2} or below. Residual excitation can be caused by an improperly compensated ac-Stark shift. In that case, a new repetition of both the ac-Stark shift compensation and the phase calibration should be carried out.

After setting the phase[4] $\phi = \phi_{XX}$ for the H_{XX} interactions, the time evolution can be tested [Fig. 4.4(b)]. The $|x\rangle$ state is evolved for a few milliseconds. For $\phi = \phi_{XX}$, the excitation remains constant, as expected for an eigenstate of H_{XX}. For a different phase, the state time-evolves and the excitation changes.

4.2.3 *Rotation errors caused by ac-Stark shifts*

The ac-Stark shift on the qubit transition $|S_{1/2}, m_j = 1/2\rangle \leftrightarrow |D_{5/2}, m_j = 5/2\rangle$ causes noticeable rotation errors when driving the transition with full laser power. A light field that couples to a two-level system and to further, far-detuned levels creates an ac-Stark shift

$$\delta_{ac,tot} = -\frac{\Omega^2}{2\Delta} + \delta_{ac}, \tag{4.29}$$

where Δ is the detuning from the resonance, Ω the Rabi frequency of the resonant interaction, and δ_{ac} is the ac-Stark shift from coupling to the far-detuned levels. Even when the transition is driven resonantly, coupling to far-detuned levels can cause a frequency shift.

A Ramsey experiment [85] was used to measure the ac-Stark shift [Fig. 4.5(a)]. An initial $\pi/2$ pulse brings the ion into the state $(|\uparrow\rangle + |\downarrow\rangle)/\sqrt{2}$. Then a light field illuminates the ion and causes an ac-Stark shift $\delta_{ac,tot}$. During the probe time τ, the shift of the energy levels changes the superposition to $(|\uparrow\rangle + e^{-i\phi}|\downarrow\rangle)/\sqrt{2}$ with phase $\phi = \delta_{ac,tot}\tau$. A final analysis $\pi/2$ pulse measures the accumulated phase ϕ, allowing us to extract $\delta_{ac,tot}$. The measurement is repeated for different detunings Δ and a fit with Eq. (4.29) is used to extract δ_{ac}. When the qubit transition is driven resonantly with a Rabi frequency of $\Omega = 2\pi \times 230(2)$ kHz, the shift is $\delta_{ac} = 2\pi \times 2.76(7)$ kHz.

This frequency shift was found to become problematic when *multiple* alternating π pulses are used in a sequence. Figure 4.5(b) shows the underlying mechanism: Consider a qubit that is initially prepared in the state $|x\rangle = (|\uparrow\rangle + |\downarrow\rangle)/\sqrt{2}$ (step 1). Ideally, a π pulse of phase $\phi = 0$ rotates around the x axis leaving this state unchanged. However, the (ac Stark) frequency shift tilts the rotation axis by an angle $\alpha = \arctan(\delta_{ac}/\Omega)$. A π pulse of phase $\phi = 0$ around this tilted axis brings the state $|x\rangle$ below the equator (step 2). For small detunings, $\delta_{ac} \ll \Omega$, the error is described by an effective rotation around the y axis by an angle 2α. Application of a π pulse with opposite phase accumulates this error and brings the state above the equator by an angle 4α (step 3). In general, the error caused by an ac-Stark shift during an alternating π pulse sequence of n pulses is

$$\theta_{ac} = (-1)^n 2n\frac{\delta_{ac}}{\Omega} \quad \text{for } \delta_{ac} \ll \Omega. \tag{4.30}$$

4 The phase offset between the light used for global rotations and the bichromatic light is initially unknown. Therefore, a phase scan needs to be carried out. The phase offset originates from using two different RF sources for global rotations and entangling operations, respectively. Once the phase is set it remains stable, as the RF sources are supplied with a common reference.

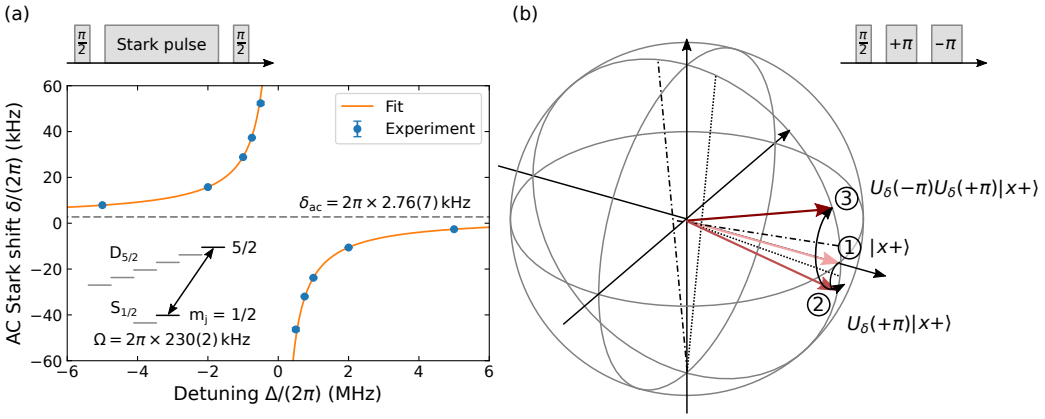

Figure 4.5: Ac-Stark shifts and rotation errors. (a) Ac-Stark shift on the qubit transition. The ac-Stark shift on the $|S_{1/2}, m_j = 1/2\rangle \leftrightarrow |D_{5/2}, m_j = 5/2\rangle$ transition was measured with a Ramsey experiment. The ac-Stark shift δ_{ac} was extracted from the data by a fit with Eq. (4.29). The error bars are too small to be visible. For a Rabi frequency of $\Omega = 2\pi \times 230(2)$ kHz the ac-Stark shift was found to be $\delta_{ac} = 2\pi \times 2.76(7)$ kHz. (b) Rotation errors introduced by ac-Stark shifts. The presence of a frequency shift tilts the rotation axis, causing an error when applying a π pulse ($1 \rightarrow 2$). Using alternating π pulses leads to an accumulation of this error ($2 \rightarrow 3$). Alternating π pulses are routinely used to mitigate rotation errors caused by inhomogeneous coupling to the global laser beam.

For the measured ac-Stark shift this leads to a rotation error of $\theta = -2 \times (2.76/230) = -2.4 \times 10^{-2}$ after a single π pulse. In a Trotter sequence tens of π pulses are applied, leading to a significant total error.

This error source can be weakened easily by reducing the Rabi frequency of the π pulses. The ac-Stark shift scales quadratically with the Rabi frequency, $\delta_{ac} = -\Omega^2/(2\Delta)$. For the Trotter sequences used in this work, the Rabi frequency of the rotations was set to $\Omega \approx 2\pi \times 2.5\,\text{kHz}$, resulting in an ac-Stark shift of $\delta_{ac} \approx 2\pi \times 0.3\,\text{Hz}$, which leads to a rotation error of only $\theta = -2 \times 10^{-4}$ after a single π pulse. This approach is sufficient for the Trotter sequences used in this thesis, as the total duration of such weak rotations is still small compared to the entangling operations. Using weak rotations also comes with the advantage of reducing the impact of spectral broadening that is created by turning on and off the light. This effect is described in more detail in Section 4.2.4.

4.2.4 *Resonant coupling to spectrally broadened light*

When a Hamiltonian is approximated by a Trotter sequence, light fields must be switched on and off repeatedly for each Trotter step. The finite duration of each light pulse in the order of 100 µs leads to a spectral broadening of the light spanning tens of kilo-Hertz. This becomes a problem for the bichromatic light field used in our experiment for creating entangling interactions. Despite the components of the bichromatic light field being detuned by approx. 20 to 40 kHz, the spectrally broadened light still causes resonant excitation of the motional

sidebands of the ion crystal. This erroneous excitation was found to be as large as $p_\uparrow \approx 0.4$, completely dominating over other sources of error. This problem becomes more prominent with increasing number of motional modes of large ion crystals.

The resonant coupling of spectrally broadened light can be demonstrated in an experiment that uses a single light field instead of a bichromatic field, as shown in Figure 4.6. Figure 4.6(a) details the light pulses used in the experiment: In a train of 20 light pulses, each light pulse has a finite duration $t_{\text{period}} = 147\,\mu\text{s}$. The rise (fall) time t_{slope} of the pulses is controlled by pulse shaping (segmented Blackman window [86, p. 25]). The periodic pulse repetition, the finite pulse duration, and the pulse shape leads to a spectral broadening of the light, as qualitatively depicted in Fig. 4.6(b). Even if the central light frequency ν_0 is detuned by a frequency Δ from the qubit transition frequency ν_0, there are still spectral components that resonantly couple to the carrier transition. Figure 4.6(c) shows a quantitative analysis of this coupling. By scanning over the detuning Δ, the overlap of the broadened light spectrum with the carrier transition can be observed. In this first measurement, pulse shaping was turned off ($t_{\text{slope}} = 0\,\mu\text{s}$), leading to a series of peaks where resonant coupling occurred. The peaks occurring at frequencies $n/147\,\mu\text{s} = n \times 6.8\,\text{kHz} = 6.8\,\text{kHz},\ 13.6\,\text{kHz},\ 20.4\,\text{kHz}, \ldots$ are the result of the periodic repetition of the light pulses with period 147 µs. The position and height of the peaks are found to be in good agreement with numerical simulations. In the experiment, the Rabi frequency was set to $\Omega = 2\pi \times 4\,\text{kHz}$ to avoid power broadening. In a second measurement shown in Fig. 4.6(d), pulse shaping was used to reduce spectral broadening. A rise (fall) time of $t_{\text{slope}} = 60\,\mu\text{s}$ is sufficient to diminish most of the peaks. The strengths of the remaining peaks depend on the details of pulse shaping and detuning.

The situation becomes worse, when considering a bichromatic light field that is set close to the radial motional modes. Figure 4.7(a) shows the calculated light spectrum of the Trotter sequence for the Heisenberg model[5] overlaid with the numerous radial modes. Without pulse shaping ($t_{\text{slope}} = 0\,\mu\text{s}$), the light spectrum has overlap with the radial modes over tens of kilohertz. This overlap can be reduced by fine-tuning the slope ($t_{\text{slope}} = 42\,\mu\text{s}$). In the experiment, the influence of pulse shaping on the sequence error can be observed [Fig.4.7(b)]. A crystal of 21 ions is prepared in the $|\downarrow\rangle$ state and evolved under the Trotterized Heisenberg model. The $|\downarrow\rangle$ state is an eigenstate of Heisenberg model and the excitation ideally remains constant. Any rise in excitation indicates an error in the realized Hamiltonian. The light spectrum is varied by changing the total duration of the Trotter sequence while keeping the number of pulses constant. Without pulse shaping, the excitation peaks at several sequence lengths, pointing towards coupling between the broadened spectrum and one of the radial modes. With pulse shaping, the peaks vanish. For comparison, a third measurement was taken for which the intensity of the entangling light was set to zero, leaving only rotation and dephasing errors. The operating point is the Trotter sequence length at which the main measurements were later taken.

5 For the details of the Trotter sequence see Fig. 4.9(a).

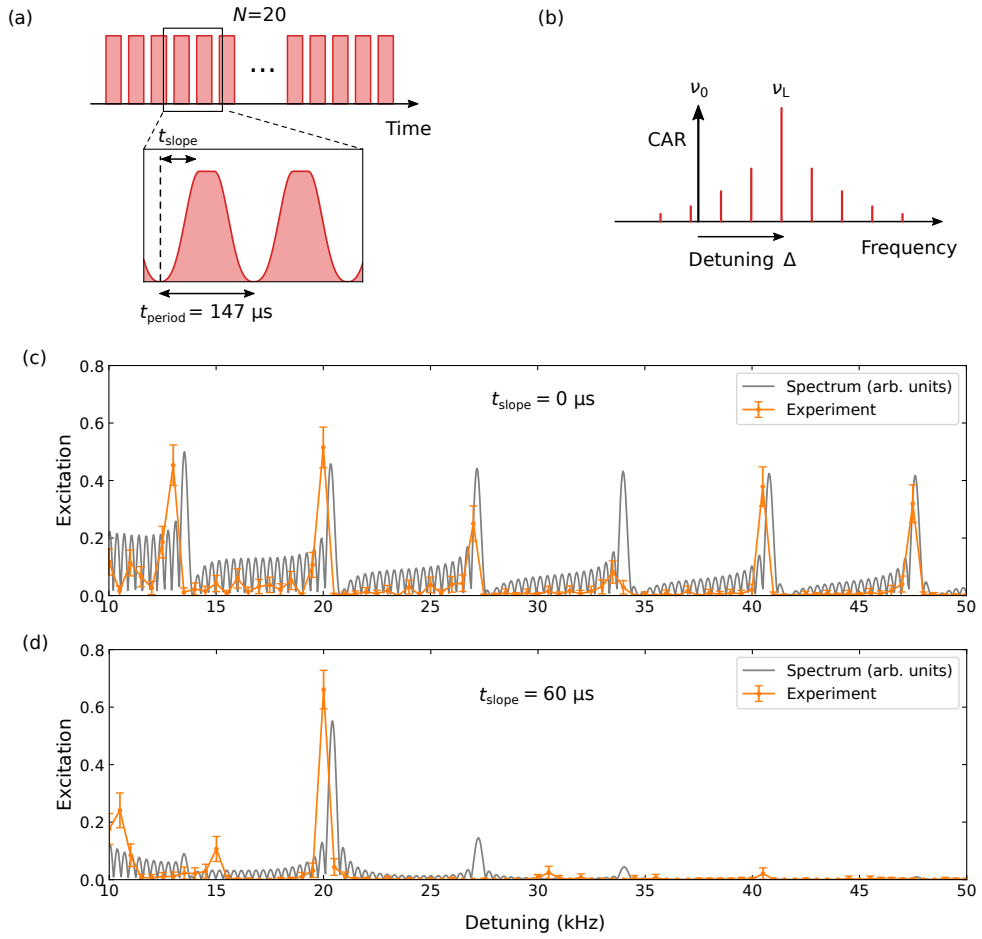

Figure 4.6: Spectral broadening of a pulse train. (a) A pulse train consists of 20 pulses where each pulse has a duration of t_{period} and a rise and fall time of t_{slope}, respectively (segmented Blackman window [86, p. 25]). (b) The light is detuned by a frequency Δ from the carrier transition ν_0. The finite duration of the pulses leads to a spectral broadening of the exciting light. This results in some resonant coupling of the spectrally broadened light with the carrier. (c) In an experiment, 20 off-resonant pulses of period $t_{\text{period}} = 147\,\mu\text{s}$ (6.8 kHz spectral width) illuminate a crystal of 21 ions (Rabi frequency $\Omega = 2\pi \times 4\,\text{kHz}$). Pulse shaping is turned off in this first measurement ($t_{\text{slope}} = 0\,\mu\text{s}$), leading to a spectrum with a series of peaks that couple to the carrier. A numerical simulation (grey line) predicts this behavior. (d) In a second experiment, pulse shaping was set to $t_{\text{slope}} = 60\,\mu\text{s}$. The shaped pulses have a spectrum that leads to significantly less unwanted coupling to the carrier.

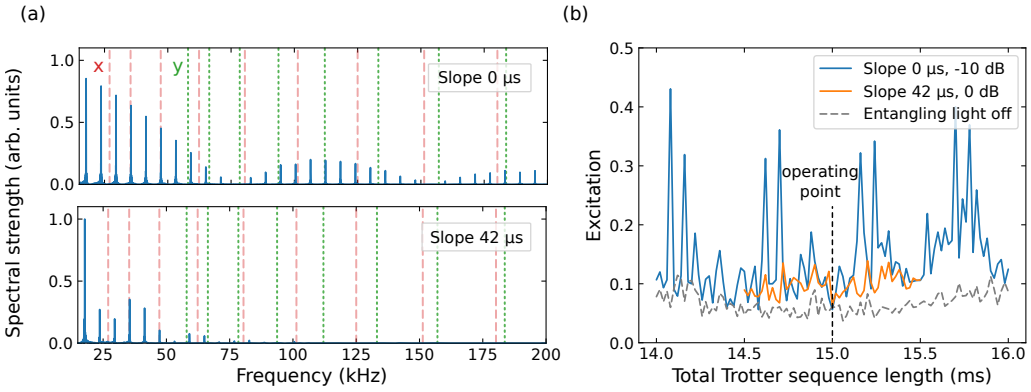

Figure 4.7: Spectral overlap of the Trotter sequence with radial modes. (a) Calculated spectrum of the Trotter sequence (32 Trotter steps) for rectangular pulses (slope 0 µs). The spectrum shows significant overlap with the radial motional modes along the x (y) direction. Pulse shaping (slope 42 µs) reduces the strength of the peaks in the spectrum of the light pulses. (b) The overlap of the spectrum of the Trotter sequence with the radial motional modes is measured by varying the total length of the Trotter sequence.

Resonant coupling from spectrally broadened light constitutes one of the leading error sources for the Trotter sequences presented in this thesis. It becomes more and more problematic for ion crystals of growing ion number, as the number and density of radial modes increases as well. For example, a crystal of 21 ions has already $2 \times 21 = 42$ radial modes, with a spacing of around 10 kHz in the vicinity of the c.o.m. mode (for $\omega_{ax} \approx 2\pi \times 200\,\text{kHz}$). Placing the peaks of the light spectrum of the Trotter sequence in such a way that no radial motional mode is hit becomes increasingly difficult, even with pulse shaping. Furthermore, the frequencies of the radial modes fluctuate over time, as the power of the trap drive cannot be perfectly stabilized — placing a spectral peak too close (few hundred hertz) to a radial mode can lead to unpredictable increases in the error rate, as was observed in our experiment[6].

4.2.5 *Resonant coupling to laser noise*

The entangling interactions are created by light fields that are detuned by a few tens of kilohertz from the motional modes of the ion crystal. If the light has noise components at those frequencies that coincide with a motional mode, the noise will couple to the motional mode and cause an error. When setting up the new 729 nm Ti:Sa laser in our experiment, we found strong noise components created by the servo bumps of the laser lock. This leads to increased error rates in the entangling interactions and will require further improvements on the locking scheme.

The effect of laser noise on the entangling interactions can be probed with a simple experiment, as shown in Figure 4.8. A 12-ion crystal is initially prepared

6 In such a case, it can be sufficient to change the axial tip electrode voltage by a few tenths of a volt, shifting radial motional modes in the order of 1 kHz.

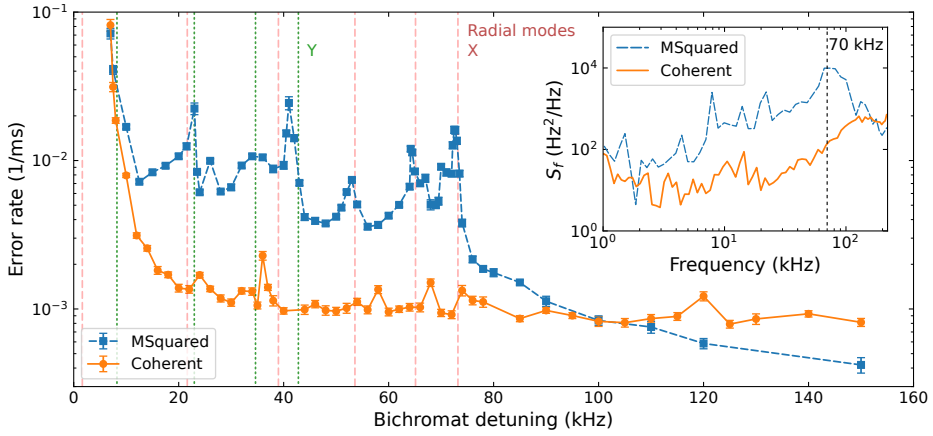

Figure 4.8: Spectral overlap with laser noise. In an experiment, the initial state $|\downarrow\rangle^{\otimes 12}$ evolves under the XY Hamiltonian (rotating-wave approximation), which conserves total magnetization. Any rise in magnetization implies an error. The experiment was repeated for two different 729 nm Ti:Sa lasers (Coherent 899 Ti:Sa ring laser, MSquared SolsTiS SA PSX R). The error rate [Eq. (4.31)] peaks when the lasers noise peak couples to a radial mode (vertical lines). The laser noise frequency power spectral density S_f was measured with spin-locking spectroscopy (inset), see Sec. 5. The MSquared laser exhibits a noise peak at 70 kHz.

in the $|\downarrow\rangle$ state (axial trapping frequency $\omega_{\mathrm{ax}} = 2\pi \times 217\,\mathrm{kHz}$, Rabi frequency of each bichromatic beam component $\Omega^{\pm} = 2\pi \times 107\,\mathrm{kHz}$). Then, the system is evolved under the XY Hamiltonian and the final state is measured in the z basis. The XY Hamiltonian is realized as a rotating-wave approximation (without Trotter approximation) [35]. As H_{XY} conserves the total magnetization, any rise in magnetization implies an error during the evolution. Under the presence of laser noise, the mean excitation is described with the empirical model

$$e(t) = \frac{1}{2}\left(1 - \mathrm{e}^{-Rt}\right), \tag{4.31}$$

where R is the error rate and t is the evolution time under H_{XY}.

The measurement was carried out for two different 729 nm Ti:Sa lasers. First, for the Coherent system[7], which was used for the measurements presented in this thesis. Second, for the MSquared system[8] which has been set up recently at our experiment but is not yet in use due to its high noise level. The error rate for the Coherent system is $R \approx 10^{-3}\,\mathrm{ms}^{-1}$ for all bichromatic detunings from 20 to 150 kHz. Only when the bichromatic detuning is less than 20 kHz, the error rate increases drastically. In this regime, the weak-coupling condition, $\eta\Omega \ll \Delta$, starts to be violated, as for instance $\eta\Omega/\Delta = \frac{0.04}{\sqrt{12}} \times 107\,\mathrm{kHz}/20\,\mathrm{kHz} = 0.06$. In contrast, the error rate for the MSquared system shows a series of strong peaks in the range from 20 to 150 kHz. These peaks can be explained when comparing with the noise spectrum of the laser [Fig. 4.8(inset)]. The noise spectrum exhibits

7 Coherent 899 Ti:Sa ring laser [87]
8 MSquared SolsTiS SA PSX R

a peak around 70 kHz which is caused by the servo bump of the slow locking branch feeding back to the intra-cavity piezo. If the bichromatic detuning has a value such that this noise peak coincides with a radial mode, the noise couples to the radial mode, leading to an error in the XY interactions.

This measurement has an important implication for the laser that is used for implementing the XY model: To allow for low error rates, the laser has to have low noise at the frequencies that overlap with the motional modes of the crystal. In particular, the servo bump, which necessarily shows up in the noise spectrum of the laser, has to be at the highest frequency possible. The MSquared system currently uses an intra-cavity piezo in combination with an external acousto-optic modulator (AOM). The delay time of the AOM limits the servo bump to a maximal frequency in the order of 100 kHz. In contrast, the Coherent system uses an intra-cavity electro-optic modulator (EOM), leading to a servo bump at approx. 1 MHz. A possible solution for the MSquared system could be the use of an external EOM instead of the AOM.

4.2.6 *Example: Quench dynamics in the long-range Heisenberg chain*

As an example of an evolution under the Trotter-approximated long-range Heisenberg model, a quench dynamics was observed in the experiment. A 21-ion crystal was confined at a radial trapping frequency of $\omega_x = 2\pi \times 2.930\,\mathrm{MHz}$ and an axial trapping frequency of $\omega_{\mathrm{ax}} = 2\pi \times 217\,\mathrm{kHz}$. The bichromatic light field was detuned by $\Delta = 2\pi \times 27\,\mathrm{kHz}$ from the radial c.o.m. mode. A third beam at $2\pi \times 1.4\,\mathrm{MHz}$ was used to compensate ac-Stark shifts. The resulting approximate power-law interaction $H_{\mathrm{XX}} \approx \sum_{i<j} J_0/|i-j|^{\alpha} \sigma_x^{(i)} \sigma_x^{(j)}$ is described by $J_0 = 468\,\mathrm{rad/s}$ and $\alpha = 0.86$. The bichromatic light field is created by the global beam which had a variation of the Rabi frequency of 10% over the ion crystal in this case (crystal length 136 µm). The temporal magnetic-field variations were reduced with a feed-forward compensation [61, 62]. The magnetic field was compensated for 50-Hz harmonics from 50 to 900 Hz. The remaining magnetic field resulted in variations of the transition frequency of the qubit $|\mathrm{S}_{1/2}, m_j = 1/2\rangle \leftrightarrow |\mathrm{S}_{5/2}, m_j = 5/2\rangle$ of an amplitude of less than 3 Hz per 50-Hz harmonics frequency component of the magnetic field.

The Heisenberg model is implemented via Trotter approximation. To approximate the Heisenberg model, steps of the form XX, YY, and ZZ are required. As only interactions of the form XX and YY can be implemented directly in our experiment by changing the light phase, the ZZ interaction is realized by a base rotation. The Trotter sequence follows the scheme discussed in Sec. 4.1.2, which would involve a global rotation around the z axis. To avoid this z rotation that is not available as a *global* operation in our experiment, the Trotter sequence is transformed into a sequence that uses global x rotations. The derivation of this transformation is simple but lengthy and can be found in Ref. [83], resulting in a Trotter approximation of the Heisenberg model of the form

$$U_{\mathrm{Heis}}(t) \approx R_y^{\dagger} R_x [(E_-)^4 (E_+)^4]^N R_x^{\dagger} R_y, \tag{4.32}$$

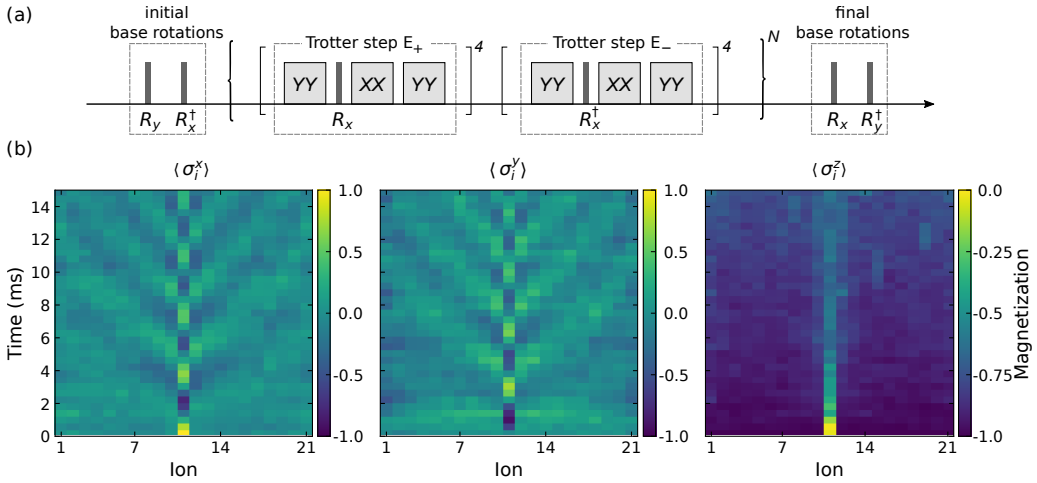

Figure 4.9: Quench dynamics in a Heisenberg chain. A 21-ion crystal evolves in time under the Trotter-approximated isotropic Heisenberg model ($J_{0,\mathrm{eff}} = 398\,\mathrm{rad/s}$, $\alpha = 0.86$). (a) Trotter sequence for the isotropic Heisenberg model. After initial base rotations, a Trotter step E_+ is repeated four times, followed by a Trotter step E_- that is also repeated four times. These eight steps are repeated N times. Final rotations restore the original basis. (b) Time evolution. The initial state $|z{-}_1, \ldots, z{-}_{10}, x{+}_{11}, z{-}_{12}, \ldots, z{-}_{21}\rangle$ evolves under the Trotter-approximated Heisenberg model. The excitation spreads in a wave-like manner in two of the three bases.

where $E_- = U_{YY}U_{XX}R_x^\dagger U_{YY}$ and $E_+ = U_{YY}U_{XX}R_x U_{YY}$ is a Trotter step, respectively. The block of eight Trotter steps is repeated N times. A Trotter step consist of the evolution operators $U_{\gamma\gamma} = \exp(-\mathrm{i}H_{\gamma\gamma}\Delta t)$ for $\gamma = x, y$ with time Δt and a global rotation $R_x = \exp\left(-\mathrm{i}\pi/4 \sum_i \sigma_x^{(i)}\right)$ around the x axis by an angle of $\pi/2$.

The Trotter sequence is depicted in Figure 4.9(a). Initially, global rotations are applied to the system. Then, the Trotter step E_+ is applied four times and the Trotter step E_- is applied four times as well. This block of eight Trotter steps is repeated N times. The Trotter sequence finishes by another set of global rotations.

In the experiment, a total of 36 Trotter steps is used. [9] [10] Each of the three entangling interactions $U_{XX(YY)}$ has a duration of 139 µs. Pulse shaping is used to slowly turn on and off the light pulses to avoid spectral broadening of the light, as described in Sec. 4.2.4. The effective pulse duration is measured by fitting a rectangular pulse that has the same area under the intensity curve as the shaped pulse, leading to an effective duration of approx. 115 µs. This effective pulse duration reduces the spin-spin coupling rate to an effective value of $J_{0,\mathrm{eff}} = 398\,\mathrm{rad/s}$. The base rotations are carried out with attenuated light power to avoid ac-Stark shifts (Rabi freq. 12 kHz).

For observation of a quench dynamics, the system is initially prepared in the product state where all ions are initialized in $|z-\rangle = |\downarrow\rangle$, except for the central

9 The fact that the number of Trotter steps is not an integer multiple of 8 is corrected by modifying the final base rotations, as listed in Appendix C.2.

10 The maximum number of Trotter steps is limited by the currently used hardware for generation of r.f. pulses (*Pulsebox* [88]).

ion 11 which was prepared in $|x+\rangle = (|\uparrow\rangle + |\downarrow\rangle)/\sqrt{2}$. Figure 4.9(b) shows the experimental result of the quench dynamics. In the x and in the y basis, the magnetization spreads in a wave-like manner. Coherent oscillations are clearly visible over the entire ion crystal and until late times. In the z basis, the evolution is dominated by a drop of the initially prepared single-ion magnetization.

5

MOTIONAL SPIN-LOCKING SPECTROSCOPY

Manuscript for publication in preparation.

The ability to coherently control a quantum system is a prerequisite for any quantum experiment. A limited degree of control or an unstable environment can be described by noise and manifests as decoherence. Noise can be probed by interference experiments in which laser pulses coherently transform a qubit's quantum state to make it sensitive to the influence of noise. A well-known type of experiment is a Ramsey experiment, in which noise is picked up during a free-evolution period. If the free-evolution period is replaced by a continuous rotation around a fixed axis on the Bloch sphere, a so-called spin-locking spectroscopy experiment is realized. Spin-locking spectroscopy was first used in nuclear magnetic resonance experiments [89, 90] and later applied to nitrogen-vacancy centers [91] and superconducting qubits [92] to probe noise spectra. An extension of this idea is presented in the following chapter: Spin-locking spectroscopy is applied to measure the motional noise of a single ion trapped in a linear Paul trap. While a Ramsey experiment on a superposition of motional states allows one to measure the motional coherence time, spin-locking spectroscopy gives detailed information about the motional noise spectrum. Characterizing motional noise is important for trapped-ion based quantum simulators, as entanglement between the ions is mediated by motional modes of an ion crystal. The work that is presented in this chapter was carried out together with an intern student, A. Rospars from École Normale Supérieure de Lyon. Parts of the results are presented in A. Rospars' internship report [93].

In this chapter, first an introduction is given on how to calculate the time evolution of a quantum system that is governed by a noisy Hamiltonian. Examples of a few important noise spectroscopy protocols are provided. Then, spin-locking spectroscopy and its experimental protocol is introduced. Measurements of the noise spectrum of several narrow-linewidth 729 nm lasers, both at IQOQI and the University, are presented. Finally, motional spin-locking spectroscopy is described in detail and the measured motional noise spectrum is discussed.

5.1 NOISE SPECTROSCOPY

While the outcome of an individual experimental run that is affected by noise cannot be predicted, there are a number of statistical quantities which can be calculated and measured. Since the evolution of a noisy quantum system is described by a Hamiltonian that includes a stochastic part, a stochastic differential equation needs to be solved. This can be done by solving a stochastic Liouville equation as described by Kubo [94]. A helpful description of this approach and the underlying idea can be found in Ref. [95]. The brief theoretical introduction below follows these two references.

5.1.1 *Evolution under noise*

Let a system be described by the Hamiltonian

$$H(t) = H_0 + H_1(t), \tag{5.1}$$

where H_0 is time-independent and the time-dependent part $H_1(t)$ is regarded as a stochastic process. Consequently, the state $\rho(t)$ of the system is a random variable. The state evolution is described by the von Neumann equation

$$\frac{\mathrm{d}}{\mathrm{d}t}\rho(t) = -\frac{\mathrm{i}}{\hbar}\left[H(t), \rho(t)\right]. \tag{5.2}$$

This equation can be rearranged such that it is expressed by the action of a single operator: First, the rows of the density matrix are stacked in a single vector. For a 2×2 density matrix this is $\hat{\rho} = (\rho_{1,1}, \rho_{1,2}, \rho_{2,1}, \rho_{2,2})^{\mathrm{T}}$. Second, the action of the commutator is described by the Liouville operator

$$L = \frac{1}{\mathrm{i}\hbar}(H \otimes \mathbb{1} - \mathbb{1} \otimes H^{\mathrm{T}}). \tag{5.3}$$

This leads to the Liouville equation

$$\frac{\mathrm{d}}{\mathrm{d}t}\hat{\rho}(t) = L(t)\hat{\rho}(t). \tag{5.4}$$

In general, the Liouville operator does not commute with itself at different times, $[L(t_1), L(t_2)] \neq 0$, which means that the solution has to be expressed by the time-ordered exponential $\exp_{\mathrm{O}}[\cdot]$,

$$\hat{\rho}(t) = \exp_{\mathrm{O}}\left[\int_0^t L(t')\mathrm{d}t'\right]\hat{\rho}(0). \tag{5.5}$$

The time-evolved state can be evaluated as

$$\langle\hat{\rho}(t)\rangle = \underbrace{\left\langle \exp_{\mathrm{O}}\left[\int_0^t L(t')\mathrm{d}t'\right]\right\rangle}_{\equiv\Phi(t)}\hat{\rho}(0) = \Phi(t)\hat{\rho}(0), \tag{5.6}$$

where the expectation value $\langle\cdot\rangle$ is the ensemble average of the random variable $\hat{\rho}(t)$. Here, the decay function $\Phi(t)$ was introduced. The initial state $\hat{\rho}(0)$ was

pulled out from the expectation value as $\hat{\rho}(0)$ is assumed to be the same in each realization of the experiment.

Next, the decay function is written in terms of a cumulant function $K(t)$,

$$\Phi(t) = \exp[K(t)]. \tag{5.7}$$

The crucial step now is to express the cumulant function as an expansion $K(t) = \sum_{n=1}^{\infty} K_n(t)$. In this expansion, the n^{th} cumulant $K_n(t)$ of the cumulant function depends on a combination of n evaluations of the Liouville operator at different times, $L(t_1)$, $L(t_2)$, ..., $L(t_n)$. Cumulants of higher order are difficult to compute in general. However, the first two cumulants are sufficient for most applications, as they fully characterize Gaussian noise, a type of noise that describes a large number of processes. In Appendix B.1, a derivation is given of how to compute the cumulants.

Using a cumulant expansion has the advantage that higher cumulants can be neglected if the noise has a sufficiently small correlation length.[1] Additionally, if the Liouville operator vanishes on average, $\langle L(t)\rangle = 0$, the first cumulant is zero, $K_1(t) = 0$, and the decay function can be approximated by the second cumulant $K_2(t)$, yielding

$$\langle\hat{\rho}(t)\rangle \approx \exp[K_2(t)]\hat{\rho}(0) = \exp\left[\int_0^t \mathrm{d}t_1 \int_0^{t_1} \mathrm{d}t_2 \,\langle L(t_1)L(t_2)\rangle\right]\hat{\rho}(0). \tag{5.8}$$

The autocorrelation function $\langle L(t_1)L(t_2)\rangle$ can be related to the power spectral density by the Wiener-Khinchine theorem. The Wiener-Khinchine theorem states that for a random variable $x(t)$ the autocorrelation function $C(\tau) = \langle x(t)x(t+\tau)^*\rangle$ is connected to the power spectral density $S_x(\omega)$ by $C(\tau) = \frac{1}{2\pi}\int_{-\infty}^{\infty} \mathrm{d}\omega\, \mathrm{e}^{\mathrm{i}\omega\tau} S_x(\omega)$. Then, Eq. (5.8) can be written as

$$\langle\hat{\rho}(t)\rangle \approx \exp\left[\int_{-\infty}^{\infty} \mathrm{d}\omega\, S(\omega)F(t,\omega)\right]\hat{\rho}(0), \tag{5.9}$$

with the operator-valued filter function

$$F(t,\omega) \equiv \frac{1}{2\pi}\int_0^t \mathrm{d}t_1 \int_0^{t_1} \mathrm{d}t_2\, \mathrm{e}^{\mathrm{i}\omega(t_1-t_2)}\,\langle L(t_1)L(t_2)\rangle\,. \tag{5.10}$$

All quantities of interest can be calculated from the ensemble average of the density matrix, $\langle\rho(t)\rangle$. For instance, the evolution of the magnetization $\langle\sigma_x(t)\rangle$ of a qubit can be computed from $\langle\sigma_x(t)\rangle = \mathrm{Tr}[\langle\rho(t)\rangle\,\sigma_x]$.

5.2 EXAMPLES FOR NOISE SPECTROSCOPY PROTOCOLS

The effect of noise on an experiment depends on the details of the experimental sequence, for example on the timing of the applied operations. By tailoring the timing of the light pulses in the right way, noise can be probed at one frequency and suppressed at other frequencies. In Figure 5.1, an overview over a few important noise spectroscopy protocols is given. The left column presents an example for the filter function and the right column presents experimental data for the decay of contrast with increasing probe time. In the following subsections, these examples are discussed.

1 For more details, see [95, Sec. 6].

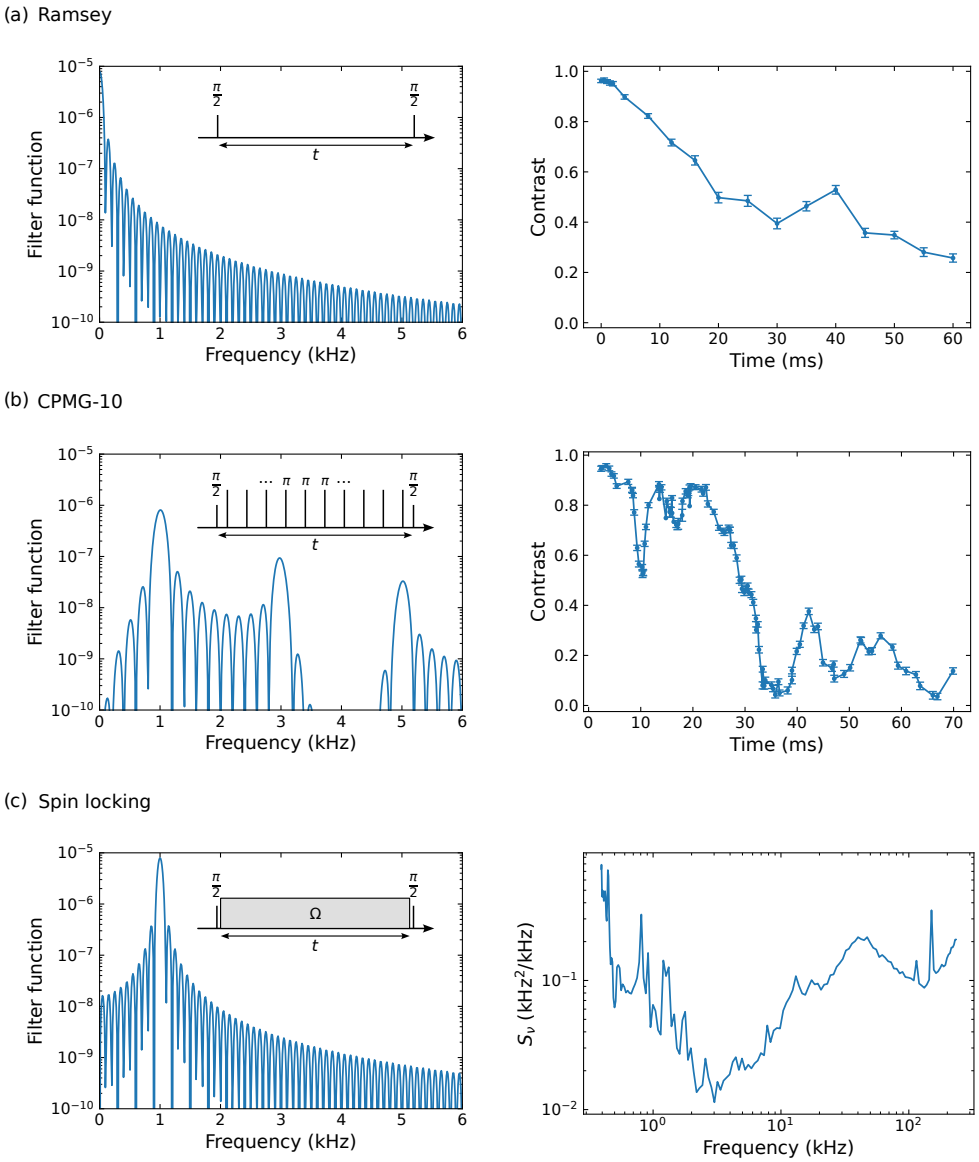

Figure 5.1: Filter function and typical experimental data for various noise-spectroscopy experiments. The filter functions are given in Tab. 5.1. (a) Ramsey experiment. The filter function predominantly senses low frequencies ($t = 10\,\mathrm{ms}$). The contrast is approximately described by an exponential decay in time t. (b) Carr-Purcell-Meiboom-Gill (CPMG) sequence. The filter function has one main peak that is accompanied by higher harmonics ($n = 10$, $t = 5\,\mathrm{ms}$). The decay of contrast shows a complicated dynamics, as the peaks of the filter function coincide with different noise components during the scan. (c) Spin locking. The filter function is a single, sharp peak with a center frequency that is equal to the driving Rabi frequency ($\Omega = 2\pi \times 1\,\mathrm{kHz}$, $t = 10\,\mathrm{ms}$). The contrast drops in a simple exponential decay. More interesting is the frequency noise power spectral density, as it gives a detailed characterization of the present noise.

Table 5.1: Filter functions of spectroscopy experiments. The scalar part of the filter function (5.10) is given for various important spectroscopy experiments: Ramsey experiment, Carr-Purcell-Meiboom-Gill sequence (CPMG), and spin-locking spectroscopy. Here, $\mathrm{sinc}(x) \equiv \sin(x)/x$ denotes the non-normalized sinc function, t the duration of the experiment, ω the angular frequency, and Ω the Rabi frequency. For the CPMG sequence n is the number of π pulses which occur at relative times $\delta_j = (j - \frac{1}{2})/n$ for $j = 1, \ldots, N$.

Experiment	Filter function	Ref.
Ramsey	$\frac{t^2}{4\pi}\,\mathrm{sinc}^2\left(\frac{\omega t}{2}\right)$	[96][a]
Spin echo	$\frac{t^4\omega^2}{64\pi}\,\mathrm{sinc}^4\left(\frac{\omega t}{4}\right)$	[96][b]
CPMG	$\frac{1}{4\pi\omega^2}\left\lvert 1 + (-1)^{n+1}e^{i\omega t} + 2\sum_{j=1}^{n}(-1)^j e^{i\delta_j \omega t}\right\rvert^2$	[96, 97][c]
Spin locking	$\frac{t^2}{8\pi}\left[\mathrm{sinc}^2\left(\frac{\omega+\Omega}{2}t\right) + \mathrm{sinc}^2\left(\frac{\omega-\Omega}{2}t\right)\right]$	[98]

[a] Ref. [96] and calculated from Eq. (5.10)

[b] Ref. [96] and calculated from CPMG with $n = 1$.

[c] An additional factor $\frac{1}{4}$ had to be added to Ref. [97] for consistency with Ref. [96].

5.2.1 *Ramsey experiment*

A Ramsey experiment consists of an initial $\pi/2$ pulse that prepares the qubit in $|x\rangle$, followed by a waiting time t and a final $\pi/2$ pulse that measures $\langle\sigma_x(t)\rangle$. The spectroscopy signal is the magnetization measured in x. This type of experiment is used to measure the coherence time of a qubit under noise $\delta(t)$ of a Hamiltonian $H(t) = \frac{1}{2}\delta(t)\sigma_z$. The Liouville operator (5.3) is

$$L(t) = \delta(t)\begin{pmatrix} 0 & 0 & 0 & 0 \\ 0 & 1 & 0 & 0 \\ 0 & 0 & -1 & 0 \\ 0 & 0 & 0 & 0 \end{pmatrix} \tag{5.11}$$

and the decay function in second order evaluates to

$$\exp[K_2(t)] = \exp\left[-\int_{-\infty}^{\infty} \mathrm{d}\omega\, S(\omega)\frac{t^2}{4\pi}\,\mathrm{sinc}^2\left(\frac{\omega t}{2}\right)\begin{pmatrix} 0 & 0 & 0 & 0 \\ 0 & 1 & 0 & 0 \\ 0 & 0 & 1 & 0 \\ 0 & 0 & 0 & 0 \end{pmatrix}\right] \tag{5.12}$$

$$= \begin{pmatrix} 1 & 0 & 0 & 0 \\ 0 & e^{-\chi(t)} & 0 & 0 \\ 0 & 0 & e^{-\chi(t)} & 0 \\ 0 & 0 & 0 & 1 \end{pmatrix}, \tag{5.13}$$

where $\mathrm{sinc}(x) = \sin(x)/x$,

$$\chi(t) = \int_{-\infty}^{\infty} \mathrm{d}\omega\, S(\omega)\tilde{F}(t,\omega), \tag{5.14}$$

and

$$\tilde{F}(t,\omega) = \frac{t^2}{4\pi}\,\mathrm{sinc}^2\left(\frac{\omega t}{2}\right). \tag{5.15}$$

The decay function can directly be used to calculate the ensemble average of the density operator, $\langle\hat{\rho}(t)\rangle \approx \exp[K_2(t)]\hat{\rho}_0$. For a qubit initially prepared in $|x\rangle$, this leads to the magnetization $\langle\sigma_x(t)\rangle = \mathrm{Tr}[\langle\rho(t)\rangle\,\sigma_x] = \mathrm{e}^{-\chi(t)}$.

The filter function $\tilde{F}(t,\omega)$ probes noise predominantly at low frequencies[2], as shown in Fig. 5.1(a). For a simple type of noise, such as white noise where $S(\omega) = S_0$, the effect of noise can be characterized by a single number. The decay of magnetization is exponential in time for white noise,

$$\langle\sigma_x(t)\rangle = \mathrm{e}^{-\chi(t)} = \mathrm{e}^{-t/t_\mathrm{c}}, \tag{5.16}$$

with the coherence time $t_\mathrm{c} = 2/S_0$.

5.2.2 *CPMG sequence*

A modification of the Ramsey experiment introduces additional π pulses during the free-evolution time. If the π pulses are temporally equally spaced and have equal phase, this results in a Carr-Purcell-Meiboom-Gill (CPMG) sequence [Fig. 5.1(b)]. The filter function has a series of peaks with the highest peak occurring at the frequency $f_\mathrm{max} = n/(2t)$ for a sequence of n π pulses and total duration t. Due to the frequency sensitivity of the CPMG sequence, the decay of contrast shows a more complicated behavior. In our experiment, we use CPMG sequences for sensing oscillating magnetic fields in the frequency range of 50 to 1000 Hz. Furthermore, a CPMG sequence was used in our experiment to probe noise and optimize locking parameters of the 729 nm laser. For the optimization, a CPMG sequence with fixed duration was applied to the ions and the loss of contrast was used as a measure for optimization.

5.2.3 *Spin-locking spectroscopy*

In a spin-locking experiment, the free-evolution time of a Ramsey experiment is replaced with continuous Rabi flops around the x-axis [Fig. 5.1(c)]. The experimental sequence of a spin-locking experiment will be described in detail in Sec. 5.3.2. As the qubit is initially prepared in the $|x\rangle$ state, a continuous rotation around the x axis ideally leaves the initial state unchanged. However, if there are phase fluctuations in the driving light field, the state no longer remains constant but starts to evolve. The filter function of a spin-locking experiment is particularly

2 In our experiments, we do not measure $\langle\sigma_x(t)\rangle$, but perform a full phase scan over $\langle\cos(\phi)\sigma_x(t) + \sin(\phi)\sigma_y(t)\rangle$ and measure the contrast. This approach removes the effects of the deterministic part of the Hamiltonian $H(t)$ (e.g. detunings) from the measured contrast and allows us to measure only the influence of the stochastic part of $H(t)$.

simple and is approximated in the long-time limit by a single δ-function peak. The noise frequency that coincides with the Rabi frequency is probed by the spin-locking sequence, while all other frequencies are suppressed. If the phase fluctuates around zero, the decay of contrast is described by a simple exponential. The rate of decay is linked to the noise power spectral density at the driving frequency. The details will be given in the following Section 5.3.

5.3 SPIN-LOCKING SPECTROSCOPY

Spin-locking spectroscopy relies on the frequency-selective response of a continuous drive. The underlying pulse sequence is known as a Hartmann-Hahn sequence and was first used to measure spin-relaxation times in nuclear magnetic resonance systems [89, 90]. The Hartmann-Hahn sequence is sensitive to one frequency while all other frequencies are suppressed. This can be used in two ways: On the one hand, the broad suppression of frequencies can be used to decouple a qubit against environmental noise (spin locking). A number of experiments demonstrated the application of the Hartmann-Hahn sequence for continuous dynamical decoupling of a qubit from environmental noise [99, 100]. On the other hand, the sensitivity to a single frequency can be used to probe noise. Spin-locking spectroscopy has been used to measure magnetic fields with a single nitrogen-vacancy center [91], to measure noise acting on a superconducting qubit [92], or to characterize laser noise with a single ion [101].

5.3.1 *Hamiltonian and spectroscopic signal*

The light-atom interaction is described by the Hamiltonian

$$H_{\text{int}} = \frac{\hbar\Omega}{2}\left(\mathrm{e}^{-\mathrm{i}\phi(t)}\sigma_+ + \mathrm{e}^{\mathrm{i}\phi(t)}\sigma_-\right), \tag{5.17}$$

where Ω denotes the Rabi frequency, $\phi(t)$ the phase between the light field and the qubit, and σ_+ (σ_-) the raising (lowering) operator. For small phases $|\phi(t)| \ll 1$, the interaction can be approximated in first order by

$$H_{\text{int}} \approx \underbrace{\frac{\hbar\Omega}{2}\left(\sigma_+ + \sigma_-\right)}_{H_0} \underbrace{-\mathrm{i}\frac{\hbar\Omega}{2}\left[\phi(t)\sigma_+ - \phi(t)\sigma_-\right]}_{H_1(t)}. \tag{5.18}$$

Going into the interaction picture with respect to H_0 yields

$$H = U(t)^\dagger H_1 U(t) = \frac{\hbar\Omega}{2}\phi(t)\left[\cos(\Omega t)\sigma_y - \sin(\Omega t)\sigma_z\right]. \tag{5.19}$$

This Hamiltonian can be solved by applying the stochastic Liouville equation approach [Eq. (5.8)]. The Liouville operator of (5.19) is

$$L(t) = \frac{1}{\mathrm{i}\hbar}\frac{\Omega}{2}\phi(t)\begin{pmatrix} 0 & -\mathrm{i}c(t) & -\mathrm{i}c(t) & 0 \\ \mathrm{i}c(t) & -2s(t) & 0 & -\mathrm{i}c(t) \\ \mathrm{i}c(t) & 0 & 2s(t) & -\mathrm{i}c(t) \\ 0 & \mathrm{i}c(t) & \mathrm{i}c(t) & 0 \end{pmatrix} \tag{5.20}$$

with the abbreviations $c(t) \equiv \cos(\Omega t)$ and $s(t) \equiv \sin(\Omega t)$. The phase noise $\phi(t)$ is assumed to have zero mean. Then, the decay function $\Phi(t)$ can be approximated in second order by

$$\Phi(t) \approx \exp[K_2(t)] = \exp\left[\int_0^t \mathrm{d}t_1 \int_0^{t_1} \mathrm{d}t_2 \, \langle L(t_1)L(t_2)\rangle\right]. \tag{5.21}$$

The correlation function $\langle L(t_1)L(t_2)\rangle$ leads to products of cos and sin functions. When carrying out the integration using the power spectral density (5.9), terms with some of the products can be neglected in the long-time limit $t \to \infty$, and some can be approximated by a single peak at the driving frequency, leading to the scalar part of the filter function

$$\tilde{F}(t,\omega) = \frac{t^2}{8\pi}\left[\mathrm{sinc}^2\left(\frac{\omega+\Omega}{2}t\right) + \mathrm{sinc}^2\left(\frac{\omega-\Omega}{2}t\right)\right], \tag{5.22}$$

where $\mathrm{sinc}(x) = \sin(x)/x$. This leads to the approximation of the decay function in the long-time limit,

$$\Phi(t) \approx \exp\left[-\chi(t)\begin{pmatrix} 1 & 0 & 0 & -1 \\ 0 & 3 & 1 & 0 \\ 0 & 1 & 3 & 0 \\ -1 & 0 & 0 & 1 \end{pmatrix}\right], \tag{5.23}$$

where $\chi = \frac{\Omega^2}{8} S_\phi(\Omega) t$ and $S_\phi(\omega)$ is the power spectral density of $\phi(t)$. The matrix exponential in (5.23) can be evaluated by diagonalization of the matrix and one finds

$$\Phi(t) \approx \frac{1}{2}\begin{pmatrix} 1+\mathrm{e}^{-2\chi(t)} & 0 & 0 & 1-\mathrm{e}^{-2\chi(t)} \\ 0 & \mathrm{e}^{-2\chi(t)}+\mathrm{e}^{-4\chi(t)} & -\mathrm{e}^{-2\chi(t)}+\mathrm{e}^{-4\chi(t)} & 0 \\ 0 & -\mathrm{e}^{-2\chi(t)}+\mathrm{e}^{-4\chi(t)} & \mathrm{e}^{-2\chi(t)}+\mathrm{e}^{-4\chi(t)} & 0 \\ 1-\mathrm{e}^{-2\chi(t)} & 0 & 0 & 1+\mathrm{e}^{-2\chi(t)} \end{pmatrix} \tag{5.24}$$

The evolution of the expectation value of the density operator is

$$\langle\hat{\rho}(t)\rangle = \Phi(t)\hat{\rho}(0) = \Phi(t)\begin{pmatrix} \rho_{1,1}(0) \\ \rho_{1,2}(0) \\ \rho_{2,1}(0) \\ \rho_{2,2}(0) \end{pmatrix}. \tag{5.25}$$

Using this expression, the spectroscopic signal in a spin-locking experiment can be evaluated. Consider a qubit initialized in $|x\rangle$, respectively $\hat{\rho}(0) = \frac{1}{2}(1,1,1,1)^{\mathrm{T}}$. Then, the qubit is driven with a Rabi frequency Ω for a duration t. The density matrix evolves as

$$\langle\rho(t)\rangle = \frac{1}{2}\begin{pmatrix} 1 & \mathrm{e}^{-4\chi(t)} \\ \mathrm{e}^{-4\chi(t)} & 1 \end{pmatrix}. \tag{5.26}$$

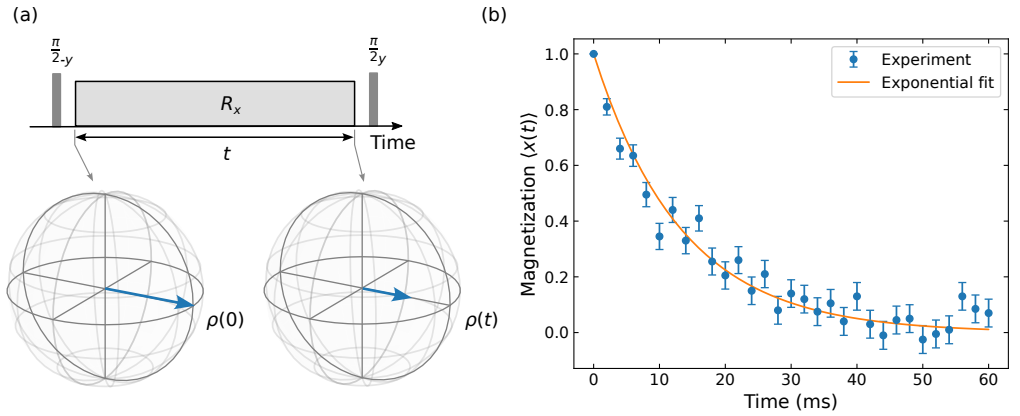

Figure 5.2: Spin-locking. (a) Experimental protocol. The qubit is initialized in $|x\rangle$. Then, the qubit is evolved under a continuous drive with Rabi frequency Ω around the x axis. Finally, the magnetization $\langle x(t) \rangle$ is measured. (b) Spectroscopic signal. The measured magnetization $\langle x(t) \rangle$ decays exponentially in time. The exponential decay constant is proportional to the noise spectral density, as described by Eq. (5.29).

The spectroscopy signal is the magnetization measured in x,

$$\langle \sigma_x(t) \rangle = \mathrm{Tr}[\langle \rho(t) \rangle \, \sigma_x] = \mathrm{e}^{-4\chi(t)} \tag{5.27}$$

$$= \mathrm{e}^{-\frac{1}{2}\Omega^2 S_\phi(\Omega) t}. \tag{5.28}$$

The factor Ω^2 is present as the *phase* noise power spectral density S_ϕ is used. Alternatively, the noise can be expressed by the *frequency* noise power spectral density $S_\omega = \Omega^2 S_\phi$.

The spectroscopy signal (5.28) reveals important properties of the spin-locking protocol: First, the magnetization evolves as a simple exponential decay in time. Such a decay is easily accessible in an experiment. Second, the decay rate is proportional to the power spectral density, evaluated at the driving Rabi frequency. Hence, spin-locking spectroscopy probes noise at only a single frequency. This makes this technique very convenient for measuring a noise spectrum.

5.3.2 *Experimental protocol*

For a spin-locking spectroscopy measurement the following experiment is carried out, as shown in Figure 5.2: First, the qubit is initialized in the state $|x\rangle$ by applying a $\pi/2$ pulse. Then, the qubit is continuously rotated around the x axis with a Rabi frequency Ω for a duration t. During this spin-locking pulse, the state picks up noise that is present at the frequency Ω, resulting in a depolarization of the spin. The rate of depolarization is proportional to the noise power spectral density $S_\phi(\Omega)$. Finally, a $\pi/2$ pulse is applied to measure the population in $\langle x(t) \rangle$. The experiment is repeated for a number of different evolution times t. The decay of magnetization is [92, 98]

$$\langle x(t) \rangle = \mathrm{e}^{-\frac{1}{2}\Omega^2 S_\phi(\Omega) t}, \tag{5.29}$$

where t denotes the duration of the spin-locking pulse, Ω the Rabi frequency of the spin-locking pulse, and $S_\phi(\Omega)$ the noise power spectral density. The value of $S_\phi(\Omega)$ is extracted by an exponential fit. Again, it is important to note that the noise power spectral density gets probed only at the frequency that matches the Rabi frequency. By scanning the Rabi frequency, a full noise spectrum can be obtained.

5.3.3 *Comparison of laser noise spectra*

The noise spectrum of three different lasers was measured with spin-locking spectroscopy, as shown in Figure 5.3. The first laser was the laser used for the measurements presented in this thesis (Coherent[3], QSim). The second laser is a new 729 nm laser that was set up at our experiment (MSquared[4], QSim). The third laser (MSquared[5], AQTION) is of the same type as our new 729 nm laser and served as a template for setting up our new laser. The measurements with the third laser were carried out by I. Pogorelov with the AQTION experiment at the University. Interestingly, all three lasers show very similar noise spectra. At low frequencies, the noise drops with the same power-law behavior. This is remarkable, as either the laser system was different (Coherent, QSim), or the measurements were carried out in different experimental setups (MSquared, AQTION). At higher frequencies, the noise spectrum is dominated by the servo bumps of the laser lock. Our current laser system (Coherent, QSim) has a prominent servo bump at 60 kHz. The new 729 nm laser in our experiment (MSquared, QSim) has strong servo bumps spanning from 1 kHz to 100 kHz which are prohibitively high and require further improvements on the locking system before this laser can be used in quantum simulation experiments. The laser at the University (MSquared, AQTION) has two servo bumps, one at approx. 50 kHz (slow lock acting on intracavity piezo) and one at approx. 250 kHz (fast lock acting on external AOM).

5.3.4 *Finite-lifetime limit*

The lowest level of noise that can be detected by spin-locking spectroscopy is limited by the finite lifetime of the upper level used in the superposition of the initial state $|x\rangle = (|\uparrow\rangle + |\downarrow\rangle)/\sqrt{2}$. The finite-lifetime limit for the phase noise spectral density is (B.2.3)

$$S_{\phi,\mathrm{lim}} = \frac{\Gamma}{\Omega^2}, \tag{5.30}$$

where Γ is the decay rate from the upper to the lower level and Ω is the Rabi frequency of the spin-locking pulse. For $^{40}Ca^+$, the decay rate from the $D_{5/2}$ level to the $S_{1/2}$ level is $\Gamma \approx 0.9\,\mathrm{s}^{-1}$ [33]. As can be seen in Figure 5.3, the finite-lifetime limit is close to being a limiting factor in the frequency range around 1 kHz, where the lasers have low noise.

3 Coherent 899 Titanium Sapphire ring laser
4 MSquared SolsTiS SA PSX R
5 MSquared SolsTiS-PSX, located at the University; Characterized in [102].

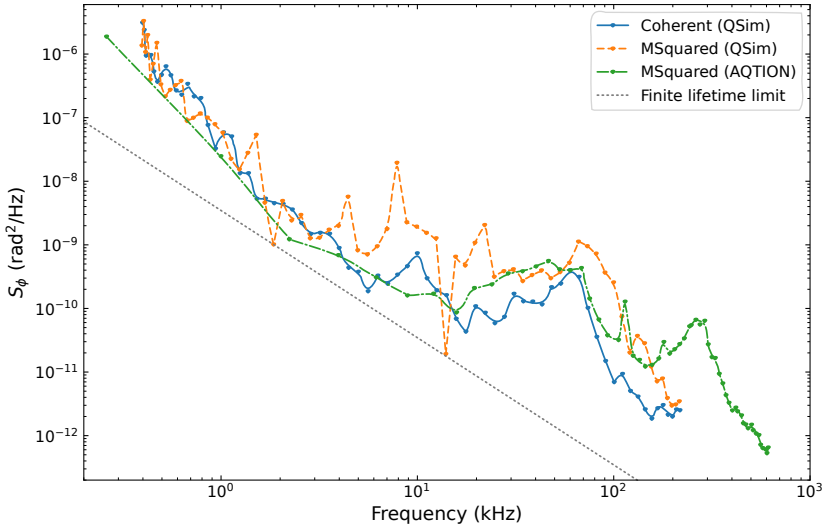

Figure 5.3: Phase noise spectra of different 729 nm lasers measured with spin-locking spectroscopy. Two of the lasers were operated in our Quantum Simulation experiment at IQOQI (Coherent and MSquared, QSim) and one laser was operated at the University (MSquared, AQTION). The measurement at the University was carried out by I. Pogorelov in the AQTION experiment. The smallest detectable phase noise power spectral density under a finite lifetime of the excited level is shown as a dotted gray line [Eq. (5.30)].

5.4 MOTIONAL SPIN-LOCKING SPECTROSCOPY

Instabilities in the trapping potential lead to fluctuations of the trapping frequency and consequently to noise on the motional state of a trapped ion. This motional noise reduces the fidelity with which operations that rely on the motional degree of freedom can be carried out. For example, the entangling interactions in our experiment are mediated by the motional modes of the ion crystal. Hence, motional noise needs to be characterized and minimized. The motional coherence of a trapped ion can be probed by a Ramsey experiment on a superposition of two motional states. While a Ramsey experiment enables a measurement of the coherence time, one does not obtain any information on the structure of noise acting on the motional state.

In recent years, a number of experimental techniques were introduced to measure motional noise of trapped particles. Ramsey experiments were conducted on Fock-state superpositions up to large phonon numbers [103]. Spin-echo experiments with coherent r.f. drives were used to test for noise components [104]. Displaced cat states were probed with CPMG-type experiments, allowing for reconstruction of the motional noise spectrum [105]. The response of a trapped particle to a modulated periodic drive was used to measure the motional noise spectrum [106]. However, these techniques either give only indirect information about the motional noise spectrum [103–105], or require the measurement of an experimental response function for reconstruction of the spectrum [106].

Motional spin-locking spectroscopy is an interesting addition to these existing techniques, as it allows one to directly measure a noise spectrum with a sim-

ple experimental protocol. Applying spin-locking spectroscopy on a motional transition gives access to the full motional noise spectrum of a trapped ion.

The experimental protocol of motional spin-locking spectroscopy is in principle the same as for the usual case of probing the carrier transition. However, care has to be taken to avoid ac Stark shifts while driving the sideband transition. The ac Stark shift from off-resonantly coupling to the carrier transition can be significantly reduced by using a coherent motional state. This approach is described in the following section.

5.4.1 *Avoiding ac-Stark shifts by using coherent motional states*

Applying the continuous drive of the noise spectroscopy sequence on the blue sideband of a ground-state cooled ion comes with a problem: The coupling strength to the blue sideband, $\Omega_{\mathrm{bsb}} = \eta\Omega_{0,0}$, is considerably weaker than the coupling to the carrier, as the Lamb-Dicke parameter in our experiment is small, $\eta = 0.04$. First, this reduces the maximal noise frequency that can be probed with spin-locking. Second, this results in a noticeable ac-Stark shift Δ_{ac} caused by coupling to the carrier transition, despite a detuning of $\Delta \approx 2\pi \times 3.2\,\mathrm{MHz}$. The ac-Stark shift of a ground-state cooled ion is $\Delta_{\mathrm{ac}} = -(\Omega_{\mathrm{bsb}}/\eta)^2/(2\Delta) \approx -0.1 \times (2\pi \times \mathrm{kHz})^{-1} \times \Omega_{\mathrm{bsb}}^2$. Spin-locking spectroscopy can only suppress constant frequency detunings if the detuning is small compared to the Rabi frequency, $\Delta_{\mathrm{ac}}/\Omega_{\mathrm{bsb}} \ll 1$, which leads to the condition $\Omega_{\mathrm{bsb}} \ll 2\pi \times 10\,\mathrm{kHz}$. This condition is not satisfied, as the Rabi frequencies of a ground-state cooled ion are of similar order, $\Omega_{\mathrm{bsb}} = 0.1 \ldots 10\,\mathrm{kHz}$.

This problematic ac-Stark shift can be reduced significantly by performing the spin-locking experiment on a coherent motional state with high mean phonon number. A high mean phonon number increases the coupling to the blue sideband. The coupling strength between the Fock states $|n\rangle$ and $|n+m\rangle$ is [19, 30]

$$\Omega_{n,n+m} = \Omega \mathrm{e}^{-\frac{1}{2}\eta^2} \eta^{|m|} \sqrt{\frac{n_<!}{n_>!}} \mathrm{L}_{n_<}^{(|m|)}(\eta^2), \tag{5.31}$$

where $n_<$ ($n_>$) is the lesser (greater) of $n+m$ and n, $L_n^{(\alpha)}$ is the generalized Laguerre polynomial. The coupling to the first blue sideband is maximized for $\bar{n}_{\mathrm{max}} = 529$ phonons ($\eta = 0.04$). For a mean phonon number $\bar{n}$, the coupling strength to the first blue sideband is $\Omega_{\mathrm{bsb}} = \eta\sqrt{\bar{n}+1}\Omega_{\mathrm{car}}$. The ac-Stark shift reduces to

$$\Delta_{\mathrm{ac}} = -\frac{\Omega_{\mathrm{bsb}}^2}{2\Delta} \frac{1}{\eta^2(\bar{n}+1)}, \tag{5.32}$$

which is a $(\bar{n}+1)$-fold decrease with respect to the ground-state cooled case. Compared to directly using a Fock state of high phonon number, the coherent state has the advantage that it can be created easily in the experiment with a resonant r.f. drive.[6]

6 For the r.f. drive, we simply connected a signal generator (SRS DS 345 at $8.49\,\mathrm{V_{pp}}$) to our loading oven. A drive of approx. 170 µs created a coherent state with mean phonon number $\bar{n} \approx 529$, maximizing the coupling to the first blue sideband.

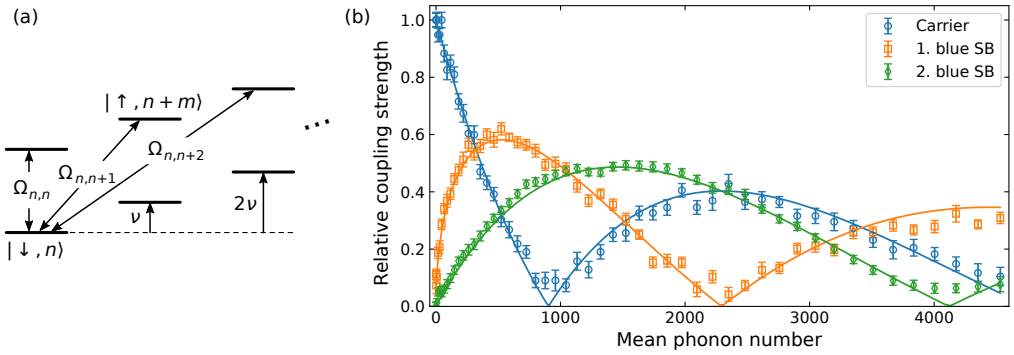

Figure 5.4: Relative coupling strength for a coherent motional state. (a) The harmonic trapping potential with trapping frequency ν gives rise to Fock states $|n\rangle$. A transition between the state $|\downarrow, n\rangle$ and the state $|\uparrow, n+m\rangle$ has the Rabi frequency $\Omega_{n,n+m}$. (b) The relative coupling strength $\Omega_{n,n+m}/\Omega_{0,0}$ for the carrier ($m = 0$), the first blue sideband ($m = 1$), and the second blue sideband ($m = 2$) transition. In the experiment, a coherent motional state with mean phonon number $\bar{n}$ was created by exciting the ion motion with a resonant r.f. drive. The coupling strength $\Omega_{n,n+m}$ was measured by driving Rabi flops on the transition $|\downarrow, n\rangle \leftrightarrow |\uparrow, n+m\rangle$. Points are experimental data, lines are theory curves for a Fock state [Eq. (5.31)]. The coupling strength of the coherent state is approximated by the coupling strength of a Fock state, as $\bar{n}$ is large.

Using a coupling-maximized coherent state has another important aspect: A coupling-maximized coherent state with high mean phonon number can be treated as an effective two-level system, allowing one to abstract from the motional states. The mean phonon number $\bar{n}_{\max}$ that maximizes the coupling is large for small values of the Lamb-Dicke parameter η. For such large $\bar{n}_{\max}$, the phonon population is limited to a narrow band $[\bar{n}_{\max} - \sqrt{\bar{n}_{\max}}, \bar{n}_{\max} + \sqrt{\bar{n}_{\max}}]$, as its width $\sqrt{\bar{n}_{\max}}/\bar{n}_{\max}$ becomes small. In this narrow band around the maximum, the coupling strength to the sideband is approximately equal for all populated states, as it is in first order insensitive to n. Therefore, when driving the sideband transition, the two-level systems of all populated states experience the same coherent rotation.

For creating a coherent motional state, the ion is first cooled to the motional ground state. Next, a coherent motional state is produced by applying an r.f. drive that is resonant with the c.o.m. mode (3.167 MHz). The relative coupling strength for the carrier and the first two sideband transitions is shown in Figure 5.4. For a mean phonon number of $\bar{n} = 529$, the coupling of the first blue sideband is maximized, reaching a value of $\Omega_{\max} = 0.58 \times \Omega_{0,0}$. This is a 15-fold increase of the coupling strength compared to the ground-state cooled case.

5.4.2 *Experimental protocol*

The measurements of the motional noise spectrum are carried out with a single ion. The trapping potential is made anisotropic in the two radial directions to

separate the two c.o.m. modes ($\nu_x = 2\pi \times 3.167\,\mathrm{MHz}$ and $\nu_y = 2\pi \times 2.909\,\mathrm{MHz}$). This ensures that only the motional mode along the x axis gets probed by the spectroscopy.

The experimental protocol is the following [Fig. 5.5(a)]: First, the ion is cooled to the motional ground state along the x axis by sideband cooling. Then, a coherent motional state is created by a resonant r.f. drive. The coherent motional state $|\alpha\rangle$ with $\alpha = \sqrt{\bar{n}} \approx \sqrt{529}$ is the state with maximum sideband coupling strength. Application of a $\pi/2$ pulse on the first blue sideband prepares a superposition of two coherent motional states with mean phonon number $\bar{n}$ and $\bar{n}+1$, i.e. $|x(t=0)\rangle = |\downarrow, \alpha_{\bar{n}}\rangle + |\uparrow, \alpha_{\bar{n}+1}\rangle$. Then, the sideband transition between these two motional states is continuously driven around the x axis for a time t. During this period, both noise on the transition frequency and laser noise is picked up. Finally, the remaining magnetization $\langle x(t)\rangle$ is measured. Likewise as in the previous case (carrier transition), the rate of decay of $\langle x(t)\rangle$ is a measure for the noise spectral density at the driving Rabi frequency.

As depicted in the level scheme in Figure 5.5(a), the sideband transition between the two motional states is sensitive both to changes in the trapping frequency ν_{trap} and to changes in the qubit transition frequency ν_0. Furthermore, noise on the laser light itself also impacts a measurement on the sideband transition. In contrast to this, the carrier transition is unaffected by motional noise. To identify the contribution of motional noise ν_{trap}, the spin-locking spectroscopy measurement is performed on the sideband transition as well as on the carrier transition. A comparison of the two signals is presented in Figure 5.5(b) and 5.5(c). For low frequencies up to 5 kHz, noise on the blue sideband is dominated by motional noise, as the signal on the carrier is small in comparison. Interestingly, the motional noise is exhibiting a series of distinct peaks. This feature will be analyzed in the next section in more detail. Above 5 kHz, laser noise becomes the limiting factor in the measurement and motional noise cannot be identified anymore.

5.4.3 *Motional noise spectrum*

In this section, the noise measurements presented in Figure 5.5(b) are discussed in detail. The motional noise is analyzed in two steps: In a first step, an estimate for the noise spectral density is obtained while ignoring possible coherent properties of the data. In a second step, detailed scans of the observed coherent features of the spectrum are analyzed.

Figure 5.6(a) shows the estimate for the incoherent part of the motional noise spectrum. The data was measured as described in the previous section 5.4.2. The temporal evolution of the magnetization during a spin-locking experiment is described by a simple exponential decay for the case of zero-mean noise,

$$\langle x(t)\rangle = \mathrm{e}^{-\frac{1}{2}S_\nu(\Omega)t}, \tag{5.33}$$

where t is the duration of the spin-locking pulse and $S_\nu(\Omega)$ is the *frequency* noise spectral density at the Rabi frequency Ω of the spin-locking pulse. For each set Rabi frequency of the spin-locking pulse, the noise spectral density $S_\nu(\Omega)$ is obtained by a least-squares fit to the measured $\langle x(t)\rangle$. The measured motional

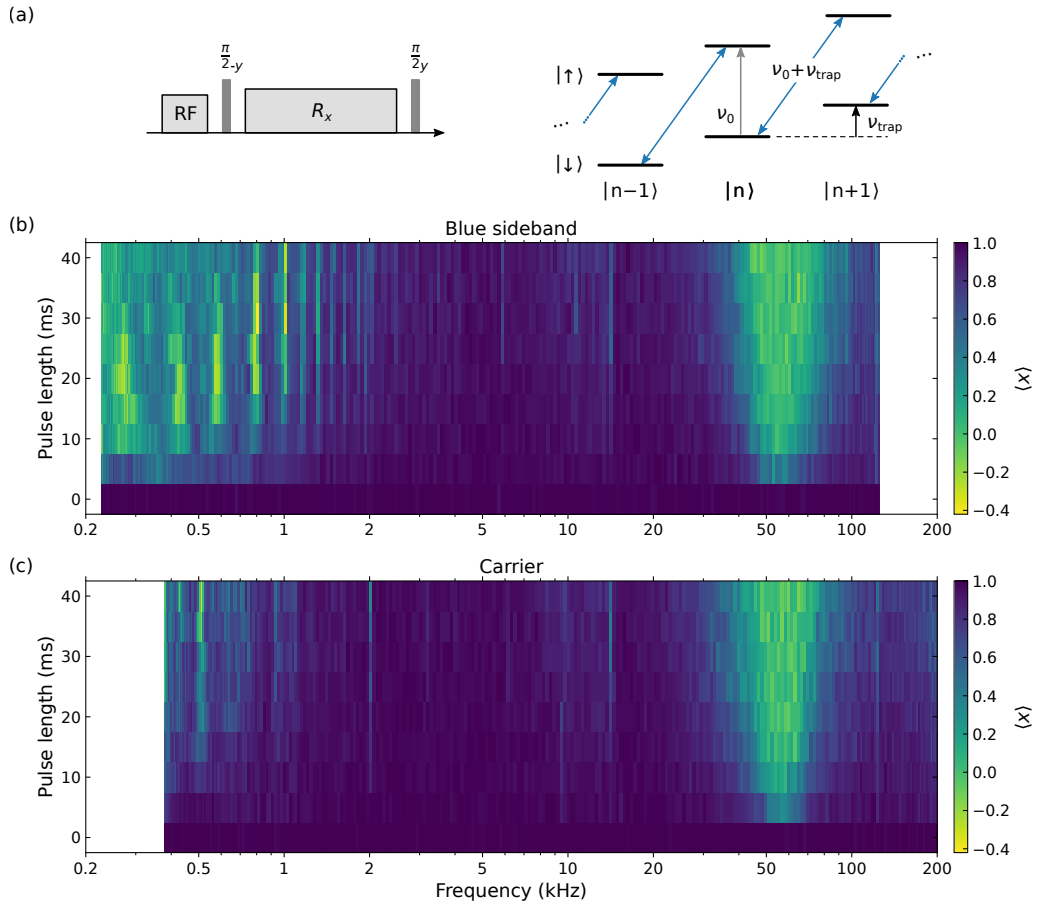

Figure 5.5: Motional noise spectroscopy. (a) Experimental protocol for motional spin-locking spectroscopy. A resonant radiofrequency pulse (RF) creates a coherent motional state of a single trapped ion. A $\pi/2$ pulse around the $-y$ axis creates an equal superposition of two motional states, $|x(t=0)\rangle = |\downarrow, \alpha(\bar{n})\rangle + |\uparrow, \alpha(\bar{n}+1)\rangle$. A continuous rotation R_x with Rabi frequency Ω around the x axis probes noise on the sideband transition for a pulse length t. A final $\pi/2$ pulse measures the remaining magnetization $\langle x(t)\rangle$. (b) Spectroscopy on the blue sideband shows motional noise at low frequencies up to 5 kHz. The noise is dominated by a series of distinct peaks. The frequency axis is scanned by varying the Rabi frequency Ω of the continuous rotation R_x. (c) A measurement on the carrier reveals that laser noise becomes dominant at high frequencies, as noise shows up both on the carrier and the blue sideband transition. The strong peak around 60 kHz is a servo bump of the laser lock.

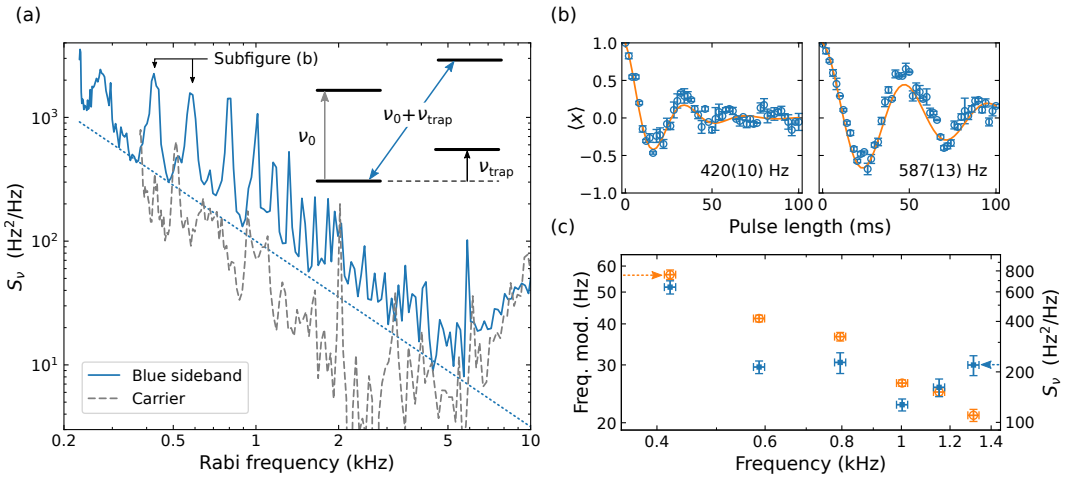

Figure 5.6: Motional noise spectrum. (a) The frequency noise spectral density S_ν is probed by spin-locking spectroscopy on the blue sideband transition. The spectrum shows a series of distinct peaks. For comparison, noise on the carrier transition was measured. Above approx. 5 kHz, laser noise becomes dominant, as the noise on the carrier becomes as large as on the blue sideband. The dotted line is a power-law function $\propto \omega^{-1.5}$ indicating the overall drop of S_ν. The noise is extracted from Eq. (5.33), ignoring coherent evolution in this first coarse analysis. (b) In a more detailed analysis, it can be seen that the peaks in the motional noise spectrum exhibit considerable coherence. This coherence can be probed by observing the time-evolution of a spin-locking experiment. The solid lines are least-squares fits of Eq. (5.35) to the experimental data. The two plots show the oscillatory behavior pertaining to two peaks at 420 and 587 Hz, respectively. (The frequencies given inside the plots are the peak positions.) (c) The analysis of damped oscillations that was exemplified in subfigure (b) was carried out for all peaks between 420 and approx. 1300 Hz. This analysis reveals the strength of the frequency modulation at each peak and the damping rate that is related to the noise spectral density S_ν, as described by Eq. (5.35).

noise spectrum shows a series of distinct peaks in the frequency range from 200 Hz to 5 kHz. The peaks are multiples of approximately 200 Hz. The background of the noise spectral density drops over the measured range as approx. $\propto 1/\omega^{1.5}$, as indicated by the dotted line.

The spin-locking signal shows considerable coherence at frequencies for which peaks occur. The coherent behavior of the spin-locking signal is analyzed in Fig. 5.6(b) and (c). Two examples of damped oscillations that the spin-locking sequence exhibits at peaks is presented in Fig. 5.6(b). The observed damped oscillations can be modeled by assuming that the trapping frequency is the sum of a coherent modulation part ν_c and a zero-mean noise part ν_n,

$$\nu(t) = \nu_c(t) + \nu_n(t) = \omega_m \beta \sin(\omega_m t + \delta) + \nu_n(t), \tag{5.34}$$

where ω_m is the modulation frequency, β is the modulation index, and δ is the phase of the modulation. The noise part $\nu(t)$ is related to the power spectral density by the Wiener-Khinchin theorem, $S_\nu(\omega) = \int_{-\infty}^{\infty} C_\nu(t) e^{i\omega t}$, with the autocorrelation function $C_\nu(t_1 - t_2) = \langle \nu(t_1)\nu(t_2) \rangle$. For this ansatz, the coherent

evolution and the incoherent decay separate into a product, as detailed in Appendix B.2.2. The magnetization then evolves according to damped oscillations of the form

$$\langle x(t) \rangle = \mathrm{e}^{-\frac{1}{2} S_\nu(\Omega) t} \cos\left(\frac{1}{2}\beta\Omega t\right). \tag{5.35}$$

These damped oscillations are observed when non-zero mean noise is probed at the modulation frequency, $\Omega = \omega_\mathrm{m}$.

By fitting damped oscillations to the measured evolution $\langle x(t) \rangle$ at several noise peaks, the modulation index β and the noise spectral density $S_\nu(\Omega)$ is obtained. The results are presented in Fig. 5.6(c) for peaks between approx. 400 Hz and 1400 Hz.

5.5 CONCLUSION

Motional spin-locking spectroscopy represents a method to measure the motional noise spectrum of a trapped ion. A transition between two motional states is probed by a continuous drive, resulting in a sharp filter function which rejects all but a single frequency. The coupling strength between the two motional states can be increased by an order of magnitude, compared to the ground-state cooled case, by the use of a coherent motional state. A measurement of the motional noise spectrum of a single trapped ion in our linear Paul trap was presented, revealing both incoherent and coherent perturbations of the trapping frequency. The coherent perturbations occur at multiples of 200 Hz, indicating a noise source that creates a series of higher harmonics. Motional spin-locking spectroscopy provides a tool that allows for further future investigations of the stability of the trapping potential in ion traps.

6

NON-ABELIAN THERMAL STATES

The work presented here is published in
Physical Review X Quantum **4**, 020318 (2023)

How do we understand "thermalization" of a quantum system? It is experience from everyday observation that systems tend towards an equilibrium: hot bodies cool down until they reach the same temperature as their environment, concentrations of solutions equalize, or directed motion is turned into the disordered motion that is associated with heat. For classical systems this process of thermalization is well studied and explained by a statistical argument: In equilibrium, a system takes the macroscopic state that has the highest probability of occurrence. The underlying idea is to count the number of points in phase space that realize a particular macroscopic state. This approach only works if a system is *ergodic*, i.e. a trajectory evenly covers the full allowed energy shell[1] in phase space, because then the area of the energy shell is a measure for the probability of realizing a particular macrostate.[2]

The concept of ergodicity cannot be directly applied to states in the Hilbert space of quantum mechanics.[3] The problem is that in quantum mechanics not only energy is conserved but also the energy distribution, as was realized early [111]. Consider some initial state $|\psi_0\rangle = \sum_n c_n |\phi_n\rangle$ that is expressed by the eigenstates $|\phi_n\rangle$ of some Hamiltonian H. During time evolution $|c_n(t)|^2 = |c_n|^2$ remains constant. Therefore, the time average

$$\left\langle |\psi(t)\rangle \langle\psi(t)| \right\rangle_t = \sum_n |c_n|^2 |\phi_n\rangle \langle\phi_n| \tag{6.1}$$

usually does *not* equal the microcanonical ensemble average, as this time average depends on the details of the initial state. One solution is to consider a sufficiently

1 The energy shell is the set of points in phase space with energy between E and $E + \delta E$. As δE is assumed to be small, the points lie on a (multidimensional) shell.

2 Remarkably, only very few classical systems have been proven to be ergodic. One example is N hard spheres confined in some volume, the "Sinai Billiard" [107]. Another example is a single point particle in a stadium with hard walls, the "Bunimovich Stadium" [108], where two semicircular sides are connected by two straight mid-sections.

3 The following overview is based on the well-readable review articles [109, 110].

small subsystem of a total system. Even when the state of the closed, total system is pure, the subsystem is found to be in a canonical state after tracing out the rest of the total system [112, 113]. The other solution is to consider macroscopic observables instead of the quantum states themselves. Then the property of ergodicity can be defined for quantum systems by demanding that the time average of a macroscopic observable M equals the expectation value of the microcanonical ensemble,

$$\left\langle \langle\psi(t)| M |\psi(t)\rangle \right\rangle_t = \mathrm{Tr}[M\rho_{\mathrm{mc}}] = \langle M\rangle_{\mathrm{mc}}\,, \tag{6.2}$$

where the microcanonical ensemble $\rho_{\mathrm{mc}}(E) = \sum_{\alpha\in\mathcal{H}(E)} 1/\mathcal{N}\,|\phi_\alpha\rangle\langle\phi_\alpha|$ contains all eigenstates with energy between E and $E+\delta E$ with equal weight. Here, $\mathcal{H}(E)$ denotes the set of all eigenstates in the energy shell between E and $E+\delta E$, and $\mathcal{N}$ is the total number of states in the energy shell.

Thus, using macroscopic observables allows one to define the notion of ergodicity for quantum systems. However, it still remains not fully understood under which conditions quantum systems are ergodic and thermalize. For instance, integrable systems hinder thermalization. In an integrable system there is a large number of conserved quantities that restrict the area in the energy shell that is accessible. It was conjectured that the resulting thermal state is of the form [114]

$$\hat{\rho}_{\mathrm{GGE}} = Z^{-1}\mathrm{e}^{-\sum_m \lambda_m \hat{I}_m}, \tag{6.3}$$

the so-called generalized Gibbs ensemble (GGE). Here, $\{\hat{I}_m\}$ is the set of integrals of motion, $Z = \mathrm{Tr}[\exp(-\sum_m \lambda_m \hat{I}_m)]$ the partition function, and $\{\lambda_m\}$ are the Lagrange multipliers that are fixed by the initial conditions $\mathrm{Tr}[\hat{I}_m\hat{\rho}] = \langle\hat{I}_m\rangle\,(t=0)$. The structure of the GGE becomes clear when comparing it to the canonical thermal state. In the canonical thermal state only the energy determines the form of the thermal state, resulting in $\hat{\rho}_{\mathrm{can}} = Z^{-1}\mathrm{e}^{-\beta H}$. In the GGE, the additional conserved quantities from the integrals of motion show up in the thermal state as well. Integrability can even prevent a system from thermalizing at all. In an experiment, the absence of thermalization was observed for an integrable, one-dimensional Bose gas [115].

One set of macroscopic observables that is important in classical thermodynamics is position and momentum, which form classical phase space. In quantum mechanics, using the concept of phase space to describe a thermal state comes with the difficulty that position and momentum are described by noncommuting observables and therefore cannot be determined simultaneously. One approach to this problem is to approximate the noncommuting observables with a set of commuting observables. However, it is not clear whether such an approximation is possible [116].

From this point of view, the question was raised how noncommuting operators affect the resulting thermal state. Consider a system that is described by a Hamiltonian with operators that do not commute with each other. Will such a system still thermalize towards a state of the form of a generalized Gibbs ensemble? Theorists have predicted that this will be the case and termed the state "non-Abelian thermal state", referring to its underlying noncommuting operators [117]. The following chapter presents the results of an experiment that

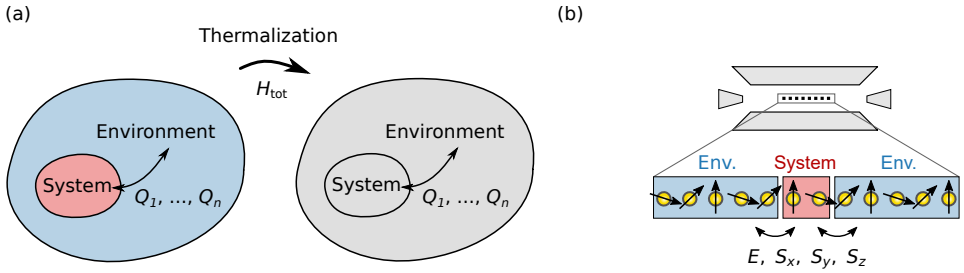

Figure 6.1: Thermalization of a closed quantum system. (a) Initially, a system is brought out of equilibrium with its environment. A Hamiltonian H_{tot} creates an interaction between system and environment which leads to an exchange of globally conserved quantities $Q_1, \ldots, Q_n$ (e.g. energy or magnetization). After some time, the system is in an equilibrium with its environment and reaches a thermal state. (b) Experimental realization. A crystal of up to 21 ions forms both system and environment. The interactions are created by the long-range Heisenberg model, which conserves energy E, and the three components of magnetization S_x, S_y, S_z.

observed the thermalization of a closed quantum system under the Heisenberg Hamiltonian, following the proposal of Ref. [118].

6.1 EXPERIMENTAL SETUP

The thermalization of a closed quantum system is studied by observing the dynamics of a quench, as shown in Figure 6.1(a). A closed quantum system is divided into two parts: One part forms the system, the other part the environment. Initially, the total system (system and environment) is prepared in a pure state. At this initial state, the system is out of equilibrium. For instance, it may have more energy than the environment. Then a Hamiltonian H_{tot} lets the system interact with the environment under unitary evolution. During the interaction, the system can exchange energy with the environment (and other quantities such as magnetization). Eventually, the state of the total system reaches an equilibrium and the system is in a thermal state.

In an experiment, this setup can be realized by a crystal of ions interacting with each other under the (isotropic) Heisenberg model [Fig. 6.1(b)]. The ion crystal forms a closed quantum system that is initialized in a pure state at the start of the experiment. The interactions are realized by a long-range, isotropic Heisenberg model. The long-range nature of the interactions breaks the integrability of the system, which facilitates thermalization. A nonintegrable system has fewer conserved quantities than an integrable system. Hence, the evolution of the system is less restricted and can more easily explore the full energy shell, as in the case of ergodic, classical systems. The long-range Heisenberg model still globally conserves energy E and the three components of total magnetization S_x, S_y, and S_z. In the context of this work, globally conserved quantities are called *charges*. During the time evolution of the experiment, these quantities are

exchanged between a subsystem (or simply "system") and the total system (the "environment"). It has to be highlighted at this point, that the operators of the total magnetization components do not commute with each other. This property is referred to as *non-Abelian*[4] in the context of this work. The central question is what impact the noncommutative character of the operators have on the process of thermalization. After the system had enough time to reach an equilibrium state, it is in a thermal state. The globally conserved quantities give rise to a thermal state that was conjectured to be of the form of a generalized Gibbs ensemble [118],

$$\rho_S = Z^{-1} e^{-\beta(H_S - \sum_\gamma \mu_\gamma S_\gamma)}, \tag{6.4}$$

where $Z = \mathrm{Tr}[\exp(-\beta(H_S - \sum_\gamma \mu_\gamma S_\gamma))]$ is the partition function, $\beta = 1/T$ the inverse temperature, H_S the Hamiltonian of the system, μ_γ the generalized chemical potential, and S_γ is the magnetization of the system for $\gamma = x, y, z$.

In the following sections, the setup, the creation of the interactions by Trotter approximation, and the analysis of the thermal state are described in detail.

6.2 IMPLEMENTATION OF THE HEISENBERG MODEL

6.2.1 *Trotter approximation of the Heisenberg model*

The Heisenberg model is not directly implemented by the bichromatic light field in our experiment. Instead, the model is approximated by a Trotter approximation using the available interactions of the XX and YY type. The Hamiltonian of the long-range Heisenberg model is

$$H_{\mathrm{Heis}} = \frac{1}{3} \sum_{i<j} J_{ij} \left(\sigma_x^{(i)} \sigma_x^{(j)} + \sigma_y^{(i)} \sigma_y^{(j)} + \sigma_z^{(i)} \sigma_z^{(j)} \right) \tag{6.5}$$

$$= \frac{1}{3} \left(H_{XX} + H_{YY} + H_{ZZ} \right), \tag{6.6}$$

where J_{ij} is the spin-spin coupling matrix and $\sigma_x^{(i)}$ etc. is the Pauli matrix acting on ion i. In the second line, abbreviations for the three parts of the Hamiltonian have been introduced, $H_{XX} = \sum_{i<j} J_{ij} \sigma_x^{(i)} \sigma_x^{(j)}$ etc. The Trotter approximation of the time evolution $U = \exp[-iH_{\mathrm{Heis}} t]$ is shown in Figure 6.2(a). In the simplest case, the evolution is approximated by the first-order sequence

$$U^{(1)} = \left[U_{ZZ} U_{YY} U_{XX} \right]^N, \tag{6.7}$$

where N is the number of Trotter steps and $U_{XX} = \exp[-iH_{XX} t]$ is the time evolution operator under H_{XX}. The first term U_{XX} is directly implemented in the experiment by interactions created by the bichromatic light field. The second term U_{YY} is also directly obtained by adjusting the phase of the light field. The third term U_{ZZ}, however, is generated by a base rotation utilizing the identity $U_{ZZ} = R_y^\dagger U_{XX} R_y$.

The number of required base rotations can be reduced to a single rotation per Trotter step. This reduction is achieved by introducing a base rotation

4 Compare to an *Abelian group* in group theory, i.e. a commutative group.

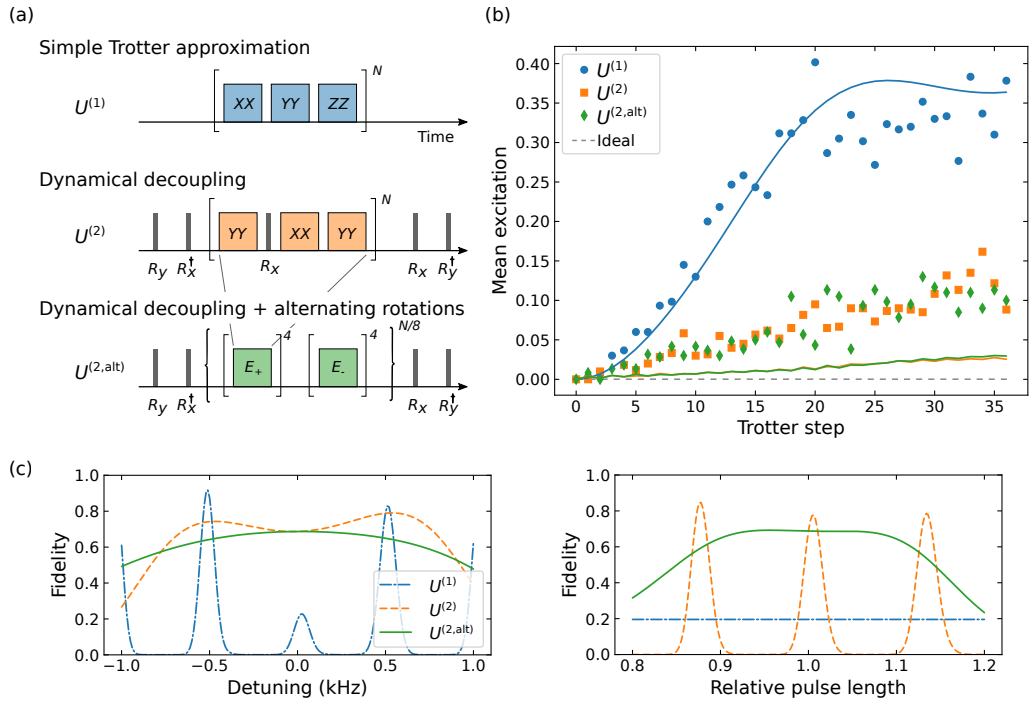

Figure 6.2: Trotter approximations of the Heisenberg model. (a) First-order sequence $U^{(1)}$ with N Trotter steps. Second-order sequence $U^{(2)}$ incorporating dynamical decoupling with base rotations $R_x = \exp\left[-i\pi/4 \sum_k \sigma_x^{(k)}\right]$. Second-order sequence $U^{(2\text{alt})}$ with alternating base rotations R_x and $R_x^\dagger$ that mitigate systematic rotation errors. (b) Evolution of the $|S\rangle$ state under different Trotter sequences. Ideally, the mean excitation is conserved (dashed line). The second-order sequences have a significantly lower error. Points are experimental data using 12 ions, lines are numerical simulations. (c) Numerical simulations showing the Trotter-approximated state fidelity after 32 Trotter steps under detuning and pulse length errors, respectively. Here, the initial state is $(|y\rangle\,|x\rangle\,|z\rangle)^{\otimes 4}$.

$R_z = \exp\left[-i\pi/4 \sum_k \sigma_z^{(k)}\right]$ in each Trotter step and mathematically simplifying the resulting sequence, finally yielding the second sequence in Figure 6.2(a). A derivation can be found in the Appendix of Ref. [83]. The approximation is a second-order sequence,

$$U^{(2)} = R_y^\dagger R_x \left[U_{YY} U_{XX} R_x U_{YY}\right]^N R_x^\dagger R_y. \tag{6.8}$$

Here, additional initial and final $\pi/2$ rotations are required, $R_x = \exp\left[-i\pi/4 \sum_k \sigma_x^{(k)}\right]$ and $R_y = \exp\left[-i\pi/4 \sum_k \sigma_y^{(k)}\right]$. If the number of Trotter steps is not an integer multiple of 4, the final base rotation needs to be adapted, see Appendix C.2. In addition to faster convergence, the repeated base rotations R_x realize a dynamical decoupling.

Systematic rotation errors can be mitigated by alternating the direction of rotation, as shown in the last sequence of Figure 6.2(a). After four steps, the base rotation R_x is replaced by $R_x^\dagger$.

In an experiment, the different behavior of these three Trotter sequences can be observed [Fig. 6.2(b)]. The ions are initially prepared in the $|S\rangle$ state. The total magnetization is conserved under the Heisenberg model, hence the $|S\rangle$ state ideally remains unchanged. The first-order sequence $U^{(1)}$ accumulates a large error over the evolution time, both in the measurement (points) and the numerical simulation (line). In contrast, the second-order sequences $U^{(2)}$ and $U^{(2,\mathrm{alt})}$ exhibit a lower error rate. The experiment was carried out for 12 ions and an approximate power-law spin-spin coupling of $J_{\max} = 540\,\mathrm{rad/s}$ and $\alpha = 1.0$. The maximal evolution time was 13.6 ms, divided into up to 36 steps.

The different behavior between these three Trotter sequences is further evaluated by a numerical simulation [Fig. 6.2(c)]. Both dynamically decoupled sequences $U^{(2)}$ and $U^{(2,\mathrm{alt})}$ mitigate detuning errors. Furthermore, by using alternating rotations in $U^{(2,\mathrm{alt})}$ the fidelity remains high for rotation errors up to $\pm 10\%$. The numerical simulation was carried out for the initial state $(|y\rangle\,|x\rangle\,|z\rangle)^{\otimes 4}$, which is the state that is used to create a non-Abelian thermal state in the present study. The number of Trotter steps was 32, as the alternating pulse sequence has a period of 8 steps. If a different number of Trotter steps is used, mitigation of rotation errors remains incomplete.

There are two important technical remarks on the implementation of the Trotter steps: First, the light pulse of each Trotter steps needs to be switched on and off gradually. The effect of pulse shaping is explained in detail in Section 4.2.4. Second, the base rotation pulses are carried out with reduced light intensity to avoid ac-Stark shifts, see Section 4.2.3.

6.2.2 *Quantum tomography on long ion crystals*

When performing quantum state tomography (QST) on long crystals of trapped ions systematic errors become eminent. In particular, QST requires base rotations of the individual qubits. Part of these rotations are realized as global rotations generated by the global laser beam. Due to the large spatial extent of ion crystals with many ions, the global laser beam inhomogeneously couples to the ions. Ions

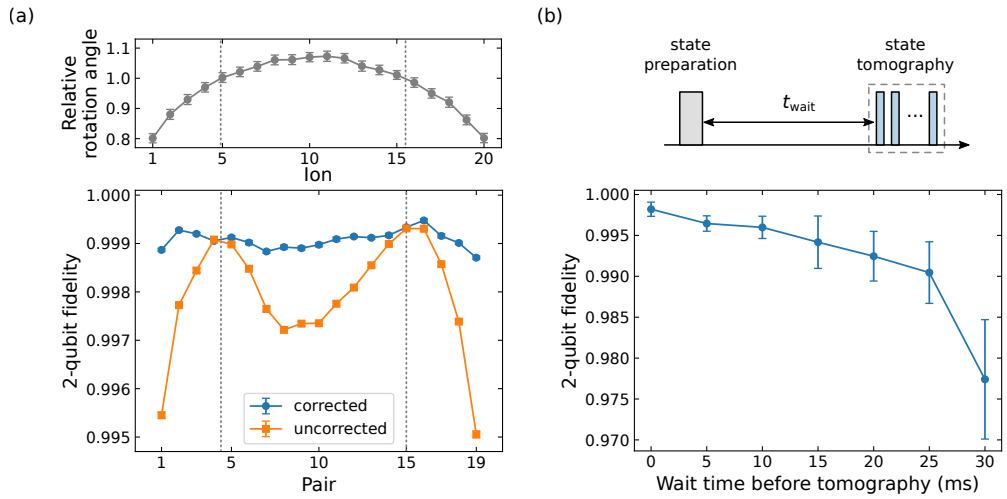

Figure 6.3: Quantum state tomography under imperfections. Here, a 21-ion crystal was used. (a) Effect of rotation errors during tomography. Top: The global laser beam couples inhomogeneously to the ion crystal, causing over- and under-rotations. At two points, the rotations have the correct value (dotted lines). Bottom: Fidelity of the experimentally reconstructed 2-qubit state with and without correction of the rotation errors. The ions are prepared in the $|S\rangle$ state with negligible preparation error. (b) Effect of axial heating. The ions are prepared in the $|S\rangle$ state and after a waiting time, quantum state tomography is carried out. The fidelity drops due to axial heating of the crystal, which compromises the single-qubit operations.

in the center are overrotated, ions at the edges are underrotated. If these errors are not taken into account, QST reconstructs the quantum state erroneously.

The QST is based on a maximum-likelihood estimation [119]. In the tomographic measurements positive operator-valued measures (POVM) Π_l are observed. For example, measuring all n qubits in the x basis is represented by

$$\Pi_x = \bigotimes_{i=1}^{n} \sigma_x^{(i)}. \tag{6.9}$$

The measurement in the x basis requires a global rotation $R_y^\dagger = \exp\left[+i\pi/4 \sum_k \sigma_y^{(k)}\right]$. In practice the laser beam has an inhomogeneous profile with Rabi frequencies $\Omega^{(k)} = \alpha^{(k)}\Omega_0$, with $\alpha^{(k)} = 1$ for perfect rotations. The error of the rotation angle is $\delta = \alpha - 1$. For such an inhomogeneous rotation the actual measurement is carried out in

$$\Pi_x = \bigotimes_{i=1}^{n} \left[\cos\left(\delta^{(k)}\frac{\pi}{2}\right)\sigma_x^{(i)} - \sin\left(\delta^{(k)}\frac{\pi}{2}\right)\sigma_z^{(i)}\right]. \tag{6.10}$$

The exact form of these corrected POVMs depends on the details of how global rotations are used in the tomographic measurements.

An example of the impact of systematic rotation errors on quantum state tomography and its correction is shown in Figure 6.3(a). A crystal of 21 ions is prepared in the $|S\rangle$ state. The $|S\rangle$ state was chosen as its preparation error is negligible in this context. The global rotation suffers from systematic errors of up to 20% (top panel). When these rotation errors are not taken into account, the tomographically reconstructed state is affected. The 2-qubit fidelity $F = \left(\mathrm{Tr}\sqrt{\sqrt{\rho}\rho_{\mathrm{exp}}\sqrt{\rho}}\right)^2$ drops as low as 0.995. At the two points on the ion crystal where the rotation has the correct value (dotted lines), the fidelity reaches its maximum. In contrast, when the information on the rotation errors is incorporated into the maximum-likelihood estimation, the fidelity of the tomography process is close to 0.999 or above over the entire ion crystal.

Another effect that compromises quantum state tomography is axial heating (see Sec. 3.3) of the ion crystal. Single-qubit addressing operations with the tightly focused laser beam have a reduced fidelity if the ion is axially hot. A simple experiment addresses the question of whether QST still can be carried out with a fidelity that is sufficiently high for observations of the non-Abelian thermal state. Initially, the ions are prepared in the $|S\rangle$ state. Then the ions are left idle for a wait time, during which they can heat up. Finally, QST is carried out. The measured 2-qubit fidelity is shown in Figure 6.3(b). During the relevant times of up to 15 ms, the 2-qubit fidelity does not drop lower than 0.994(3). This value is not limiting for observations of the non-Abelian state.

6.2.3 *Hiding of ions – Computational and physical qubits*

When studying thermalization of a quantum system it can be of interest to vary the size of the system to study finite-size effects. In a trapped-ion experiment this can be done by trapping a different number of ions for each system size.

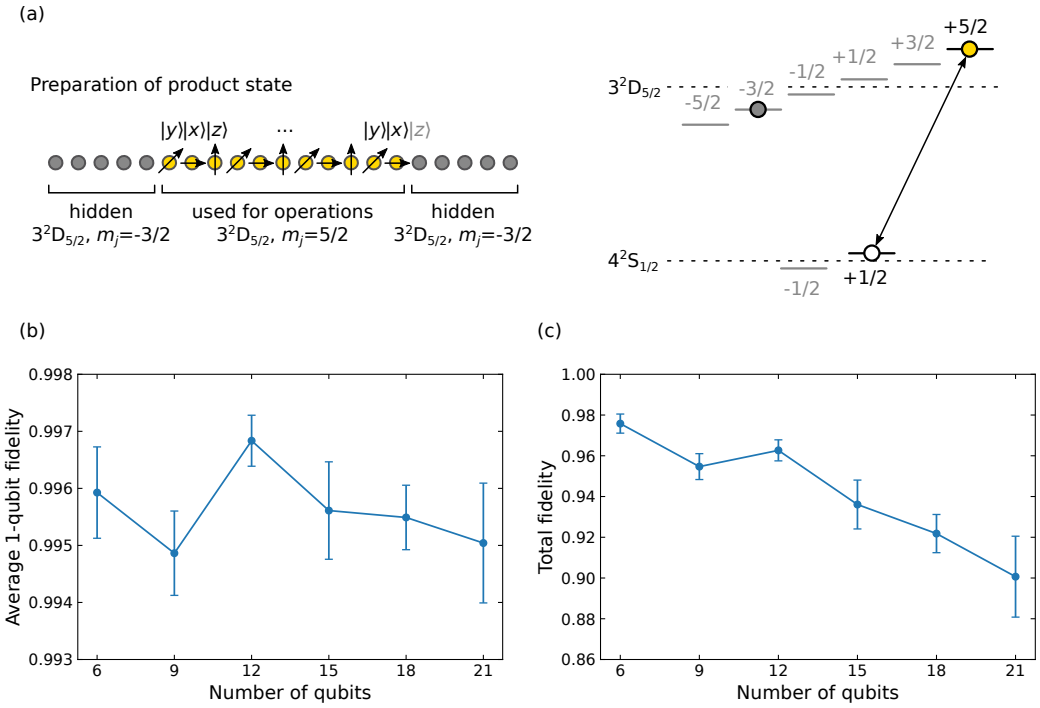

Figure 6.4: Hiding operation on a 21-ion system. (a) Qubits in the $|\mathrm{D}_{5/2}, m = 5/2\rangle$ state participate in the interactions, while ions in the $|\mathrm{D}_{5/2}, m = -3/2\rangle$ state are hidden from the interactions. Qubits that are used for operations are initially prepared in a product state. (b) Fidelity of the hiding operation. For a crystal of 21 ions, the average 1-qubit fidelity of the product state $(|y\rangle\,|x\rangle\,|z\rangle)^{\otimes 7}$ was measured as a function of the number of qubits (i.e. non-hidden ions). (c) Fidelity of the total product state.

However, this approach makes it time-consuming to change between system sizes. It is much more convenient to keep the size of the ion crystal constant and hide unused ions in a quantum state that does not participate in the interactions. In our experiment, the operations are carried out on the $|S_{1/2}, m = 1/2\rangle \leftrightarrow |D_{5/2}, m = 5/2\rangle$ transition. Unused ions can be hidden in the $|D_{5/2}, m = -3/2\rangle$ state, as depicted in Figure 6.4(a). In the following, only the non-hidden ions are referred to as "qubits".

The fidelity of the hiding operation was assessed for a 21-ion crystal. Some of the ions are hidden, the rest is kept as qubits. The qubits are prepared in the product state $(|y\rangle\,|x\rangle\,|z\rangle)^{\otimes M}$ ($M = 7$ for $N = 21$ qubits). The average 1-qubit fidelity remains constant for up to 21 qubits [Fig. 6.4(b)]. Consequently, the fidelity of the total product state varies between 0.976(4) and 0.90(2) for 6 to 21 qubits [Fig. 6.4(b)]. The fidelity of the hiding operations is not a limiting factor for the experiments on the observation of the non-Abelian state.

6.2.4 *Quench dynamics under the Heisenberg model*

A quench dynamics was observed as a test of the fidelity of the Trotter-approximated Heisenberg interaction. The Heisenberg Hamiltonian

$$H_{\text{Heis}} = \frac{1}{3}\sum_{i<j} J_{ij}\left(\sigma_x^{(i)}\sigma_x^{(j)} + \sigma_y^{(i)}\sigma_y^{(j)} + \sigma_z^{(i)}\sigma_z^{(j)}\right) \tag{6.11}$$

is approximated as described in Sec. 6.2.1. The J_{ij} matrix can approximately be described by the power law $J_{ij} \approx J_0/|i-j|^\alpha$ with $J_0 = 508\,\text{rad/s}$, $\alpha = 1.0$. A 12-ion crystal[5] was initially prepared in the product state $|z-, \cdots, z-, x+, z-, \cdots, z-\rangle$. Then the system was time-evolved under the Trotter-approximated Heisenberg Hamiltonian. Finally, the single-qubit magnetization $\langle\sigma_\gamma^{(i)}\rangle$ was observed in all three bases $\gamma = x, y, z$.

The measured quench dynamics is shown in Figure 6.5(a). The magnetization of the central, flipped spin spreads in a wave-like manner through the entire system. For three of the qubits the evolution is compared with numerical simulations individually, as shown in Figure 6.5(b). The numerical simulation is carried out for both the Trotter-approximated Hamiltonian (solid line) and the exact Hamiltonian (6.11) (dashed line). The Trotter approximation is implemented with up to 36 steps[6] and closely follows the exact simulation. The fidelity of the Trotter approximation will be evaluated later quantitatively (Fig. 6.7). The largest experimental error is observed in the z basis: Ideally, each component of the total magnetization is conserved under the Heisenberg model. However, the mean magnetization per ion $1/N\sum_{i=1}^{N}\langle\sigma_z^{(i)}\rangle$ changes by approx. $0.02\,\text{ms}^{-1}$.

5 A small 12-ion crystal was chosen to allow for easy numerical computations as a comparison.

6 The total number of Trotter steps is limited by the experiment control hardware, the *Pulse Box*, to approx. 36 steps with 4 pulses each. The hardware supports at most approx. 200 individual pulses.

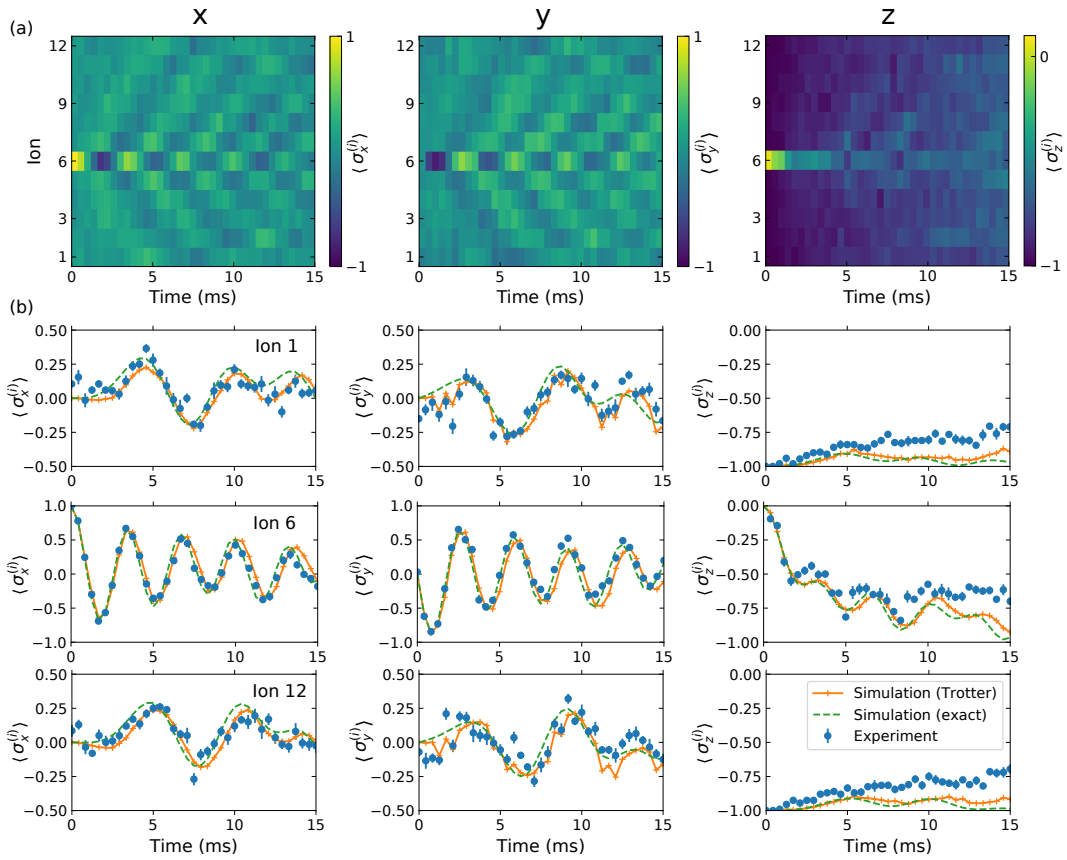

Figure 6.5: Evolution under the Trotterized Heisenberg model. A quench of the initial state $|z-,\cdots,z-,x+,z-,\cdots,z-\rangle$ is observed in the experiment for a 12-ion crystal (approx. power-law interactions with $J_0 = 508\,\mathrm{rad/s}$, $\alpha = 1.0$, Eq. (6.11), 36 Trotter steps max.). The single-qubit magnetization $\langle\sigma_\gamma^{(i)}\rangle$ is measured in the $\gamma = x, y, z$ basis, respectively. (a) In each basis, the excitation propagates through the crystal in a wave-like manner. (b) The measurements are in good agreement with numerical simulations. For the central and the two outermost ions, the measured excitation (points) is compared against the numerical simulation of the Trotter approximation (solid line) and against the numerical simulation of the exact Hamiltonian (dashed line). Only the magnetization in the z basis shows a noticeable increase over time.

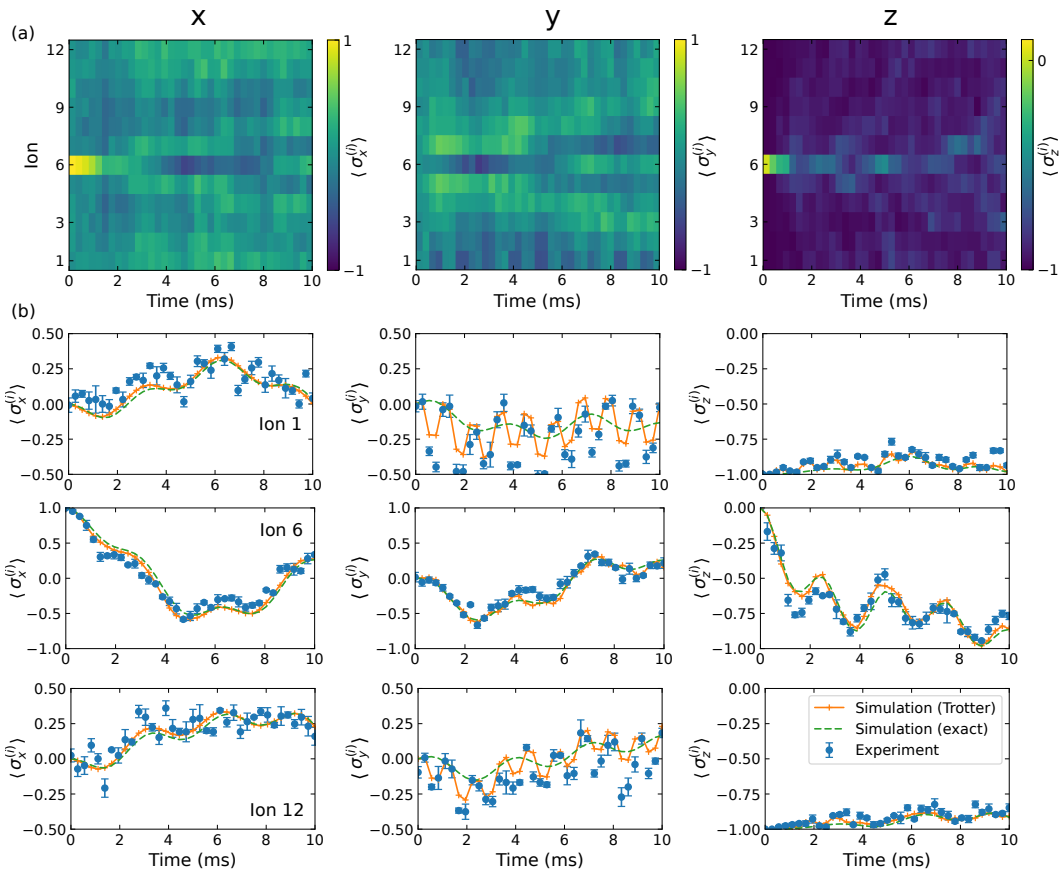

Figure 6.6: Evolution under the Trotterized XY model. A quench of the initial state $|z-,\cdots,z-,x+,z-,\cdots,z-\rangle$ is observed in the experiment for a 12-ion crystal ($J_0 = 491\,\mathrm{rad/s}$, $\alpha = 1.0$). The single-qubit magnetization $\langle\sigma_\gamma^{(i)}\rangle$ is measured in the $\gamma = x, y, z$ basis, respectively. (a) In each basis, the excitation propagates through the crystal in a wave-like manner. (b) The measurements are in good agreement with numerical simulations. For the central and the two outermost ions, the measured excitation (points) is compared against the numerical simulation of the Trotter approximation (solid line) and against the numerical simulation of the exact Hamiltonian (dashed line). Only the magnetization in the y basis shows a considerable Trotterization error for the outermost ions. This error is caused be the inhomogeneous coupling of the global laser beam to the ion crystal.

6.2.5 *Quench dynamics under the XY model*

The quench dynamics was also observed for the Trotter-approximated XY model. The time-evolution operator $U_{\mathrm{XY}}(t)$ of the Hamiltonian

$$H_{\mathrm{XY}} = \frac{1}{2}\sum_{i<j} J_{ij}\left(\sigma_x^{(i)}\sigma_x^{(j)} + \sigma_y^{(i)}\sigma_y^{(j)}\right) \tag{6.12}$$

is approximated by

$$U_{\mathrm{XY}}(t) \approx \left[(R_x^\dagger)^2\right]^N (R_x^2 U_{\mathrm{YY}} U_{\mathrm{XX}})^N, \tag{6.13}$$

where N is the number of Trotter steps and $R_x = \exp\left[-\mathrm{i}\pi/4\sum_i \sigma_x^{(i)}\right]$ is a $\pi/2$ rotation around the x axis. After four Trotter steps each, the base rotation is alternated and R_x is replaced with $R_x^\dagger$. As was the case for the Heisenberg model, additional final base rotations are required if the number of Trotter steps is not an integer multiple of 2 (see Appendix C.2).

The measured quench dynamics is shown in Figure 6.6. Again, the 12-ion crystal is initially prepared in the product state $|z-,\cdots,z-,x+,z-,\cdots,z-\rangle$. The y basis shows the impact of systematic rotation errors at the ends of the ion crystal. Due to the alternating base rotations, the rotation error has a period of 4 Trotter steps.

6.2.6 *Fidelity of the Trotter approximation*

The fidelity of the Trotter approximation was evaluated both for the Heisenberg and for the XY Hamiltonian. Figure 6.7 shows two cases: First, the fidelity of the numerically computed Trotter approximation is evaluated with respect to the exact evolution (lines). Second, the fidelity of the experimentally observed Trotter approximation is evaluated with respect to the exact evolution (markers). The ions were initially prepared in the product state $(|y\rangle\,|x\rangle\,|z\rangle)^{\otimes 4}$. After an evolution for a time t, the final state is measured by performing quantum state tomography on all 2-qubit subsystems. The fidelity is computed as $F = (\mathrm{Tr}\,\sqrt{\sqrt{\rho_{\mathrm{exact}}}\rho_{\mathrm{exp}}\sqrt{\rho_{\mathrm{exact}}}})^2$. At the initial time, the mean 2-qubit fidelity is limited by the state preparation error to $F_{\mathrm{initial}} = 0.995(4)$. At the end of the time evolution the mean fidelity drops to $F_{\mathrm{final}} = 0.97(1)$. This value is close to the limit given by the Trotter approximation itself, $F_{\mathrm{final,\ theor.}} = 0.98$. When looking at the fidelity of the individual pairs of qubits, a drop towards the ends of the ion crystal becomes apparent. This drop is caused by systematic rotation errors, caused by the Gaussian shape of the laser beam.

The experimentally observed points were taken for two cases: In one case the measurements were carried out for a crystal of 12 ions. In the other case, a crystal of 21 ions was used where all but 12 ions were hidden from the interactions (see Sec. 6.2.3). The data shows that the evolution that makes use of hiding of unused ions in a large ion crystal has a fidelity that is close (approx. within one standard deviation) to the one when working directly with a small ion crystal.

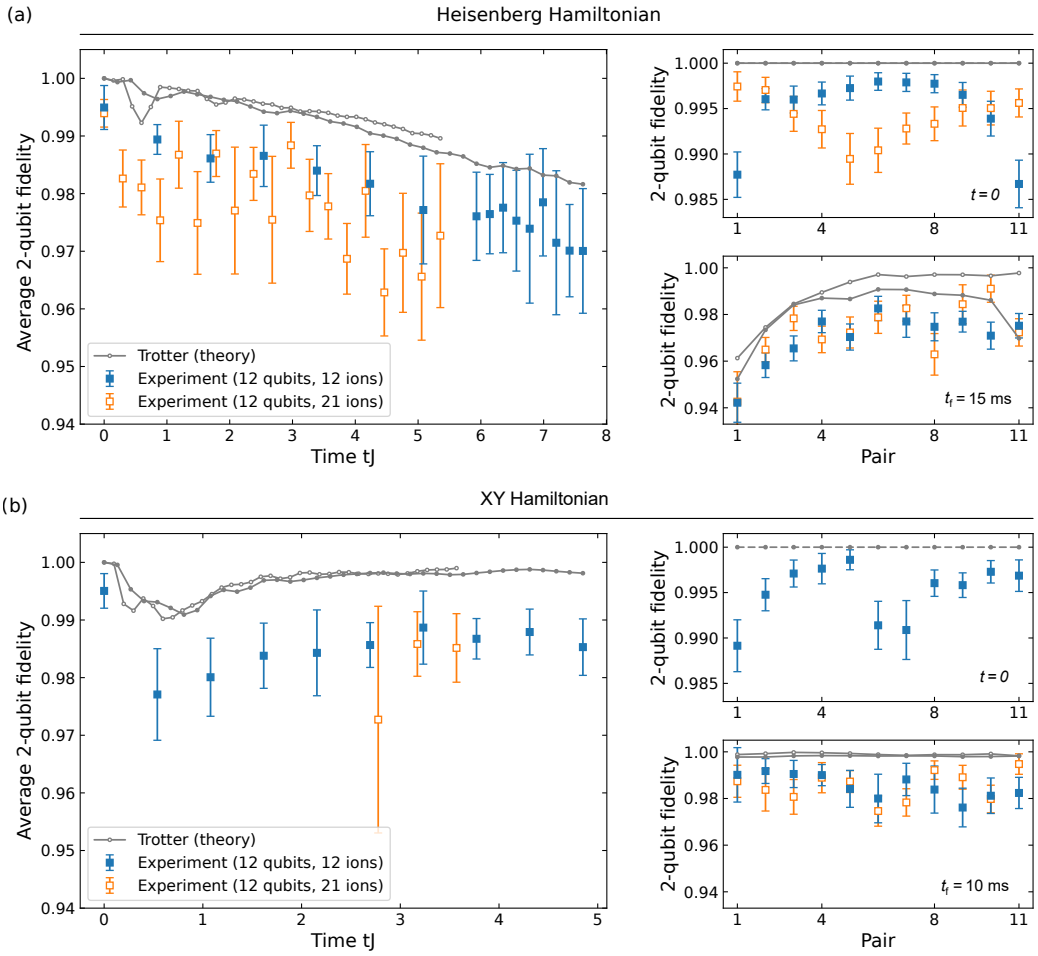

Figure 6.7: Fidelity of the Trotter approximation of the Heisenberg model and of the XY model. The system is initially prepared in the product state $(|y\rangle\,|x\rangle\,|z\rangle)^{\otimes 4}$. After an evolution for a time t, the density matrices of all 2-qubit subsystems of neighboring qubits (1-2, 2-3, 3-4, ...) were measured with quantum state tomography. The evolution was observed experimentally (markers) and simulated numerically (lines). On the left column, the average 2-qubit fidelity $F = (\mathrm{Tr}\sqrt{\sqrt{\rho_{\mathrm{exact}}}\rho_{\mathrm{exp}}\sqrt{\rho_{\mathrm{exact}}}})^2$ is shown for the (a) Heisenberg model and for the (b) XY model. On the right column, the 2-qubit fidelity is evaluated for individual pairs at the initial and the final time. Coupling parameters for Hamiltonian (6.11) respectively (6.12) for 21 ions: $J_0 = 357\,\mathrm{rad/s}$, $\alpha = 0.7$; and for 12 ions: $J_0 = 508\,\mathrm{rad/s}$, $\alpha = 1.0$

6.3 OBSERVATION OF THERMALIZATION UNDER NONCOMMUTING CHARGES

The observation of thermalization under noncommuting charges is carried out in the following steps: Initially, the total system is prepared in a state from the microcanonical subspace. Then, the total system is evolved under the Heisenberg Hamiltonian. During the evolution, the subsystem exchanges noncommuting globally conserved quantities with its environment (i.e. the total system). Finally, the state of the subsystem is measured and compared to the predicted thermal state.

The total system is realized with a 21-ion crystal. The Trotter-approximated spin-spin coupling (6.11) has an effective coupling strength of $J_0 = 357\,\mathrm{rad/s}$. For some of the measurements smaller total systems were required. Then, the size of the total system was varied by hiding unused ions, as described in Sec. 6.2.3.

Preparation of the system in a microcanonical subspace comes with a difficulty: The microcanonical subspace consists of all states that have given expectation values for the observables H, S_x, S_y, and S_z. However, as the components of the total magnetization components do not commute with each other, $[S_\gamma, S_{\gamma'}] \neq 0$, they cannot be determined simultaneously. An approach to this problem is to approximate the microcanonical subspace with states that have a high probability of yielding the expected values for the observables H, S_x, S_y, and S_z. This leads to the approximate microcanonical subspace [117]. In particular, each tensor product of single-qubit pure states lies in the approximate microcanonical subspace. For the present experiment, the product state

$$|\psi_0\rangle = |y, x, z\rangle^{\otimes N/3} \tag{6.14}$$

is chosen as the initial state, where N denotes the number of qubits in the total system. The alignment of the individual qubits along the three axes leads to large chemical potentials μ_γ in the thermal state. The chemical potentials distinguish the thermal state from the usual (grand) canonical thermal state. The conjectured equilibrium state of the total system is the so-called non-Abelian thermal state[118]

$$\rho^{\mathrm{tot}}_{\mathrm{NATS}} = \mathrm{e}^{-\beta(H - \sum_\gamma \mu_\gamma S_\gamma)} / Z_{\mathrm{NATS}}, \tag{6.15}$$

where the inverse temperature β and the chemical potentials μ_γ ($\gamma = x, y, z$) are determined by the initial state by the conserved quantities

$$E^{\mathrm{tot}} = \langle\psi_0| H |\psi_0\rangle = \mathrm{Tr}(H\rho^{\mathrm{tot}}_{\mathrm{NATS}}) \tag{6.16}$$

and

$$Q^{\mathrm{tot}} = \langle\psi_0| S^{\mathrm{tot}}_\gamma |\psi_0\rangle = \mathrm{Tr}(S^{\mathrm{tot}}_\gamma \rho^{\mathrm{tot}}_{\mathrm{NATS}}) \quad \text{for } \gamma = x, y, z. \tag{6.17}$$

When considering a small subsystem that has a high temperature and low chemical potentials, the energy and chemical potentials can be approximated as [118]

$$\beta = -\frac{E^{\mathrm{tot}}}{3(2N-3)J_0^2} \tag{6.18}$$

and

$$\mu_\gamma = -\frac{3(2N-3)}{N}\frac{Q^{\mathrm{tot}} J_0^2}{E^{\mathrm{tot}}}, \tag{6.19}$$

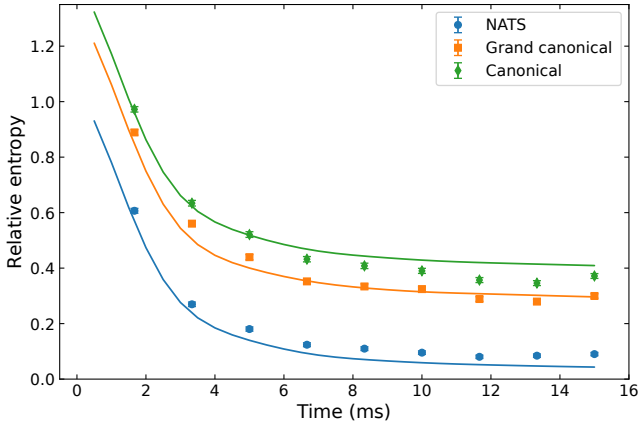

Figure 6.8: Thermalization under noncommuting charges. The initial state $|\psi_0\rangle = |y, x, z\rangle^{\otimes 7}$ is time-evolved under the Heisenberg Hamiltonian (6.11), approaching an equilibrium. The relative entropy (6.20) of the measured quantum state is plotted as a function of the evolution time (points). The measured quantum state is compared against the non-Abelian thermal state (NATS), the grand canonical state and the canonical state. The observed state is best described by the NATS, as the relative entropy has the smallest value. Each data point consists of 250 repetitions. The error bars are evaluated by bootstrapping. Solid lines are numerical simulations.

where N is the number of qubits in the total system and J_0 is the spin-spin coupling strength. The condition for this approximation is $\sqrt{N}|\beta|J_0 \ll 1$, $\sqrt{N\sum_\gamma \mu_\gamma^2}|\beta| \ll 1$, and $|\beta|\sum_\gamma \mu_\gamma^2/J_0 \ll 1$.

In general, the inverse temperature and the chemical potentials are calculated from Eq. (6.16) and (6.17) numerically. For small total system sizes $N \lesssim 12$ the equations can be solved directly by a least-squares minimization. For the large $N = 21$ system that was used for observing the thermalization dynamics, the solution can be obtained from a maximum-entropy problem [83], yielding $\beta = 1.3 \times 10^{-3}\,\mathrm{s/rad}$ and $\mu_{x,y,z} = -1046\,\mathrm{rad/s}$.

The experimentally observed thermalization dynamics is presented in Figure 6.8. The initial state 6.14 is time-evolved under the Heisenberg Hamiltonian (6.11) for a time t. Finally, the states $\rho_i(t)$ of all pairs $i = 1, ..., N-1$ of neighboring qubits are measured by quantum state tomography. After an evolution time of up to $J_0 t = 357\,\mathrm{rad/s} \times 15\,\mathrm{ms} \approx 5.4$ the total system has largely approached its equilibrium state. The observed state of the system is compared to the predicted non-Abelian thermal state by the relative entropy. The relative entropy is a measure for the distance between two quantum states. The smaller the relative entropy, the closer two states are. The relative entropy between two states (density operators) χ and ξ is [120]

$$D(\chi\|\xi) = \mathrm{Tr}[\chi(\log\chi - \log\xi)]. \tag{6.20}$$

For each pair of qubits, the relative entropy is evaluated, $D(\rho_i(t)\|\rho_{\mathrm{NATS}})$. Then, the average $\langle D(\rho_i(t)\|\rho_{\mathrm{NATS}})\rangle$ over all pairs is computed to average over spatial fluctuations.

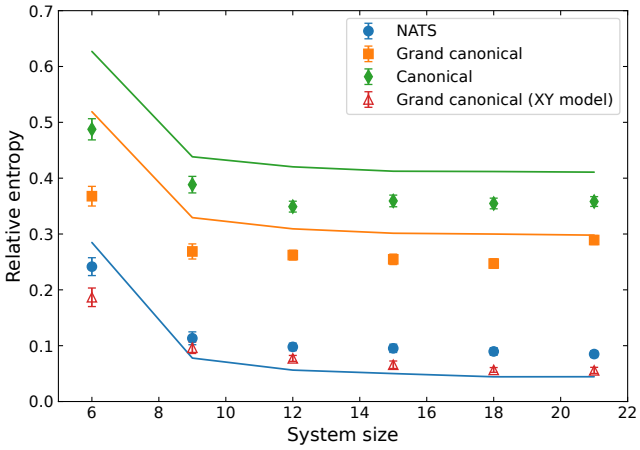

Figure 6.9: Thermalization for different system sizes. The relative entropy at late times ($t_f = 12 \ldots 15\,\text{ms}$) is plotted against the size of the total system. The experimentally observed state is predicted best by the non-Abelian state for all system sizes (blue filled markers). As a comparison, thermalization under the XY model with commuting charges was measured (open triangles). Solid lines are numerical simulations. Each data point consists of 250 repetitions. The error bars are statistical uncertainties which are calculated from bootstrapping.

As a comparison, the distance to two other thermal states is evaluated as well, namely the canonical state $\rho_{\text{can}} = \exp(-\beta H)/Z_{\text{can}}$ and the grand canonical state $\rho_{\text{GC}} = \exp(-\beta[H - \mu_z S_z])/Z_{\text{GC}}$. The state is normalized by the partition function Z_{can}, respectively Z_{GC}. Of the three thermal states, the non-Abelian thermal state is the closest to the experimentally observed state at all times. This supports the claim that the system thermalizes towards the non-Abelian thermal state. Thus, the thermal state is of the form of a generalized Gibbs ensemble, even if the thermalization is governed by a Hamiltonian that gives rise to non-commuting conserved quantities.

The measurements are compared against numerical simulations (solid lines). The plotted simulation curves were carried out for the ideal evolution, ignoring decoherence. Additional simulations (not shown) tested the effect of decoherence: Dephasing noise increases the relative entropy of the non-Abelian state and decreases the relative entropy of the grand canonical and of the canonical state. If dephasing noise is present in the experiment, it closes the gap between the non-Abelian state and the competitor states. In other words, a decoherence-affected experiment will give a lower bound for the separation of the non-Abelian state.

In a second measurement, the influence of the size of the total system was studied. The number of qubits was varied between $N = 6$ to 21 by hiding unused ions. The result is shown in Figure 6.9. The relative entropy was calculated as the average over the last three time steps $t_f = 12 \ldots 15\,\text{ms}$ in order to reduce the effect of temporal fluctuations. For all system sizes, the non-Abelian thermal state is the best prediction for the observed state. More detailed theoretical questions cannot be answered with the present experimental data: It has been shown theoretically [83] that the distance between the state of the system and ρ_{NATS} is

nonzero even in the thermodynamic limit $N \to \infty$. However, the thermodynamic limit is out of reach for a few-body system in a trapped-ion quantum simulator. Furthermore, the scaling behavior of the long-time distance to the thermal state was conjectured to decrease as $N^{-1/2}$ [117]. For determining the scaling behavior, smaller systematic errors and a wider range of system sizes would be required.

Finally, a comparison was carried out between thermalization under noncommuting charges and thermalization just under commuting charges. A Hamiltonian that realizes thermalization under commuting charges is the XY Hamiltonian (6.12). The XY model conserves the energy and the z component of the total magnetization. Thus, the expected thermal state is of the form of the grand canonical state $\rho_{\mathrm{GC}} = \exp(-\beta[H - \mu_z S_z])/Z_{\mathrm{GC}}$. The system was initially prepared in the same product state 6.14 as for the previous measurements and time-evolved for 10 ms with $J_0 = 398\,\mathrm{rad/s}$. The measured relative entropy is shown in Figure 6.9 as open markers. The observed state in the commuting case lies consistently closer to the predicted thermal state than the corresponding state in the noncommuting case. This is consistent with the theoretical conjecture that thermalization under noncommuting charges hinders thermalization [118].

6.4 CONCLUSIONS

In this work, thermalization of a closed quantum system under noncommuting charges was observed. The interactions in the system were governed by a long-range Heisenberg model which conserves energy and the three components of total magnetization, resulting in four noncommuting charges. The Heisenberg Hamiltonian was implemented by a Trotter approximation. The Trotter sequence was designed in such a way that the number of base rotations was minimized. Furthermore, the sequence mitigates dephasing errors by dynamical decoupling and systematic rotation errors by alternating base rotations. Observation of a quench dynamics showed that the system thermalizes towards the predicted non-Abelian thermal state. This behavior was observed for different system sizes of up to 21 qubits.

Trapped-ion quantum simulators offer a platform to study thermalization. They constitute a fully controllable, closed quantum system and interaction Hamiltonians can be engineered to some degree. The current system size of approximately 20 ions is large enough to keep finite-size effects small. One limitation is the finite evolution time determined by decoherence. In order to observe the thermalization of larger quantum systems – which require longer times to thermalize – the effect of decoherence needs to be decreased. One, if not the, leading cause of decoherence in a Trotterized experiment is resonant excitations from spectrally broadened light. This error source depends on the particular timing of the light pulses and the motional mode frequencies of the ion crystal, making it hard to control. If Trotterization should be scaled to larger system sizes, a simple and robust solution is needed to handle spectral broadening.

7

OBSERVATION OF MAGNON BOUND STATES

The work presented here is published in
Physical Review X **13**, 031017 (2023)

7.1 INTRODUCTION

The behavior of quantum systems is difficult to compute when they are governed by strong interactions. Perturbative approximations fail and for large system sizes direct computation becomes intractable. In such cases, quantum simulators may provide a tool to study the interactions between excitations in the system. Excitations in a spin chain have already been studied theoretically early in the 1930s [121]. Excitations of elementary spin waves can be considered as quasi-particles, the so-called *magnons*. For short-range interactions, the formation of bound states between two magnons has been observed experimentally in a one-dimensional chain of bosonic ^{87}Rb atoms [122]. In a recent experiment, the bound states of up to five magnons have been studied in a superconducting 24-qubit device [123].

For long-range interactions however, the situation is more complicated, as magnons can have unbounded group velocity. The question is whether in this case the formation of stable bound states is still possible. The impact of long-range interactions on magnon dynamics has first been studied for single magnons in a long-range Ising chain [124, 125]. Depending on the long-rangeness of the interactions, the spread of the excitation is bounded by a light cone, or is unbounded and instantaneous. The case of two magnons was analyzed theoretically for the long-range anisotropic Heisenberg model [126]. The spin-spin interactions were described by a power-law $1/|i-j|^{\alpha}$ with exponent α. Two regimes were identified: For long-range interactions with $\alpha > 1$, bound states were dynamically populated. For long-range interactions with $\alpha \leq 1$, magnons were unbound with almost instantaneous propagation.

The question that was addressed in the work presented in this chapter is whether the predicted formation of bound states under long-range interactions can be observed experimentally. For this purpose, interactions of the long-range,

anisotropic Heisenberg model were engineered by a Trotter approximation. By variation of the Trotter step length, the anisotropy could be adjusted. The bound states were analyzed experimentally in a number of ways: First, the dispersion relation of single-magnon and two-magnon states were measured. Second, the formation of two-magnon bound states was observed via spin-spin correlations. And third, entanglement entropy was quantified to study the impact of bound state formation on the spread of entanglement in the system.

7.2 BOUND STATES

The XY model supports the propagation of individual quasiparticles (magnons) in a spin-$\frac{1}{2}$ chain. Adding a Z term introduces interactions between the magnons and leads to the anisotropic Heisenberg model. The Hamiltonian is

$$H = \frac{1}{3}\sum_{i<j} J_{ij}\left(\sigma_x^{(i)}\sigma_x^{(j)} + \sigma_y^{(i)}\sigma_y^{(j)} + \Delta\sigma_z^{(i)}\sigma_z^{(j)}\right) \tag{7.1}$$

where Δ determines the overall strength of Ising interaction and $\sigma_{x,y,z}$ are the Pauli matrices. The spin-spin coupling matrix J_{ij} is described by a power law, $J_{ij} = |i-j|^{-\alpha}$ with $0 \leq \alpha$. This Hamiltonian can also be written in terms of the raising and lowering operators σ_+ and σ_- as

$$H = \frac{1}{3}\sum_{i<j} J_{ij}\left[2\Big(\underbrace{\sigma_+^{(i)}\sigma_-^{(j)} + \sigma_-^{(i)}\sigma_+^{(j)}}_{\text{long-ranged hopping}}\Big) + \underbrace{\Delta\sigma_z^{(i)}\sigma_z^{(j)}}_{\text{interactions}}\right]. \tag{7.2}$$

The first term describes long-ranged hopping of an excitation: An excitation is created (destroyed) at site i and destroyed (created) at site j. The second term gives rise to interactions between two magnons at site i and j. This Hamiltonian conserves the total z magnetization, as can be seen from $\left[H, \sum_{i=1}^{N}\sigma_z^{(i)}\right] = 0$.

7.2.1 *Short-range interactions*

The basic mechanism that is responsible for the formation of bound states can be illustrated in the short-range case $\alpha \to \infty$. In the short-range case only the interaction between neighboring spins contributes to the interaction energy. The interaction energy between two parallel spins is $\langle\uparrow\uparrow|H|\uparrow\uparrow\rangle = \langle\downarrow\downarrow|H|\downarrow\downarrow\rangle = J\Delta/3$ and between antiparallel spins $\langle\uparrow\downarrow|H|\uparrow\downarrow\rangle = -J\Delta/3$. For N spins, the total interaction energy is given by the number of pairs $N-1$. Thus, the configuration in which all spins are pointing down has the energy $E(|\psi\rangle) \equiv \langle\psi|H|\psi\rangle$,

$$E(|\downarrow\cdots\downarrow\rangle) = \frac{J\Delta}{3}(N-1). \tag{7.3}$$

The configuration in which two flipped spins are placed next to each other (but not at the edges) has the energy

$$E(|\downarrow\cdots\downarrow\uparrow\uparrow\downarrow\cdots\downarrow\rangle) = \frac{J\Delta}{3}[(N-1)-4]. \tag{7.4}$$

In contrast, placing the spins further apart leads to the energy

$$E(|\downarrow\cdots\downarrow\uparrow\downarrow\uparrow\downarrow\cdots\downarrow\rangle) = \frac{J\Delta}{3}[(N-1)-8]. \tag{7.5}$$

Separating two neighboring spins is only possible if the energy difference between the configurations can be absorbed by the rest of the system. For short-range interactions there is a gap in the spectrum between the bound state and the bottom of the band [127]. This gap stabilizes two neighboring spins, resulting in a bound state.

7.2.2 *Long-range interactions*

In the long-range Heisenberg model, the formation of bound states depends on how fast the interactions decay over the spin chain. To illustrate this point, we first consider the dispersion relation of a single quasiparticle. A single flipped spin is embedded in spins pointing down, $|\downarrow\cdots\downarrow\uparrow\downarrow\cdots\downarrow\cdots\rangle$. The dispersion relation of this single-magnon state in the thermodynamic limit $N\to\infty$ [128] is obtained from solving the eigenvalue problem

$$E\psi(n) = \frac{2J}{3}\sum_{l>0}\frac{1}{|l|^\alpha}\left[\psi(n+l)+\psi(n-l)\right]. \tag{7.6}$$

A transformation into Fourier space gives the single-magnon dispersion relation

$$\epsilon_1(k) = \frac{4J}{3}\sum_{l=1}^{\infty}\frac{\cos(kl)-\Delta}{l^\alpha}, \tag{7.7}$$

where k is the momentum of the magnon.[1] The anisotropy Δ only creates an offset in energy but does not change the dependency on the momentum k. Fig. 7.1(a) shows the dispersion relation for different values of the power-law exponent α. For $\alpha<1$, the dispersion relation diverges in the long-wavelength limit $k\to 0$. For $1\le\alpha\le 2$, the dispersion relation is finite but shows a cusp at $k=0$. For $\alpha>2$, the dispersion relation is smooth at $k=0$. The different behavior has implications for the single-magnon velocity which is given by the group velocity

$$v(k) = \frac{\partial\epsilon_1}{\partial k}(k). \tag{7.8}$$

The single-magnon group velocity is unbounded[2] in the range $1<\alpha\le 2$. As a consequence, parts of the wave function of a single magnon can propagate with an arbitrary velocity.

As a consequence of this unbounded group velocity, it is not obvious whether bound states can form between two magnons. The behavior of a potential bound state is described by the two-magnon dispersion relation. The dispersion relation

1 The sum $\sum_{l=1}^{\infty}\frac{\cos(kl)}{l^\alpha} = \mathrm{Re}[\mathrm{Li}_\alpha(e^{ik})]$ can be expressed in terms of the polylogarithmic function Li_α [129].

2 The region of bounded group velocity $v(k) = -\mathrm{Im}[\mathrm{Li}_{\alpha-1}(e^{ik})]$, for $k\to 0$, can be derived from the defining series of $\mathrm{Li}_s(z)$ that converges for $|z|=1$ provided that $\mathrm{Re}[s]>1$ [129]; hence $\alpha>2$ for finite group velocity.

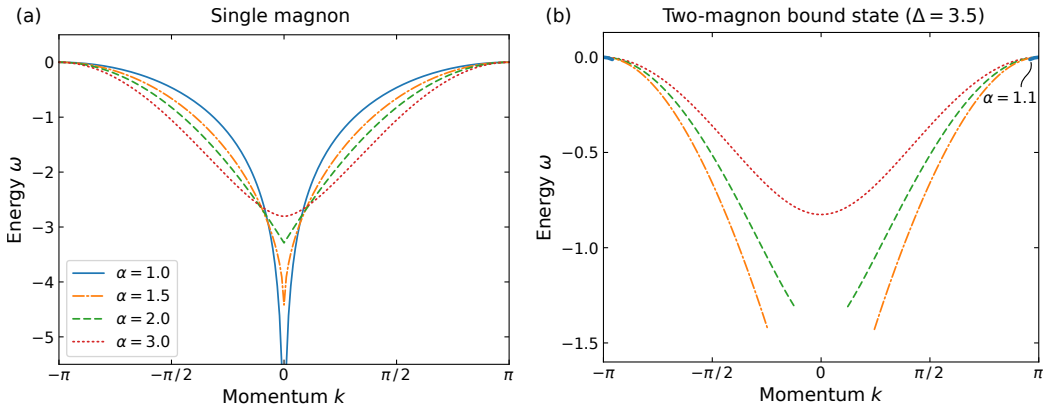

Figure 7.1: Dispersion relation of the long-range, anisotropic Heisenberg model. (a) Single magnon ($\Delta = 1$). The dispersion relation (7.7) in the thermodynamic limit is evaluated for $J = 1\,\mathrm{rad/s}$ for various α. The plotted energy is $\epsilon_1(\pi) - \epsilon_1(k)$ for each α to get a common energy origin. For $\alpha \leq 2$, the dispersion relation exhibits a cusp at $k \to 0$, indicating a divergent group velocity $v(k) = \partial_k \epsilon_1(k)$. (b) Two-magnon bound state ($\Delta = 3.5$). For $1 < \alpha \leq 2$, the bound states become unstable at low momenta, which is visible by the gap in the dispersion curves.

is obtained from solving the eigenvalue problem (already transformed into Fourier space)

$$E(k)\phi(n) = \frac{2J}{3} \sum_{l>0} \frac{2\cos(kl)}{|l|^\alpha} \left[\phi(n+l) + \phi(n-l)\right] + \frac{4J\Delta}{3|n|^\alpha}\phi(n). \tag{7.9}$$

The numerically computed bound-magnon dispersion relation is shown in Fig. 7.1(b). For $\alpha < 1$ the kinetic energy is unbounded (not shown). For long-range interactions with $1 < \alpha \leq 2$, the bound state exists, but becomes unstable at small momentum k. An unstable bound state is indicated by the gap in the dispersion relation. For $\alpha > 2$, the short-range nature of the interactions dominate and the bound state is stable over the entire Brillouin region.

7.3 IMPLEMENTATION OF THE ANISOTROPIC HEISENBERG MODEL

The anisotropic Heisenberg model was implemented by a Trotter approximation, similar to Sec. 6. The anisotropy in the Heisenberg model (7.1) was realized by Trotter steps of different length. The Trotter sequence is depicted in Figure 7.2. The basic building blocks are interactions of the XX and the YY type, while the ZZ part of the Hamiltonian (7.1) is implemented using global base rotations. Each Trotter step (dashed boxes) consists of four substeps. For anisotropies $\Delta > 1$, the long duration of the ZZ substep makes the sequence susceptible to dephasing errors. To mitigate the impact of dephasing errors, the ZZ substep is split into two parts that are separated by a spin-echo pulse. The base rotations make the system return to its original basis after 8 Trotter steps. If the number of Trotter steps is not an integer multiple of 8 an additional base rotation is required, as listed in Fig. 7.2(b).

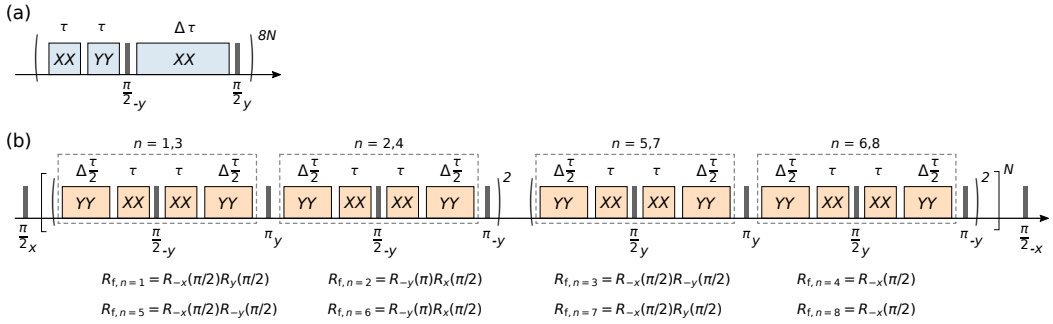

Figure 7.2: Trotter sequence of the long-range, anisotropic Heisenberg model with anisotropy Δ. (a) Basic Trotter approximation. The ZZ-type interaction of length $\Delta\tau$ is implemented by a XX-type interaction closed by two base rotations. (b) Four Trotter steps (dashed boxes) are combined with alternating base rotations ($\pi/2_{\pm y}$) to mitigate rotation errors. Between the Trotter steps, spin-echo pulses ($\pi_{\pm y}$) reduce the impact of dephasing errors. The sequence repeats after $n = 8$ Trotter steps. If the number of Trotter steps is not an integer multiple of eight, the final $\pi/2$ pulse is replaced by rotations $R_{\mathrm{f},n}$.

An additional complication arises from the requirement to realize a large value of $\alpha > 1$. A large power-law exponent can be achieved in two ways: First, the bichromat detuning can be increased. This has the disadvantage of reducing the spin-spin coupling strength. Second, the radial modes can be compressed to a smaller range by relaxing the axial confinement. This has the disadvantage of increasing the size of the ion crystal which leads to larger global rotation errors; furthermore the axial heating rate increases. As a compromise, the largest value that could be realized was $\alpha = 1.4$ by setting the radial trapping frequencies to approx. 2.93 MHz and 2.90 MHz, the axial trapping frequency to values as low as 92 kHz and choosing a bichromat detuning of 40 kHz.

The quality of the Trotter approximation was assessed with a quench dynamics. A crystal of 20 ions was prepared in the $|\downarrow\rangle^{\otimes 20}$ state. Then the central spin was flipped and the dynamics of the system was observed. The experimental observations are shown in Figure 7.3, including numerical simulations [Fig. 7.3(a)]. The experiment was carried out for the edge case $\Delta = 0$, realizing the XY model. This allowed us to observe the dynamics for two independent cases: First, the interactions were directly realized with the center-line detuned bichromat beam in the rotating-frame approximation [Fig. 7.3(b)]. Second, the interactions were Trotter-approximated [Fig. 7.3(c)]. The Trotter approximation suffers from more errors than the direct implementation. Two effects are clearly visible: The mean excitation increases with progressing evolution time, indicating a violated conservation of total z magnetization. This increase in mean excitation is mainly driven by coupling to spectrally broadened light. This error can be reduced by pulse shaping, and fine-adjustment of the temporal spacing of the Trotter steps, see Sec. 4.2.4. Furthermore, rotation errors from the global base rotations are apparent towards the edges of the ion crystal. The periodicity in the rotation error is caused by the alternating pulses used in the Trotter sequence.

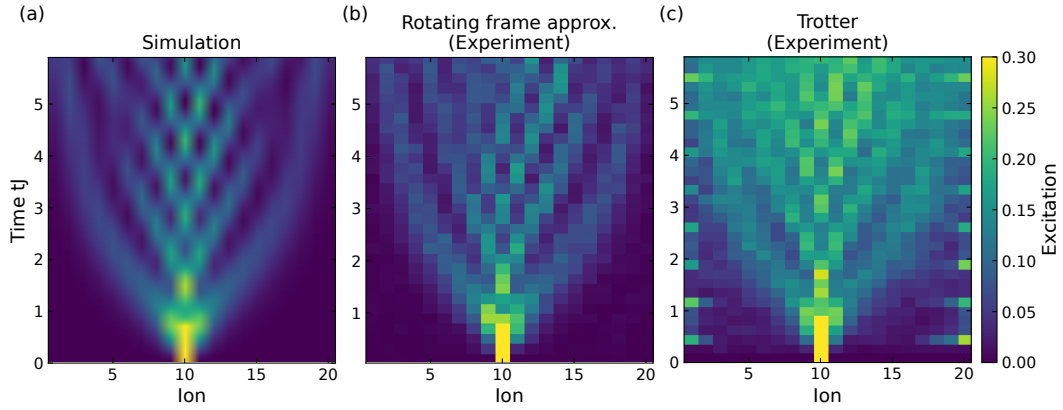

Figure 7.3: Implementation of the anisotropic Heisenberg model (7.1) for the edge case $\Delta = 0$. (a) Numerical simulation. (b) Experimental rotating-frame approximation using a center-line-detuned bichromat beam. (c) Experimental Trotter approximation with up to 36 Trotter steps. The maximal experimental evolution time was $t = 17\,\mathrm{ms}$ with the parameters $J = 348\,\mathrm{rad/s}$ and $\alpha = 1.4$.

7.4 SPECTROSCOPY OF SINGLE- AND TWO-MAGNON BOUND STATES

7.4.1 *Single-magnon dispersion relation*

The dispersion relation of a single-magnon excitation was measured by the spectroscopic technique described in [130]. The dispersion relation connects the wave number k of a standing wave with its energy. The system is first prepared in a standing wave and then time-evolved under its Hamiltonian. The standing wave oscillates with a frequency that is given by its energy, which enables a measurement of the dispersion relation. It is important to note that the standing wave has to be at least an approximation of an eigenstate. Only then its oscillation frequency directly relates to the energy $\epsilon_1(k)$ of the mode.

In the experiment, the system is initialized in $|0\rangle = |\downarrow\downarrow \ldots \downarrow\downarrow\rangle$. Single-ion addressing prepares a standing wave with momentum k of the form

$$|\psi_1\rangle = \mathrm{e}^{\mathrm{i}\sum_j \gamma A_j^{(k)} \hat{\sigma}_x^{(j)}} |0\rangle = |0\rangle + \mathrm{i}\gamma \sum_j A_j^{(k)} \hat{\sigma}_x^{(j)} |0\rangle + \mathcal{O}(\gamma^2) \tag{7.10}$$

with amplitudes $A_j^{(k)} = \sqrt{\frac{2}{L}} \sin(kj)$ and $k = \pi n/(L+1)$ for $n = 1, \ldots, L$. The contributions in second order γ^2 or higher are kept small by setting $\gamma = 0.7$. Then the system is evolved under its Hamiltonian. For this measurement, the directly implemented XY model in the rotating-frame approximation was used, as it has a higher fidelity than the Trotter approximation. The anisotropy $\Delta = 0$ does not have an impact on the measured single-magnon dispersion relation, as it only adds a constant offset.

To reduce the impact of dephasing noise on the measurement precision, the initial standing wave is prepared as a superposition of two momenta k and q. This allows one to measure the relative energy $\epsilon_1(k) - \epsilon_1(q)$ in a decoherence-free

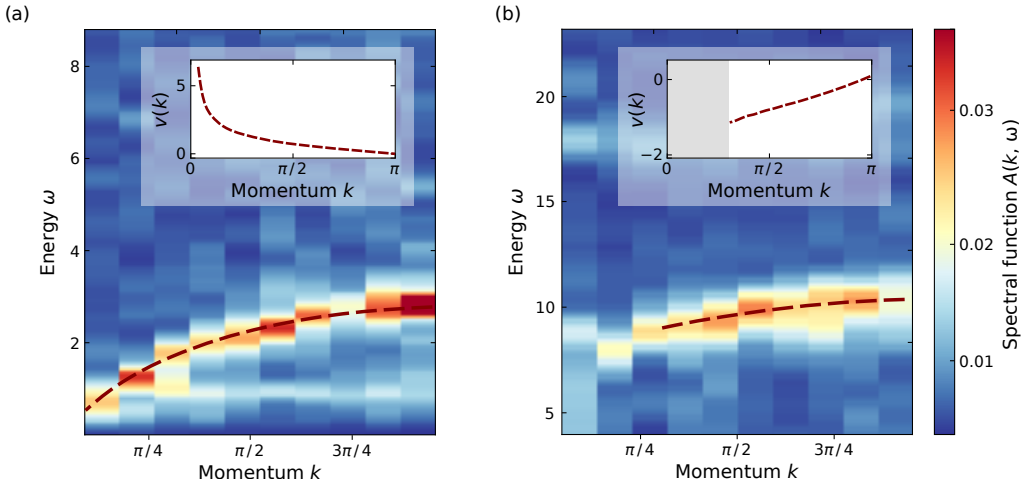

Figure 7.4: Plane-wave spectroscopy. (a) One-magnon spectroscopy. The dispersion relation (7.12) shows a clear signal over the entire Brillouin zone. The dashed line is the theoretical calculation. A cusp at low momentum indicates a diverging group velocity, which is expected from theory (inset). (b) Two-magnon spectroscopy. The dispersion relation (7.15) exhibits a broadened signal at low momenta, indicating an unstable bound state (region with missing dashed line).

subspace with fixed excitation number. To this end, the standing wave used in the experiment had the amplitudes

$$A_j^{(k)} = \sqrt{\frac{2}{L}}\big[\sin(kj) + \sin(qj)\big], \tag{7.11}$$

where the reference momentum is $q = 1$.

After time evolution under the long-range, anisotropic Heisenberg model ($\Delta = 0$) a measurement in the z basis was carried out to obtain the expectation value of the magnon projector $P_j^{\uparrow} = \frac{1}{2}\hat{\sigma}_z^{(j)}$,

$$\langle\psi_1(t)|\, P_j^{\uparrow}\, |\psi_1(t)\rangle = \gamma^2\, 2\,\mathrm{Re}\left[\mathrm{e}^{-\mathrm{i}t(\epsilon_1(k)-\epsilon_1(q))}\left(\langle q|\, P_j^{\uparrow}\, |k\rangle + \langle -q|\, P_j^{\uparrow}\, |k\rangle\right)\right] + \mathcal{O}(\gamma^3). \tag{7.12}$$

The experimentally observed energy difference $\epsilon_1(k) - \epsilon_1(q)$ is shown in Figure 7.4. A clear signal is observed in the whole Brillouin zone, pointing towards a well-defined single-magnon excitation. The theoretical dispersion relation (dashed line) is in good agreement with the measurement. At low momentum, the dispersion relation exhibits a sharp cusp, which leads to a diverging group velocity (inset).

7.4.2 *Two-magnon dispersion relation*

Spectroscopy of the two-magnon dispersion relation requires a wave of pairwise excitations. Direct creation of such a plane wave would require two-qubit operations, which are not available in the current setup. However, it is possible to

create a plane wave consisting predominantly of two-magnon states with the help of the global entangling operations. The strength of the entangling interactions $\sum_{j<j'} J_{jj'}\sigma_x^{(j)}\sigma_x^{(j')}$ drops with distance $|j-j'|$ by a power law. Thus, for short times the creation of neighboring entangled pairs is dominant and farther-reaching contributions can be neglected. In a first step, the global entangling interactions act on the state $|0\rangle$ for a time $tJ = 0.19$, where $J = \max_{j,j'}(J_{jj'})$. For this time the probability of creating two excitations first reaches its maximum. In a second step, a phase ϕ_j is imprinted on each ion. The resulting two-magnon initial state is

$$|\psi_2\rangle = \mathrm{e}^{-\mathrm{i}\sum_j \frac{\phi_j}{2}\hat{\sigma}_z^{(j)}} \mathrm{e}^{-\mathrm{i}\gamma\sum_{j<j'} J_{jj'}\hat{\sigma}_x^{(j)}\hat{\sigma}_x^{(j')}} |0\rangle \tag{7.13}$$

$$\approx \mathrm{e}^{\mathrm{i}\sum_j \frac{\phi_j}{2}} \Big(|0\rangle - \mathrm{i}\gamma J \sum_j e^{-\mathrm{i}(\phi_j+\phi_{j+1})} |\ldots\uparrow_j\uparrow_{j+1}\ldots\rangle \Big) + \mathcal{O}(\gamma^2). \tag{7.14}$$

In the second line, the two-magnon states have phase $\phi_j + \phi_{j+1}$. The sum of two phases shows up as both ion j and ion $j+1$ of the pair are addressed. In the experiment, the pairs are imprinted with a phase $\phi_j + \phi_{j+1} = jk$ for a given momentum k.

The initial state is evolved under the long-range, anisotropic Heisenberg Hamiltonian. After the time evolution the expectation value of $\hat{\sigma}_-^{(j)}\hat{\sigma}_-^{(j+1)}$ is measured. The lowering operators map the two-magnon state back to the ground state. This allows one to compare the energy of the two-magnon state $\epsilon_2(k)$ with the energy of the ground state ϵ_0. The spectroscopic signal of the two-magnon state is

$$\langle\psi_2(t)|\,\hat{\sigma}_j^-\hat{\sigma}_{j+1}^-\,|\psi_2(t)\rangle = -\mathrm{i}\gamma\Gamma J \mathrm{e}^{-\mathrm{i}jk}\mathrm{e}^{-\mathrm{i}[\varepsilon_2(k)-\varepsilon_0]t} + \mathcal{O}(\gamma^2), \tag{7.15}$$

where the probability amplitude Γ takes the measurement contrast into account. The energy difference $\epsilon_2(k) - \epsilon_0$ between the two-magnon state and the ground state gives rise to the temporal evolution. The operator $\hat{\sigma}_-^{(j)}\hat{\sigma}_-^{(j+1)}$ is obtained from performing measurements of $\hat{\sigma}_x^{(j)}\hat{\sigma}_x^{(j+1)}$, $\hat{\sigma}_y^{(j)}\hat{\sigma}_y^{(j+1)}$, $\hat{\sigma}_x^{(j)}\hat{\sigma}_y^{(j+1)}$, and $\hat{\sigma}_y^{(j)}\hat{\sigma}_x^{(j+1)}$ by making use of the relation $\hat{\sigma}_-^{(j)} = (\hat{\sigma}_x^{(j)} - \mathrm{i}\hat{\sigma}_y^{(j)})/2$.

The dispersion relation is obtained from a Fourier transform of the mean spectroscopic signal. The spatial modulation $\mathrm{e}^{-\mathrm{i}jk}$ is taken into account before averaging. In order to avoid finite-size effects from the edges of the ion crystal, the analysis is carried out for the central ions 8 to 13. The resulting two-magnon dispersion relation is shown in Figure 7.4(b). In contrast to the one-magnon dispersion relation, the dispersion relation exhibits a clear peak only in one part of the Brillouin zone. For low momenta, the signal becomes broadened. A broad signal indicates unstable bound states, which is depicted by the grayed-out area in the theory plot (inset). In this region, a single bound state can redistribute its energy into two separate magnons. Another feature of the dispersion relation is that the group velocity always stays finite. This has implications for the dynamics of a bound state, as discussed in the next Section.

7.5 DYNAMICS OF MAGNON BOUND STATES

The bound state of the long-range anisotropic Heisenberg model has a finite group velocity in the whole stable region [Fig. 7.4(b)]. This should lead to a

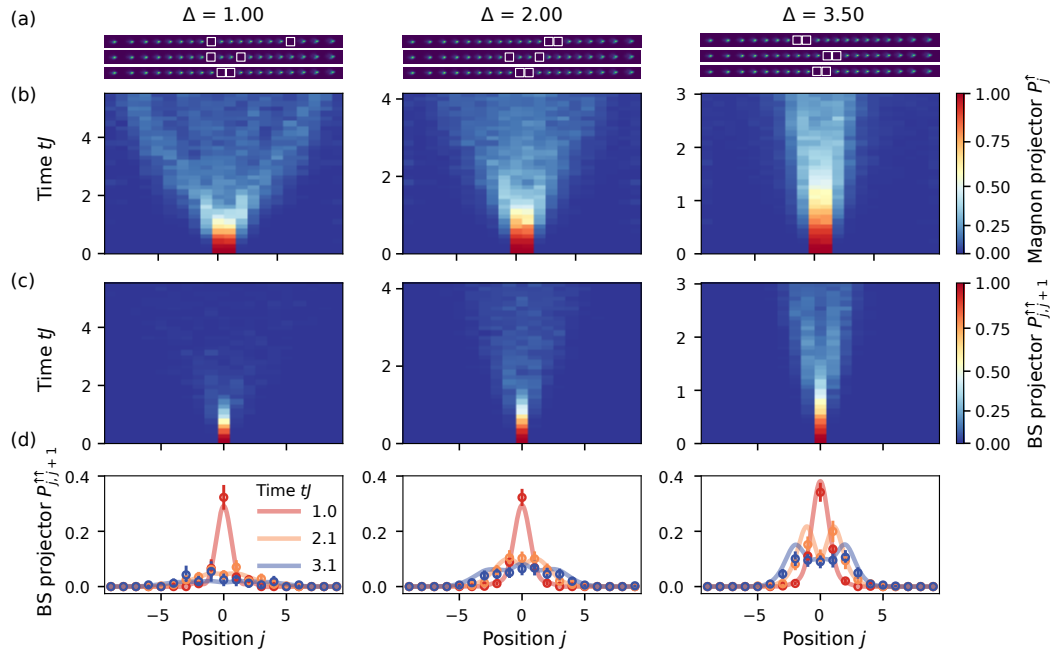

Figure 7.5: Dynamics of magnon bound states under the anisotropic Heisenberg model. The evolution was measured for different values of the anisotropy Δ, i.e. different interaction strengths. (a) Snapshots of the ion crystal at different times of the evolution $t = (0, \frac{1}{2}, 1) \times t_{\max}$. For low anisotropy, the magnons (white boxes) appear separately, whereas for large anisotropy the magnons typically group at neighboring sites. (b) With increasing interactions, the spread of the one-magnon projector $P_j^{\uparrow}$ slows down. (c) The bound-state projector $P_{j,j+1}^{\uparrow\uparrow}$ decays quickly for weak interactions. With increasing interactions, the bound-state projector starts to spread within a light cone. (d) Spatial cuts of the bound-state projector. The experimental points are in good agreement with theoretical calculations (lines).

quench dynamics of a two-magnon state that is characterized by a propagation inside a light cone. This prediction is tested in the experiment. A crystal of 20 ions is prepared in the ground state $|\downarrow \ldots \downarrow\rangle$. Then, the central two spins are flipped, creating the initial state $|\downarrow \ldots \downarrow\uparrow\uparrow\downarrow \ldots \downarrow\rangle$. The system is time-evolved under the Trotter-approximated long-range anisotropic Heisenberg model (7.1). After an evolution time t, the single-qubit magnetizations $\langle \sigma_j^z \rangle$ are measured.

The experimental results of the quench dynamics are shown in Figure 7.5. The evolution is shown for different values of the interaction strength $\Delta = 1$ (left), $\Delta = 2$ (middle), and $\Delta = 3.5$ (right). The different behavior of magnons is illustrated by snapshots of the ion crystal during the evolution [7.5(a)]. For small interactions, the magnons appear separated over the crystal. When the interactions are increased, the magnons start to group at neighboring sites. The formation of bound states is quantified with the one-magnon and the two-magnon projector. The spread of the one-magnon projector $P_j^{\uparrow}$ gives the probability of finding a magnon at site j and slows down with increasing interactions [Fig. 7.5(b)]. The two-magnon projector $P_{j,j+1}^{\uparrow\uparrow}$ gives the probability of finding two magnons at neighboring sites j and $j+1$. On the one hand, for weak interactions no bound

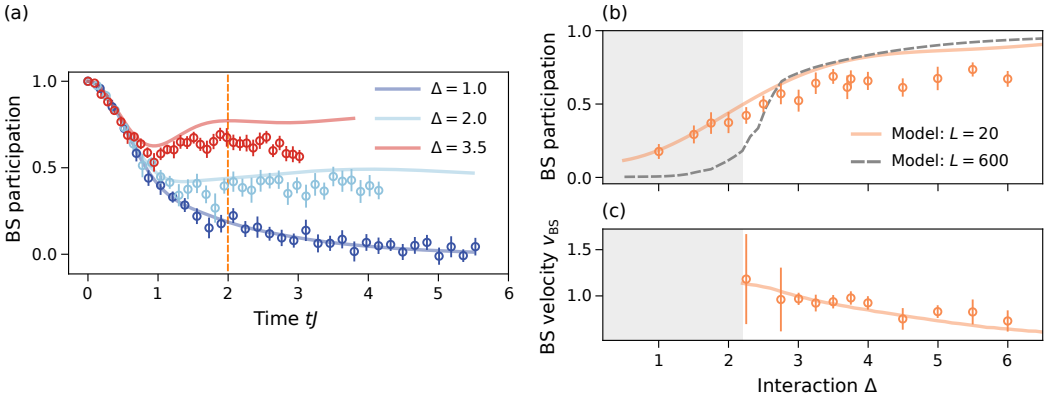

Figure 7.6: Bound states for different interaction strengths. (a) The bound-state (BS) participation (7.16) decays quickly with time for weak interaction $\Delta = 1$, as no bound states are formed. For strong interactions, the BS participation remains high during time evolution, indicating the formation of bound states. Points are experimental data and lines are theory calculations. (b) At time $tJ = 2$ [dashed line in (a)], a transition from a regime of weak interactions with no bound states to a regime of strong interactions that leads to bound states can be observed. For large system sizes $L \to \infty$ the bound states become unstable below $\Delta \approx 2.2$ (grey region). (c) The bound state velocity decreases with increasing interaction strength. The experimental data is formed from approx. 1000 repetitions and post-selected for magnetization-conserving two-magnon data, retaining 22% of the repetitions (latest time). Error bars are obtained from bootstrapping.

state is formed and the two-magnon projector decays quickly. On the other hand, for strong interactions two magnons form a bound state and the observed two-magnon projector remains large. Furthermore, the spatial spread of the bound state is contained within a light cone [Fig. 7.5(c)]. For each experimental data point approximately 1500 repetitions were taken. The data is post-processed to keep only the repetitions that conserved the number of magnons, keeping 20-25% of the data. The error bars are obtained from bootstrapping.

The formation of bound states was analyzed for a large range of interaction strengths. The formation of bound states was quantified by the bound-state participation ratio. This quantity measures the probability of finding two neighboring magnons in the system while correcting for the probability of randomly finding two single magnons next to each other. When two single magnons are placed in a system of L sites there is a probability of $\frac{2}{L}$ of finding the magnons at neighboring sites.[3] The bound-state participation (BS) ratio is

$$\text{BS participation} = \frac{1}{1-\frac{2}{L}} \sum_{j=1}^{L-1} \left(\langle P^{\uparrow\uparrow}_{j,j+1}(t) \rangle - \frac{2}{L} \right). \tag{7.16}$$

The measured BS participation ratio is shown in Figure 7.6. For weak interactions, the BS participation decays fast during the time evolution, indicating the absence

3 Total number of configurations of placing two magnons $= L(L-1)$. Number of configurations with neighboring sites $= 2(L-1)$.

of bound states [Fig. 7.6(a)]. In contrast, for strong interactions bound states are formed and the BS participation remains at a high level during the entire evolution. This behavior is well described by theoretical calculations (lines). The transition from a regime without bound states to a regime where bound states are formed can be observed by analyzing the BS participation at a fixed time (vertical dashed line). The BS participation is plotted against the interaction strength [Fig. 7.6(b)]. Around $\Delta \approx 2.2$, bound states start to form. Due to the finite size of the system, the transition occurs gradually. A numerical simulation for a large system size (dashed line) shows a steeper transition. The velocity of the bound state is extracted from the propagation front of the light-cone [Fig. 7.6(c)]. With increasing interaction strength, the BS velocity decreases.

7.6 DYNAMICS OF MUTUAL INFORMATION

Bound states have an impact on the spread of entanglement in a system. Consider a subsystem with two strongly interacting quasiparticles. On the one hand, if the quasiparticles are situated next to each other the entanglement grows slowly, as the bound state restricts the movement of the magnons. On the other hand, if there is a gap between the quasiparticles the magnons are mostly free to move and the entropy grows faster. This behavior can be studied by measuring a proxy of the entanglement between subregions.

The entanglement between two separated subregions A and B of a larger system can be quantified by the mutual information $I = S_A + S_B - S_{A\cup B}$, where S_A is the von Neumann entanglement entropy between the interval A and the rest of the system $\bar{A}$. For large systems it is time expensive to measure the entanglement entropy directly by quantum state tomography or by randomized measurements. However, for systems that conserve the number of excitations and for short times and small correlations it is possible to use the mutual configurational entropy between A and $\bar{A}$ as an approximation for the mutual information. The mutual configurational entropy is [131, 132]

$$S_{C;A} \simeq \sum_n p(n) \sum_{\{A_n\},\{\bar{A}_n\}} \left[p(A_n \otimes \bar{A}_n) - p(A_n)p(\bar{A}_n)\right], \tag{7.17}$$

where the summation takes place over all the possible magnon configurations $\{A_n\}$ and $\{\bar{A}_n\}$ in the local basis of the subsystems A and $\bar{A}$, $p(n)$ is the probability of having n magnons in the subsystem, and $p(A_n)$ is the probability of finding configuration A_n. The mutual configurational entropy is a proxy for the mutual information I_c.

In the experiment, two configurations for placing two magnons were tested. In one case, the two magnons were placed directly next to each other at the beginning of the experiment [Fig. 7.7(a)]. In the other case, the two magnons were separated by one site [Fig. 7.7(b)]. The initial configuration was evolved under the long-range anisotropic Heisenberg Hamiltonian. At the end of the evolution the system was measured in the z basis and post-selected for magnetization-conserving data, retaining approximately 19% of the data. The growth of mutual information was measured both for weak interactions and for strong interactions.

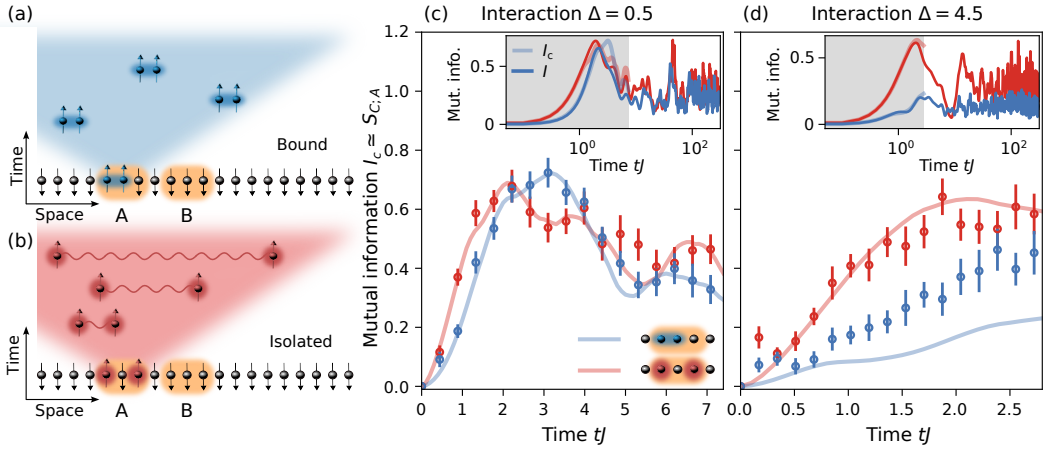

Figure 7.7: Entanglement growth for magnons. The growth of entanglement is quantified by the mutual information (7.17) and measured for two different initial configurations. (a) Initial configuration with two magnons placed next to each other and (b) initial configuration where the two magnons are separated by one site. (c) For weak interaction strength, the mutual information dynamics is similar for both configurations. The mutual information is approximated by the mutual configurational entropy (7.17). (d) For strong interactions, the neighboring configuration leads to the formation of bound states, hindering the growth of entanglement. Points are experimental data, lines theory curves. The insets show numerical simulations up to long times, with the gray region indicating the experimentally accessible times. The error bars were obtained from jackknife analysis.

In the case of weak interactions [Fig. 7.7(c)], bound states cannot form and the mutual information grows with similar speed for both magnon configurations. This changes when increasing the interaction strength. In the case of strong interactions [Fig. 7.7(d)], the two configurations show different dynamics. When the magnons are placed next to each other, a bound state forms which hinders the growth of entanglement. Numerical simulations confirm that the evolution of the mutual information at early times is representative of the late time state [insets in Fig. 7.7(c) and (d)].

7.7 SUMMARY AND CONCLUSION

In this work, the formation of bound states of quasiparticles was observed in the long-range, anisotropic Heisenberg model. The anisotropy of the model gives rise to interactions between quasiparticles, the magnons. Depending on the strength of interaction the bound states were observed to either be stable or become unstable. In the experiment, the long-range, anisotropic Heisenberg model was engineered by Trotter approximation. When designing the Trotter sequence care was taken to reduce the impact of dephasing errors and rotation errors by incorporation of dynamical decoupling pulses and rotations of alternating direction.

A number of properties of bound states were observed in the experiment: First, the dispersion relation was measured for single-magnon and for two-magnon

states. For the two-magnon case, the dispersion relation was observed to become broadened at low momenta indicating unstable bound states. Second, the dynamics of magnon bound states was measured in a quench dynamics. Measurements at different interaction strengths revealed a transition from unstable to stable bound states. Third, the impact of bound states on the growth of entanglement was studied. Measurement of mutual information between two subsystems — one of which contains two magnons — revealed a hindered growth of entanglement in the presence of magnon bound states.

The measurements faced a number of challenges: The bound-state formation required long-range interactions that decay fast enough with distance. In particular, a power-law exponent $\alpha \approx 1.4$ was required. Setting such a high value comes with the downside of low spin-spin coupling rates and weak axial confinement of the ion crystal. The low coupling rates lengthened the experiment, making it more prone to decoherence. The weak axial confinement increased axial heating rates and drifts of the crystal position. For the present work, this problem could be overcome by fine-tuning the detuning of the entangling light fields and the axial confinement. However, such an approach is hardly scalable to larger system sizes. One possible solution would be to increase the ratio of spin-spin coupling strength to dephasing rate, i.e. increase the power of the entangling light or increase the coherence time. An increase in light power is the objective of the new 729 nm laser that is being set up at the time of the writing of this thesis.

Approximating the Hamiltonian by a Trotter sequence leads to errors in the interactions. The leading sources of error are of technical nature. First, the entanglement beam creates inhomogeneous coupling. The entanglement beam has an inhomogeneous intensity profile, leading to systematic rotation errors over the ion crystal. While this kind of error was reduced by the use of alternating rotations, the outermost ions still were significantly affected. If the system size should be increased in the future, the entanglement beam needs to be enlarged, which comes at the expense of light intensity. Second, the switching of light pulses during the Trotter sequence broadens the light spectrum, as discussed in Sec. 4.2.4. This problem is harder to overcome, as large ion crystals have a densely packed motional mode spectrum that can overlap with spectral components. A possible solution could be pulse shaping to a sinusoidal profile to reduce the spectral broadening to a single frequency.

8

SUMMARY AND OUTLOOK

In recent years, much work has been spent on scaling quantum simulation experiments to larger and larger number of qubits. Our experiment is now capable of performing experiments with up to approximately 50 ions. The work presented in this thesis investigates an additional option of enhancing the capabilities of quantum simulators: Making new Hamiltonians available by Trotter approximation. The two main results of this thesis are on quantum simulations of the Heisenberg model. The first experiment studied thermalization under conditions given by the Heisenberg Hamiltonian. The second experiment observed properties of bound states in an anisotropic Heisenberg model.

Chapter 2 gave a brief overview over the theoretical concepts used in this thesis. Chapter 3 presented the experimental setup and a characterization of properties of long crystals of trapped ions of up to 50 ions. It was found that the axial heating rate of our current trap has a rather high value of 4000 phonons/(s · ion) at 130 kHz axial trapping frequency. Such a high heating rate poses a problem when working with ion crystals, as the fidelity of individual-ion addressing operations decreases for hot ions. This problem should be fixed with the next generation of trap that is to be installed at a time after completion of this thesis. Tilted wavefronts of the radial global beam were identified as one source of error which becomes noticeable for axially weakly confined long ion crystals. Implementation of a new beam shaping optics that delivers plane and parallel wavefronts eliminated this error. Lastly, correlation spectroscopy was demonstrated to be a useful tool for measuring phase differences between ions in large ion crystals. This method was applied to measure ion distances with an accuracy of only a few nanometers.

Chapter 4 gave an overview over the concept of Trotter approximation of Hamiltonians. Technical details on the Trotter approximation were given in the second part of the chapter. While in theory a Trotter approximation is straightforward, in an experiment caution is required to avoid errors from a number of sources: Base rotations introduce undesired ac-Stark shifts if the light power is too high. Light gets spectrally broadened when light pulses are of short, finite duration, which can give rise to unwanted coupling to motional modes. Decoherence is caused by magnetic-field fluctuations and laser noise. These errors can be reduced to some extent by careful adjustment of the experimental parameters. A quench under the Heisenberg Hamiltonian was demonstrated for a crystal of up to 21 ions.

Chapter 5 introduced the technique of motional spin-locking spectroscopy for directly measuring the motional noise spectrum of a quantum harmonic oscillator. To this end, spin-locking spectroscopy is applied to the blue sideband transition, revealing phase noise on the harmonic oscillator. Key to efficiently utilizing this technique is the preparation of a coherent motional state. A coherent motional state increases the coupling strength and makes the technique insensitive to changes in the phonon number, as caused by motional heating. The motional noise spectrum was measured in a range from 200 Hz to 5 kHz, while being able to resolve the noise spectral density over two orders of magnitude.

Chapter 6 reported on the experimental observation of the thermalization within a closed quantum system under noncommuting charges. The question was to what thermal state a quantum system would thermalize if a system has multiple conserved charges connected to operators that do not commute with each other. It was conjectured theoretically that such a system should still thermalize to a state of the form of a Gibbs ensemble, which is referred to as non-Abelian thermal state in this context. By implementing the Heisenberg model in a crystal of up to 21 ions with a Trotter approximation, we were able to show that the experimentally observed state is of the predicted form.

Chapter 7 presented an observation of bound states in the long-range, anisotropic Heisenberg model. So far, the formation of bound states has been studied for short-range systems. However, the long-range nature of interactions between spins qualitatively alters the properties of quasiparticles, the magnons. Specifically, the group velocity of a single magnon can diverge. From this background it was unclear, whether bound states can form between two magnons, despite a diverging group velocity. Motivated by theoretical predictions, we were able to experimentally demonstrate the formation of two-magnon bound states in the long-range case. To enable this observation, the anisotropic Heisenberg model was implemented by a Trotter approximation. The anisotropy determined the interaction strength between the magnons. Depending on the interaction strength, the magnons were observed to propagate with different velocity. The dispersion relation was measured for a two-magnon bound state, revealing an unstable bound state for low momenta in the Brillouin zone. Finally, the growth of entanglement between two magnons was quantified by measuring the mutual information. A bound state between two magnons was found to hinder the growth of entanglement.

These two experiments demonstrated the feasibility of approximating the Heisenberg model in large systems of trapped ions with Trotter sequences. At the same time, the Trotter sequences were designed in a way to exhibit some degree of robustness against dephasing and rotation errors. One leading type of error was found to be caused by coupling of spectrally broadened light to the radial motional modes of the ion crystal. This error could be reduced by pulse shaping and careful adjustment of the pulse timing to reduce spectral overlap. However, such an approach is hardly feasible when scaling to larger number of ions, as the number of motional modes increases with the number of ions. A possible solution could be to use pulse shaping to realize a sinusoidal modulation of the

light intensity. While this reduces the average light power, the resulting spectrum only has two narrow sidebands that can be placed between motional modes.

In the near future, our experiment will undergo a major upgrade. The ion trap, the vacuum chamber, and the experiment control system will be replaced by new versions. This upgrade should allow us to work with up to 100 ions. The ion trap is provided by *Alpine Quantum Technologies* and should feature lower axial heating rates than our current trap. The vacuum chamber will contain a target for ablation loading, reducing the time to reload ions. The quantization axis will be newly aligned with respect to the laser fields, allowing to drive a $\Delta m = 0$ transition which is less sensitive to magnetic field fluctuations than the currently used $\Delta m = 2$ transition. Furthermore, the experiment control system for control of the laser pulses will be replaced with the "Sinara" system developed by *M-LABS*. This will increase the number of laser pulses that we can apply to our ions, which is currently limited to less than 200 pulses. In particular for Trotter sequences, a larger number of operations will be of great use.

A

COUPLING TO AXIAL MODES DUE TO TILTED WAVEFRONTS

A trapped ion is manipulated with a radial beam. The wavefronts of the radial beam are tilted, such that the wave vector has an overlap with the axial trapping direction. In this case, an axial ion motion will affect the outcome of experiments performed with the radial beam. This section gives a derivation of the result of a Ramsey experiment under tilted wavefronts. The case of a CPMG experiment is treated in the Appendix of Ref. [62].

A.1 RAMSEY EXPERIMENT WITH SIMPLE PULSES

The motion of a trapped ion is approximated by the classical trajectory

$$\boldsymbol{r}(t) = a\hat{\mathbf{z}}\sin(\omega_z t), \tag{A.1}$$

where a is the oscillation amplitude, $\hat{\mathbf{z}}$ is the unit vector pointing along the z axis, ω_z the frequency, and t is the time. If the light field that interacts with the ion is tilted, the light's $\boldsymbol{k}$ vector has a nonzero overlap with the z axis and the light phase is changing with time,

$$\phi(t) = \boldsymbol{k}\cdot\boldsymbol{r}(t) = k_z a\sin(\omega_z t). \tag{A.2}$$

In this case, the outcome of a Ramsey experiment depends on the timing of the pulses.

The pulse sequence of a Ramsey experiment that uses simple $\pi/2$ pulses is sketched in Fig. A.1(a). The action of a $\pi/2$ pulse with phase ϕ is described by

$$U_\phi\left(\frac{\pi}{2}\right) = \frac{1}{\sqrt{2}}\begin{pmatrix} 1 & -\mathrm{i}\mathrm{e}^{-\mathrm{i}\phi} \\ -\mathrm{i}\mathrm{e}^{\mathrm{i}\phi} & 1 \end{pmatrix}. \tag{A.3}$$

The duration of the $\pi/2$ pulse is assumed to be negligible. Consider a Ramsey experiment that ideally applies the first pulse with phase $\frac{\pi}{2}$ and the second pulse with phase $\frac{\pi}{2}+\pi$. Let ϕ_1 and ϕ_2 denote the deviation from these ideal phases. Then, the Ramsey sequence is described by the matrix

$$U = U_{\frac{\pi}{2}+\pi+\phi_2}U_{\frac{\pi}{2}+\phi_1}. \tag{A.4}$$

If the qubit is initially in $|\downarrow\rangle$, the probability of finding the qubit in the final state $|\uparrow\rangle$ is given by a single matrix element and evaluates to

$$p_\uparrow = |\langle\uparrow|U|\downarrow\rangle|^2 \tag{A.5}$$

$$= \frac{1}{2}\left[1-\cos\left(\phi_2-\phi_1\right)\right] \approx \frac{1}{4}(\phi_2-\phi_1)^2. \tag{A.6}$$

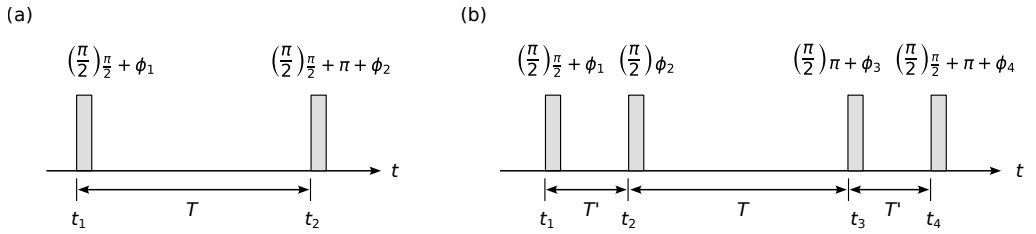

Figure A.1: Ramsey experiment under phase variations. The phase deviations $\phi_1, \ldots, \phi_4$ depend on the timing of the pulses $t_1, \ldots, t_4$. (a) Ramsey experiment with simple $\pi/2$ pulses. (b) Ramsey experiment with composite $\pi/2$ pulses.

In the last step it was assumed that the phase deviation is small, $|\phi_2 - \phi_1| \ll 1$.

The change in the light phase at the beginning of the pulses is

$$\phi_1(t_1) = k_z a \sin(\omega_z t_1) \tag{A.7}$$
$$\phi_2(t_2) = k_z a \sin(\omega_z t_2) = k_z a \sin(\omega_z (t_1 + T)). \tag{A.8}$$

These phases give the deviation from the light phase that is ideally set in the Ramsey experiment. The ion motion is not controlled. Thus, the measured excitation e is the average over all initial times t_1,

$$e = \langle p_\uparrow \rangle_{t_1} \approx \left\langle \frac{1}{4}[\phi_2(t_1 + T) - \phi_1(t_1)]^2 \right\rangle_{t_1} \tag{A.9}$$
$$= \frac{1}{2}(k_z a)^2 \sin^2\left(\frac{1}{2}\omega_z T\right) \tag{A.10}$$

A.2 RAMSEY EXPERIMENT WITH COMPOSITE PULSES

The pulse sequence of a Ramsey experiment that uses composite $\pi/2$ pulses is sketched in Fig. A.1(b). Analogous to the previous case, the Ramsey experiment is described by

$$U = U_{\frac{\pi}{2}+\pi+\phi_4} U_{\pi+\phi_3} U_{\phi_2} U_{\frac{\pi}{2}+\phi_1}. \tag{A.11}$$

The probability of transferring the qubit from $|\downarrow\rangle$ to the final state $|\uparrow\rangle$ is approximated by

$$p_\uparrow = |\langle\uparrow|U|\downarrow\rangle|^2 \tag{A.12}$$
$$\approx \frac{1}{4}[(\phi_3 - \phi_2)^2 + (\phi_1 - \phi_2 + \phi_3 - \phi_4)^2]. \tag{A.13}$$

The change in the light phase at the beginning of the pulses is

$$\phi_1(t_1) = k_z a \sin(\omega_z t_1) \tag{A.14}$$
$$\phi_2(t_2) = k_z a \sin\big(\omega_z (t_1 + T')\big) \tag{A.15}$$
$$\phi_3(t_3) = k_z a \sin\big(\omega_z (t_1 + T' + T)\big) \tag{A.16}$$
$$\phi_4(t_4) = k_z a \sin\big(\omega_z (t_1 + 2T' + T)\big). \tag{A.17}$$

Averaging over the initial time t_1 yields after a lengthy but simple calculation

$$e = \langle p_\uparrow \rangle_{t_1} \approx \left\langle \frac{1}{4}[(\phi_3 - \phi_2)^2 + (\phi_1 - \phi_2 + \phi_3 - \phi_4)^2] \right\rangle_{t_1} \tag{A.18}$$

$$= \frac{1}{2}(k_z a)^2 \left[\sin^2\left(\frac{1}{2}\omega_z T\right) + 4\cos^2\left(\frac{1}{2}\omega_z (T + T')\right) \sin^2\left(\frac{1}{2}\omega_z T'\right) \right]. \tag{A.19}$$

B

SPIN-LOCKING SPECTROSCOPY

B.1 STOCHASTIC LIOUVILLE EQUATIONS

Solving the time evolution of quantum systems that are governed by stochastic Hamiltonians is a difficult task. The random nature of the Hamiltonian only allows one to make predictions about average values of the solution. The concept of stochastic Liouville equations makes it possible to express the average time-evolved state in a simple form. The following short introduction into stochastic Liouville equations is based on Refs. [94, 95].

Let a quantum system be described by the von Neumann equation

$$\frac{\mathrm{d}}{\mathrm{d}t}\rho(t) = -\frac{\mathrm{i}}{\hbar}\left[H(t), \rho(t)\right], \tag{B.1}$$

where the Hamiltonian $H(t)$ is regarded as a stochastic process. The von Neumann equation can be written in the form of the Liouville equation

$$\frac{\mathrm{d}}{\mathrm{d}t}\hat{\rho}(t) = L(t)\hat{\rho}(t). \tag{B.2}$$

where $\hat{\rho} = (\rho_{1,1}, \rho_{1,2}, \rho_{2,1}, \rho_{2,2})^{\mathrm{T}}$ is the state vector that is obtained from stacking the elements of the density matrix ρ, and

$$L = \frac{1}{\mathrm{i}\hbar}(H \otimes \mathbb{1} - \mathbb{1} \otimes H^{\mathrm{T}}), \tag{B.3}$$

is the Liouville operator.

In general, L will not commute with itself at different times, $[L(t_1), L(t_2)] \neq 0$. Therefore, the solution of the differential equation requires the time-ordered exponential $\exp_{\mathrm{O}}[\cdot]$,

$$\hat{\rho}(t) = \exp_{\mathrm{O}}\left[\int_0^t \mathrm{d}t' L(t')\right]\hat{\rho}(0) = \tag{B.4}$$

$$= \Big[1 + \int_0^t \mathrm{d}t_1 L(t_1) + \int_0^t \mathrm{d}t_1 \int_0^{t_1} \mathrm{d}t_2 L(t_1)L(t_2) + \dots \tag{B.5}$$

$$+ \int_0^t \mathrm{d}t_1 \int_0^{t_1} \mathrm{d}t_2 \cdots \int_0^{t_{n-1}} \mathrm{d}t_n L(t_1)L(t_2)\cdots L(t_n) + \dots\Big]\hat{\rho}(0). \tag{B.6}$$

The expected value of this solution can be expressed by introducing the decay function $\Phi(t)$,

$$\langle\hat{\rho}(t)\rangle = \left\langle \exp_{\mathrm{O}}\left[\int_0^t \mathrm{d}t' L(t')\right]\right\rangle \hat{\rho}(0) \equiv \Phi(t)\hat{\rho}(0), \tag{B.7}$$

where $\langle\cdot\rangle$ denotes the ensemble average. The task is to determine the decay function Φ.

The first thought might be to approximate $\Phi(t)$ by the first elements of the series expansion of the time-ordered exponential,

$$\Phi(t) = 1 + \int_0^t \mathrm{d}t_1 \langle L(t_1)\rangle + \int_0^t \mathrm{d}t_1 \int_0^{t_1} \mathrm{d}t_2 \langle L(t_1)L(t_2)\rangle + \dots. \tag{B.8}$$

The problem with this approach is that the higher-order moments $\langle L(t_1)\cdots L(t_n)\rangle^n$ do not vanish fast and therefore, the first few orders give a poor approximation for long times. The idea is to approximate the time evolution with a cumulant expansion. The cumulants are constructed in such a way that they vanish quickly if the correlation time is short.

The cumulant expansion is obtained by noting that the decay function Φ is itself again described by a differential equation [94],

$$\frac{\mathrm{d}}{\mathrm{d}t}\Phi(t) = F(t)\Phi(t). \tag{B.9}$$

Again, the solution is written formally by using the time-ordered exponential,

$$\Phi(t) = \exp_{\mathrm{O}}\left[\int_0^t \mathrm{d}t' F(t')\right]. \tag{B.10}$$

Next, F is expanded in powers of an expansion parameter α,

$$F = \sum_{n=1}^{\infty} \alpha^n F_n. \tag{B.11}$$

This ansatz is plugged into the series expansion of the time-ordered exponential,

$$\Phi(t) = 1 + \int_0^t \mathrm{d}t_1 \left[\alpha F_1(t_1) + \alpha^2 F_2(t_1) + \dots\right] + \tag{B.12}$$

$$+ \int_0^t \mathrm{d}t_1 \int_0^{t_1} \mathrm{d}t_2 \left[\alpha F_1(t_1) + \alpha^2 F_2(t_1) + \dots\right]\left[\alpha F_1(t_2) + \alpha^2 F_2(t_2) + \dots\right] + \dots \tag{B.13}$$

$$= 1 + \alpha\left\{\int_0^t \mathrm{d}t_1 F_1(t_1)\right\} + \tag{B.14}$$

$$\alpha^2\left\{\int_0^t \mathrm{d}t_1 F_2(t_1) + \int_0^t \mathrm{d}t_1 \int_0^{t_1} \mathrm{d}t_2 F_1(t_1)F_1(t_2)\right\} + \mathcal{O}(\alpha^3). \tag{B.15}$$

When the same expansion parameter α is used in Eq. (B.8), we get

$$\Phi(t) = 1 + \alpha\int_0^t \mathrm{d}t_1 \langle L(t_1)\rangle + \alpha^2 \int_0^t \mathrm{d}t_1 \int_0^{t_1} \mathrm{d}t_2 \langle L(t_1)L(t_2)\rangle + \mathcal{O}(\alpha^3). \tag{B.16}$$

Comparing the powers of α defines the functions F_m recursively,

$$\langle L(t_1)\rangle = F_1(t_1) \tag{B.17}$$

$$\int_0^{t_1} \mathrm{d}t_2 \langle L(t_1)L(t_2)\rangle = F_2(t_1) + \int_0^{t_1} \mathrm{d}t_2 F_1(t_1)F_1(t_2) \tag{B.18}$$

$$\vdots \tag{B.19}$$

The higher orders have increasingly complex expressions. The first two orders of F_n are

$$F_1(t) = \langle L(t) \rangle \tag{B.20}$$

$$F_2(t) = \int_0^t \mathrm{d}t_1 \left[\langle L(t)L(t_1) \rangle - \langle L(t) \rangle \langle L(t_1) \rangle \right] \tag{B.21}$$

$$\vdots \tag{B.22}$$

With these functions the differential equation of the decay function can be approximated,

$$\frac{\mathrm{d}}{\mathrm{d}t}\Phi(t) = F(t)\Phi(t) \approx \left[\langle L(t) \rangle + \int_0^t \mathrm{d}t_1 \left(\langle L(t)L(t_1) \rangle - \langle L(t) \rangle \langle L(t_1) \rangle \right) \right] \Phi(t). \tag{B.23}$$

However, in practice this expression might be of limited use as $F(t)$ depends again on time and the differential equation cannot easily be solved. At least, this equation gives a deterministic (i.e. non-stochastic) equation for the expectation value $\langle \hat{\rho}(t) \rangle$ which can be solved numerically.

If one wants to obtain an expression for $\langle \hat{\rho}(t) \rangle$, then this can be done for zero-mean noise in second order. As the mean vanishes by assumption, $\langle L(t) \rangle = 0$, the time-ordered exponential (B.10) is approximated in second order F_2 as

$$\Phi(t) \approx \exp_{\mathrm{O}} \left[\int_0^t \mathrm{d}t_1 \int_0^{t_1} \mathrm{d}t_2 \, \langle L(t_1)L(t_2) \rangle \right] \tag{B.24}$$

$$\approx \exp \left[\int_0^t \mathrm{d}t_1 \int_0^{t_1} \mathrm{d}t_2 \, \langle L(t_1)L(t_2) \rangle \right]. \tag{B.25}$$

In the second step, the time-ordered exponential is approximated by the ordinary exponential. This is possible because the two series expansions match up to first order, which is enough in the present case.

B.2 SPIN-LOCKING

B.2.1 *Spin-locking under coherent modulation*

We consider a coherent phase modulation of the light driving the spin-locking sequence. The phase between light and qubit is phase modulated at a modulation frequency ω and with a modulation index β,

$$\phi(t) = \beta \cos(\omega t + \delta), \tag{B.26}$$

where δ is the modulation phase offset. In the following, we assume the modulation index to be small, $|\beta| \ll 1$. Then, the evolution of the qubit is described in the interaction picture by the Hamiltonian (5.19) which takes the form

$$H = \hbar\Omega^{(1)} \cos(\omega t + \delta) \left[\cos(\Omega t)\sigma_y - \sin(\Omega t)\sigma_z \right] \tag{B.27}$$

$$\approx \hbar \frac{\Omega^{(1)}}{2} \left\{ \cos[(\omega - \Omega)t + \delta]\sigma_y + \sin[(\omega - \Omega)t + \delta]\sigma_z \right\}, \tag{B.28}$$

where $\Omega^{(1)} = \frac{1}{2}\beta\Omega$ is the Rabi frequency of the 1st order modulation sideband. In the second step, we have applied a rotating-wave approximation, neglecting terms oscillating at $\Omega + \omega$.

When the Rabi frequency is made resonant with the modulation frequency, $\Omega = \omega$, this leads to the Hamiltonian of a coherent, small phase modulation at resonance,

$$H = \hbar\frac{\Omega^{(1)}}{2}[\cos(\delta)\sigma_y + \sin(\delta)\sigma_z]. \tag{B.29}$$

This time-independent Hamiltonian has the time-evolution operator

$$U(t) = \cos\left(\frac{\Omega^{(1)}t}{2}\right)\mathbb{1} - \mathrm{i}\sin\left(\frac{\Omega^{(1)}t}{2}\right)\left[\cos(\delta)\sigma_y + \sin(\delta)\sigma_z\right] \tag{B.30}$$

and leads to the evolution of magnetization

$$\langle x(t)\rangle = \cos\left(\Omega^{(1)}t\right), \tag{B.31}$$
$$\langle y(t)\rangle = \sin\left(\Omega^{(1)}t\right)\sin\left(\Omega t + \delta\right), \tag{B.32}$$
$$\langle z(t)\rangle = -\sin\left(\Omega^{(1)}t\right)\cos\left(\Omega t + \delta\right). \tag{B.33}$$

An example of the evolution under coherent phase modulation is shown in Fig. B.1. We carried out a spin-locking experiment on the carrier transition of a ground-state cooled ion. The light that was driving the spin-locking sequence was phase modulated at $\omega = 2\pi \times 5\,\mathrm{kHz}$ at a modulation index of $\beta = 200\,\mathrm{mrad}$. The modulation frequency of $\omega = 2\pi \times 5\,\mathrm{kHz}$ was chosen as our laser has negligible frequency noise around this frequency. The observed evolution of magnetization is described well by equations (B.31)-(B.33). The magnetization $\langle x(t)\rangle$ oscillates at a frequency $\Omega^{(1)}t$. In the experiment, the phase relation δ between modulation signal and light is kept constant but its value is unknown. Therefore, we obtained $\delta = 1.48(2)\,\mathrm{rad}$ from a least-squares fit to the experimental data.

B.2.2 *Spin-locking under non-zero mean noise*

In the case where both a coherent modulation and noise is present,

$$\phi(t) = \phi_\mathrm{c}(t) + \phi_\mathrm{n}(t) = \beta\sin(\omega_m t + \delta) + \phi_\mathrm{n}(t), \tag{B.34}$$

the Hamiltonian is a sum of a deterministic part H_0 and a stochastic part H_1,

$$H(t) = H_0 + H_1(t) \tag{B.35}$$
$$= \hbar\frac{\Omega^{(1)}}{2}[\cos(\delta)\sigma_y + \sin(\delta)\sigma_z] \tag{B.36}$$
$$+ \hbar\frac{\Omega}{2}\phi(t)\left[\cos(\Omega t)\sigma_y - \sin(\Omega t)\sigma_z\right]. \tag{B.37}$$

The stochastic part is transformed into the interaction picture

$$H_{1,\mathrm{I}}(t) = U_0(t)^\dagger H_1(t) U_0(t), \tag{B.38}$$

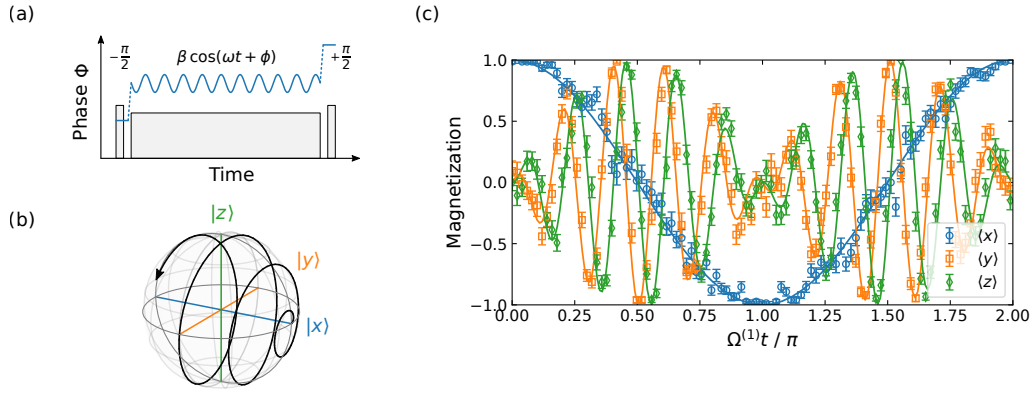

Figure B.1: Spin-locking under coherent phase modulation. (a) Experimental sequence. A $\pi/2$ pulse prepares the qubit in $|x\rangle$. Then the qubit is continuously driven with a Rabi frequency Ω by a light field. During this time, the phase of the light is modulated with a frequency ω and a modulation index β. A final $\pi/2$ pulse analyzes the state of the qubit. (b) The state evolves on the Bloch sphere on a spiral trajectory. The spiral oscillates between the two poles. (c) Observed evolution in a spin-locking experiment. Experimental data (markers) and numerical simulation (lines). The experiment was carried out for $\Omega = \omega = 2\pi \times 5\,\mathrm{kHz}$ and a modulation index $\beta = 200\,\mathrm{mrad}$.

with $U_0(t)$ given by Eq. (B.30). This operator is of the form $H_{1,I}(t) = \phi(t)(a(t)\sigma_x + b(t)\sigma_y + c(t)\sigma_z)$, where $\phi(t)$ is again assumed to be a zero-mean random process. Therefore, the evolution of the density matrix in the interaction picture $\rho_I(t)$ is described by the stochastic Liouville equation in the same way as described in Sec. 5.3.1. The cumulant $\langle \mathcal{L}(t_1)\mathcal{L}(t_2)\rangle_c$ contains a large number of terms; however, in the limit $\Omega^{(1)} \to 0$ one finds that $\Phi(t)$ is equal to the case of zero-mean noise, Eq. (5.23). If the qubit is initially prepared in the $|+x\rangle$ state, the magnetization evolves as

$$\langle x(t)\rangle = \mathrm{Tr}\left[U_0(t)\,\langle\rho_I(t)\rangle\,U_0^\dagger(t)\sigma_x\right] \tag{B.39}$$

$$= \mathrm{Tr}\left[U_0(t)\frac{1}{2}(\mathbb{1} + \mathrm{e}^{-4\chi(t)}\sigma_x)U_0^\dagger(t)\sigma_x\right] \tag{B.40}$$

$$= \frac{1}{2}\mathrm{e}^{-4\chi(t)}\,\mathrm{Tr}\left[U_0(t)\sigma_x U_0^\dagger(t)\sigma_x\right]. \tag{B.41}$$

Since we have assumed $\rho_0 = \frac{1}{2}(\mathbb{1} + \sigma_x)$, we can express σ_x by ρ_0 and get

$$\langle x(t)\rangle = \frac{1}{2}\mathrm{e}^{-4\chi(t)}\,\mathrm{Tr}\left[U_0(t)(2\rho_0 - \mathbb{1})U_0^\dagger(t)\sigma_x\right] \tag{B.42}$$

$$= \mathrm{e}^{-4\chi(t)}\,\langle x(t)\rangle_0 \tag{B.43}$$

$$= \mathrm{e}^{-\frac{1}{2}\Omega^2 S_\phi(\Omega)t}\cos\left(\Omega^{(1)}t\right). \tag{B.44}$$

In the second-to-last step, $\langle x(t)\rangle_0 \equiv \mathrm{Tr}[U_0(t)\rho_0 U_0^\dagger(t)\sigma_x]$ denotes the magnetization under coherent evolution, as described by Eq. (B.31). **The main result of this calculation is that a coherent drive with noise is simply described by the product of the incoherent part and the coherent part, leading to damped oscillations.**

B.2.3 *Spin-locking under finite life time*

The effect of the finite lifetime of the excited level on the spin-locking spectroscopy signal is derived in this section. The derived expression will be a lower bound for the detectable minimal noise strength under finite lifetime. Therefore, as a simplification, it is assumed that the noise acting on the spin is weak and can be neglected. The light-atom interaction is then described by the Lindblad equation

$$\frac{\mathrm{d}}{\mathrm{d}t}\rho(t) = -\mathrm{i}\,[H,\rho] + \mathcal{L}(\rho), \tag{B.45}$$

with the Hamiltonian

$$H = \frac{\Omega}{2}\sigma_x \tag{B.46}$$

and the Lindblad operator

$$\mathcal{L}(\rho) = F\rho F^\dagger - \frac{1}{2}(F^\dagger F\rho + \rho F^\dagger F). \tag{B.47}$$

Here, Ω is the Rabi frequency, σ_x the Pauli-x operator, $F = \sqrt{\Gamma}\sigma^-$ the jump operator, and σ^- the lowering operator. Γ is the decay rate from the excited level to the ground level. For $^{40}Ca^+$, the decay rate from the $D_{5/2}$ level to the $S_{1/2}$ level is $\Gamma \approx 0.9\,\mathrm{s}^{-1}$ [33]. Plugging these expressions into the Lindblad equation gives

$$\frac{\mathrm{d}}{\mathrm{d}t}\begin{pmatrix}\rho_{11}\\ \rho_{12}\\ \rho_{21}\\ \rho_{22}\end{pmatrix} = \begin{pmatrix} -\Gamma & \mathrm{i}\frac{\Omega}{2} & -\mathrm{i}\frac{\Omega}{2} & 0\\ \mathrm{i}\frac{\Omega}{2} & -\frac{\Gamma}{2} & 0 & -\mathrm{i}\frac{\Omega}{2}\\ -\mathrm{i}\frac{\Omega}{2} & 0 & -\frac{\Gamma}{2} & \mathrm{i}\frac{\Omega}{2}\\ \Gamma & -\mathrm{i}\frac{\Omega}{2} & \mathrm{i}\frac{\Omega}{2} & 0\end{pmatrix}\begin{pmatrix}\rho_{11}\\ \rho_{12}\\ \rho_{21}\\ \rho_{22}\end{pmatrix}. \tag{B.48}$$

We do not need to find the general solution to this system of equations, as we are only interested in the expectation value $\langle x(t)\rangle = \rho_{12}(t) + \rho_{21}(t)$. By adding rows 2 and 3, we find

$$\frac{\mathrm{d}}{\mathrm{d}t}\underbrace{(\rho_{12}+\rho_{21})}_{\langle x(t)\rangle} = -\frac{1}{2}\Gamma\underbrace{(\rho_{12}+\rho_{21})}_{\langle x(t)\rangle}, \tag{B.49}$$

from where the solution can be obtained easily,

$$\langle x(t)\rangle = \langle x(0)\rangle\,\mathrm{e}^{-\frac{1}{2}\Gamma t}. \tag{B.50}$$

This means that spontaneous decay gives the same exponential decay as phase noise with power spectral density $S_\phi(\Omega)$,

$$\langle x(t)\rangle = \langle x(0)\rangle\,\mathrm{e}^{-\frac{1}{2}\Omega^2 S_\phi(\Omega)t}. \tag{B.51}$$

Equating the exponents gives the lower bound $S_{\phi,\mathrm{lim}}$ for the phase noise power spectral density that can be sensed with a spin that decays from an excited level with rate Γ. The lower bound is

$$S_{\phi,\mathrm{lim}} = \frac{\Gamma}{\Omega^2}. \tag{B.52}$$

C

SOME OPERATOR ALGEBRA

C.1 OPERATOR IDENTITIES FOR TROTTER ALGEBRA

In this section a number of useful identities for algebraic manipulations of Trotter sequences are collected.

C.1.1 *Definitions*

The following definitions are used with $\gamma = x, y, z$ and a system size of $n \geq 2$ qubits. The spin-spin coupling matrix is denoted by J_{ij}. For simplicity, $\hbar = 1$. The Hamiltonian $H_{\gamma\gamma}$ is

$$H_{\gamma\gamma} = \sum_{i<j} J_{ij} \sigma_\gamma^{(i)} \sigma_\gamma^{(j)}. \tag{C.1}$$

The time-evolution operator is

$$U_{\gamma\gamma} = \mathrm{e}^{-\mathrm{i} H_{\gamma\gamma} t}. \tag{C.2}$$

A $\pi/2$ rotation of all qubits is described by

$$R_\gamma = \mathrm{e}^{-\mathrm{i} \frac{\pi}{4} \sum_i \sigma_\gamma^{(i)}}. \tag{C.3}$$

C.1.2 *Identities for substituting a rotation*

$$R_x = R_z^\dagger R_y R_z = R_z R_y^\dagger R_z^\dagger \tag{C.4}$$
$$R_x = R_y^\dagger R_z^\dagger R_y = R_y R_z R_y^\dagger \tag{C.5}$$
$$R_y = R_x^\dagger R_z R_x = R_x R_z^\dagger R_x^\dagger \tag{C.6}$$
$$R_y = R_z^\dagger R_x^\dagger R_z = R_z R_x R_z^\dagger \tag{C.7}$$
$$R_z = R_y^\dagger R_x R_y = R_y R_x^\dagger R_y^\dagger \tag{C.8}$$
$$R_z = R_x^\dagger R_y^\dagger R_x = R_x R_y R_x^\dagger \tag{C.9}$$

C.1.3 *Identities for combinations of rotations*

These identities are directly derived from Sec. C.1.2

$$R_x R_y = R_y R_z = R_z R_x \tag{C.10}$$
$$R_y R_x = R_z^\dagger R_y = R_x R_z^\dagger \tag{C.11}$$
$$R_x R_z = R_z R_y^\dagger = R_y^\dagger R_x \tag{C.12}$$
$$R_z R_y = R_x^\dagger R_z = R_y R_x^\dagger \tag{C.13}$$

C.1.4 *Identities for conversion between U_{xx}, U_{yy}, and U_{zz}*

$$U_{xx} = R_z^\dagger U_{yy} R_z = R_z U_{yy} R_z^\dagger \tag{C.14}$$
$$U_{xx} = R_y^\dagger U_{zz} R_y = R_y U_{zz} R_y^\dagger \tag{C.15}$$
$$U_{yy} = R_x^\dagger U_{zz} R_x = R_x U_{zz} R_x^\dagger \tag{C.16}$$
$$U_{yy} = R_z^\dagger U_{xx} R_z = R_z U_{xx} R_z^\dagger \tag{C.17}$$
$$U_{zz} = R_y^\dagger U_{xx} R_y = R_y U_{xx} R_y^\dagger \tag{C.18}$$
$$U_{zz} = R_x^\dagger U_{yy} R_x = R_x U_{yy} R_x^\dagger \tag{C.19}$$
$$\tag{C.20}$$

C.2 BASE ROTATIONS OF THE HEISENBERG TROTTERIZATION

The Heisenberg-Hamiltonian was approximated by decomposing the time-evolution into

$$U^{(2\text{alt})}(\Delta t, 8N) = R_{-y} R_x \left[(E_-(\Delta t))^4 (E_+(\Delta t))^4 \right]^N R_{-x} R_y, \tag{C.21}$$

where the sub-step

$$E_\pm(\Delta t) = U_{yy}(\Delta t) U_{xx}(\Delta t) R_{\pm x} U_{yy}(\Delta t) \tag{C.22}$$

has been introduced and R_x (R_y, R_z) denotes a global $\pi/2$-rotation around the x-axis (y, z) and

$$U_{xx}(\Delta t) = \mathrm{e}^{-\mathrm{i}\Delta t H_{xx}}, \quad H_{xx} = \sum_{i=1}^{N_{\text{ions}}} \sum_{j>i} J_{i,j} \sigma_x^{(i)} \sigma_x^{(j)}, \tag{C.23}$$

$U_{yy}(\Delta t)$, H_{yy} respectively.

If the Trotter decomposition is stopped after a sub-step the Trotter decomposition is of a slightly different form. To return to the initial basis various final rotations must be used. The following scheme of Trotter steps was implemented in the experiment:

$$U^{(2\text{alt})}(\Delta t, 1) = R_{-y} \left[(E_+(\Delta t))^1 \right] R_{-x} R_y \tag{C.24}$$

$$U^{(2\text{alt})}(\Delta t, 2) = R_{-y} R_{-x} \left[(E_+(\Delta t))^2 \right] R_{-x} R_y \tag{C.25}$$

$$U^{(2\text{alt})}(\Delta t, 3) = R_x R_x R_y \Big[\big(E_+(\Delta t)\big)^3 \Big] R_{-x} R_y \tag{C.26}$$

$$U^{(2\text{alt})}(\Delta t, 4) = R_{-y} R_x \Big[\big(E_+(\Delta t)\big)^4 \Big] R_{-x} R_y \tag{C.27}$$

$$U^{(2\text{alt})}(\Delta t, 5) = R_x R_x R_y \Big[\big(E_-(\Delta t)\big)^1 \big(E_+(\Delta t)\big)^4 \Big] R_{-x} R_y \tag{C.28}$$

$$U^{(2\text{alt})}(\Delta t, 6) = R_{-y} R_{-x} \Big[\big(E_-(\Delta t)\big)^2 \big(E_+(\Delta t)\big)^4 \Big] R_{-x} R_y \tag{C.29}$$

$$U^{(2\text{alt})}(\Delta t, 7) = R_{-y} \Big[\big(E_-(\Delta t)\big)^3 \big(E_+(\Delta t)\big)^4 \Big] R_{-x} R_y \tag{C.30}$$

$$U^{(2\text{alt})}(\Delta t, 8) = R_{-y} R_x \Big[\big(E_-(\Delta t)\big)^4 \big(E_+(\Delta t)\big)^4 \Big] R_{-x} R_y \tag{C.31}$$

After these 8 steps, the scheme is repeating.

LIST OF PUBLICATIONS

PUBLICATIONS DISCUSSED IN THIS THESIS

1. F. Kranzl, M. K. Joshi, C. Maier, T. Brydges, J. Franke, R. Blatt, and C. F. Roos – *Controlling long ion strings for quantum simulation and precision measurements*, Phys. Rev. A **105**, 052426 (2022).

2. F. Kranzl*, A. Lasek*, M. K. Joshi, A. Kalev, R. Blatt, C. F. Roos, and N. Y. Halpern – *Experimental Observation of Thermalization with Noncommuting Charges*,
Phys. Rev. X Quantum **4**, 020318 (2023).

3. F. Kranzl*, S. Birnkammer*, M. K. Joshi, A. Bastianello, R. Blatt, M. Knap, and C. F. Roos – *Observation of Magnon Bound States in the Long-Range, Anisotropic Heisenberg Model*,
Phys. Rev. X **13**, 031017 (2023).

4. F. Kranzl, A. Rospars, J. Franke, M. K. Joshi, R. Blatt, and C. F. Roos – *Motional spin-locking spectroscopy*, Manuscript in preparation.

FURTHER PUBLICATIONS

5. M. K. Joshi, F. Kranzl, A. Schuckert, I. Lovas, C. Maier, R. Blatt, M. Knap, and C. F. Roos – *Observing emergent hydrodynamics in a long-range quantum magnet*,
Science **724**, 720-724 (2022).

6. H. Hainzer, D. Kiesenhofer, T. Ollikainen, M. Bock, F. Kranzl, M. K. Joshi, G. Yoeli, R. Blatt, T. Gefen, and C. F. Roos – *Correlation Spectroscopy with Multiqubit-Enhanced Phase Estimation*,
Phys. Rev. X **14**, 011033 (2024).

7. J. Franke, S. R. Muleady, R. Kaubruegger, F. Kranzl, R. Blatt, A. M. Rey, M. K. Joshi, and C. F. Roos – *Quantum-enhanced sensing on optical transitions through finite-range interactions*,
Nature **621**, 740-745 (2023).

8. M. K. Joshi, C. Kokail, R. van Bijnen, F. Kranzl, T. V. Zache, R. Blatt, C. F. Roos, and P. Zoller – *Exploring large-scale entanglement in quantum simulation*, Nature **624**, 539–544 (2023).

9. L. Kh. Joshi, J. Franke, A. Rath, F. Ares, S. Murciano, F. Kranzl, R. Blatt, P. Zoller, B. Vermersch, P. Calabrese, C. F. Roos, M. K. Joshi – *Observing the Quantum Mpemba Effect in Quantum Simulations*,
Phys. Rev. Lett. **133**, 010402 (2024).

10. M. K. Joshi, M. Guevara-Bertsch, F. Kranzl, R. Blatt, and C. F. Roos – *Characterization of ion-trap-induced ac magnetic fields*,
Phys. Rev. A **110**, 063101 (2024)

BIBLIOGRAPHY

[1] Feynman, R. P. *"Simulating Physics with Computers"*. *International Journal of Theoretical Physics* **21,** 467–488 (1982).

[2] Szymanski, B., Dubessy, R., Dubost, B., Guibal, S., Likforman, J.-P. & Guidoni, L. *"Large two dimensional Coulomb crystals in a radio frequency surface ion trap"*. *Applied Physics Letters* **100,** 171110 (2012).

[3] Kiesenhofer, D., Hainzer, H., Zhdanov, A., Holz, P. C., Bock, M., Ollikainen, T. & Roos, C. F. *"Controlling two-dimensional Coulomb crystals of more than 100 ions in a monolithic radio-frequency trap"*. *PRX Quantum* **4,** 020317 (2023).

[4] Guo, S.-A., Wu, Y.-K., Ye, J., Zhang, L., Lian, W.-Q., Yao, R., Wang, Y., Yan, R.-Y., Yi, Y.-J., Xu, Y.-L., *et al. "A site-resolved two-dimensional quantum simulator with hundreds of trapped ions"*. *Nature* **630,** 613–618 (2024).

[5] Lloyd, S. *"Universal Quantum Simulators"*. *Science* **273,** 1073–1078 (1996).

[6] Lanyon, B. P. *et al. "Universal Digital Quantum Simulation with Trapped Ions"*. *Science* **334,** 57–60 (2011).

[7] Greiner, M., Mandel, O., Esslinger, T., Hänsch, T. W. & Bloch, I. *"Quantum phase transition from a superfluid to a Mott insulator in a gas of ultracold atoms"*. *Nature* **415,** 39–44 (2002).

[8] Friedenauer, A., Schmitz, H., Glueckert, J. T., Porras, D. & Schaetz, T. *"Simulating a quantum magnet with trapped ions"*. *Nature Physics* **4,** 757–761 (2008).

[9] Kim, K., Chang, M., Korenblit, S., Islam, R., Edwards, E. E., Freericks, J. K., Lin, G., Duan, L. & Monroe, C. *"Quantum simulation of frustrated Ising spins with trapped ions"*. *Nature* **465,** 590–593 (2010).

[10] Britton, J. W., Sawyer, B. C., Keith, A. C., Wang, C. J., Freericks, J. K., Uys, H., Biercuk, M. J. & Bollinger, J. J. *"Engineered two-dimensional Ising interactions in a trapped-ion quantum simulator with hundreds of spins"*. *Nature* **484,** 489–492 (2012).

[11] Lanyon, B. P. *et al. "Towards quantum chemistry on a quantum computer"*. *Nature Chemistry* **2,** 106–111 (2010).

[12] Du, J., Xu, N., Peng, X., Wang, P., Wu, S. & Lu, D. *"NMR Implementation of a Molecular Hydrogen Quantum Simulation with Adiabatic State Preparation"*. *Physical Review Letters* **104,** 030502 (2010).

[13] Hempel, C. *et al. "Quantum Chemistry Calculations on a Trapped-Ion Quantum Simulator"*. *Physical Review X* **8,** 31022 (2018).

[14] Gerritsma, R., Kirchmair, G., Zähringer, F., Solano, E., Blatt, R. & Roos, C. F. *"Quantum simulation of the Dirac equation"*. *Nature* **463,** 68–71 (2010).

[15] Georgescu, I. M., Ashhab, S. & Nori, F. *"Quantum simulation"*. *Reviews of Modern Physics* **86,** 153–185 (2014).

[16] Cirac, J. I. & Zoller, P. *"Goals and opportunities in quantum simulation"*. *Nature Physics* **8,** 264–266 (2012).

[17] DiVincenzo, D. P. *"The Physical Implementation of Quantum Computation"*. *Fortschritte der Physik* **48,** 771–783 (2000).

[18] Hempel, C. *"Digital quantum simulation, Schrödinger cat state spectroscopy and setting up a linear ion trap"*. PhD thesis (University of Innsbruck, 2014).

[19] Leibfried, D., Blatt, R., Monroe, C. & Wineland, D. *"Quantum dynamics of single trapped ions"*. *Reviews of Modern Physics* **75,** 281–324 (2003).

[20] Myerson, A. H., Szwer, D. J., Webster, S. C., Allcock, D. T. C., Curtis, M. J., Imreh, G., Sherman, J. A., Stacey, D. N., Steane, A. M. & Lucas, D. M. *"High-Fidelity Readout of Trapped-Ion Qubits"*. *Physical Review Letters* **100,** 200502 (2008).

[21] Kokail, C. *et al. "Self-verifying variational quantum simulation of lattice models"*. *Nature* **569,** 355–360 (2019).

[22] Carrasco, J., Elben, A., Kokail, C., Kraus, B. & Zoller, P. *"Theoretical and Experimental Perspectives of Quantum Verification"*. *PRX Quantum* **2,** 010102 (2021).

[23] Shaffer, R., Megidish, E., Broz, J., Chen, W.-T. & Häffner, H. *"Practical verification protocols for analog quantum simulators"*. *npj Quantum Information* **7,** 46 (2021).

[24] Feynman, R. P., Vernon Jr., F. L. & Hellwarth, R. W. *"Geometrical representation of the Schrödinger equation for solving maser problems"*. *Journal of Applied Physics* **28,** 49–52 (1957).

[25] Horodecki, R., Horodecki, P., Horodecki, M. & Horodecki, K. *"Quantum entanglement"*. *Reviews of Modern Physics* **81,** 865–942 (2009).

[26] Werner, R. F. *"Quantum states with Einstein-Podolsky-Rosen correlations admitting a hidden-variable model"*. *Physical Review A* **40,** 4277–4281 (1989).

[27] Plenio, M. B. & Virmani, S. *"An introduction to entanglement measures"*. *Quantum Information and Computation* **7,** 001–051 (2007).

[28] Neuhauser, W., Hohenstatt, M., Toschek, P. & Dehmelt, H. *"Optical-Sideband Cooling of Visible Atom Cloud Confined in Parabolic Well"*. *Physical Review Letters* **41,** 233–236 (1978).

[29] Wineland, D. J., Drullinger, R. E. & Walls, F. L. *"Radiation-Pressure Cooling of Bound Resonant Absorbers"*. *Physical Review Letters* **40,** 1639–1642 (1978).

[30] Wineland, D. J. & Itano, W. M. *"Laser cooling of atoms"*. *Physical Review A* **20,** 1521–1540 (1979).

[31] Nagourney, W., Sandberg, J. & Dehmelt, H. *"Shelved Optical Electron Amplifier: Observation of Quantum Jumps"*. *Physical Review Letters* **56,** 2797–2799 (1986).

[32] Sauter, T., Neuhauser, W., Blatt, R. & Toschek, P. E. *"Observation of Quantum Jumps"*. *Physical Review Letters* **57,** 1696–1698 (1986).

[33] Barton, P. A., Donald, C. J., Lucas, D. M., Stevens, D. A., Steane, A. M. & Stacey, D. N. *"Measurement of the lifetime of the $3d^2D_{5/2}$ state in $^{40}Ca^+$"*. *Physical Review A* **62,** 032503 (2000).

[34] Marzoli, I., Cirac, J. I., Blatt, R. & Zoller, P. *"Laser cooling of trapped three-level ions: Designing two-level systems for sideband cooling"*. *Physical Review A* **49,** 2771–2779 (1994).

[35] Jurcevic, P. *"Quantum Computation and Many-Body Physics with Trapped Ions"*. PhD thesis (University of Innsbruck, 2017).

[36] Paul, W., Osberghaus, O. & Fischer, E. *"Ein Ionenkäfig"*. *Forschungsber. Wirtsch.-Verkehrminist. Nordrhein-Westfalen* **415** (1958).

[37] Wineland, D., Ekstrom, P. & Dehmelt, H. *"Monoelectron Oscillator"*. *Physical Review Letters* **31,** 1279–1282 (1973).

[38] Neuhauser, W., Hohenstatt, M., Toschek, P. E. & Dehmelt, H. *"Localized visible Ba^+ mono-ion oscillator"*. *Physical Review A* **22,** 1137–1140 (1980).

[39] Paul, W. *"Electromagnetic traps for charged and neutral particles"*. *Reviews of Modern Physics* **62,** 531–540 (1990).

[40] James, D. F. V. *"Quantum dynamics of cold trapped ions with application to quantum computation"*. *Applied Physics B: Lasers and Optics* **66,** 181–190 (1998).

[41] Marquet, C., Schmidt-Kaler, F. & James, D. F. V. *"Phonon–phonon interactions due to non-linear effects in a linear ion trap"*. *Applied Physics B: Lasers and Optics* **76,** 199–208 (2003).

[42] Schiffer, J. P. *"Phase Transitions in Anisotropically Confined Ionic Crystals"*. *Physical Review Letters* **70,** 818–821 (1993).

[43] Candido, L., Rino, J.-P., Studart, N. & Peeters, F. M. P. *"The structure and spectrum of the anisotropically confined two-dimensional Yukawa system"*. *Journal of Physics: Condensed Matter* **10,** 11627–11644 (1998).

[44] Fishman, S., Chiara, G. D., Calarco, T. & Morigi, G. *"Structural phase transitions in low-dimensional ion crystals"*. *Physical Review B* **77,** 064111 (2008).

[45] Raizen, M. G., M., G. J., Bergquist, J. C., Itano, W. M. & Wineland, D. J. *"Ionic crystals in a linear Paul trap"*. *Physical Review A* **45,** 6493–6501 (1992).

[46] Enzer, D. G. *et al. "Observation of Power-Law Scaling for Phase Transitions in Linear Trapped Ion Crystals"*. *Physical Review Letters* **85,** 2466–2469 (2000).

[47] Steane, A. *"The ion trap quantum information processor"*. *Applied Physics B* **64,** 623–643 (1997).

[48] Brownnutt, M., Kumph, M., Rabl, P. & Blatt, R. *"Ion-trap measurements of electric-field noise near surfaces"*. *Reviews of Modern Physics* **87,** 1419–1482 (2015).

[49] Freedhoff, H. S. *"Classical Oscillator Model for Electric Quadrupole Transitions"*. *The Journal of Chemical Physics* **54,** 1618–1626 (1971).

[50] Cirac, J. I., Parkins, A. S., Blatt, R. & Zoller, P. *"Nonclassical states of motion in ion traps"*. *Advances in Atomic, Molecular, and Optical Physics* **37,** 237–296 (1996).

[51] Roos, C. *"Controlling the quantum state of trapped ions"*. PhD thesis (University of Innsbruck, 2000).

[52] Benhelm, J. *"Precision Spectroscopy and Quantum Information Processing with Trapped Calcium Ions"*. PhD thesis (University of Innsbruck, 2008).

[53] Mølmer, K. & Sørensen, A. *"Multiparticle Entanglement of Hot Trapped Ions"*. *Physical Review Letters* **82,** 1835–1838 (1999).

[54] Porras, D. & Cirac, J. I. *"Effective Quantum Spin Systems with Trapped Ions"*. *Physical Review Letters* **92,** 207901 (2004).

[55] Itano, W. M. *"External-Field Shifts of the* $^{199}Hg^{+}$ *Optical Frequency Standard"*. *Journal of Research of the National Institute of Standards and Technology* **105,** 829–837 (2000).

[56] Roos, C. F., Chwalla, M., Kim, K., Riebe, M. & Blatt, R. *"'Designer atoms' for quantum metrology"*. *Nature* **443,** 316–319 (2006).

[57] Kim, K. *et al. "Quantum simulation of the transverse Ising model with trapped ions"*. *New Journal of Physics* **13,** 105003 (2011).

[58] Joshi, M. K., Kokail, C., van Bijnen, R., Kranzl, F., Zache, T. V., Blatt, R., Roos, C. F. & Zoller, P. *"Exploring large-scale entanglement in quantum simulation"*. *Nature* **624,** 539–544 (2023).

[59] Maier, C. *"A quantum simulator with long strings of trapped ions"*. PhD thesis (University of Innsbruck, 2020).

[60] Brydges, T. *"Randomised Measurements with Strings of Trapped Ions"*. PhD thesis (University of Innsbruck, 2021).

[61] Franke, J. *"Magnetic field noise cancellation for quantum simulation experiment with trapped ions"*. Master's thesis (University of Innsbruck, 2021).

[62] Kranzl, F., Joshi, M. K., Maier, C., Brydges, T., Franke, J., Blatt, R. & Roos, C. F. *"Controlling long ion strings for quantum simulation and precision measurements"*. *Physical Review A* **105,** 052426 (2022).

[63] Gosselin, R. N., Pinnington, E. H. & Ansbacher, W. *"Measurement of the lifetimes of the 4p levels in Ca II using laser excitation of a fast beam"*. *Physical Review A* **38,** 4887–4890 (1988).

[64] Joshi, M. K., Fabre, A., Maier, C., Brydges, T., Kiesenhofer, D., Hainzer, H., Blatt, R. & Roos, C. F. *"Polarization-gradient cooling of 1D and 2D ion Coulomb crystals"*. *New Journal of Physics* **22,** 103013 (2020).

[65] Diedrich, F., Bergquist, J. C., Itano, W. M. & Wineland, D. J. *"Laser Cooling to the Zero-Point Energy of Motion"*. *Physical Review Letters* **62,** 403–406 (1989).

[66] Winkler, A. *"Frequency Stabilization of a 729 nm Ti:Sa Laser for Qubit Manipulation in Trapped Calcium Ions"*. Master's thesis (University of Innsbruck, 2023).

[67] Carr, H. Y. & Purcell, E. M. *"Effects of diffusion on free precession in nuclear magnetic resonance experiments"*. *Physical Review* **94,** 630 (1954).

[68] Johansson, J. R., Nation, P. D. & Nori, F. *"QuTiP 2: A Python framework for the dynamics of open quantum systems"*. *Comput. Phys. Commun.* **184,** 1234–1240 (2013).

[69] Chwalla, M., Kim, K., Monz, T., Schindler, P., Riebe, M., Roos, C. F. & Blatt, R. *"Precision spectroscopy with two correlated atoms"*. *Applied Physics B: Lasers and Optics* **89,** 483–488 (2007).

[70] Hainzer, H., Kiesenhofer, D., Ollikainen, T., Bock, M., Kranzl, F., Joshi, M. K., Yoeli, G., Blatt, R., Gefen, T. & Roos, C. F. *"Correlation spectroscopy with multiqubit-enhanced phase estimation"*. *Physical Review X* **14,** 011033 (2024).

[71] Araneda, G., Walser, S., Colombe, Y., Higginbottom, D. B., Volz, J., Blatt, R. & Rauschenbeutel, A. *"Wavelength-scale errors in optical localization due to spin–orbit coupling of light"*. *Nature Physics* **15,** 17–21 (2019).

[72] Qian, Z.-H., Cui, J.-M., Luo, X.-W., Zheng, Y.-X., Huang, Y.-F., Ai, M.-Z., He, R., Li, C.-F. & Guo, G.-C. *"Super-resolved imaging of a single cold atom on a nanosecond timescale"*. *Physical Review Letters* **127,** 263603 (2021).

[73] Trotter, H. F. *"On the product of semi-groups of operators"*. *Proceedings of the American Mathematical Society* **10,** 545–551 (1959).

[74] Suzuki, M. *"Decomposition formulas of exponential operators and Lie exponentials with some applications to quantum mechanics and statistical physics"*. *Journal of Mathematical Physics* **26,** 601–612 (1985).

[75] Suzuki, M. *"Fractal decomposition of exponential operators with applications to many-body theories and Monte Carlo simulations"*. *Physics Letters A* **146,** 319–323 (1990).

[76] Suzuki, M. *"General theory of fractal path integrals with applications to many-body theories and statistical physics"*. *Journal of Mathematical Physics* **32,** 400–407 (1991).

[77] Janke, W. & Sauer, T. *"Properties of higher-order Trotter formulas"*. *Physics Letters A* **165,** 199–205 (1992).

[78] Brown, K. R., Clark, R. J. & Chuang, I. L. *"Limitations of quantum simulation examined by simulating a pairing hamiltonian using nuclear magnetic resonance"*. *Physical Review Letters* **97,** 050504 (2006).

[79] Barends, B. *et al. "Digital quantum simulation of fermionic models with a superconducting circuit"*. *Nature Communications* **6,** 7654 (2015).

[80] Geier, S., Thaicharoen, N., Hainaut, C., Franz, T., Salzinger, A., Tebben, A., Grimshandl, D., Zürn, G. & Weidemüller, M. *"Floquet Hamiltonian engineering of an isolated many-body spin system"*. *Science* **374,** 1149–1152 (2021).

[81] Scholl, P. *et al.* *"Microwave Engineering of Programmable XXZ Hamiltonians in Arrays of Rydberg Atoms"*. *PRX Quantum* **3,** 020303 (2022).

[82] Choi, J., Zhou, H., Knowles, H. S., Landig, R., Choi, S. & Lukin, M. D. *"Robust Dynamic Hamiltonian Engineering of Many-Body Spin Systems"*. *Physical Review X* **10,** 31002 (2020).

[83] Kranzl, F., Lasek, A., Joshi, M. K., Kalev, A., Blatt, R., Roos, C. F. & Halpern, N. Y. *"Experimental observation of thermalization with noncommuting charges"*. *Physical Review X Quantum* **4,** 020318 (2023).

[84] Morong, W., Collins, K. S., De, A., Stavropoulos, E., You, T. & Monroe, C. *"Engineering dynamically decoupled quantum simulations with trapped ions"*. *PRX Quantum* **4,** 010334 (2023).

[85] Häffner, H., Gulde, S., Riebe, M., Lancaster, G., Becher, C., Eschner, J., Schmidt-Kaler, F. & Blatt, R. *"Precision Measurement and Compensation of Optical Stark Shifts for an Ion-Trap Quantum Processor"*. *Physical Review Letters* **90,** 143602 (2003).

[86] Schindler, P. *"Frequency synthesis and pulse shaping for quantum information processing with trapped ions"*. Master's thesis (University of Innsbruck, 2008).

[87] Kirchmair, G. *"Frequency stabilization of a Titanium-Sapphire laser for precision spectroscopy on Calcium ions"*. Master's thesis (University of Innsbruck, 2006).

[88] Pham, P. *"A general-purpose pulse sequencer for quantum computing"*. Master's thesis (Massachuseetts Institute of Technology, 2005).

[89] Hartmann, S. R. & Hahn, E. L. *"Nuclear double resonance in the rotating frame"*. *Physical Review* **128,** 2042 (1962).

[90] Look, D. C., Lowe, I. J. & Northby, J. A. *"Nuclear magnetic resonance study of molecular motions in solid hydrogen sulfide"*. *The Journal of Chemical Physics* **44,** 3441–3452 (1966).

[91] Loretz, M., Rosskopf, T. & Degen, C. L. *"Radio-Frequency Magnetometry Using a Single Electron Spin"*. *Physical Review Letters* **110,** 017602 (2013).

[92] Yan, F., Gustavsson, S., Bylander, J., Jin, X., Yoshihara, F., Cory, D. G., Nakamura, Y., Orlando, T. P. & Oliver, W. D. *"Rotating-frame relaxation as a noise spectrum analyser of a superconducting qubit undergoing driven evolution"*. *Nature Communications* **4,** 2337 (2013).

[93] Rospars, A. *"Investigation of Noise in Trapped Ions for Quantum Simulation Experiments Using Continuous Dynamical Decoupling"*. Preprint.

[94] Kubo, R. *"Stochastic Liouville Equations"*. *Journal of Mathematical Physics* **4,** 174–183 (1963).

[95] Van Kampen, N. G. *"Stochastic differential equations"*. *Physics Reports* **24,** 171–228 (1976).

[96] Cywinski, L., Lutchyn, R. M., Nave, C. P. & Sarma, S. D. *"How to enhance dephasing time in superconducting qubits"*. *Physical Review B* **77,** 174509 (2008).

[97] Biercuk, M. J., Uys, H., VanDevender, A. P., Shiga, N., Itano, W. M. & Bollinger, J. J. *"Optimized dynamical decoupling in a model quantum memory"*. *Nature* **458,** 996–1000 (2009).

[98] Willick, K., Park, D. K. & Baugh, J. *"Efficient continuous-wave noise spectroscopy beyond weak coupling"*. *Physical Review A* **98,** 013414 (2018).

[99] Plenio, M. B., Retzker, A., Timoney, N., Baumgart, I., Johanning, M. & Varo, A. F. *"Quantum gates and memory using microwave-dressed states"*. *Nature* **476,** 185–188 (2011).

[100] Xu, X., Wang, Z., Duan, C., Huang, P., Wang, P., Wang, Y., Xu, N., Kong, X., Shi, F., Rong, X., *et al. "Coherence-protected quantum gate by continuous dynamical decoupling in diamond"*. *Physical Review Letters* **109,** 070502 (2012).

[101] Zhang, M., Xie, Y., Zhang, J., Wang, W., Wu, C., Chen, T., Wu, W. & Chen, P. *"Estimation of the Laser Frequency Noise Spectrum by Continuous Dynamical Decoupling"*. *Physical Review Applied* **15,** 014033 (2021).

[102] Stricker, R. *"Gatteroperationen hoher Güte in einem optischen Quantenbit"*. Master's thesis (University of Innsbruck, 2017).

[103] McCormick, K. C., Keller, J., Burd, S. C., Wineland, D. J., Wilson, A. C. & Leibfried, D. *"Quatnum-enhanced sensing of a single-ion mechanical oscillator"*. *Nature* **572,** 86–90 (2019).

[104] McCormick, K. C., Keller, J., Wineland, D. J., Wilson, A. C. & Leibfried, D. *"Coherently displaced oscillator quantum states of a single trapped atom"*. *Quantum Science and Technology* **4,** 024010 (2019).

[105] Milne, A. R., Hempel, C., Li, L., Edmunds, C. L., Slatyer, H. J., Ball, H., Hush, M. R. & Biercuk, M. J. *"Quantum Oscillator Noise Spectroscopy via Displaced Cat States"*. *Physical Review Letters* **126,** 250506 (2021).

[106] Keller, J., Hou, P. Y., McCormick, K. C., Cole, D. C., Erickson, S. D., Wu, J. J., Wilson, A. C. & Leibfried, D. *"Quantum Harmonic Oscillator Spectrum Analyzers"*. *Physical Review Letters* **126,** 250507 (2021).

[107] Sinai, Y. G. *"Dynamical systems with elastic reflections"*. *Russian Mathematical Surveys* **25,** 137–189 (1970).

[108] Bunimovich, L. A. *"On the Ergodic Properties of Nowhere Dispersing Billiards"*. *Communications in Mathematical Physics* **65,** 295–312 (1979).

[109] Polkovnikov, A., Krishnendu, S. & Silva, A. *"Colloquium: Nonequilibrium dynamics of closed interacting quantum systems"*. *Reviews of Modern Physics* **83,** 863–883 (2011).

[110] Deutsch, J. M. *"Eigenstate Thermalization Hypothesis"*. *Reports on Progress in Physics* **81,** 082001 (2018).

[111] Von Neumann, J. *"Beweis des Ergodensatzes und des H-Theorems in der neuen Mechanik"*. *Zeitschrift für Physik* **57,** 30–70 (1929).

[112] Popescu, S., Short, A. J. & Winter, A. *"Entanglement and the foundations of statistical mechanics"*. *Nature Physics* **2,** 754–758 (2006).

[113] Tasaki, H. *"From quantum dynamics to the canonical distribution: General picture and a rigorous example"*. *Physical Review Letters* **80,** 1373–1376 (1998).

[114] Rigol, M., Dunjko, V., Yurovsky, V. & Olshanii, M. *"Relaxation in a completely integrable many-body Quantum system: An Ab initio study of the dynamics of the highly excited states of 1D lattice hard-core bosons"*. *Physical Review Letters* **98,** 050405 (2007).

[115] Kinoshita, T., Wenger, T. & Weiss, D. S. *"A quantum Newton's cradle"*. *Nature* **440,** 900–903 (2006).

[116] Davidson, K. R. *"Almost commuting Hermitian matrices"*. *Mathematica Scandinavica* **56,** 222–240 (1985).

[117] Yunger Halpern, N., Faist, P., Oppenheim, J. & Winter, A. *"Microcanonical and resource-theoretic derivations of the thermal state of a quantum system with noncommuting charges"*. *Nature Communications* **7,** 12051 (2016).

[118] Yunger Halpern, N., Beverland, M. E. & Kalev, A. *"Noncommuting conserved charges in quantum many-body thermalization"*. *Physical Review E* **101,** 42117 (2020).

[119] Ježek, M., Fiurášek, J. & Hradil, Z. *"Quantum inference of states and processes"*. *Physical Review A* **68,** 012305 (2003).

[120] Nielsen, M. A. & Chuang, I. L. *"Quantum Computation and Quantum Information"* (Cambridge University Press, 2010).

[121] Bethe, H. *"Zur Theorie der Metalle"*. *Zeitschrift für Physik* **71,** 205–226 (1931).

[122] Fukuhara, T., Schauß, P., Endres, M., Hild, S., Cheneau, M., Bloch, I. & Gross, C. *"Microscopic observation of magnon bound states and their dynamics"*. *Nature* **502,** 76–79 (2013).

[123] Morvan, A. *et al. "Formation of robust bound states of interacting microwave photons"*. *Nature* **612,** 240–245 (2022).

[124] Hauke, P. & Tagliacozzo, L. *"Spread of correlations in long-range interacting quantum systems"*. *Physical Review Letters* **111,** 207202 (2013).

[125] Jurcevic, P., Lanyon, B. P., Hauke, P., Hempel, C., Zoller, P., Blatt, R. & Roos, C. F. *"Quasiparticle engineering and entanglement propagation in a quantum many-body system"*. *Nature* **511,** 202–205 (2014).

[126] Macrì, T., Lepori, L., Pagano, G., Lewenstein, M. & Barbiero, L. *"Bound state dynamics in the long-range spin-1/2 XXZ model"*. *Physical Review B* **104,** 214309 (2021).

[127] Hanus, J. *"Bound states in the Heisenberg ferromagnet"*. *Physical Review Letters* **11,** 336–338 (1963).

[128] Kranzl, F., Birnkammer, S., Joshi, M. K., Bastianello, A., Blatt, R., Knap, M. & Roos, C. F. *"Observation of Magnon Bound States in the Long-Range, Anisotropic Heisenberg Model"*. *Physical Review X* **13,** 031017 (2023).

[129] Abramowitz, M. & Stegun, I. A. *"Handbook of Mathematical Functions"*, 1143 (Cambridge University Press, 2010).

[130] Jurcevic, P., Hauke, P., Maier, C., Hempel, C., Lanyon, B. P., Blatt, R. & Roos, C. F. *"Spectroscopy of interacting quasiparticles in trapped ions"*. *Physical Review Letters* **115,** 100501 (2015).

[131] Lukin, A., Rispoli, M., Schittko, R., Tai, M. E., Kaufman, A. M., Choi, S., Khemani, V., Léonard, J. & Greiner, M. *"Probing entanglement in a many-body-localized system"*. *Science* **364,** 256–260 (2019).

[132] Wolf, M. M., Verstraete, F., Hastings, M. B. & Cirac, J. I. *"Area laws in quantum systems: Mutual information and correlations"*. *Physical Review Letters* **100,** 070502 (2008).

COLOPHON

This document was typeset using the typographical look-and-feel `classicthesis` developed by André Miede and Ivo Pletikosić. The style was inspired by Robert Bringhurst's seminal book on typography *"The Elements of Typographic Style"*. `classicthesis` is available for both LaTeX and LyX:

https://bitbucket.org/amiede/classicthesis/